



저작자표시-비영리-변경금지 2.0 대한민국

이용자는 아래의 조건을 따르는 경우에 한하여 자유롭게

- 이 저작물을 복제, 배포, 전송, 전시, 공연 및 방송할 수 있습니다.

다음과 같은 조건을 따라야 합니다:



저작자표시. 귀하는 원저작자를 표시하여야 합니다.



비영리. 귀하는 이 저작물을 영리 목적으로 이용할 수 없습니다.



변경금지. 귀하는 이 저작물을 개작, 변형 또는 가공할 수 없습니다.

- 귀하는, 이 저작물의 재이용이나 배포의 경우, 이 저작물에 적용된 이용허락조건을 명확하게 나타내어야 합니다.
- 저작권자로부터 별도의 허가를 받으면 이러한 조건들은 적용되지 않습니다.

저작권법에 따른 이용자의 권리는 위의 내용에 의하여 영향을 받지 않습니다.

이것은 [이용허락규약\(Legal Code\)](#)을 이해하기 쉽게 요약한 것입니다.

[Disclaimer](#)

Rational Design, Preparation, and Analysis of
Chemical Reagents for Investigating Multiple
Pathological Factors in Alzheimer's Disease

Jeffrey S. Derrick

Department of Chemistry

Graduate School of UNIST

Rational Design, Preparation, and Analysis of Chemical Reagents for Investigating Multiple Pathological Factors in Alzheimer's Disease

A thesis submitted to the Graduate School of UNIST
In partial fulfillment of the requirements
for the degree of Master of Science

Jeffrey S. Derrick

06. 10. 2016

Approved by

Advisor

Associate Professor Mi Hee Lim

Rational Design, Preparation, and Analysis of Chemical Reagents for Investigating Multiple Pathological Factors in Alzheimer's Disease

Jeffrey S. Derrick

This certifies that the thesis of Jeffrey S. Derrick is approved

06. 10. 2016

Signature

Advisor: Associate Professor Mi Hee Lim

Signature

Assistant Professor Jung-Min Kee

Signature

Assistant Professor Tae-Hyuk Kwon

Abstract

Alzheimer's disease (AD) is the most common form of neurodegenerative disease that is currently affecting over 28 million people worldwide. Even after more than a century of research, there still is no cure or even effective, long-term therapeutics for AD. As a result, AD continues to increase in prevalence and presents a major socioeconomic burden for today's society. The absence of a cure is most certainly a result of our limited understanding of the cause(s) of AD. For example, due to the involvement of many pathological factors, such as misfolded and aggregated proteins, dysregulated metal ions, and overproduced reactive oxygen species, it is very difficult to unravel and identify the most up-stream causative factors of AD to which a drug can be designed to correct. Therefore, it is clear that in order to begin to determine the underlying cause of AD, we first must develop tools that can be used to probe and investigate the interconnections between these pathological facets. The work presented in this dissertation highlights our efforts toward this goal. Following a detailed introduction given in Chapter 1, a structure-reactivity study is presented in Chapter 2 to determine key pharmacophores that have potential applications for the development of multifunctional chemical tools for AD. In Chapter 3, a small, compact redox-active molecule is identified as a potential anti-amyloidogenic agent for AD that relies on the formation of intramolecular ligand-peptide crosslinks and represents a novel strategy for amyloid management. The applicability of transition metal complexes to control the self-assembly of amyloid- β ($A\beta$) peptides is further probed in Chapter 4 with the use of tetramethylcyclam metal complexes which are shown to hydrolytically cleave amide bonds of $A\beta$ peptides. Finally, Appendix A proposes a novel method to synthetically generate specific diastereomers of our tetramethylcyclam metal complexes based on a newly identified anion effect. Overall, our findings presented herein offer significant contributions toward advancing the development of chemical tools and therapeutics for AD, and our particular emphasis on establishing reaction mechanisms and biological applicability gives us further directions to improve our next-generation reagents.

Table of Contents

Abstract.....	IV
Table of Contents.....	V
List of Tables.....	X
List of Schemes.....	XII
List of Figures.....	XIV
List of Appendices.....	XXXI
List of Abbreviations.....	XXXII

Chapter 1. Tools of the Trade: Investigations into Design Strategies of Small Molecules to Target Components in Alzheimer’s Disease

1.1. Introduction.....	2
1.2. Alzheimer’s Disease.....	2
1.3. Anti-Amyloidogenic Compounds.....	5
1.4. Metal Chelators and Ionophores.....	11
1.5. Multifunctionality.....	15
1.6. Tau-Related Strategies.....	20
1.7. Conclusions.....	22
1.8. References.....	22

Chapter 2. Importance of the Dimethylamino Functionality on a Multifunctional Framework for Regulating Metals, Amyloid- β , and Oxidative Stress in Alzheimer’s Disease

2.1. Introduction.....	29
2.2. Results and Discussion.....	30
2.2.1. Design Rationale and Preparation for Structural Modifications to a Multifunctional Framework.....	31
2.2.2. Effect of AQ Derivatives on Metal-Free and Metal-Induced A β Aggregation.....	33
2.2.3. Direct Interaction Between Soluble Metal-Free A β and AQ Derivatives.....	38
2.2.4. Analysis of AQ Derivatives Incubated with A β_{40} by Ion Mobility–Mass Spectrometry.....	42
2.2.5. Metal Binding Properties of AQ Derivatives.....	45

2.2.6. Biological Properties: ROS Formation Control, Free Radical Scavenging Capacity and Cytotoxicity.....	51
2.3. Conclusions.....	53
2.4. Experimental Section.....	55
2.4.1. Materials and Methods.....	55
2.4.2. Synthesis.....	55
2.4.3. Preparation of 2-(((2-Methylquinolin-8-yl)amino)methyl)phenol (AQP2).....	55
2.4.4. Preparation of Methyl 8-((2-hydroxybenzyl)amino)quinoline-2-carboxylate (AQP3).....	56
2.4.5. Preparation of 2-(((2-(Hydroxymethyl)quinolin-8-yl)amino)methyl)phenol (AQP4).....	56
2.4.6. Preparation of 4-(Dimethylamino)-2-((quinolin-8-ylamino)methyl)phenol (AQDA1).....	57
2.4.7. Preparation of 4-(Dimethylamino)-2-(((2-methylquinolin-8-yl)amino)methyl)phenol (AQDA2).....	57
2.4.8. Preparation of Methyl 8-((5-(dimethylamino)-2-hydroxybenzyl)amino)quinoline-2-carboxylate (AQDA3).....	58
2.4.9. A β Aggregation Experiments.....	58
2.4.10. Gel Electrophoresis with Western Blotting.....	59
2.4.11. Transmission Electron Microscopy (TEM).....	59
2.4.12. 2D NMR Experiments.....	59
2.4.13. Docking Studies.....	60
2.4.14. Ion Mobility–Mass Spectrometry.....	60
2.4.15. Metal Binding Experiments.....	61
2.4.16. Solution Speciation Studies.....	61
2.4.17. 2-Deoxyribose Assay.....	62
2.4.18. Trolox Equivalent Antioxidant Capacity (TEAC) Assay.....	62
2.4.19. Parallel Artificial Membrane Permeability Adapted for the Blood-Brain Barrier (PAMPA-BBB) Assay.....	63
2.4.20. Cell Viability Measurements.....	63
2.5. Acknowledgements.....	64
2.6. References.....	64

Chapter 3. A Redox-Active, Compact Molecule for Cross-Linking Amyloidogenic Peptides into Nontoxic, Off-Pathway Aggregates: *In Vitro* and *In Vivo* Efficacy and Molecular Mechanisms

3.1. Introduction.....	69
3.2. Results and Discussion.....	70
3.2.1. Rational Selection of DMPD Toward Redirecting Both Metal-free and Metal-induced A β Aggregation <i>In Vitro</i> and in Biological Systems.....	70
3.2.2. Effects of DMPD on Both Metal-Free and Metal-Induced A β Aggregation <i>In Vitro</i>	73
3.2.3. Proposed Mechanism of DMPD 's Control Against A β Aggregation Pathways.....	76
3.2.4. Attenuation of Metal-Free A β -/Metal-A β -Induced Toxicity in Living Cells by DMPD	86
3.2.5. <i>In Vivo</i> Efficacy of DMPD Against Amyloid Pathology and Cognitive Impairment.....	89
3.3. Conclusions.....	90
3.4. Experimental Section.....	92
3.4.1. Materials and Methods.....	92
3.4.2. A β Aggregation Experiments.....	92
3.4.3. Gel Electrophoresis and Western Blot.....	93
3.4.4. Transmission Electron Microscopy (TEM).....	93
3.4.5. Computational Procedure.....	94
3.4.6. 2D Band-Selective Optimized Flip-Angle Short Transient (SOFAST)-Heteronuclear Multiple Quantum Correlation (HMQC) NMR Spectroscopy.....	95
3.4.7. Cu K-edge X-ray Absorption Spectroscopy.....	95
3.4.8. Mass Spectrometric Studies.....	96
3.4.9. Animals and Drug Administration.....	97
3.4.10. Tissue Preparation.....	97
3.4.11. A β_{40} /A β_{42} Quantification.....	97
3.4.12. Quantification of A β Plaques.....	98
3.4.13. Behavioral Evaluation.....	98
3.4.14. Statistics.....	98
3.4.15. Trolox Equivalent Antioxidant Capacity (TEAC) Assay.....	98
3.4.16. Parallel Artificial Membrane Permeability Adapted for the Blood-Brain Barrier (PAMPA-BBB) Assay.....	99
3.4.17. Metabolic Stability Measurements.....	99
3.4.18. Cell Viability Measurements.....	100
3.5. Acknowledgements.....	100
3.6. References.....	101

Chapter 4. Tunable Divalent Metal Tetramethylcyclam Complexes: Hydrolytic Reactivities Toward Amyloidogenic Proteins and Mechanisms

4.1. Introduction.....	107
4.2. Results and Discussion.....	109
4.2.1. Design Rationale and Preparation of M(II)(TMC) Complexes.....	109
4.2.2. Effects of M(II)(TMC) on A β Aggregation.....	110
4.2.3. Mechanistic Studies.....	113
4.2.4. Computational Mechanistic Insights.....	129
4.2.5. Proposed Mechanisms for the Hydrolysis of A β by Co(II)(TMC).....	133
4.2.6. Biological Applicability of M(II)(TMC) Complexes.....	136
4.3. Conclusions.....	138
4.4 Experimental Section.....	139
4.4.1. Materials and Methods.....	139
4.4.2. Preparation of M(II)(TMC) Complexes.....	140
4.4.3. [Ni(TMC)](NO ₃) ₂	140
4.4.4. [Co(TMC)(NO ₃)](NO ₃).....	140
4.4.5. [Cu(TMC)(CH ₃ CN)](ClO ₄) ₂	140
4.4.6. [Zn(TMC)(CH ₃ CN)](ClO ₄) ₂	140
4.4.7. A β Aggregation Experiments.....	141
4.4.8. Gel Electrophoresis with Western Blotting.....	141
4.4.9. Transmission Electron Microscopy (TEM).....	142
4.4.10. Electron Paramagnetic Resonance Spectroscopy (EPR).....	142
4.4.11. Matrix-Assisted Laser Desorption Ionization Mass Spectrometry (MALDI-MS).....	143
4.4.12. Computational Details.....	143
4.4.13. Competition Experiments.....	144
4.4.14. Internal Standard Calibration.....	144
4.4.15. Electrospray Ionization–Mass Spectrometry (ESI-MS).....	145
4.4.16. Isomerization Experiments.....	145
4.4.17. Parallel Artificial Membrane Permeability Adapted for the Blood-Brain Barrier (PAMPA- BBB) Assay.....	145
4.4.18. Cell Viability Measurements.....	146
4.5. Acknowledgements.....	146
4.6. References.....	147

Acknowledgements.....176
Curriculum Vitae.....178

List of Tables

Table 2.1. Values (MW, $clogP$, HBA, HBD, PSA, $logBB$, and $-logP_e$) of **AQDA1-3** and **ML**.^a

Table 2.2. Values (MW, $clogP$, HBA, HBD, PSA, $logBB$, and $-logP_e$) of **AQ1-AQ4** and **AQP1-AQP4**.^a

Table 2.3. Calculated collision cross section data from observed 4^+ ligated $A\beta_{40}$ species.

Table 3.1. Brain uptake and antioxidant properties of **DMPD**.

Table 4.1. Selected crystallographic metrics for $Co(II)(TMC)$ and $Ni(II)(TMC)$. The two sets of measurements for $Ni(II)(TMC)$ correspond to the two unique structures found in the asymmetric unit.

Table 4.2. Selected distances and angle measurements of TDDFT-predicted $M(II)(TMC)$ complexes.

Table 4.3. Relative Gibbs free energies (a) of $[M(TMC)(L)]^{2+/+}$ complexes ($M = Co, Ni, Cu, \text{ or } Zn$; $L = H_2O$ or OH^-), and experimental and TDDFT-calculated pK_a values. The Gibbs free energy change (b) for the ligand exchange of the coordinated water molecule with the carbonyl group of the amide bond.

Table 4.4. pK_a s of amino acids.

Table 4.5. Potential blood-brain barrier (BBB) permeability of $Co(II)(TMC)$.

Table A.1. Selected crystallographic metrics for $[Cu(TMC)](NO_3)_2$ and $[Cu(TMC)](ClO_4)_2$.

Table B.1. The monoisotopic mass (m/z), the charge state (z), and sequence for each fragment ion observed in the ESI-MS spectra (Figure 4.9). Detected peaks are denoted as D. Newly generated $A\beta_{40}$ fragments formed upon $M(II)(TMC)$ treatment are labeled in blue. Ions only detected in the samples treated with $Co(II)(TMC)$ or $Cu(II)(TMC)$ are labeled in red and green, respectively.

Table B.2. Crystal data and structure refinement for $[Co(TMC)(NO_3)](NO_3)$.

Table B.3. Crystal data and structure refinement for $[\text{Ni}(\text{TMC})(\text{CH}_3\text{CN})](\text{NO}_3)_2$.

Table B.4. Crystal data and structure refinement for $[\text{Cu}(\text{TMC})](\text{NO}_3)_2$.

List of Schemes

Scheme 1.1. Chemical structures of β -secretase (BACE1) inhibitors. The parent compounds, **KMI-358** and **KMI-370**, were replaced with a tetrazole to afford **KMI-420** and **KMI-429** with improved BACE1 inhibition. **KMI-358**, (5*S*,8*S*,11*S*,14*S*,15*R*)-5-amino-14-benzyl-16-((3-carboxyphenyl)amino)-15-hydroxy-11-isobutyl-8-isopropyl-2,6,9,12,16-pentaoxo-3,7,10,13-tetraazahex-adeconoic acid; **KMI-370**, 5-((4*S*,7*S*,10*S*,13*S*,14*R*)-4-amino-13-benzyl-1-carboxy-14-hydroxy-10-isobutyl-7-isopropyl-1,5,8,11-tetraoxo-2,6,9,12-tetra-azapentadecan-15-amido)isophthalic acid; **KMI-420**, 3-((4*S*,7*S*,10*S*,13*S*,14*R*)-4-amino-13-benzyl-14-hydroxy-10-isobutyl-7-isopropyl-1,5,8,11-tetraoxo-1-(1*H*-tetrazol-5-yl)-2,6,9,12-tetraazapentadecan-15-amido)benzoic acid; **KMI-429**, 5-((4*S*,7*S*,10*S*,13*S*,14*R*)-4-amino-13-benzyl-14-hydroxy-10-isobutyl-7-isopropyl-1,5,8,11-tetraoxo-1-(1*H*-tetrazol-5-yl)-2,6,9,12-tetraazapentadecan-15-amido)isophthalic acid.

Scheme 1.2. The chemical structure of an *apo*-cyclen framework with the A β self-recognition sequence (KLVFF) installed for protein specificity. The amino acid sequence of A β_{42} is provided with the self-recognition sequence highlighted and underlined in blue. The *apo*-compound abstracts Cu(II) from Cu(II)-A β , forming a proteolytically active complex capable of degrading monomeric and oligomeric A β forms.

Scheme 1.3. The chemical structures of 8-hydroxyquinoline (**8-HQ**)-based prochelators (protecting group highlighted in grey) and their respective active forms. The carbamyl protecting group from the dimethylcarbamate (**1**) is cleaved upon inhibition of acetylcholinesterase (AChE) to give 5-((4-(prop-2-yn-1-yl)piperazin-1-yl)methyl)quinolin-8-ol (**2**). **QBP** [8-((3*aR*,4*R*,6*R*,7*R*)-3*a*,5,5-trimethylhexahydro-4,6-methanobenzo[*d*][1,3,2]dioxaborol-2-yl)quino-line] is converted into its active form, **8-HQ**, upon oxidation of its boronic ester-mask.

Scheme 1.4. The chemical structures of the multifunctional molecules. **L2-b**, *N*¹,*N*¹-dimethyl-*N*⁴-(pyridine-2-ylmethyl)benzene-1,4-diamine; **ML**, 4-(dimethylamino)-2-(((2-(hydroxymethyl)-quinolin-8-yl)amino)methyl)phenol; **41**, 5,6-dihydroxy-2-(4-(methyl(propyl)amino)benzylidene)-2,3-dihydro-1*H*-inden-1-one 4-methylbenzenesulfonate; **GL₃**, 2-methyl-1-(4-(methylamino)phenyl)-3-(((2*S*,3*R*,4*S*,5*S*,6*R*)-3,4,5-trihydroxy-6-(hydroxymethyl)tetrahydro-2*H*-pyran-2-yl)oxy)pyridin-4(1*H*)-one; **GL₄**, 1-(4-

aminophenyl)-2-methyl-3-(((2*S*,3*R*,4*S*,5*S*,6*R*)-3,4,5-trihydroxy-6-(hydroxymethyl)tetrahydro-2*H*-pyran-2-yl)oxy)pyridin-4(1*H*)-one.

Scheme 1.5. The chemical structures of the naturally occurring, MT stabilizers, paclitaxel and epothilone D.

Scheme 2.1. Synthetic routes to **AQ**, **AQP**, and **AQDA** derivatives.

List of Figures

Figure 1.1. A schematic representation of the amyloid cascade hypothesis and the metal ion hypothesis. The processing of the amyloid precursor protein (APP) by β - and γ -secretases [green segment: the respective soluble N-terminal cleavage products, sAPP α and sAPP β ; red segment: amyloidogenic isoforms, A β ₄₀ and A β ₄₂; blue segment: the APP intracellular domain (AICD)] leads to the production of A β ₄₀ and A β ₄₂ monomers that can go through a slow nucleation stage followed by a fast elongation phase resulting in the formation of mature aggregated fibrils. The overproduction of A β aggregates and the ineffective clearance cause A β plaque deposition. Metal interaction with A β species can facilitate peptide aggregation pathways, stabilize toxic conformations, and generate the production of reactive oxygen species (ROS) through Fenton-like reactions.

Figure 1.2. The oxidative stress hypothesis. The ROS generated from labile metal pools and redox active metal bound to A β can engender damage of DNA, lipids, and proteins, as well as induce mitochondrial dysfunction, all of which can contribute to neuronal death.

Figure 1.3. The tau hypothesis. Alternative splicing of exons 2, 3, and 10 produces six different isoforms of tau ranging from 352 to 441 amino acids in length. The isoforms can have 0-2 acid repeats (0N-2N) (orange) and 3 or 4 microtubule binding domains (3R or 4R) (blue). Tau is a highly charged protein with an acidic N-terminus (pI 3.8) and extremely basic central, proline-rich domain (pI 11.4) and C-terminus (pI 10.8). Tau, along with other microtubule-associated proteins (MAPs), stabilizes microtubules (MTs). The hyperphosphorylation of tau catalyzes its dissociation from the MTs leading to MT destabilization, which may cause impairment in axonal transport and synaptic plasticity.

Figure 1.4. A diagram of design rationales toward control of A β aggregation. Anti-amyloidogenic compounds can be divided into pre-/post-A β production management. Pre-A β production pathways are directed at controlling the activity of the secretases that excise APP. Inhibition of β - and γ -secretases leads to a reduction in the amyloidogenic forms of A β while stimulation of α -secretase increases the production of the shorter, non-amyloidogenic forms and sAPP α , the neuroprotective N-terminal cleavage product.

Figure 1.5. A representation of the tetravalent foldamer-dendrimer conjugates developed to target low molecular weight (LMW) A β species (*i.e.*, oligomers, black sphere). Attached to a dendrimer scaffold (dark grey rectangle) were foldamer segments (light grey rectangles) that were designed to mimic the hydrophobic core and surrounding zwitterionic residues of A β . Binding affinity for LMW A β was increased through tetravalent structural modifications.

Figure 1.6. A proposed mode of action of clioquinol (CQ) and other similar ionophores. CQ diffuses into the brain where it interacts with extracellular A β plaques and metals. CQ binds copper and enters adjacent cells. Once in the cell, the complex dissociates and the metal ions can activate the phosphorylation of glycogen synthase kinase-3 (GSK3) which along with activation of Jun N-terminal kinase (JNK) promotes the activation of matrix metalloproteinase 2 and 3 (MMP2/MMP3). MMP2/MMP3 then can aid in the breakdown and clearance of extracellular, metal-free and metal-bound A β plaques.

Figure 1.7. A schematic model of the single-molecule-multiple target strategy (*i.e.*, integration approach). A chemical linker can be used to connect two or more independent structural portions to gain multimodal action (right) (*i.e.*, linkage approach). An incorporation approach (left) can install multiple moieties for the desired reactivities into a single structural entity.

Figure 2.1. Structural variations on a multifunctional ligand (ML) framework. Modifications were performed on the multimodal scaffold to identify a structure-reactivity understanding of ML's multifunctionality as well as to tune its metal binding characteristics. The quinoline portion of the structure was examined by cleavage of the HN-CH₂ bond (site 1, purple) and modulating the functionalities at the R₂ position (site 3, blue). Furthermore, simultaneous structural alterations at the R₁ and R₂ positions (sites 2 and 3, green and blue, respectively) allowed the role of the dimethylamino group and the 4-(dimethylamino)phenol in ML's activities to be illuminated.

Figure 2.2. Ability of compounds (AQ1-3, AQP1-4, and AQDA1-3) to control the formation of A β ₄₀ aggregates in the absence and presence of metal ions [Cu(II) and Zn(II)]. (a) Scheme of the inhibition experiments. (b) Visualization of the resultant A β species from the inhibition experiments by gel/Western blot utilizing an anti-A β antibody (6E10). Experimental conditions: [A β ₄₀] = 25 μ M; [CuCl₂ or ZnCl₂] = 25 μ M; [compound] = 50 μ M; incubated for 4, 8, and 24 h; pH 7.4 (for metal-free and Zn(II)

experiments) or 6.6 (for Cu(II) experiments); 37 °C; constant agitation. The control lane (without compound treatment) is identified by the letter “C”, and the lane number refers to the specific compound within each small molecule group (*i.e.*, **AQ**, **AQP**, **AQDA**).

Figure 2.3. Capability of compounds (**AQ1-3**, **AQP1-4**, and **AQDA1-3**) to inhibit the formation of A β ₄₂ aggregates in the absence and presence of metal ions [Cu(II) and Zn(II)]. (a) Scheme of the inhibition experiments. (b) Visualization of the resultant A β species from the inhibition experiments by gel/Western blot utilizing an anti-A β antibody (6E10). Experimental conditions: [A β ₄₂] = 25 μ M; [CuCl₂ or ZnCl₂] = 25 μ M; [compound] = 50 μ M; incubation for 4, 8, and 24 h; pH 7.4 (for metal-free and Zn(II) experiments) or 6.6 (for Cu(II) experiments); 37 °C; constant agitation. The control lane (without compound treatment) is identified by the letter “C”, and the lane number refers to the specific compound within each small molecule group (*i.e.*, **AQ**, **AQP**, **AQDA**).

Figure 2.4. Morphologies of the resultant metal-free A β ₄₂ and metal–A β ₄₂ aggregates upon treatment with **AQ1**, **AQP1**, and **AQDA1-3**. (a) Scheme of the inhibition experiments. (b) TEM images for the A β ₄₂ samples (24 h incubation). Insets represent the minor species.

Figure 2.5. Morphologies of the resultant metal-free and metal–associated A β aggregates. (a) Scheme of the inhibition experiments upon treatment with **AQ1**, **AQP1**, and **AQDA1-3**. (b) TEM images for the A β ₄₀ samples (24 h incubation). Insets represent the minor species.

Figure 2.6. Ability of compounds (**AQ1-3**, **AQP1-4**, and **AQDA1-3**) to reverse preformed A β ₄₀ aggregates in the absence and presence of metal ions [Cu(II) and Zn(II)]. (a) Scheme of the disaggregation experiments. (b) Visualization of the resultant A β species from the disaggregation experiments by gel/Western blot utilizing an anti-A β antibody (6E10). Experimental conditions: [A β ₄₀] = 25 μ M; [CuCl₂ or ZnCl₂] = 25 μ M; [compound] = 50 μ M; incubation for 4, 8, and 24 h; pH 7.4 (for metal-free and Zn(II) experiments) or 6.6 (for Cu(II) experiments); 37 °C; constant agitation. The control lane (without compound treatment) is identified by the letter “C”, and the lane number refers to the specific compound within each chemical group (*i.e.*, **AQ**, **AQP**, **AQDA**).

Figure 2.7. Capability of compounds (**AQ1-3**, **AQP1-4**, and **AQDA1-3**) to reverse preformed A β ₄₂ aggregates in the absence and presence of metal ions [Cu(II) and Zn(II)]. (a) Scheme of the

disaggregation experiments. (b) Visualization of the resultant A β species from the disaggregation experiments by gel/Western blot utilizing an anti-A β antibody (6E10). Experimental conditions: [A β_{42}] = 25 μ M; [CuCl₂ or ZnCl₂] = 25 μ M; [compound] 50 μ M; incubation for 4, 8, and 24 h; pH 7.4 (for metal-free and Zn(II) experiments) or 6.6 (for Cu(II) experiments); 37 °C; constant agitation. The control lane (without compound treatment) is identified by the letter “C”, and the lane number refers to the specific compound within each chemical group (*i.e.*, **AQ**, **AQP**, **AQDA**).

Figure 2.8. Interactions of **AQ1**, **AQP1**, and **AQDA1** with monomeric A β_{40} , monitored by SOFAST-HMQC NMR. (a-c) SOFAST-HMQC NMR spectra (zoomed in view from 7.9 to 8.4 ppm; top) and chemical shift perturbations (CSPs) (bottom) of A β_{40} upon treatment with (a) **AQDA1**, (b) **AQP1**, or (c) **AQ1**. Two horizontal lines represent the average chemical shift (dashed line) plus one standard deviation (dotted line). Residues which show no CSP are the result of unresolved peaks in the spectra.

Figure 2.9. Interactions of **AQDA2**, **AQP2**, **AQ2**, **AQP4**, and **AQDA3** with monomeric A β_{40} , monitored by SOFAST-HMQC NMR. (a-e) SOFAST-HMQC NMR spectra (top) and chemical shift perturbations (CSPs) (bottom) of A β_{40} upon treatment with (a) **AQDA2**, (b) **AQP2**, (c) **AQ2**, (d) **AQP4**, and (e) **AQDA3**. Two horizontal lines represent the average chemical shift (dashed line) plus one standard deviation (dotted line). Residues which show no CSP are the result of unresolved peaks in the spectra.

Figure 2.10. Docking studies of **AQ** derivatives with A β_{40} monomer. Top: The two lowest energy cartoon conformations of (a) **AQ1**, (b) **AQ2**, (c) **AQP1**, (d) **AQP2**, (e) **AQP4**, (f) **AQDA1**, (g) **AQDA2**, and (h) **AQDA3** with A β_{40} (PDB 2LFM) by AutoDock Vina. Hydrogen bonding is indicated with dashed lines (2.0–2.7 Å). Bottom: Summary of calculated binding energies of the **AQ** series to each A β conformation.

Figure 2.11. Mass spectrometric and ion mobility–mass spectrometric analyses of **AQ1**, **AQ4**, **AQP1**, **AQP4**, **AQDA1-3**, and **ML** upon addition of CuCl₂. MS spectra of (a) **AQ1**, (b) **AQ4**, (c) **AQDA1**, (d) **AQDA2**, (e) **AQDA3**, (f) **ML**, (g) **AQP1**, and (h) **AQP4**. (i) IM–MS drift time analysis. Collision cross section data for all ion mobility data sets are presented in Table 2.3. L = ligand (*i.e.*, **AQ1**, **AQ4**, **AQDA1-3**, **ML**, **AQP1**, **AQP4**). *Indicates a contaminant refractory to our purification methods.

Figure 2.12. Analysis of the amount of copper-bound A β_{40} as a function of ligand concentration.

Compared to baseline levels of metal-bound $A\beta_{40}$, **AQDA1**, **AQDA2**, **ML**, and **AQP1** are all shown to be capable of reducing the concentration of Cu(II)-associated peptide species.

Figure 2.13. Cu(II) binding studies of **AQ1-3**, **AQP1-4**, and **AQDA1-3**. (a-j) UV-vis spectra of ligands [(a) **AQ1**, (b) **AQ2**, (c) **AQ3**, (d) **AQP1**, (e) **AQP2**, (f) **AQP3**, (g) **AQP4**, (h) **AQDA1**, (i) **AQDA2**, and (j) **AQDA3**; black lines] with the addition of increasing amounts of $CuCl_2$ (colored lines; 30 min incubation; room temperature). Experimental conditions: for **AQ1** and **AQ3**, $[M(II)]:[L] = 1:2$, 20 mM HEPES, pH 7.4, 150 mM NaCl; for **AQ2**, $[M(II)]:[L] = 1:2$, CH_3CN ; for **AQP1-2**, $[M(II)]:[L] = 1:1$, 20 mM HEPES, pH 7.4, 150 mM NaCl; for **AQP3**, $[M(II)]:[L] = 1:2$, CH_3CN ; for **AQP4**, $[M(II)]:[L] = 1:2$, 20 mM HEPES, pH 7.4, 150 mM NaCl; for **AQDA1-3**, $[M(II)]:[L] = 1:1$, 20 mM HEPES, pH 7.4, 150 mM NaCl.

Figure 2.14. Zn(II) binding experiments. (a-j) UV-vis spectra of [(a) **AQ1**, (b) **AQ2**, (c) **AQ3**, (d) **AQP1**, (e) **AQP2**, (f) **AQP3**, (g) **AQP4**, (h) **AQDA1**, (i) **AQDA2**, and (j) **AQDA3**; black lines] with the addition of increasing amounts of $ZnCl_2$ (colored lines; 30 min incubation; room temperature). Experimental conditions: for **AQ1**, $[M(II)]:[L] = 1:2$, 20 mM HEPES, pH 7.4, 150 mM NaCl; for **AQ2**, $[M(II)]:[L] = 1:2$, CH_3CN ; for **AQ3**, $[M(II)]:[L] = 1:2$, EtOH; for **AQP1-2**, $[M(II)]:[L] = 1:1$, 20 mM HEPES, pH 7.4, 150 mM NaCl; for **AQP3**, $[M(II)]:[L] = 1:2$, EtOH; for **AQP4**, $[M(II)]:[L] = 1:2$, 20 mM HEPES, pH 7.4, 150 mM NaCl; for **AQDA1-3**, $[M(II)]:[L] = 1:1$, 20 mM HEPES, pH 7.4, 150 mM NaCl.

Figure 2.15. Zn(II) binding studies, measured by 1H NMR. 1H NMR spectra of **AQ3** (red) with 3.5 equiv of $ZnCl_2$ (black) were obtained at room temperature. Experimental conditions: CD_3CN ; $[AQ3] = 5$ mM; $[ZnCl_2] = 17.5$ mM; 10 min incubation. Note that Zn(II) binding to **AQP3** could not be determined due to limited solubility under experimental conditions.

Figure 2.16. Solution speciation studies of **AQP1**, **AQP4**, and **AQDA1-3**. UV-vis variable-pH titration spectra (left) and solution speciation diagrams (right) of (a) **AQP1** (pH 2–11), (b) **AQP4** (pH 2–11), (c) **AQDA1** (pH 2–10), (d) **AQDA2** (pH 2–10), and (e) **AQDA3** (pH 2–10) (F_L = fraction of species at given pH). Acidity constants (pK_a) of L (L = **AQP1**, **AQP4**, and **AQDA1-3**) are summarized in the table. Experimental conditions: $[L] = 50$ μ M (L = **AQP4** or **AQDA1**) or 25 μ M (L = **AQP1**, **AQDA2**, and **AQDA3**); $I = 0.10$ M NaCl; room temperature. Charges are omitted for clarity. ^aThe error in the last digit is shown in the parentheses.

Figure 2.17. Solution speciation studies of **AQP1**, **AQP4**, and **AQDA1-3** in the presence of Cu(II). UV-vis variable-pH titration spectra (left) and solution speciation diagrams (right) of (a) **AQP1**, (b) **AQP4**, (c) **AQDA1**, (d) **AQDA2**, and (e) **AQDA3** upon incubation with Cu(II) (F_{Cu} = fraction of species at given pH). Stability constants ($\log\beta$) of Cu(II)-L complexes (L = **AQP1**, **AQP4**, and **AQDA1-3**) are summarized in the table. Charges are omitted for clarity. ^a The error in the last digit is shown in parentheses. Experimental conditions: [**AQP1**] = 25 μM , [CuCl_2] = 12.5 μM , pH 2–11 (titrated from basic to acidic); [**AQP4**] = 100 μM , [CuCl_2] = 50 μM , pH 2–9 (titrated from basic to acidic); [**AQDA1**] = 25 μM , [CuCl_2] = 12.5 μM , pH 2–8 (titrated from basic to acidic); [**AQDA2**] = 25 μM , [CuCl_2] = 12.5 μM , pH 2–8 (titrated from acidic to basic); [**AQDA3**] = 25 μM , [CuCl_2] = 12.5 μM , pH 2–8 (titrated from acidic to basic); incubated for 1 h; I = 0.10 M NaCl; room temperature.

Figure 2.18. Metal selectivity of **AQP4** and **AQDA1-3** for Cu(II) over other biologically relevant divalent metal ions. Gray bars represent the subsequent addition of CuCl_2 (50 μM) to solutions containing ligand (50 μM) with (a) 1 equiv or (b) 20 equiv of the other divalent metal ions (MgCl_2 , CaCl_2 , MnCl_2 , FeCl_2 , CoCl_2 , NiCl_2 , and ZnCl_2). The absorbance wavelengths of **AQP4**, **AQDA1**, **AQDA2**, and **AQDA3** used to calculate A_M/A_{Cu} are listed as follows: 290 nm, 449 nm, 449 nm, and 338 nm, respectively. *Due to similar optical bands of the ligand upon binding to Cu(II) and the other metal ions, accurate metal ion selectivity cannot be obtained.

Figure 2.19. Biological activities of small molecules. (a) Inhibitory activity of **AQ1**, **AQ3**, **AQ4**, **AQDA1**, and **AQDA3** toward Cu-mediated ROS formation as determined by the 2-deoxyribose assay. The absorbance values are normalized to the ligand-free condition ([CuCl_2] = 10 μM ; [ligand] = 125 μM). (b) Antioxidant activity of **AQ1-3**, **AQP1**, **AQP2**, **AQP4**, and **AQDA1-3**, identified by the TEAC assay using cell lysates. The TEAC values are relative to that of the vitamin E analogue, Trolox (6-hydroxy-2,5,7,8-tetramethylchroman-2-carboxylic acid).

Figure 2.20. Cell viability of **AQ1-4**, **AQP1-4**, **AQDA1-3**, and **ML** in N2a cells in the absence and presence of Cu(II) and Zn(II). (a) Cu(II):ligand (1:1) (5 μM), (b) Zn(II):ligand (1:1) (5 μM), (c) Cu(II):ligand (1:1) (10 μM), and (d) Zn(II):ligand (1:1) (10 μM). Cell viability (%) was determined by the MTT assay compared to cells treated with DMSO only (1% v/v) [MTT = 3-(4,5-dimethyl-2-thiazolyl)-2,5-diphenyl-2H-tetrazolium bromide]. Black, blue, and green bars indicate cell viability upon incubation with ligand only and ligand with CuCl_2 or ZnCl_2 , respectively.

Figure 3.1. Solution and metabolic stability of **DMPD**. (a) FAME calculation of **DMPD**. ^aPredicts the sites of metabolism, the atom where a metabolic reaction is initiated. The number reported is the probability of each atom being a site of metabolism. Therefore, the closer the number is to one, the more likely that atom is a site of metabolism [see Kirchmair, J. *et al. J. Chem. Inf. Model.* **2013**, *53*, 2896–2907]. (b) Stability of **DMPD** in DMSO and PBS. **DMPD** is shown to be degraded by *ca.* 20% in PBS for 12 h. (c) Oxidation of **DMPD** by hydrogen peroxide (H₂O₂) in PBS (*t*_{1/2} = 55 min). Conditions: **DMPD** (0.5 mM); H₂O₂ (5 mM); pseudo-first order kinetics. (d) Metabolic stability of **DMPD** using liver microsomes. Based on Lineweaver–Burk analysis, the values of *V*_{max} and *K*_M (*ca.* 22.9 nM/min and *ca.* 2.07 mM, respectively) are obtained.

Figure 3.2. Effects of **DMPD** toward metal-free/metal-induced Aβ₄₀ aggregation *in vitro*. (a) Chemical structure of **DMPD** (*N,N*-dimethyl-*p*-phenylenediamine) and amino acid sequence of Aβ (the self recognition site is underlined and highlighted in red). (b) Scheme of the (I) inhibition or (II) disaggregation experiments. The metal-free samples were prepared in both the absence (left) and presence (right) of O₂. (c) Analyses of the resultant Aβ species from (I) and (II) by gel electrophoresis with Western blotting (gel/Western blot) using an anti-Aβ antibody (6E10). For the experiment (I), the samples containing metal-free Aβ₄₀ were prepared under anaerobic (left, white background) and aerobic (right, gray background) conditions. Conditions: Aβ (25 μM); CuCl₂ or ZnCl₂ (25 μM); **DMPD** (50 μM); 24 h; pH 6.6 (for Cu(II) experiments) or pH 7.4 (for metal-free and Zn(II) experiments); 37 °C; constant agitation. (d) TEM images of the Aβ₄₀ samples prepared under aerobic conditions (from (c)). Inset: Minor species from TEM measurements. White and black scale bars indicate 200 and 500 nm, respectively.

Figure 3.3. Effects of **DMPD** on metal-free and metal-induced Aβ₄₂ aggregation. (a) Scheme of (I) inhibition and (II) disaggregation experiments. (b) Analyses of the resultant Aβ species from I and II by gel/Western blot using an anti-Aβ antibody (6E10). Conditions: Aβ (25 μM); CuCl₂ or ZnCl₂ (25 μM); **DMPD** (50 μM); 24 h; pH 6.6 (for Cu(II) experiments) or pH 7.4 (for metal-free and Zn(II) experiments); 37 °C; constant agitation. (c) TEM images of the Aβ₄₂ samples from (b). White scale bars indicate 500 nm.

Figure 3.4. Effect of **DMPD** toward metal-free and metal-induced Aβ₄₀ aggregation in a cell culture medium. Gel/Western blot analyses of the resultant Aβ₄₀ species upon treatment with **DMPD** in a cell culture medium containing 1:1 Minimum Essential Media (MEM) and Ham's F12K Kaighn's

Modification Media (F12K), 10% (v/v) fetal bovine serum (FBS), 100 U/mL penicillin, and 100 mg/mL streptomycin. Conditions: A β (25 μ M); CuCl₂ or ZnCl₂ (25 μ M); **DMPD** (50 μ M); 24 h; 37 °C; constant agitation. The experimental scheme is depicted in Figure 3.2b.

Figure 3.5. Interactions of **DMPD** with monomeric A β and fibrillar Cu(II)–A β , observed by 2D NMR spectroscopy and Cu K-edge X-ray absorption spectroscopy, respectively. (a) 2D ¹H–¹⁵N SOFAST-HMQC NMR investigation of **DMPD** with ¹⁵N-labeled A β ₄₀. (b) Chemical shift perturbations (CSPs) of A β ₄₀ were determined upon addition of **DMPD** (A β : **DMPD** = 1 : 10). On the chemical shift plot, the dashed and dotted lines represent the average CSP and one standard deviation above the average, respectively. Relatively noticeable CSPs were observed around the hydrophobic residues of the peptide. *Residues could not be resolved for analysis. (c) Molecular dynamics (MD) simulations of the A β ₄₀–**DMPD** complex. **DMPD** and A β ₄₀ are shown to interact directly with the hydrophobic region of the A β ₄₀ monomer in its lowest energy conformation (see Figure 3.6). The chemical structure of **DMPD** is colored as follows: Carbon, orange; hydrogen, white; nitrogen, blue. The self-recognition site of A β ₄₀ is highlighted in light violet. (d) Left: X-ray absorption near edge structure (XANES) region of the Cu K-edge X-ray absorption spectrum of **DMPD**-incubated Cu(I)- (red) and Cu(II)-loaded (blue) A β ₄₂ fibrils. Top right (blue): Magnitude FT and FF (inset) extended X-ray absorption fine structure (EXAFS) of **DMPD**-incubated Cu(II)-loaded A β ₄₂ fibrils showing the experimental data (solid line), simulated spectrum (dashed line), and difference spectrum (dotted line). Shell #1 (N scatterer): n = 2.3(2); r = 1.889(3) Å; σ^2 = 0.0041(4) Å²; ϵ^2 = 0.93. Bottom right (red): Magnitude FT and FF (inset) EXAFS of **DMPD**-incubated Cu(I)-loaded A β ₄₂ fibrils showing the experimental data (solid line), simulated spectrum (dashed line), and difference spectrum (dotted line). Shell #1 (N scatterer): n = 2.2(2); r = 1.882(4) Å; σ^2 = 0.0033(1) Å²; ϵ^2 = 0.85.

Figure 3.6. Conformations of the A β ₄₀–**DMPD** complexes as determined by molecular dynamics (MD) simulations. (a-c) Complexes of **DMPD** with A β ₄₀ (PDB 1BA4). **DMPD** is shown to interact with A β ₄₀. Atoms of **DMPD** are colored as follows: Carbon, orange; hydrogen, white; nitrogen, blue. The self-recognition site of A β ₄₀ is also highlighted in light violet. Gibb's binding energies ($\Delta G_{\text{binding}}$) for each conformation are summarized in the table (bottom).

Figure 3.7. XANES region of the XAS spectrum for **DMPD**-incubated Cu(II)-loaded A β ₄₂ fibrils following one (solid), two (dashed), and three (dotted) scans on the same spot. Total exposure time for each scan is *ca.* 45 min.

Figure 3.8. Transformation of **DMPD** with or without Cu(II) and/or A β ₄₀, monitored by UV-vis. (a and b) UV-vis spectra of **DMPD** with or without CuCl₂ in the absence and presence of A β under aerobic conditions. (c) UV-vis spectra of **DMPD** with or without A β under anaerobic conditions. Blue, red, and green lines correspond to incubation for 0, 4, and 24 h, respectively. Conditions: A β (25 μ M); CuCl₂ (25 μ M); **DMPD** (50 μ M); pH 6.6 (for Cu(II) experiments) or pH 7.4 (for metal-free experiments); room temperature; no agitation. (a and c) **DMPD** +/- A β ₄₀; (b) [**DMPD** + CuCl₂] +/- A β ₄₀.

Figure 3.9. UV-vis spectra of **DMPD** with or without A β ₄₀ and/or metal ions. (a) **DMPD** \pm A β ₄₀; (b) **DMPD** \pm [CuCl₂ + A β ₄₀]; (c) **DMPD** \pm [ZnCl₂ + A β ₄₀]. Black and red lines represent the absence and presence of A β ₄₀, respectively. Conditions: A β ₄₀ (25 μ M); CuCl₂ or ZnCl₂ (25 μ M); **DMPD** (50 μ M); pH 6.6 (for Cu(II) experiment) or pH 7.4 (for metal-free and Zn(II) experiments); room temperature; no agitation. The spectra were obtained right after addition of metal ions and/or A β ₄₀.

Figure 3.10. Transformation of benzoquinone (**BQ**) in the presence of A β ₄₀. (a) UV-vis spectrum of **BQ** under aerobic conditions. (b) UV-vis spectrum of **BQ** with A β ₄₀ under aerobic conditions. Blue, red, and green lines correspond to incubation periods of 0, 4, 24 h, respectively. Conditions: A β ₄₀ (25 μ M); **BQ** (50 μ M); HEPES buffer (1 mM, pH 7.4); room temperature, no agitation.

Figure 3.11. Effects of **BQ** on metal-free and metal-induced A β ₄₀ and A β ₄₂ aggregation. (a) Scheme of (I) inhibition and (II) disaggregation experiments. (b & c) Analyses of the resultant A β species [(b) A β ₄₀ and (c) A β ₄₂] from I and II by gel/Western blot using an anti-A β antibody (6E10). Conditions: A β (25 μ M); CuCl₂ or ZnCl₂ (25 μ M); **BQ** (50 μ M); 24 h; pH 6.6 (for Cu(II) experiments) or pH 7.4 (for metal-free and Zn(II) experiments); 37 °C; constant agitation.

Figure 3.12. Analysis of the resulting species upon interaction of A β ₄₀ with **DMPD** or **BQ** by mass spectrometry (MS) and ion mobility–mass spectrometry (IM–MS), as well as a proposed mechanism. (a) MS analysis showing the complex formation of A β ₄₀ (25 μ M) with **DMPD**_{transformed} (50 μ M) (red lines) in the 4⁺ and 5⁺ charge states ([A β + **DMPD**_{transformed}]⁴⁺ and [A β + **DMPD**_{transformed}]⁵⁺) (i). IM–MS was

applied to the 4⁺ charge state to resolve the conformational rearrangement of Aβ₄₀ upon addition and conversion of **DMPD** to **DMPD**_{transformed} (ii). Extracted arrival time distributions support the existence of two resolvable structural populations [collision cross section (CCS) data, inset tables]. The interaction with **DMPD**_{transformed} trapped the peptide in a more packed conformation (dominant peak = 1) when compared to the *apo* form (dominant peak = 2). (b) MS analysis showing the complex formation of Aβ₄₀ (25 μM) with **BQ** (50 μM) supports that **BQ** binds readily to the peptide (red) (i). In line with the **DMPD** data presented above, **BQ**-containing samples support a mass gain of 104 Da attributed to covalent binding with K16 (Figure 3.11). IM–MS was applied to the 4⁺ charge state to resolve the conformational rearrangement of Aβ₄₀ upon binding **BQ**. Extracted arrival time distributions indicate the existence of three resolvable structural populations (CCS data, inset table) (ii). The first two of these conformations support, within least square error analysis, CCS values consistent with the **DMPD**-bound data (Figure 3.12a). (c) Comparison of tandem MS/MS sequencing using the quadrupole isolated 5⁺ charge state (trap collision energy 90 V) of Aβ₄₀⁵⁺ (top) and [Aβ + **DMPD**_{transformed}]⁵⁺ (bottom). Analysis of these data in addition to the MS and IM–MS support the attachment of **DMPD**_{transformed} to Aβ₄₀ through a covalent modification of the peptide *via* K16 resulting in an observed mass shift of 103.93 ± 0.04 Da calculated from internal monoisotopic calibration data sets. (d) Proposed mechanistic pathways between **DMPD** and Aβ. **DMPD** may undergo an oxidative transformation under aerobic conditions to generate a cationic imine (**CI**)–Aβ complex (**1**). **CI** could then generate **BQI** (shown in **2**) through hydrolysis. Once hydrolyzed, **BQI** is proposed to undergo further hydrolytic conversion to generate **BQ** (shown in **3**). Our MS studies support that **BQ** forms covalently bound protein-ligand adducts (**4**) that are capable of forming intramolecular crosslinks (**5**) that trap Aβ in an altered conformational geometry compatible with our IM–MS dataset.

Figure 3.13. MS/MS sequencing of the samples containing **BQ** and Aβ₄₀. Complimenting **DMPD** analysis (Figure 3.12), studies were performed on incubated samples of Aβ₄₀ with **BQ**. Consistent with [Aβ₄₀ + **DMPD**] analyses, an adduct of 104.1 ± 0.1 Da was identified to be covalently linked to K16.

Figure 3.14. MS studies of the **BQ**-bound Aβ dimer. (a) MS/MS analysis used to identify if **BQ** was capable of forming intermolecular crosslinks in Aβ dimers (M: Aβ monomer; D: Aβ dimer). Upon quadrupole isolation of the **BQ**-bound 5⁺ Aβ₄₀ dimer ion (b), it was subjected to collisional activation and subsequent fragmentation (c). These results support that **BQ** forms intramolecular crosslinks, with masses corresponding to intact monomeric *apo* and **BQ**-bound peptides suggesting these conclusions.

Figure 3.15. Cytotoxicity of **DMPD** in the absence and presence of metal ions, and its effect toward metal-free/metal-treated A β_{40} -triggered cytotoxicity. The cytotoxicity of (a) **DMPD** only (2.5–100 μ M; 1% v/v DMSO); **DMPD** (2.5–50 μ M) with (b) CuCl₂ or (c) ZnCl₂ in a ratio of 1:1 using the human neuroblastoma SK-N-BE(2)-M17 (M17) cells. (d) Viability (%) of M17 cells incubated with A β_{40} (10 μ M), CuCl₂ or ZnCl₂ (10 μ M), and/or **DMPD** (20 μ M) for 24 h. Cell viability, determined in M17 cells by the MTT assay, was calculated in comparison to that treated with DMSO only (1% v/v). Error bars represent standard error from three independent experiments.

Figure 3.16. Monitoring changes in body weight. No significant difference in body weight was observed between the vehicle- and **DMPD**-treated 5 \times FAD mice. Body weights of male (squares; n = 6 for each treatment) or female (circles; n = 5 for each treatment) 5 \times FAD mice were measured for 30 days immediately before the daily injection of vehicle (black) or **DMPD** (1 mg/kg/day, i.p.; gray), starting from 3 months of age. All values represent mean + SEM.

Figure 3.17. Reduction of cerebral amyloid pathology by **DMPD** in the 5 \times FAD mice. After the total 30 daily i.p. injections of vehicle or **DMPD** (1 mg/kg/day), the brain tissues were collected from the 5 \times FAD mice at 4 months of age. (a) Bars denote the amounts of SDS-soluble, FA-soluble, or total (PBS plus SDS plus FA) A β_{40} /A β_{42} peptides in the whole brains, which were calculated from three independent sandwich A β ELISA assays (n = 14–17). (b) Representative microscopic images of 4G8-immunostained (brown) or Congo red stained (red) brain sections of 5 \times FAD mice show that **DMPD** significantly reduced the burden of amyloid deposits in the brain. Ctx, cortex; Hip, hippocampus. Scale bar = 100 μ m. (c) The load of 4G8-immunoreactive amyloid deposits and the total number of congophilic amyloid plaques in the microscopic photographs of the identical cortical areas (b) were measured in five brain sections taken from each animal. All values represent mean \pm SEM (n = 7). **P* < 0.05, ***P* < 0.01, or ****P* < 0.001 by unpaired two-tail t-test.

Figure 3.18. Cognitive enhancement by **DMPD** in the 5 \times FAD AD mouse model. Using the Morris water maze task, spatial learning and memory activities were compared in the 5 \times FAD and their littermate wild-type mice after thirty consecutive vehicle or **DMPD** (1 mg/kg/day, i.p.) treatments. (a) The escape latency time was daily measured for the final five days of the drug treatment. (b) The probe trials were performed on the day of the final treatment to assess the time when the mice spent to reach the escape platform. (c) Upper circular images display the representative swimming paths for the mice to locate the escape platform in the water maze for 60 sec. Lower graphs show the time how long they spent in the target

quadrant (NW, highlighted in gray). The statistical comparisons were performed between 5×FAD and their wild-type littermate mice with vehicle (pound), or between consecutive vehicle and **DMPD** treatments in 5×FAD mice (asterisk), according to the one-way ANOVA followed by a Student-Neuman-Keuls post hoc test. * $P < 0.05$, **, $^{##}P < 0.01$ or **, $^{###}P < 0.001$ ($n = 17$ for wild-type mice or $n = 14$ for vehicle- or **DMPD**-treated 5x FAD mice).

Figure 4.1. Chemical structures of macrocyclic polyamines and their metal complexes. (a) Chemical structures of cyclen, cyclam, and M(II)(TMC) (*trans*-I and *trans*-III isomers). Cyclen = 1,4,7,10-tetraazacyclododecane; cyclam = 1,4,8,11-tetraazacyclotetradecane; TMC = 1,4,8,11-tetramethyl-1,4,8,11-tetraazacyclotetradecane. ORTEP diagrams of (b) [Co(TMC)(NO₃)](NO₃) and (c) [Ni(TMC)(CH₃CN)](NO₃)₂ with ellipsoids drawn at the 30% probability level. Noncoordinated nitrate anions and hydrogen atoms are omitted for clarity. Selected distances (Å) and angles are summarized in Table 4.1.

Figure 4.2. Capability of M(II)(TMC) (M = Co, Ni, Cu, and Zn) to control the aggregation pathways of A β ₄₀ and A β ₄₂. (a) Scheme of the inhibition experiment. (b) Analysis of the resultant A β ₄₀ (top) and A β ₄₂ (bottom) species from the inhibition experiment visualized by gel electrophoresis with Western blotting (gel/Western blot) using an anti-A β antibody (6E10). Conditions: A β (25 μ M); M(II)(TMC) (50 μ M); incubated for 4, 8, or 24 h; pH 7.4; 37 °C; constant agitation. Lanes: “C” denotes the control lane (without compound treatment); (1) A β + TMC; (2) A β + Co(II)(TMC); (3) A β + Ni(II)(TMC); (4) A β + Cu(II)(TMC); (5) A β + Zn(II)(TMC). (c) TEM images for the A β ₄₂ samples (24 h incubation) from (b). Insets represent the minor species.

Figure 4.3. Ability of M(II)(TMC) (M = Co, Ni, Cu, and Zn) to disaggregate preformed A β ₄₀ and A β ₄₂ aggregates. (a) Scheme of the disaggregation experiment. (b) Analysis of the resultant A β ₄₀ (top) and A β ₄₂ (bottom) species from the disaggregation experiment visualized by gel electrophoresis with Western blotting (gel/Western blot) using an anti-A β antibody (6E10). Conditions: A β (25 μ M); M(II)(TMC) (50 μ M); incubated for 4, 8, or 24 h; pH 7.4; 37 °C; constant agitation. Lanes: “C” denotes the control lane (without compound treatment); (1) A β + TMC; (2) A β + Co(II)(TMC); (3) A β + Ni(II)(TMC); (4) A β + Cu(II)(TMC); (5) A β + Zn(II)(TMC). (c) TEM images for the A β ₄₀ and A β ₄₂ samples (24 h incubation) from (b). Insets represent the minor species.

Figure 4.4. Ability of M(II)(TMC) (M = Ni, Cu, and Zn) to alter the morphology of preformed A β_{40} and A β_{42} aggregates. (a) Scheme of the disaggregation experiment. (b) TEM images for the A β_{40} and A β_{42} samples (24 h incubation). Insets represent the minor species.

Figure 4.5. Competition experiments. (a) Reaction scheme. (b) Visualization of the A β_{40} species upon addition of sodium azide (NaN₃; 0–200 equiv; blue) or sodium cyanate (NaOCN; 0–200 equiv; green) by gel/Western blot utilizing an anti-A β antibody (6E10). Conditions: A β_{40} (25 μ M); NaN₃ or NaOCN (0–5 mM); Co(II)(TMC) (50 μ M); incubated for 24 h; pH 7.4; 37 °C; constant agitation. (c) Scheme and chemical equation of the complexation reaction of Co(II)(TMC) with the experimentally reported equilibrium constants obtained from spectrophotometric titrations.³³ *Indicates that the stability constant for the pentacoordinate imidazole complex was not obtained for Co(II)(TMC) and the reported value (< 0.30) is from Ni(II)(TMC).³²

Figure 4.6. MALDI–MS analysis of the A β_{40} samples incubated with M(II)(TMC) (M = Co, Ni, Cu, and Zn). (a) Mass spectra of singly-charged A β_{40} . The peak intensities are normalized to A β_{40} in the absence of M(II)(TMC). (b) The magnified low m/z range of the mass spectra. A β (1-12) [$m/z = 1424$], A β (1-18) [$m/z = 2167$], and A β (14-38) [$m/z = 2587$] are indicated in light green, cyan, and red, respectively. All measurements were conducted with the addition of an internal standard, melittin (5 μ M), and calibrated based on the linear correlation between the concentration and the signal intensity (Figure 4.7). (c) MALDI–MS spectra for A β_{40} incubated with Co(II)(TMC) at different pH values. The peak intensity is normalized to that of A β_{40} without M(II)(TMC) (a, top spectrum). (d) Magnified spectrum (x 40) for each sample. All samples were measured with the addition of an internal standard of melittin (5 μ M). (e) The amount of remaining singly-charged A β_{40} after M(II)(TMC) treatment is estimated and summarized in the table.

Figure 4.7. Calibration plot of the internal standard, melittin. Internal standards were prepared at different concentrations (100 nM–20 μ M). The signal intensity for each sample was measured using MALDI–MS. The y-axis indicates the ratio of the signal intensity for the standards to the sum of intensities for the 30 most dominant peaks. The linear regression of the data is given by the red line ($y = 0.0205x - 0.0015$; $R^2 = 0.9976$).

Figure 4.8. ESI–MS spectra of $A\beta_{40}$ incubated with $M(II)(TMC)$ ($M = Co, Ni, Cu, \text{ and } Zn$). Inset spectra indicate the magnification between 1500 and 1750 m/z . Colored peaks are assigned above the spectra.

Figure 4.9. The low m/z regions of the ESI–MS spectra for (a) $A\beta_{40}$, (b) [$A\beta_{40} + Co(II)(TMC)$], (c) [$A\beta_{40} + Ni(II)(TMC)$], (d) [$A\beta_{40} + Cu(II)(TMC)$], and (e) [$A\beta_{40} + Zn(II)(TMC)$]. The newly generated $A\beta_{40}$ fragments formed upon $M(II)(TMC)$ treatment are labeled in blue. Ions only detected in the samples treated with $Co(II)(TMC)$ or $Cu(II)(TMC)$ are labeled in red and green, respectively. All fragments are listed in Table A.3.

Figure 4.10. ESI–IM–MS spectra of $A\beta_{40}^{3+}$ or complex ions of $A\beta_{40}$ with $M(II)(TMC)$ ($M = Co, Ni, Cu, \text{ and } Zn$). The drift time values with the maximum intensity are indicated in the spectra.

Figure 4.11. Analysis of the potential isomerization of *trans*-I- $M(II)(TMC)$ ($M = Co, Ni, \text{ and } Cu$) complexes by UV-vis. Conditions: $Co(II)(TMC)$ (20 mM), $Ni(II)(TMC)$ (10 mM), or $Cu(II)(TMC)$ (2.5 mM); pH 7.4; 37 °C; no agitation.

Figure 4.12. EPR measurements of $Co(II)(TMC)$. (a) (i) X-band CW-EPR spectrum of $Co(II)(TMC)$ (solid black) and its simulated spectrum (dashed black); (ii) W-band Electron Spin Echo-detected EPR spectrum (solid blue) of $Co(II)(TMC)$ and its simulated spectrum (dashed blue). The following parameters were used in the simulation: $g = [2.42, 2.42, 2.21]$, $A_{Co} = [0, 60, 0]$ G, $D \geq 13 \text{ cm}^{-1}$, $E/D = 0.3$ (b) 1H Davies ENDOR spectra of $Co(II)(TMC)$ in H_2O (black) and in D_2O (blue). The subtracted 1H ENDOR spectrum is shown in red. 2H Mims ENDOR in D_2O (black). (c) Q-band three pulse time-domain (left) and the frequency domain (right) ESEEM spectra of $Co(II)(TMC)$. The blue dashed line in the frequency domain indicates the ^{17}O Larmor frequency at each field.

Figure 4.13. 1H -ENDOR spectra of $CoCl_2 \cdot 6H_2O$ at different magnetic fields.

Figure 4.14. Q-band ESEEM time-domain (left) and Fourier transformed frequency domain spectra (right) of $CoCl_2 \cdot 6H_2O$. The red dashed line indicates the ^{17}O Larmor frequency at each field.

Figure 4.15. Computational examination of $M(II)(TMC)$ complexes. (a) Experimental UV-vis spectrum of (i) $Co(II)(TMC)$ in aqueous solutions (red) and the TDDFT-predicted spectra of $[Co(TMC)(H_2O)]^{2+}$ (S

= 3/2) (solid black), $[\text{Co}(\text{TMC})(\text{OH})]^+$ ($S = 3/2$) (dashed black), $[\text{Co}(\text{TMC})(\text{H}_2\text{O})]^{2+}$ ($S = 1/2$) (solid gray), and $[\text{Co}(\text{TMC})(\text{OH})]^+$ ($S = 1/2$) (dashed gray); (ii) experimental UV-vis spectrum of Ni(II)(TMC) in aqueous solutions (red) and the TDDFT-predicted spectra of $[\text{Ni}(\text{TMC})]^{2+}$ ($S = 0$) (solid black), $[\text{Ni}(\text{TMC})(\text{OH})]^+$ ($S = 0$) (dashed black), $[\text{Ni}(\text{TMC})(\text{H}_2\text{O})]^{2+}$ ($S = 1$) (solid gray), and $[\text{Ni}(\text{TMC})(\text{OH})]^+$ ($S = 1$) (dashed gray); (iii) experimental UV-vis spectrum of Cu(II)(TMC) in aqueous solutions (red) and the TDDFT-predicted spectra of $[\text{Cu}(\text{TMC})(\text{H}_2\text{O})]^{2+}$ (solid black) and $[\text{Cu}(\text{TMC})(\text{OH})]^+$ (dashed black). (b-d) Calculated structures of (a) $[\text{Co}(\text{TMC})(\text{H}_2\text{O})]^{2+}$, (b) $[\text{Ni}(\text{TMC})]^{2+}$, (c) $[\text{Cu}(\text{TMC})(\text{H}_2\text{O})]^{2+}$, and (d) $[\text{Zn}(\text{TMC})(\text{H}_2\text{O})]^{2+}$. (e-f) The overlay of the ground-state M(II)(TMC) structures presented from the side and top.

Figure 4.16. Solution speciation studies of Co(II)(TMC) and Ni(II)(TMC). UV-vis variable-pH titration spectra (left) and the solution speciation diagrams (right) of (a) Co(II)(TMC) (pH 4.5–11.5); (b) Ni(II)(TMC) (pH 7–11.5) (F_L = fraction of species at given pH). Acidity constants ($\text{p}K_a$) of $[\text{M}(\text{L})(\text{H}_2\text{O})]^{2+}$ ($L = \text{TMC}$) are summarized in the table. Experimental conditions: Co(II)(TMC) = 6 mM; Ni(II)(TMC) = 4 mM; $I = 0.10 \text{ M NaCl}$; room temperature. Charges are omitted for clarity. ^aThe error in the last digit is shown in the parentheses.

Figure 4.17. Schemes of the potential modes of action of M(II)(TMC) to modulate A β aggregation. (a) The conformation of A β is altered leading to the generation of off-pathway aggregates through (i) coordination to the metal center of M(II)(TMC) [*e.g.*, A β –M(II)(TMC)]; (ii) intermolecular coordination of A β to two equivalents of M(II)(TMC); (iii) isomerization to the *trans*-III stereoisomer and subsequent formation of an octahedral complex. (b) Metal complexes facilitate the hydrolysis of amide bonds to generate A β fragments. Amide bond hydrolysis can be catalyzed by: (i) the activation of water by M(II)(TMC) to generate metal hydroxo nucleophiles; (ii) Lewis acid activation of the amide bonds; (iii) a mononuclear combined mechanisms where both substrates (*i.e.*, water and amide) are coordinated to the metal complex; (iv) a binuclear combined mechanism where two equivalents of M(II)(TMC) are used to produce the hydroxide source and activate the amide bond.

Figure 4.18. Cell viability measurements of Co(II)(TMC) using human neuroblastoma SH-SY5Y cells. Cell viability (%) was determined by the MTT assay compared to cells treated with ddH₂O [MTT = 3-(4,5-dimethyl-2-thiazolyl)-2,5-diphenyl-2H-tetrazolium bromide].

Figure 4.19. MALDI–MS analysis of ubiquitin incubated with Co(II)(TMC). The peak intensities are

normalized to ubiquitin in the absence of Co(II)(TMC). All measurements were conducted with the addition of an internal standard, melittin (5 μM), and calibrated based on the linear correlation between the concentration and the signal intensity.

Figure A.1. Chemical structures of $[\text{M}(\text{TMC})]^{2+}$ (TMC = 1,4,8,11-tetramethyl-1,4,8,11-tetraazacyclotetradecane). The two most common diastereomers are presented (*trans*-I and *trans*-III). The *trans*-I conformation forms pentacoordinate complexes by binding one ligand on the *syn* face. The *trans*-III isomer generates octahedral complexes by binding two ligands in the open axial sites.

Figure A.2. UV-vis spectra of $[\text{Cu}(\text{TMC})](\text{NO}_3)_2$ and $[\text{Cu}(\text{TMC})](\text{ClO}_4)_2$. The optical spectrum of $[\text{Cu}(\text{TMC})](\text{NO}_3)_2$ (red line) is blue shifted in comparison to $[\text{Cu}(\text{TMC})](\text{ClO}_4)_2$ (blue line) which is consistent with an octahedral *trans*-III- $[\text{Cu}(\text{TMC})](\text{NO}_3)_2$ complex.

Figure A.3. Chemical structures of $[\text{Cu}(\text{TMC})](\text{NO}_3)_2$ and $[\text{Cu}(\text{TMC})(\text{H}_2\text{O})](\text{ClO}_4)_2$. Hydrogen atoms are omitted for clarity. a) ORTEP diagram of the cationic part of $[\text{Cu}(\text{TMC})](\text{NO}_3)_2$ with thermal ellipsoids drawn at the 30% probability level. b) Ball-and-stick representation of the cationic part of $[\text{Cu}(\text{TMC})(\text{H}_2\text{O})](\text{ClO}_4)_2$ (gray C, blue N, red O, brown Cu). Selected bond distances (\AA) and angles ($^\circ$) are summarized in Table 1. The crystal structure of $[\text{Cu}(\text{TMC})(\text{H}_2\text{O})](\text{ClO}_4)_2$ is adapted from reference 29 for comparison.

Figure B.1. ^1H NMR spectrum of **AQP2** [400 MHz, $(\text{CD}_3)_2\text{SO}$].

Figure B.2. ^{13}C NMR spectrum of **AQP2** [100 MHz, $(\text{CD}_3)_2\text{SO}$].

Figure B.3. ^1H NMR spectrum of **AQP3** [400 MHz, $(\text{CD}_3)_2\text{SO}$].

Figure B.4. ^{13}C NMR spectrum of **AQP3** [100 MHz, $(\text{CD}_3)_2\text{SO}$].

Figure B.5. ^1H NMR spectrum of **AQP4** [400 MHz, $(\text{CD}_3)_2\text{SO}$].

Figure B.6. ^{13}C NMR spectrum of **AQP4** [100 MHz, $(\text{CD}_3)_2\text{SO}$].

Figure B.7. ^1H NMR spectrum of **AQDA1** [400 MHz, $(\text{CD}_3)_2\text{SO}$].

Figure B.8. ^{13}C NMR spectrum of **AQDA1** [100 MHz, $(\text{CD}_3)_2\text{SO}$].

Figure B.9. ^1H NMR spectrum of **AQDA2** [400 MHz, $(\text{CD}_3)_2\text{SO}$].

Figure B.10. ^{13}C NMR spectrum of **AQDA2** [100 MHz, $(\text{CD}_3)_2\text{SO}$].

Figure B.11. ^1H NMR spectrum of **AQDA3** [400 MHz, $(\text{CD}_3)_2\text{SO}$].

Figure B.12. ^{13}C NMR spectrum of **AQDA3** [100 MHz, $(\text{CD}_3)_2\text{SO}$].

Figure B.13. Q-band ESE-EPR spectra of Co(II)(TMC) complex in H_2O (black), D_2O (blue) and H_2^{17}O (red). *indicates the background from the resonator.

Figure B.14. ^1H -ENDOR spectra of Co(II)(TMC) complex at different magnetic fields.

Figure B.15. Q-band ESE-EPR spectrum of $\text{CoCl}_2 \cdot 6\text{H}_2\text{O}$ in aqueous solution.

Figure B.16. Electronic absorption spectra of (a) *trans*-I-Cu(II)(TMC) experimentally obtained in aqueous solution; (b) TDDFT-predicted *trans*-I-[Cu(TMC)(OH)]⁺ (dotted gray) and *trans*-I-[Cu(TMC)(H₂O)]²⁺ (solid gray) models obtained using the BP functional; (c) TDDFT-predicted *trans*-I-[Cu(TMC)(OH)]⁺ (dotted black) and *trans*-I-[Cu(TMC)(H₂O)]²⁺ (solid black) models obtained using the B3LYP functional; (d) *trans*-III-Cu(II)(TMC) experimentally obtained in aqueous solution; (e) TDDFT-predicted *trans*-III-[Cu(TMC)(OH)]⁺ (dotted gray) and *trans*-III-[Cu(TMC)(H₂O)]²⁺ (solid gray) models obtained using the BP functional; and (f) TDDFT-predicted *trans*-III-[Cu(TMC)(OH)]⁺ (dotted black) and *trans*-III-[Cu(TMC)(H₂O)]²⁺ (solid black) models obtained using the B3LYP functional.

List of Appendices

Appendix A: Stereochemistry of Tetramethylcyclam Metal Complexes Directed by Unexpected

Anion Effects

A.1. Introduction.....	153
A.2. Results and Discussion.....	154
A.2.1. Preparation and Optical Properties of [Cu(TMC)] ²⁺	154
A.2.2. X-ray Crystallographic Analysis of [Cu(TMC)] ²⁺	155
A.3. Conclusions.....	156
A.4. Experimental Section.....	157
A.4.1. Materials and Methods.....	157
A.4.2. X-ray Crystallography.....	157
A.4.3. Preparation of [Cu(TMC)](NO ₃) ₂ (H ₂ O) _{0.5}	157
A.4.4. Preparation of [Cu(TMC)](ClO ₄) ₂	158
A.5. Acknowledgements.....	158
A.6. References.....	158

Appendix B: Additional Supplementary Data

B.1. ¹ H/ ¹³ C NMR Characterization of the Multifunctional Derivatives (AQP2-4 and AQDA1-3)....	162
B.2. Supplemental EPR Data for Co(II)(TMC).....	168
B.3. Supplemental Computational Data for M(II)(TMC).....	171
B.4. Supplemental Mass Spectrometry Fragmentation Data for M(II)(TMC).....	172
B.5. Supplemental X-ray Crystallographic Data.....	173

List of Abbreviations

5Y cells	Human neuroblastoma SH-SY5Y cells
8-HQ	8-Hydroxyquinoline
ABTS	2,2'-azino-bis(3-ethylbenzothiazoline-6-sulfonic acid)
ACPC	(<i>S,S</i>)-2-aminocyclopentanecarboxylic acid
AD	Alzheimer's disease
ADAM	A disintegrin and metalloprotease
AICD	APP intracellular domain
ANOVA	Analysis of variance
APP	Amyloid precursor protein
AQ1	Quinolin-8-amine
AQ2	2-Methylquinolin-8-amine
AQ3	8-Aminoquinoline-2-carboxylate
AQ4	(8-Aminoquinolin-2-yl)methanol
AQDA1	4-(Dimethylamino)-2-((quinolin-8-ylamino)methyl)phenol
AQDA2	4-(Dimethylamino)-2-(((2-methylquinolin-8-yl)amino)methyl)phenol
AQDA3	Methyl 8-((5-(dimethylamino)-2-hydroxybenzyl)amino)quinoline-2-carboxylate
AQP1	2-((Quinolin-8-ylamino)methyl)phenol
AQP2	2-(((2-Methylquinolin-8-yl)amino)methyl)phenol
AQP3	Methyl 8-((2-hydroxybenzyl)amino)quinoline-2-carboxylate
AQP4	2-(((2-(Hydroxymethyl)quinolin-8-yl)amino)methyl)phenol
AChE	Acetylcholinesterase
ApoE4	Apolipoprotein E4
A β	Amyloid- β
BACE1	β -Secretase 1
BBB	Blood-brain barrier
BQ	Benzoquinone
BQI	Benzoquinoneimine
BSB	Brain sink buffer
CCS	Collisional cross-section
CD	Circular dichroism
CI	Cationic imine

CID	Collision induced dissociation
CNS	Central nervous system
CQ	Clioquinol; 5-chloro-6-iodoquinolin-8-ol
CSF	Cerebrospinal fluid
CSP	Chemical shift perturbation
CW-EPR	Continuous wave electron paramagnetic resonance
Ctx	Cortex
Cyclam	1,4,8,11-Tetraazacyclotetradecane
Cyclen	1,4,7,10-Tetraazacyclododecane
DCE	1,2-Dichloroethane
DCM	Dichloromethane
DFT	Density functional theory
DHB	5-(Dimethylamino)-2-hydroxybenzaldehyde
ddH ₂ O	Doubly-distilled water
DM	Diabetes mellitus
DMF	Dimethylformamide
DMPD	<i>N,N</i> -Dimethyl- <i>p</i> -phenylenediamine
DMSO	Dimethyl sulfoxide
ELISA	Enzyme-linked immunosorbent assay
ENDOR	Electron nuclear double resonance
EPR	Electron paramagnetic resonance
ESEEM	Electron spin echo envelope modulation
ESI-MS	Electrospray ionization-mass spectrometry
EXAFS	Extended X-ray absorption fine structure
EtOH	Ethanol
F12K	Ham's F12K Kaighn's modification media
FA	Formic acid
FAME	FAst MEtabolizer
FAD	Flavin adenine dinucleotide
FBS	Fetal bovine serum
F_{Cu}	Fraction of copper bound species at given pH
F_L	Fraction of species at given pH
FTDP-17	Frontotemporal dementia and parkinsonism linked to chromosome 17

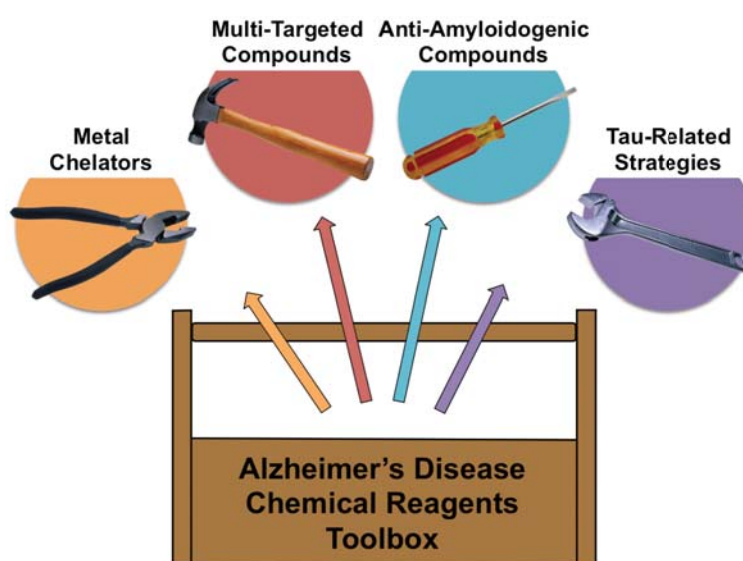
GABA-A	γ -Aminobutyric acid-A
GL ₃	2-methyl-1-(4-(methylamino)phenyl)-3-(((2 <i>S</i> ,3 <i>R</i> ,4 <i>S</i> ,5 <i>S</i> ,6 <i>R</i>)-3,4,5-trihydroxy-6-(hydroxymethyl)tetrahydro-2 <i>H</i> -pyran-2-yl)oxy)pyridin-4(1 <i>H</i>)-one
GL ₄	1-(4-aminophenyl)-2-methyl-3-(((2 <i>S</i> ,3 <i>R</i> ,4 <i>S</i> ,5 <i>S</i> ,6 <i>R</i>)-3,4,5-trihydroxy-6-(hydroxymethyl)tetrahydro-2 <i>H</i> -pyran-2-yl)oxy)pyridin-4(1 <i>H</i>)-one
GSK-3(β)	Glycogen synthase kinase-3(β)
HBA	Hydrogen bond acceptor
HBD	Hydrogen bond donor
H ₂ O ₂	Hydrogen peroxide
HD	Huntington's disease
HEPES	4-(2-Hydroxyethyl)-1-piperazineethanesulfonic acid
HFIP	Hexafluoro-2-propanol
Hip	Hippocampus
Htau40	Full length human tau
Hx	Hexanes
IM	Ion mobility
IM-MS	Ion mobility-mass spectrometry
i.p.	Intraperitoneal injection
JNK	Jun N-terminal kinase
K_d	Dissociation constant
KMI-358	(5 <i>S</i> ,8 <i>S</i> ,11 <i>S</i> ,14 <i>S</i> ,15 <i>R</i>)-5-amino-14-benzyl-16-((3-carboxyphenyl)amino)-15-hydroxy-11-isobutyl-8-isopropyl-2,6,9,12,16-pentaoxo-3,7,10,13-tetraazahexadecanoic acid
KMI-370	5-((4 <i>S</i> ,7 <i>S</i> ,10 <i>S</i> ,13 <i>S</i> ,14 <i>R</i>)-4-amino-13-benzyl-1-carboxy-14-hydroxy-10-isobutyl-7-isopropyl-1,5,8,11-tetraoxo-2,6,9,12-tetra-azapentadecan-15-amido)isophthalic acid
KMI-420	3-((4 <i>S</i> ,7 <i>S</i> ,10 <i>S</i> ,13 <i>S</i> ,14 <i>R</i>)-4-amino-13-benzyl-14-hydroxy-10-isobutyl-7-isopropyl-1,5,8,11-tetraoxo-1-(1 <i>H</i> -tetrazol-5-yl)-2,6,9,12-tetraazapentadecan-15-amido)benzoic acid
KMI-429	5-((4 <i>S</i> ,7 <i>S</i> ,10 <i>S</i> ,13 <i>S</i> ,14 <i>R</i>)-4-amino-13-benzyl-14-hydroxy-10-isobutyl-7-isopropyl-1,5,8,11-tetraoxo-1-(1 <i>H</i> -tetrazol-5-yl)-2,6,9,12-tetraazapentadecan-15-amido)isophthalic acid
L2-b	N^1,N^1 -dimethyl- N^4 -(pyridin-2-ylmethyl)benzene-1,4-diamine

LDL	Low density lipoprotein
LF	Ligand-field
LMW	Low molecular weight
$\log\beta$	Stability constant
$\log\text{BB}$	Calculated BBB partition coefficients
M17 cells	Human neuroblastoma SK-N-BE(2)-M17 cells
MALDI-MS	Matrix assisted laser desorption ionization-Mass spectrometry
MAO	Monoamine oxidase
MAPs	Microtubule-associated proteins
MD	Molecular dynamics
MEM	Minimal Essential Media
ML	Multifunctional ligand; 4-(dimethylamino)-2-(((2-(hydroxymethyl)quinolin-8-yl)amino)methyl)phenol
MMP	Matrix metalloproteinase
MS	Mass spectrometry
MS/MS	Tandem mass spectrometry
MTBD	Microtubule binding domain
MTT	3-(4,5-Dimethyl-2-thiazolyl)-2,5-diphenyl-2 <i>H</i> -tetrazolium bromide
MTs	Microtubules
MW	Molecular weight
N2a cells	Mouse neuro-2a neuroblastoma cells
nESI-MS	Nano-electrospray-ionization mass spectrometry
NFTs	Neurofibrillary tangles
NICD	Notch intracellular domain
NMDA	<i>N</i> -methyl- <i>D</i> -aspartate
NMR	Nuclear magnetic resonance
NOTCH1	Notch receptor 1
PBC	Periodic boundary conditions
PBS	Phosphate buffered saline
PBT2	5,7-Dichloro-2-[(dimethylamino)methyl]quinolin-8-ol
PD	Parkinson's disease
PHFs	Paired helical filaments
$\text{p}K_{\text{a}}$	Acidity Constant

PKC	Protein kinase C
PME	Particle-Mesh Ewald method
PSA	Polar surface area
PS(1/2)	Presenilin(1/2)
PVDF	Polyvinylidene fluoride
ptau	Hyperphosphorylated tau
QBP	8-((3 <i>aR</i> ,4 <i>R</i> ,6 <i>R</i> ,7 <i>R</i>)-3 <i>a</i> ,5,5-trimethylhexahydro-4,6-methanobenzo[<i>d</i>][1,3,2]dioxabor-ol-2-yl)quinoline
RMSD	Root-mean-square deviations
ROS	Reactive oxygen species
sAPP α	Soluble N-terminal cleavage product resulting from α -secretase cleavage.
sAPP β	Soluble N-terminal cleavage product resulting from β -secretase cleavage.
SDS	Sodium dodecyl sulfate
SEM	Standard errors of the mean
SMON	Subacute myelo-optic neuropathy
SOFAST-HMQC	2D band-Selective Optimized Flip-Angle Short Transient Heteronuclear Multiple Quantum Coherence
SPC	Single point charge
SPR	Surface plasmon resonance
TBP	Trigonal bipyramidal
TBS	Tris-buffered saline
TDDFT	Time-dependent density functional theory
TEAC	Trolox equivalent antioxidant capacity
TEM	Transmission electron microscopy
TMC	Tetramethylcyclam; 1,4,8,11-tetramethyl-1,4,8,11-tetraazacyclotetradecane
ThT	Thioflavin-T
UV-vis	UV-visible spectroscopy
XANES	X-ray absorption near edge structure
XAS	X-ray absorption spectroscopy

Chapter 1.

Tools of the Trade: Investigations into Design Strategies of Small Molecules to Target Components in Alzheimer's Disease



This chapter was adapted from the publication Derrick, J. S.; Lim, M. H. *ChemBioChem* **2015**, *16*, 887–898. I thank Professor Lim for her assistance and guidance throughout the writing of this manuscript.

1.1. Introduction

Preservation may be one of the most fundamental human instincts. As a population, we seek to live as long as possible and according to current life expectancies we have been achieving this goal. The rise in longevity is no doubt a direct result of the enormous advancements that have been made within the medical and scientific domains. Unfortunately, escalations in life span are also met with new challenges; in particular, the prevalence of degenerative diseases [*i.e.*, Alzheimer's disease (AD), Parkinson's disease (PD), Huntington's disease (HD), diabetes mellitus (DM)] has increased to the point where millions of people around the world are presently affected by these insidious disorders.¹ Degenerative diseases are currently costing caregivers billions of dollars annually to supply the long-term aid required for those suffering from these illnesses.¹ Without a cure or even an effective treatment for any degenerative disorder alongside a demographic shift toward an increasingly aged population, it is unclear how the resources necessary to manage such a large scale epidemic would be provided.

The development of therapeutic interventions has been limited by a lack of information on the etiologies of degenerative diseases, mostly due to their complicated and multifactorial nature.²⁻⁶ While each degenerative disease is inherently unique, they do share some characteristics (*e.g.*, accumulated misfolded/aggregated proteins, metal ion dyshomeostasis, and oxidative stress conditions).²⁻⁶ All of these common factors that are believed to contribute to toxicity to different extents also offer promise as potential therapeutic targets. Furthermore, if the similarities between these disorders would prove to be effective targets, multiple disorders could be treated utilizing a fundamental, guiding principle. The number of tactics proposed to address these disorders in the literature is vast and therefore cannot be completely summarized. Instead, some of the key design concepts for small molecule intervention in AD are described in this chapter. In addition, these design approaches can be and are currently being translated to other degenerative disorders.⁷⁻¹¹

1.2. Alzheimer's Disease

AD is the most common neurodegenerative disease; currently affecting about 24 million people worldwide.^{1-6,12-16} Unlike the other major causes of death in the United States, such as heart disease and cancer, the numbers affected by AD are projected to increase with extrapolated values reaching around 100 million by 2050.^{1-6,12-16} This can be attributed to the absence of therapeutic agents with current FDA-approved drugs only offering symptomatic relief through control of the level and activity of neurotransmitters (*e.g.*, donepezil and memantine related to acetylcholine and glutamate, respectively).^{1,2,6} Unfortunately, these treatments are only beneficial for short periods of time (6 to 12 months), thus

stressing the urgent need for the new discovery of effective treatment options.^{1,2,6} In order to achieve these future breakthroughs in drug discovery, an advance in the current understanding of the complex disease etiology is critical.

Amyloid Cascade Hypothesis & Metal Ion Hypothesis

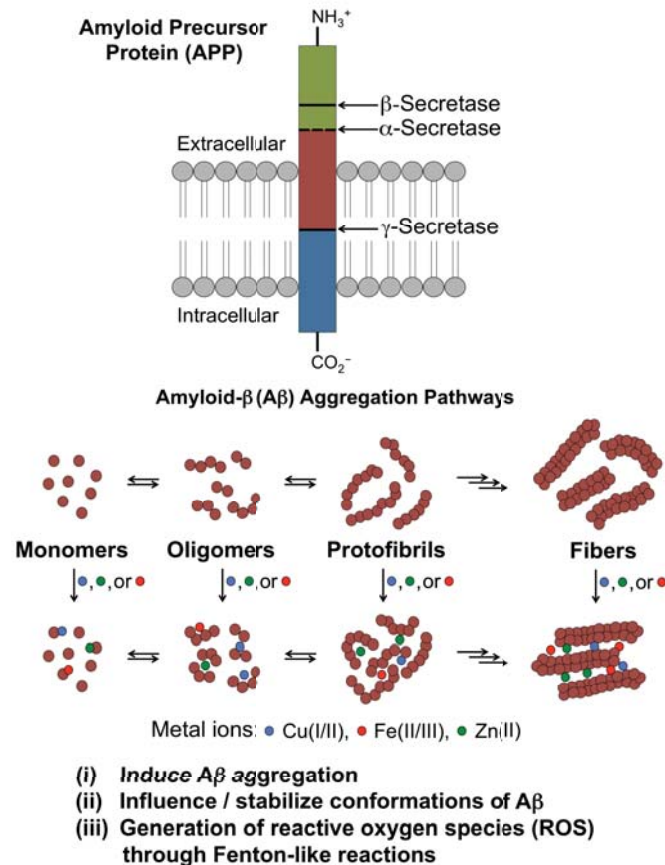


Figure 1.1. A schematic representation of the amyloid cascade hypothesis and the metal ion hypothesis. The processing of the amyloid precursor protein (APP) by β - and γ -secretases [green segment: the respective soluble N-terminal cleavage products, sAPP α and sAPP β ; red segment: amyloidogenic isoforms, A β_{40} and A β_{42} ; blue segment: the APP intracellular domain (AICD)] leads to the production of A β_{40} and A β_{42} monomers that can go through a slow nucleation stage followed by a fast elongation phase resulting in the formation of mature aggregated fibrils. The overproduction of A β aggregates and the ineffective clearance cause A β plaque deposition. Metal interaction with A β species can facilitate peptide aggregation pathways, stabilize toxic conformations, and generate the production of reactive oxygen species (ROS) through Fenton-like reactions.

Histopathologically, the AD-afflicted brain is characterized by the presence of senile plaques and neurofibrillary tangles (NFTs) composed of misfolded, aggregated amyloid- β (A β) peptides and hyperphosphorylated tau protein (p τ), respectively, both being considered hallmarks of the disease

(Figure 1.1).^{2-6,12-21} The distinct nature of A β plaques and NFTs has initially made them prime suspects as the toxic, causative agents of AD leading to the broad acceptance of their respective hypotheses (*i.e.*, amyloid cascade and tau hypotheses).^{2-6,12-16} The amyloid cascade hypothesis claims that the overproduction and/or ineffective clearance of A β , the proteolytic cleavage product of the amyloid precursor protein (APP) by β - and γ -secretases, result in the accumulation of A β , which tends to aggregate into toxic oligomeric species (Figure 1.1).^{2-6,12-17} Initial evidence supporting the amyloid cascade hypothesis has been largely supplied from the less common, familial form of the disease (*i.e.*, *ca.* 5% of all AD cases are considered to be familial) that often occurs earlier in life (45 years of age or younger) where genetic mutations in the APP, presenilin 1 (PS1) and presenilin 2 (PS2), parts of the excision machinery that composes γ -secretase, have been identified.^{2-6,12-16,18-21} Mutations in these genes can lead to various phenotypes, such as the enhanced production of APP and A β , and the generation of the more aggregation-prone isoform, A β_{42} .²⁻⁶ Carriers of these specific alleles are almost certain to be affected by the disease. How the genetic component translates to the more common sporadic form of the disease as well as a mechanistic understanding of how altered APP processing or A β production engenders toxicity, has not been fully elucidated. Although multiple hypotheses, such as inducing lipid peroxidation, impairing synapse plasticity, and disrupting membrane potentials, through the formation of pores have been proposed.^{5,6,12-17}

The aggregation and accumulation of A β may not be the only factor contributing to neuronal toxicity. The unfortunate lack of clinically successful compounds targeted at either preventing or reversing the aggregation pathways of A β , as well as the poor correlation between plaque load and neuronal function (*i.e.*, 20–40% of cognitively normal individuals have plaque loads consistent with AD) have spurred researchers to consider additional parameters and look in different locations for new, potential contributors to AD pathogenesis.^{5,6} The involvement of metal ions in AD has been evident upon the closer analysis of senile plaques where elevated levels of metals [*i.e.*, Cu(I/II), Zn(II), Fe(II/III)] are found to be co-localized.^{3,5,13-16,17,22,23} A β has been shown mainly through *in vitro* investigations to coordinate to these metal ions.^{2,5,13,16,17,23} The dyshomeostasis and miscompartmentalization of metals in the AD-affected brain consummated the metal ion hypothesis that attributes misregulated metals as a causative feature in the initiation and progression of the disease.^{2-6,13,15-17,23} Metal ions are indicated to facilitate A β aggregation and stabilize specific, toxic conformations of the peptides (Figure 1.1).^{5,13,23,24} Furthermore, redox active metal ions can induce the overproduction of reactive oxygen species (ROS) through Fenton-like reactions with and without A β , which can cause detrimental damage of biological molecules eventually leading to neuronal death (*i.e.*, oxidative stress hypothesis; Figure 1.2).^{5,13,16,17,23}

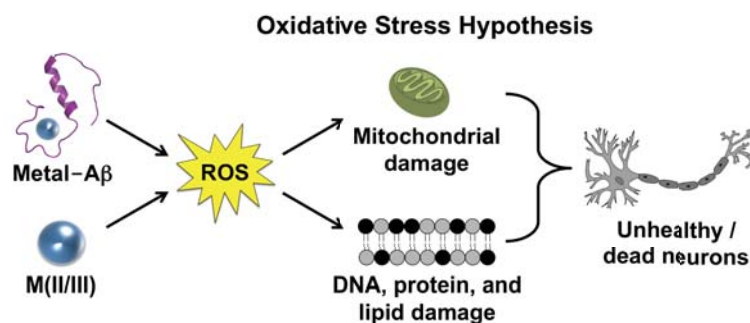


Figure 1.2. The oxidative stress hypothesis. The ROS generated from labile metal pools and redox active metal bound to A β can engender damage of DNA, lipids, and proteins, as well as induce mitochondrial dysfunction, all of which can contribute to neuronal death.

Different from A β which forms aggregates early in the disease pathway and whose plaques are poorly correlated with neuronal impairment, the generation of NFTs composed of tau aggregates occurs much closer to the appearance of clinical symptoms with a more significant connection to neuronal loss.^{6,13} Tau, along with other microtubule-associated proteins (MAPs), are essential for the structural stability and integrity of the intrinsically dynamic microtubules (MTs).^{4,6,12,13,18,19} The stabilization of MTs by tau is associated with normal anterograde and retrograde shuttling of essential nutrients, neurotransmitters, and organelles.^{6,12,13} Therefore, when hyperphosphorylation of tau catalyzes its release from MTs, toxicity arises *via* either the creation of aggregates affording paired helical filaments (PHFs) and eventually NFTs, or impaired synaptic plasticity and axonal transport processes that could be disturbed upon loss and aggregation of tau and other MAPs (Figure 1.3).^{6,12,13} Overall, A β , tau, metal ions, and oxidative stress are only a part of other possible factors that could lead to AD; however, the interconnection between these facets has suggested potential avenues and mechanisms toward neuronal death and AD, thus highlighting the extremely complex nature of the disease.^{13,25}

1.3. Anti-Amyloidogenic Compounds

The identification and overaccumulation of misfolded A β aggregates, along with the growth in acceptance of the amyloid cascade hypothesis, have spurred the development of methods to control A β aggregation. The quantity of literature regarding the design of these methods to restrain the self-association of A β is immense; therefore, instead of focusing on all design strategies, the theoretical basis for such a development of these methods will be provided with recent literature examples to highlight their applications. The production and processing of A β from APP and its subsequent aggregation pathways have been well studied through the use of various techniques, such as circular dichroism (CD)

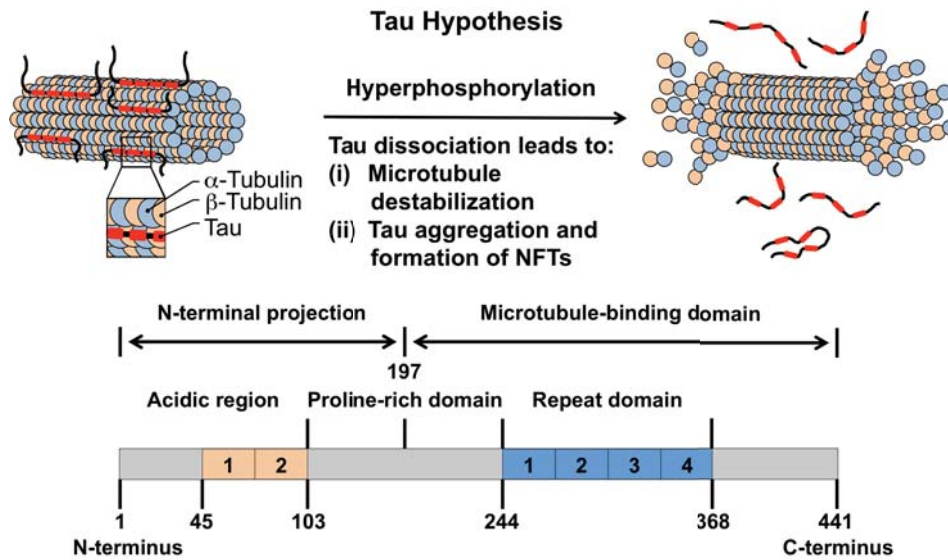


Figure 1.3. The tau hypothesis. Alternative splicing of exons 2, 3, and 10 produces six different isoforms of tau ranging from 352 to 441 amino acids in length. The isoforms can have 0-2 acid repeats (0N-2N) (orange) and 3 or 4 microtubule binding domains (3R or 4R) (blue). Tau is a highly charged protein with an acidic N-terminus (pI 3.8) and extremely basic central, proline-rich domain (pI 11.4) and C-terminus (pI 10.8). Tau, along with other microtubule-associated proteins (MAPs), stabilizes microtubules (MTs). The hyperphosphorylation of tau catalyzes its dissociation from the MTs leading to MT destabilization, which may cause impairment in axonal transport and synaptic plasticity.

and thioflavin-T (ThT) fluorescence.²⁶⁻³¹ The results from reported studies, while highly dependent upon experimental conditions, have indicated that A β undergoes a sigmoidal shaped aggregation route.^{26-28,30} During the slow lag phase, natively unfolded A β goes through a slow nucleation process that leads to the generation of oligomers and protofibrils.^{13,15,26-28} A fast elongation process then quickly follows, where oligomeric and protofibrillar A β quickly grow into mature fibrils.^{13,15,26-28} Once mature fibrils are produced, a plateau stage occurs where further growth of fibrils is slow.^{13,15,26-28} Recent computational analysis of kinetic data obtained from several amyloidogenic systems, however, suggests that fibrils may not be static, innocent bystanders.^{16,35} Instead, the findings support the occurrence of a fibril fragmentation step that ultimately magnifies the number of nuclei and overall augments the rate of the elongation period.^{16,35} A fundamental understanding of APP processing by α -, β -, and γ -secretases and A β production is critical because it allows for the identification of targets and techniques for extraneous intervention of A β aggregation. Modification of A β deposition can be envisioned through two avenues: (i) a pre-production management approach where the goal is to reduce or stop the generation of A β ; (ii) a method for post-production management pathways where the formation and distribution of specific aggregates are controlled (Figure 1.4).

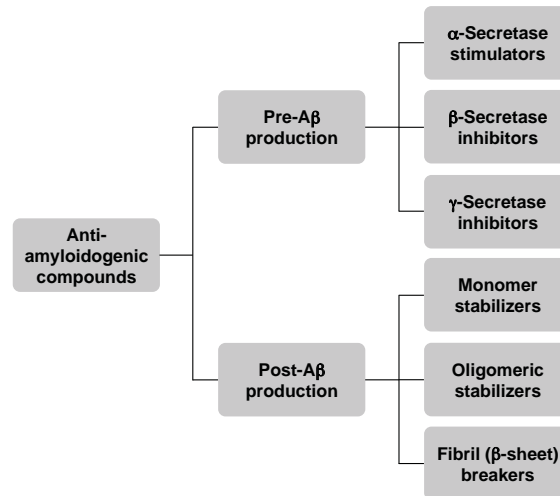
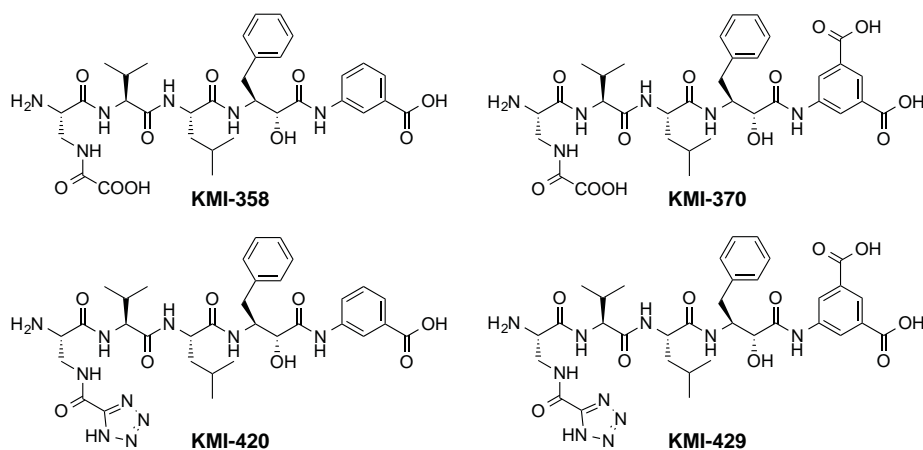


Figure 1.4. A diagram of design rationales toward control of A β aggregation. Anti-amyloidogenic compounds can be divided into pre-/post-A β production management. Pre-A β production pathways are directed at controlling the activity of the secretases that excise APP. Inhibition of β - and γ -secretases leads to a reduction in the amyloidogenic forms of A β while stimulation of α -secretase increases the production of the shorter, non-amyloidogenic forms and sAPP α , the neuroprotective N-terminal cleavage product.

The most direct way to manage A β aggregation would be to regulate its generation from APP.^{26,29,30} Reduction in the assembly of amyloidogenic A β isoforms, A β_{40} and A β_{42} , could be accomplished through the inhibition of β - or γ -secretase. Similarly, the stimulation of α -secretase would also lead to the increased production of smaller non-amyloidogenic, nontoxic forms of the peptide.^{26,29,30} The development of inhibitors for β - and γ -secretases, however, might have limited therapeutic value because each proteolytic enzyme has other substrates, in addition to A β .^{26,29} Suppression of these proteins may interfere with biologically important metabolisms of other substrates, leading to severe consequences.^{26,29} This in fact appears to be the case for nonselective inhibition of γ -secretase, the A β transmembrane protease consisting of at least four protein subunits (PS1, anterior pharynx, nicastrin, and presenilin enhancer 2).^{26,29} Knockout of PS1 results in a lethal phenotype, thought to be linked to notch receptor 1 (NOTCH1) whose proteolytic cleavage products form an essential receptor that is important in the release of the notch intracellular domain (NICD), an indispensable component needed for normal transcription processes.^{26,29,36} Therefore, efforts have been made to discover specific inhibitors that only prevent APP processing while leaving the proteolysis of other substrates, such as NOTCH1, unaffected.^{26,29,36,37} This property has been observed in non-steroidal anti-inflammatory drugs; however, an approach to provide such specificity may also come from the utilization of foldamers.^{26,37} Helical β -peptide foldamers that mimic the transmembrane domain of C99, a substrate of γ -secretase, may be useful for the generation of

NOTCH-sparing inhibitors for γ -secretase.³⁷ Imamura *et al.* identified the (*S,S*)-2-aminocyclopentanecarboxylic acid (ACPC) dodecamer as a potential foldamer framework, in addition to discerning its target site.³⁸ Through derivation and optimization of the foldamer scaffolds, some substrate recognition properties of γ -secretase were revealed, which may supply helpful information for further construction of selective γ -secretase inhibitors.³⁸

Unlike γ -secretase, abolition of the BACE1 gene in mice was not met with any gross abnormalities, suggesting that it might be a better inhibitory target.^{26,29} Unfortunately, recognizing small molecules that exhibit BACE1 inhibitory activity while also possessing necessary properties (*e.g.*, blood-brain barrier (BBB) permeability) for applications in the brain has been a challenge.^{26,29} Two examples of potent BACE1 inhibitors are **KMI-420** and **KMI-490** (Scheme 1.1).^{36,39,40} Their parent compounds, **KMI-358** and **KMI-370**, contain a β -*N*-oxalyl-DAP group that is important for enhancing inhibitory effects toward BACE1; however, the functionality in solution isomerizes to α -*N*-oxalyl-DAP, which is much less stable and potent (Scheme 1.1).³⁹⁻⁴⁰ Interestingly, replacement of the oxalyl moiety with a tetrazole significantly enhanced not only its stability but also its inhibitory activity.³⁹⁻⁴⁰ Until now, the BBB permeability of these compounds was not addressed, and those results could occlude these molecules from further applications as β -secretase-directed therapeutic interventions.³⁹⁻⁴⁰



Scheme 1.1. Chemical structures of β -secretase (BACE1) inhibitors. The parent compounds, **KMI-358** and **KMI-370**, were replaced with a tetrazole to afford **KMI-420** and **KMI-429** with improved BACE1 inhibition. **KMI-358**, (5*S*,8*S*,11*S*,14*S*,15*R*)-5-amino-14-benzyl-16-((3-carboxyphenyl)amino)-15-hydroxy-11-isobutyl-8-isopropyl-2,6,9,12,16-pentaoxo-3,7,10,13-tetraazahexadecanoic acid; **KMI-370**, 5-((4*S*,7*S*,10*S*,13*S*,14*R*)-4-amino-13-benzyl-1-carboxy-14-hydroxy-10-isobutyl-7-isopropyl-1,5,8,11-tetraoxo-2,6,9,12-tetra-azapentadecan-15-amido)isophthalic acid; **KMI-420**, 3-((4*S*,7*S*,10*S*,13*S*,14*R*)-4-amino-13-benzyl-14-hydroxy-10-isobutyl-7-isopropyl-1,5,8,11-tetraoxo-1-(1*H*-tetrazol-5-yl)-2,6,9,12-tetraazapentadecan-15-amido)benzoic acid; **KMI-429**, 5-((4*S*,7*S*,10*S*,13*S*,14*R*)-4-amino-13-benzyl-14-hydroxy-10-isobutyl-7-isopropyl-1,5,8,11-tetraoxo-1-(1*H*-tetrazol-5-yl)-2,6,9,12-tetraazapentadecan-15-amido)isophthalic acid.

An alternative to the suppression of γ - and β -secretases would be the stimulation of α -secretase; however, this has proven to be more difficult to achieve than inhibition.^{26,29} The activation of α -secretase might also possess an additional advantage over the obstruction of γ - and β -secretases. The N-terminal fragment generated from cleavage by α -secretase, sAPP α , has potent and neuroprotective, memory-enhancing effects; therefore, stimulation of α -secretase can enhance neuroprotection, in addition to diminishing the promotion of toxic, aggregation-prone A β isoforms.²⁹ Although the identity of α -secretase has not been completely elucidated, current evidence has pointed to members of the A disintegrin and metalloprotease (ADAM) family (*i.e.*, specifically, ADAM9 and ADAM10).²⁹ Particularly, overexpression of ADAM10 in transgenic animal models leads to a decrease in amyloid pathology, suggesting upregulation of ADAM10 as a possible strategy to reduce the generation of amyloidogenic A β .²⁹ Another approach might be the application of statins, a class of drugs used to lower cholesterol levels, which have been shown to have positive effects on AD patients.^{29,41} One hypothesis for the beneficial effects of statins is related to their ability to enhance sAPP α levels through activation of α -secretase; however, this is still controversial and the benefits and mode of action are still debated.^{29,41} The mobilization of protein kinase C (PKC) or the activation of receptors that work through PKC might be an alternative avenue to enhance α -secretase's activity.²⁹ Finally, selective muscarinic M₁ receptor antagonists, such as talsaclidine and AF102B, which have been shown to reduce A β concentrations in the cerebrospinal fluid (CSF) of AD patients, could be utilized.^{26,29} Most of the currently available activators for α -secretase were designed for other intended purposes; thus, they exhibit poor selectivity and have limited applicability. Nonetheless, the emergence of novel routes and molecules to promote the activation of α -secretase, such as γ -aminobutyric acid-A (GABA-A) receptor regulator, EHT-0202, offers promise for this approach in future AD research.^{26,29}

The development of anti-amyloidogenic compounds targeted at post-production of A β could be theoretically directed at any specific species (*i.e.*, monomers, oligomers, protofibrils, fibrils) along the aggregation pathway. For example, monomer blockers that are able to stabilize monomeric A β in a native, nontoxic state could prevent any toxicity associated with the aggregation process (*i.e.*, generation of A β oligomers), as well as inhibit the formation of plaques.³⁰ Similarly, stabilization or conformational alteration of oligomers toward nontoxic states through the use of oligomer blockers could be envisioned.³⁰ The rational design of these types of low molecular weight (LMW) targeting compounds is not simplistic. The natively unstructured properties of LMW A β and, in the case of oligomers, a lack of high-resolution, structural information makes achieving specificity over larger, aggregated species extremely difficult.³⁰ The utilization of foldamers offers a recent approach toward achieving this type of LMW selectivity.

Fülöp *et al.* developed foldamer-dendrimer conjugates constructed with helical foldamer segments (Figure 1.5).³⁷ The foldamer segments were designed to mimic the hydrophobic core of the self-recognition sequence of A β (KLVFF) with neighboring zwitterionic residues, similar to K16 and E22 of A β , which they hypothesized to be critical chemical properties for interaction with LMW A β species.³⁷ Preliminary nuclear magnetic resonance (NMR) investigations validated the principle of the idea and Fülöp *et al.* then further optimized the foldamers affinity for LMW A β oligomers by creating a tetravalent foldamer-dendrimer conjugate that was able to capture oligomers at sub-micromolar concentrations as well as rescue long-term potentiation effects in *ex-vivo* tissues (Figure 1.5).³⁷ The BBB permeability of these compounds was not determined, but due to their large size, structural modifications would be necessary to impart acceptable permeation for utilization in AD.

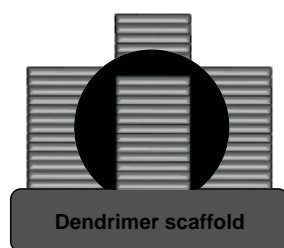


Figure 1.5. A representation of the tetravalent foldamer-dendrimer conjugates developed to target low molecular weight (LMW) A β species (*i.e.*, oligomers, black sphere). Attached to a dendrimer scaffold (dark grey rectangle) were foldamer segments (light grey rectangles) that were designed to mimic the hydrophobic core and surrounding zwitterionic residues of A β . Binding affinity for LMW A β was increased through tetravalent structural modifications.

Another example of achieving some sort of specificity toward LMW A β oligomers is the use of metal complexes (*e.g.*, L-PtCl₂ complexes).^{28,42} These metal complexes interact with the histidine residues of the metal binding region of A β where ligand exchange of the chloro ligands can occur.^{28,42} Studies with cisplatin [*cis*-Pt(NH₃)₂(Cl)₂] do not show appreciable ability to inhibit fibril formation, identifying the importance of having an aromatic auxiliary ligand, such as phenanthroline, for pivotal π - π stacking with F4, Y10, and H13; however, cisplatin has been shown to inhibit hydrogen peroxide (H₂O₂) formation by copper-catalyzed oxidation of A β , *in vitro*.²⁸⁻³⁴ These aromatic Pt complexes were able to inhibit metal-induced A β aggregation, as well as regulate A β -induced synaptotoxicity in mouse hippocampal slices.^{28,42} In addition to the positive results of this study, it also serves as a proof of concept that organometallic complexes can be utilized against A β /metal-A β . Furthermore, the selective A β inhibitory activity of these compounds suggests that targeting the metal binding site in A β could also prove to be a potential approach to gain specificity over higher MW A β species.^{28,42} The use of metal complexes, however, still

needs to be subjected to more intensive *in vivo* testing, especially because of the potential toxicity associated with the introduction of exogenous redox active metals into an environment already affected by oxidative stress. In the case of Pt complexes, Pt(II) is most likely redox inactive within the cell; however, its toxicity in biological systems presents additional challenges.^{32,33} The use of Pt(IV) complexes that can then be reduced by natural reductants (*e.g.*, glutathione) back to labile Pt(II) upon entering the cell may offer one solution to this obstacle.^{32,33}

Finally, the development of β -sheet breakers is a strategy to manage post-A β production. These molecules are able to specifically interact with high MW A β fibrils to prevent or disrupt β -sheet formation, which has been shown to be neurotoxic by *in vitro* studies.^{26,43,44} A key innovation for the generation of design strategies of these compounds has been the determination of the central hydrophobic region (*i.e.*, self-recognition motif) and the hydrophobic C-terminal residues in the aggregation process and formation of β -sheet structure.³⁰ Most of this class of inhibitors have employed short fragments, generally 5 to 11 amino acid residues in length, that are similar to or mimic the nonpolar core of A β to disrupt the hydrophobic interactions pivotal for fibril elongation.^{26,30,44} These motifs are often modified by the addition of more charged or hydrophilic substituents to help with the intrinsically poor solubility in aqueous environments.³⁰ Additionally, proline residues are often incorporated to decrease the hydrogen bonding networks with neighboring residues.³⁰ Small molecule approaches have also been devised, many taking advantage of aggregation-dependent dyes, such as ThT and Congo red derivatives.^{30,44} Within the past decade a myriad of molecular scaffolds have proven to be effective at targeting fibrils some of which include flavonoids, polyphenols, and benzofuran derivatives.^{26,30} The extensive development of such compounds has been the subject of vast literature reports; therefore, it will not be described in this chapter.³⁰

1.4. Metal Chelators and Ionophores

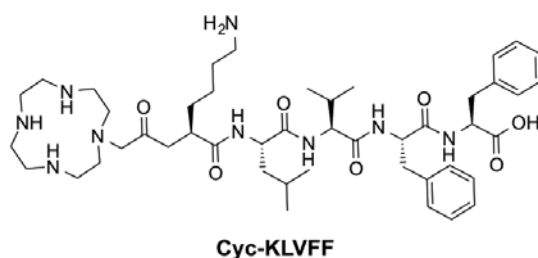
The dyshomeostasis of metal ions, as previously discussed, is a linking characteristic among many degenerative disorders, such as PD and DM, and is believed to be a contributing factor toward the onset of AD.^{2,4,5,13,15,17,20} The therapeutic use of metal chelating compounds began in the 1900's and since then has been beneficial in the treatment of metal overload diseases (*e.g.*, Wilson's disease, Friedriche's Ataxia).^{20,45} Neurodegenerative diseases, however, pose a more challenging setting for the application of classical metal chelating compounds. As a result, the concepts behind metal chelator design strategy are much more complex than creating molecules that indiscriminately chelate immense amounts of metals.^{9,45,46}

In order for metal chelators to be applicable tools to AD and other neurodegenerative disorders, they should possess the ability to permeate the BBB.^{9,45-51} This critical property alone excludes numerous potential chelators because of the intrinsic hydrophilic nature of the molecules generated by the installation of donor atoms onto a structural framework to achieve metal chelation capabilities.^{9,45,46} Although an increase in structural hydrophobicity could improve BBB penetration, lipophilic metal chelators alone are also not suitable as effective compounds for AD because they reduce water solubility and expands intracellular access where interference with important metalloproteins can occur.^{9,45,46,52} Therefore, the polarity of these molecules needs to be carefully balanced to fashion water soluble, BBB-permeable chelators. Predictive methods, including Lipinski's rules for drug likeness and calculated BBB partition coefficients (logBB) that can help to guide the design of potentially effective BBB-permeable chelators are available.^{2,25,50,51,53} The installation of secondary functionalities (*e.g.*, glucose) can also aid in promoting the passage of potential metal chelators through active transport pathways.^{2,50} The ability of the BBB to block the passive diffusion of most small molecules has led researches to come up with new, innovative ways to permit passage. An example of this is the use of nanoparticles tethered to metal chelators that can act as small molecule chaperones across the BBB through low density lipoprotein (LDL) receptor-mediated avenues.^{48,49} This approach could offer promising results because it might expand new metal chelating frameworks that would otherwise not be applicable toward neurodegenerative diseases. Further *in vivo* testing is still required to fully elucidate the utility of this method.^{48,49}

A common misconception that is often affiliated with the use of metal chelating agents in degenerative diseases is that the goal is to chelate out or completely remove metal ions from protein targets.^{9,45-51} At first glance, the sequestration of metals may seem appealing because of their aforementioned ability to promote the aggregation of misfolded proteins, stabilize toxic species, and generate oxidative stress environments, all of which have been suggested to contribute to neurotoxicity.^{5,23,24} This erroneous assumption is, in fact, one of the biggest challenges when developing metal chelators. The entrapping of essential biometals required for biological processes can lead to serious detrimental effects, including cell death.^{9,45-51} In order to prevent this undesirable outcome, metal chelating compounds should be designed to be selective for the desired metal ion and protein target, as well as have carefully tuned binding affinities in order to minimize disturbance to beneficial metalloproteins.^{9,45,46} Ideal K_d values for Cu(II) and Zn(II) chelators would be generally in the nM and mM range, respectively; however, ligands capable of forming 1:1 and 1:2 complexes make the matter less trivial, with conditional dissociation constants being concentration dependent. Some degree of metal ion specificity can be achieved through the consideration of basic inorganic principles, such as the hard-soft

acid-base principal and the Irving-Williams series.^{25,46} Furthermore, the geometry on the metal binding center, as well as the stoichiometries of the generated complexes, can be considered as additional parameters to impart metal specificity.^{25,46,54}

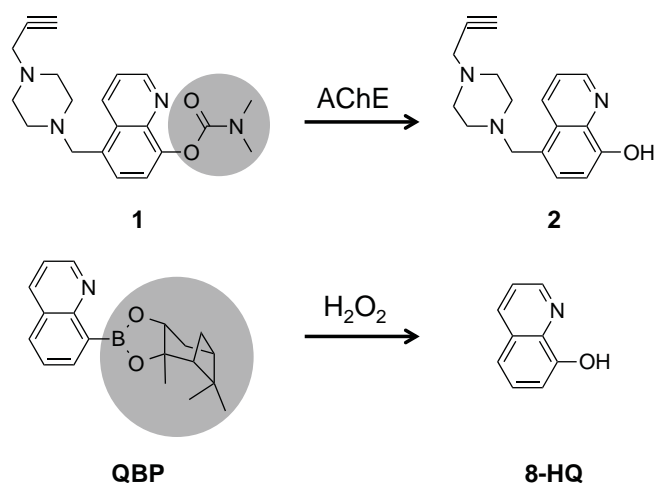
Designing ligands directed toward the correct location (*e.g.*, the brain) and protein target is conceptually as important as metal ion considerations for limiting unintended side effects, such as hypocalcemia and renal failure.^{9,45,46} Unfortunately, there are no guidelines to develop protein-specific chelators. Instead, the characteristics of the peptide must be considered in order to optimize one of its features to impart selectivity. The identity and source of these attributes obviously vary between proteins. The capitalization of the self-recognition (KLVFF) sequence of A β 's central hydrophobic core provides one example used by Wu and coworkers.⁵⁵ They attached the A β recognition sequence known to be important in the aggregation pathway and design of β -sheet breaking compounds (*vide supra*) onto an *apo*-cyclen framework (Scheme 1.2).^{26,30,44,55} The *apo*-cyclen compound, **cyc-KLVFF**, was able to interact with metal-A β , abstract the Cu(II) bound to the peptide, thus generating a proteolytically active complex that was shown to inhibit A β aggregation and disaggregate preformed A β aggregates, as well as reduce the formation of H₂O₂ (*ca.* 75% inhibition) generated by Cu(II)-A β ₄₂, and ameliorates metal-A β (Cu(II)-A β ₄₂) induced toxicity in living cells.⁵⁵ Although **cyc-KLVFF** was only evaluated in an AD model system,⁵⁵ mimicking the incorporation of amino acid residues important for self-association could be broadly applicable to any disease in which misfolded proteins and metal ions are suspected players (*i.e.*, degenerative diseases, in general).



Scheme 1.2. The chemical structure of an *apo*-cyclen framework with the A β self-recognition sequence (KLVFF) installed for protein specificity. The amino acid sequence of A β ₄₂ is provided with the self-recognition sequence highlighted and underlined in blue. The *apo*-compound abstracts Cu(II) from Cu(II)-A β , forming a proteolytically active complex capable of degrading monomeric and oligomeric A β forms.

The use of prochelators, a class of ligands containing a protecting group that masks the metal binding site of the molecules, could provide another approach to incorporate location and protein specificity

(Scheme 1.3). The Franz group reported an example of such compounds.⁵⁶ 8-Hydroxyquinoline (**8-HQ**), a prominent bioactive metal chelator that has been extensively utilized in the AD field, was protected with a boronic ester group to generate the ligand, **QBP**, [8-((3a*R*,4*R*,6*R*,7*R*)-3a,5,5-trimethylhexahydro-4,6-methanobenzo[*d*][1,3,2]dioxaborol-2-yl)quinoline] that is only active when H₂O₂ is present.⁵⁶ In the presence of H₂O₂, the boronic ester group is oxidatively cleaved releasing the active chelator, **8-HQ**, which is able to diminish Cu-catalyzed production of ROS and control the generation of A β aggregates.⁵⁶ The design strategy for this compound is especially innovative since it could allow for the control of metals and metal-mediated ROS without causing redistribution of metal ions, because **QBP** is only active in an oxidative-stress-like environment.⁵⁶ Another **8-HQ**-based prochelator, **1**, reported by Zheng *et al.*, was designed to employ a carbamyl moiety as a protecting group for the hydroxyl O donor atom and incorporate a propargylamine functionality for enhancement of neuroprotective properties.⁴⁷ These proligands were capable of gaining improved target specificity through the carbamyl mask that was found to be a selective and potent inhibitor of acetylcholinesterase (AChE), an enzyme responsible for the hydrolysis of the neurotransmitter, acetylcholine.⁴⁷ Upon interaction and inhibition of AChE, the carbamyl functionality was cleaved, releasing the active bidentate chelator (**2**).⁴⁷ The ability to generate effective metal chelating compounds from an inert prochelator could allow for the precise reactivity toward numerous pathogenic features of AD (*e.g.*, chelators stimulated by β -secretase metabolism), in addition to AChE-activated molecules.



Scheme 1.3. The chemical structures of 8-hydroxyquinoline (**8-HQ**)-based prochelators (protecting group highlighted in grey) and their respective active forms. The carbamyl protecting group from the dimethylcarbamate (**1**) is cleaved upon inhibition of acetylcholinesterase (AChE) to give 5-((4-(prop-2-yn-1-yl)piperazin-1-yl)methyl)quinolin-8-ol (**2**). **QBP** [8-((3a*R*,4*R*,6*R*,7*R*)-3a,5,5-trimethylhexahydro-4,6-methanobenzo[*d*][1,3,2]dioxaborol-2-yl)quinoline] is converted into its active form, **8-HQ**, upon oxidation of its boronic ester-mask.

One of the most prominent metal chelators within the AD field is, clioquinol (**CQ**).^{9-11,57-62} **CQ** was initially marketed as an antifungal, antiprotozoal drug; however, its use has been restricted since treatment with **CQ** in Japan might have been linked to subacute myelo-optic neuropathy (SMON), a neuronal disease that causes blindness, paralysis, and death.^{9-11,57-62} A casual correlation between **CQ** and SMON has yet to be established, and its role in the onset of the disease is a matter of debate.^{9-11,57-62} **CQ** has shown promise as a therapeutic agent for multiple neurodegenerative diseases.^{9-11,57-60,62} Encouraging results were reported for its use in AD clinical trials.^{9,57,59} Furthermore, it was also able to improve the behavioral and pathogenic phenotypes in mouse models of PD and HD.⁹⁻¹¹ Unfortunately, assessment of **CQ** was halted in AD clinical trials because of a toxic diiodo impurity during the large-scale synthesis of the compound.⁶³ The contamination associated with **CQ** lead Bush and coworkers to design the second generation compound, **PBT2**, through a more facile synthetic approach that can avoid the impurity issues indicated in the production of **CQ**.^{63,64} Surprisingly, **PBT2** possessed superior BBB permeability while still maintaining affinity for copper and zinc ions.^{63,64} Most importantly, in *in vivo* and clinical settings, **PBT2** decreased interstitial A β within hours of treatment and improved cognitive functions within several days, overall exceeding **CQ**'s performance.^{63,64} Treatment with **CQ** and **PBT2** in living cells was found to increase intracellular levels of copper and zinc.^{9,58,60,62,63} Investigations into the mode of action of **PBT2** and **CQ** revealed that they do not sequester metals like conventional chelators but instead behave more like ionophores, redistributing metal ions to regions where they can be beneficial (*i.e.*, intracellular locations).^{9,58,60,62,63} A proposed mechanism for this activity in AD is that **CQ** can complex with copper localized within A β plaques, possibly forming ternary complexes, and then deliver the metal into the cell.^{9,64} Once in the cell, the copper complexes with **CQ** can activate the phosphorylation of glycogen synthase kinase-3 (GSK-3), which can then potentiate the activation of Jun N-terminal kinase (JNK) and, along with activation of phosphoinositol 3-kinase enhance the activity of matrix metalloprotease-2/3 (MMP2 and MMP3).⁶⁴ MMPs can then facilitate the breakdown and clearance of A β plaques (Figure 1.6).^{9,64} These investigations not only report promising compounds for the intervention of degenerative disorders but also suggest that an ionophore mode of action might be the desired activity for future metal chelators.

1.5. Multifunctionality

Recently, there has been a paradigm shift in the literature for the construction of chemical tools and therapeutics to treat neurodegenerative diseases. The shortcomings from targeting a single feature of degenerative disorders, such as AChE or glutamate in AD [*i.e.*, AChE inhibitors and *N*-methyl-*D*-aspartate (NMDA) receptor antagonists] and monoamine oxidase (MAO) for PD [*i.e.*, MAO inhibitors

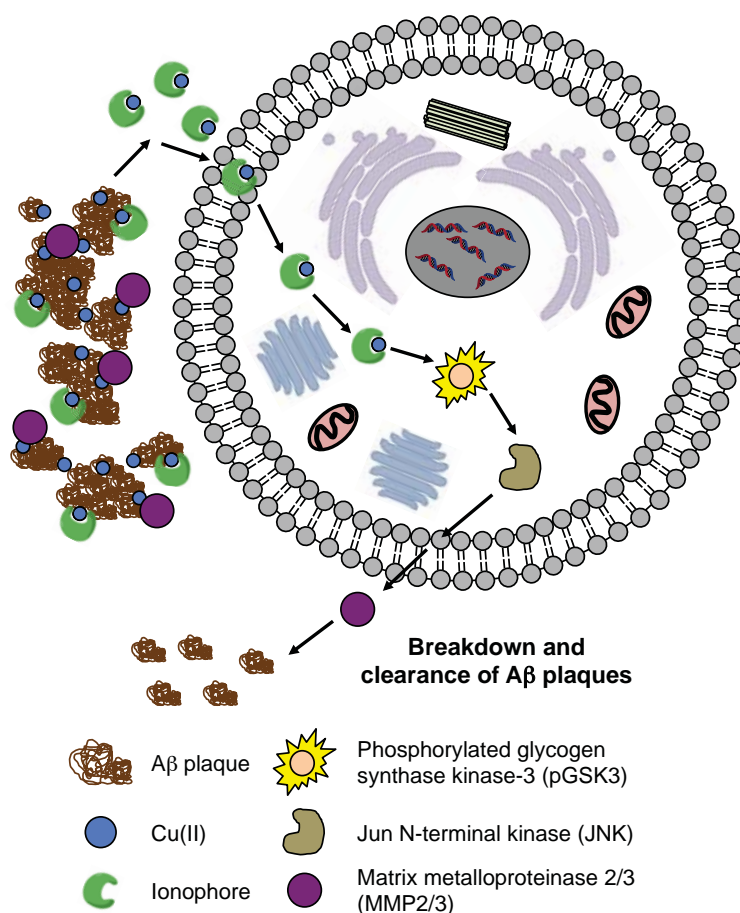


Figure 1.6. A proposed mode of action of clioquinol (CQ) and other similar ionophores. CQ diffuses into the brain where it interacts with extracellular Aβ plaques and metals. CQ binds copper and enters adjacent cells. Once in the cell, the complex dissociates and the metal ions can activate the phosphorylation of glycogen synthase kinase-3 (GSK3) which along with activation of Jun N-terminal kinase (JNK) promotes the activation of matrix metalloproteinase 2 and 3 (MMP2/MMP3). MMP2/MMP3 then can aid in the breakdown and clearance of extracellular, metal-free and metal-bound Aβ plaques.

(*e.g.*, rasagiline)] have led to the advancement of multimodal approaches aiming at multiple factors (*e.g.*, misfolded, aggregated proteins, enzyme inhibitors, metal ion homeostasis, and miscompartmentalization) of these complex diseases.^{25,52,65-67} Addressing multiple facets of AD simultaneously can be achieved through two tactics: (i) a multiple-molecule-multiple-target strategy (*i.e.*, polypharmaceutical) and (ii) a single-molecule-multiple-target strategy (*i.e.*, an integrated approach; Figure 1.7).^{65,66} In the polypharmaceutical method, two or more molecules are utilized in a cocktail solution to address different aspects of a disorder. As the name implies, the single-molecule-multiple-target strategy integrates multifunctionality within a single structural entity. The polypharmaceutical approach is not ideal for the generation of chemical tools or therapeutics because it makes identification of structure-reactivity

relationships almost impossible. Furthermore, the simultaneous utilization of multiple compounds to treat different parameters of the disease also greatly enhances the probability of generating unfavorable side effects.⁶⁵

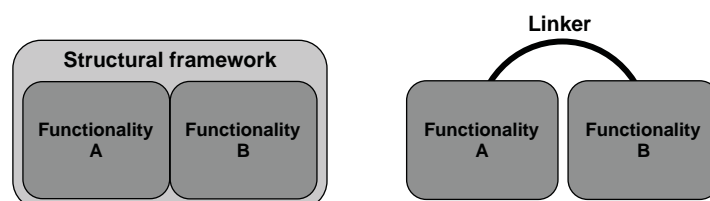
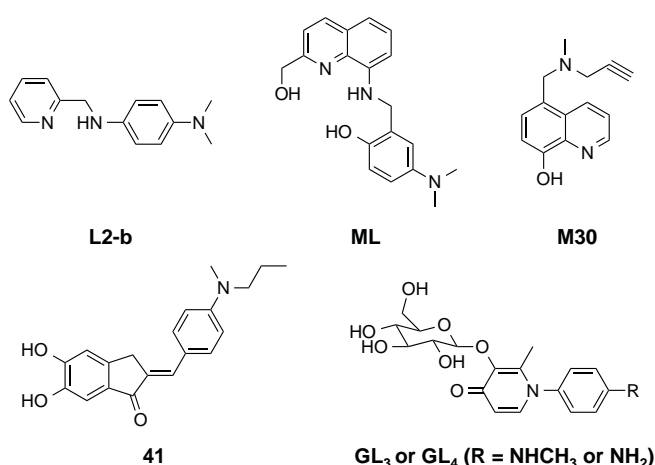


Figure 1.7. A schematic model of the single-molecule-multiple target strategy (*i.e.*, integration approach). A chemical linker can be used to connect two or more independent structural portions to gain multimodal action (right) (*i.e.*, linkage approach). An incorporation approach (left) can install multiple moieties for the desired reactivities into a single structural entity.

Integrated multifunctional molecules can be fashioned through two routes (Figure 1.7). The first tactic, referred to as the linkage approach, takes two or more intact and relatively unmodified molecules and connects them through various organic linkers (Figure 1.7).⁶⁶ The advantage of this method is that it allows for minimal modifications to the individual structural frameworks and therefore improves the probability of maintaining the individual, desired reactivity of the tethered molecules.⁶⁶ These molecules are, however, often structurally complex and highly functionalized, making them synthetically challenging to produce. The other strategy, which is one that our group commonly employs, is the incorporation approach, in which multimodality can be generated in a single molecular framework through the rational installation of specific functionalities (Figure 1.7).^{25,66} The advantage here is that size and complexity can be minimized, which is critical for BBB permeability and similar characteristics essential for applications in AD. The design principles supply the general concepts through which the construction of multi-directed compounds can be envisioned but it does not offer much instruction for specific functionalities that should be present in successful compounds. Instead, because of the extensive versatility of this method, the development and progress of these types of molecules will be propelled by structure-reactivity investigations that can be used to identify beneficial chemical moieties that can be incorporated into pre-existing frameworks and biological and biochemical discoveries of new pathways and targets.

Our group has applied the incorporation approach toward the fabrication of small chemical tools for elucidating the complex AD pathology.²⁵ In order to ascertain the role of metal-A β [*i.e.*, Cu(II)-A β , Zn(II)-A β] in AD pathogenesis, a bifunctional ligand, **L2-b**, was developed through installation of two N donor atoms onto an A β imaging framework (*p*-I-stilbene; Scheme 1.4).^{25,68,69} In addition to its favorable

BBB permeability, (examined both *in vitro* and *in vivo*) and its competitive affinity for metal ions (apparent K_d , *ca.* 10^{-10} and 10^{-6} for Cu(II) and Zn(II), respectively), **L2-b** exhibited an ability to selectively target metal-A β species and modulate their reactivity (*i.e.*, metal-A β aggregation, metal-A β -mediated ROS generation).^{25,68,69} The overall metal-A β specific property of **L2-b** not only validates the application of the incorporation approach for constructing bimodal molecules, but also provides us with a tool to directly probe the involvement of metal-A β in AD pathology *in vivo*.⁷⁰ In a recent study, the selectivity of **L2-b** for metal-A β was further evaluated through ion mobility-mass spectrometry (IM-MS).⁷⁰ IM-MS investigations showed the formation of a more compact A β conformation when Cu(II) was present; this might offer clues to explain the reactivity of **L2-b**.⁷⁰ Most importantly, metal-A β complexes were targeted and modulated within the brain upon treatment of 5XFAD mice with **L2-b**; cognitive impairment, determined by the Morris water maze task, was improved, thus demonstrating *in vivo* experimental evidence that metal-A β contributes to AD pathology.⁷⁰ A similar design strategy was applied to produce a multifunctional ligand, **ML**, to further evaluate the role and interconnections of multiple pathological factors of AD (*e.g.*, A β , metal-A β , metal ions, ROS) (Scheme 1.4).^{25,54} **ML** was able to inhibit metal-free and metal-induced A β aggregation, disaggregate preformed fibrils into off-pathway nontoxic species, improve cell viability in the presence of metal-free and metal-A β , as well as control the formation of Cu(II)-triggered hydroxyl radicals.^{25,54} The individual structural components of **ML** were also evaluated independently and in a cocktail solution. **ML** presented noticeable reactivity, validating the design concept and accentuating the versatility available with the rational incorporation design principle.^{25,54}



Scheme 1.4. The chemical structures of the multifunctional molecules. **L2-b**, N^1, N^1 -dimethyl- N^4 -(pyridine-2-ylmethyl)benzene-1,4-diamine; **ML**, 4-(dimethylamino)-2-(((2-(hydroxymethyl)-quinolin-8-yl)amino)methyl)phenol; **41**, 5,6-dihydroxy-2-(4-(methyl(propyl)amino)benzylidene)-2,3-dihydro-1H-

inden-1-one 4-methylbenzenesulfonate; **GL₃**, 2-methyl-1-(4-(methylamino)phenyl)-3-(((2*S*,3*R*,4*S*,5*S*,6*R*)-3,4,5-trihydroxy-6-(hydroxymethyl)tetrahydro-2*H*-pyran-2-yl)oxy)pyridin-4(1*H*)-one; **GL₄**, 1-(4-aminophenyl)-2-methyl-3-(((2*S*,3*R*,4*S*,5*S*,6*R*)-3,4,5-trihydroxy-6-(hydroxymethyl)tetrahydro-2*H*-pyran-2-yl)oxy)pyridin-4(1*H*)-one.

The inclusion of inhibitory activity for MAOs is an additional property that is often sought after in multi-directed compounds. MAOs (MAO-A and MAO-B) are flavin adenine dinucleotide (FAD)-dependent enzymes responsible for the metabolism of neurotransmitters (*e.g.*, dopamine, serotonin, norepinephrine) whose levels are decreased in AD and other degenerative disorders.⁷¹⁻⁷³ One of the more prominent compounds of this type is **M30**, an **8-HQ** derivative that incorporates a propargyl moiety into its basic framework (Scheme 1.4).^{72,73} The propargyl moiety was introduced into the backbone, because previous investigations suggested it was crucial for the neuroprotective and MAO inhibitory effects of the FDA-approved PD-drug, rasagiline.⁷² Studies by Zheng *et al.* indicated that, in addition to being a potent inhibitor of MAO, **M30** was capable of preventing iron-induced lipid peroxidation through its free radical scavenging and metal chelating properties.⁷² In double transgenic (APP/PS1) AD mouse models, treatment with **M30** improved cognitive defects and attenuated A β accumulation and tau phosphorylation.⁷¹ Li and coworkers have also reported an antioxidant benzylideneindanone derivative, **41**, that ThT and TEM investigations identified as an effective inhibitor of A β ₄₂ aggregation (*i.e.*, 80%).⁷¹ Unlike, **M30**, compound **41** was a potent and selective MAO-B inhibitor (IC₅₀ 7.50 μ M).⁷¹ Selectivity when designing enzyme inhibitors, as previously discussed, is critically important in order to minimally disrupt the processing of additional substrates.

The final example of the versatility that can be accomplished with a rational multi-targeted design strategy was presented by Orvig and coworkers who produced a multifunctional 3-hydroxy-4-(1*H*)-pyridinone prochelator.^{74,75} The proligand utilized a masking glucose functionality, not only to protect the O donor atom of the bidentate framework, but also to impart improved BBB penetration (Scheme 1.4).^{74,75} Furthermore, a degree of location specificity was also secured, because the active form of the molecule was only created upon the loss of the carbohydrate mask by the glycosidic bond hydrolysis from β -glucosidase enzymes upon transport across the BBB.^{74,75} This allows for minimalized complexation of essential metal ions before passage into the brain, where they are able to react with A β by installation of pendant functionalities, trap and control the formation of free radicals, and exhibit adequate brain uptake.^{74,75} Overall, these five examples of multi-target-directed compounds only give a brief glimpse into the power of this rational design approach. The recent recognition and growing acceptance of the multifactorial nature of AD and other neurodegenerative disorders have led to the rapid growth in the development of these types of molecules, and as a result, full reviews could be dedicated to this topic

alone. Innovation and progress in the design of future multifaceted compounds will only be limited by the identification and ingenuity of researchers to target new factors contributing to the disease pathogenesis and the fundamental structural investigations that discern useful structural features for attaining the desired reactivities.

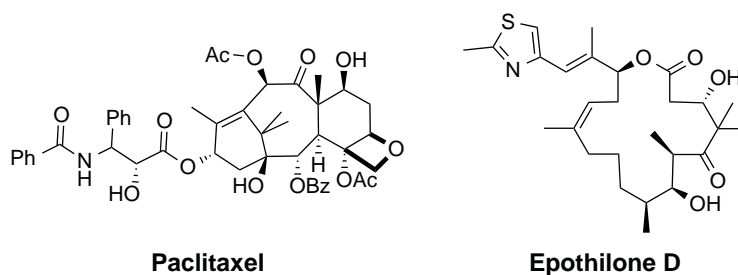
1.6. Tau-Related Strategies

Direct and indirect connections between A β and tau in AD pathogenesis have been discovered; however, the details and mechanistic understandings of these relationships have yet to be elucidated.⁷⁶⁻⁷⁹ Western blotting and enzyme-linked immunosorbent assay (ELISA) experiments have been able to detect the formation of A β -tau complexes *in vitro* and in AD tissue samples.⁸⁰ The complexes were more susceptible to glycogen synthase kinase 3 β (GSK3 β)-mediated phosphorylation.⁸⁰ Surface plasmon resonance (SPR) spectroscopy determined the binding affinity of A β for tau to be in the low nanomolar range suggesting that a critical step in AD pathogenesis may be the intracellular binding of soluble A β to nonphosphorylated tau.⁸⁰ Furthermore, A β and familial AD linked allele, apolipoprotein E4 (ApoE4), have been found to upregulate other kinases in addition to GSK3 β , and treatment with A β oligomers has been met with disruption of MT structure and function.^{13,79,80} Tau has also been found to coordinate metal ions *in vitro*.^{13,81-83} Circular dichroism (CD), mass spectrometry (MS), and NMR investigations on full length and fragmented tau have determined Cu(II) binding sites, many of which have been located proximal to the microtubule binding domains (MTBDs).^{13,81-83} Compared to A β , tau binds Cu(II) less strongly, with reported K_d values for full length tau (Htau40) in the μ M range (*i.e.*, 0.5 μ M).⁸⁴ Given the low abundance of labile Cu(II) and the relatively low binding affinities of tau for Cu(II) the possibility of coordination *in vivo* is still uncertain. Coordination of metal ions was met with slight structural alterations in the fragmented tau, but very little modifications were observed for full-length tau.^{13,81,82} Trivalent metal ions, Fe(III) and Al(III), have been shown to induce ptau aggregation and upon ascorbate-triggered reduction to the divalent form reverse the self assembly process.^{13,85} Tau's aptitude for mediating the production of ROS in the presence of metal ions is still a focus of further study, but preliminary reports describe that incubation of the R2 repeat domain with Cu(II) could lead to the generation of H₂O₂.⁸⁶

Therapeutic strategies to address the role(s) of tau in AD have been developed, but like A β -related preventative methods, have produced little success. The advancement of kinase inhibitors engineered to alter the phosphorylation state of tau and reduce its dissociation from MTs and growth into PHFs has been inadequate.^{87,88} An incomplete understanding of the enzymes responsible for the hyperphosphorylation of tau, in addition to their essential functions in the posttranslational modifications

of other substrates, makes kinase inhibitor design challenging.⁸⁶ Point mutations in tau causing frontotemporal dementia and parkinsonism linked to chromosome 17 (FTDP-17), an autosomal dominant neurodegenerative disorder, expand the aggregation propensity of tau both *in vivo* and in cell studies.⁸⁷ Small molecules capable of controlling the aggregation pathway of tau, similar to anti-amyloidogenic compounds (*vide supra*), have been tested with the most noteworthy molecule, methylene blue, making it to phase II clinical trials for AD.^{77,87} A new approach to exogenously stabilize MTs in a manner similar to tau and other MAPs has emerged. The rationale has been utilized within the cancer field for the generation of antiproliferative chemotherapeutics and has just recently been applied to AD.^{89,90}

The formation of MT stabilizing agents began with the use of paclitaxel, a natural product isolated from the bark of the Western yew (*Taxus brevifolia*).^{89,91} Michaelis *et al.* first made apparent the utility of MT stabilizers for AD when they showed that treatment with paclitaxel protected neurons against A β ₄₂-induced toxicity (Scheme 1.5).⁹² The neuroprotective effect of paclitaxel and other MT stabilizers, however, appears to be concentration-dependent.⁸⁹ Lower doses of MT stabilizers have been shown to be neuroprotective in transgenic tau models, whereas higher amounts might produce unwanted side effects, including neutropenia and peripheral neuropathy.⁸⁹ This could be a result of the careful equilibrium between the growth and degeneration stages of MTs. Overstabilization of MTs leads to mitotic dysfunction and cell death, which is desirable for tumor suppression, while unstable MTs can lead to impaired axonal transport issues that can eventually contribute to neuronal toxicity and death (*vide supra*).



Scheme 1.5. The chemical structures of the naturally occurring, MT stabilizers, paclitaxel and epothilone D.

Since the effectiveness of MT stabilizers was demonstrated with paclitaxel, more MT stabilizing compounds have been discovered, most of which have been natural products; however, a few synthetic derivatives have been recognized.^{89,91} The biggest challenge associated with paclitaxel and many other natural MT stabilizers is their inability to permeate the BBB and, therefore, their applications are limited for AD.^{89,91} Recently, Ballatore and coworkers have shown that some compound classes, such as epothilones (in particular, epothilone D), were able to pass the BBB and, when injected into mice,

normalize MT density and restore fast axonal transport (Scheme 1.5).^{89,91} Epothilone D is currently in clinical AD trials.⁸⁹ Paclitaxel is believed to stabilize MTs by binding to the lumen of the β -tubulin subunit of the MT in a location referred to as the taxane binding site.^{89,93} This is the same location targeted by tau's microtubule binding domains.⁸⁹ In fact, paclitaxel is able to displace tau from the MTs.⁸⁹ Once bound to the inside of the MT, paclitaxel is presumed to incite a conformational change within the M-loop of the β -tubulin subunit which causes the stabilization of adjacent protofilaments.^{89,93} In this sense, paclitaxel and other taxane binding compounds can be thought of as a figurative adhesive that connects and stabilizes neighboring tubulin subunits. Overall, the MT stabilizing molecules have mostly been restricted toward the analysis and testing of natural products; however, very little progress has been made for the fabrication of synthetic analogs. Furthermore, structure-reactivity studies have been limited to determine the key chemical characteristics of such compounds. Detailed structure-based examination similar to those performed for transthyretin stabilizing compounds could direct the evolution of more potentially BBB-permeable scaffolds that could direct new discovery of AD therapeutics.⁹⁴

1.7. Conclusions

It has been almost one hundred and ten years from Alois Alzheimer's observation of the first plaques and tangles in the brain of Auguste Deter. Our knowledge of AD has grown substantially since 1906. For example, the major protein constituents of the senile plaques and neurofibrillary tangles, A β and tau, respectively, have been discerned, and their processing and aggregation pathways have been investigated. The contribution of additional pathological factors, such as metal ions, to affect the self-assembly of A β , generate or stabilize toxic conformations, and produce ROS has been evaluated. These findings only begin to exemplify some of the numerous pivotal findings that have been paramount in not only furthering our understanding of the complex etiology of AD, but also for the development of therapeutics that are able to offer some minimal, temporary degree of relief. The demand for new treatment options, however, is unrelenting and has catapulted research into methods to correct for the misfolding of proteins, oxidative stress environments, metal ion dyshomeostasis, and altered neurotransmitter levels in AD. While none of these strategies have currently been proven effective, the advancement of new methods, such as multifunctional approaches, and the continued efforts to further elucidate the causative mechanisms of AD will be instrumental in providing insight into designing the next generation of therapeutics.

1.8. References

- (1) Alzheimer's Association, *Alzheimers Dement.* **2014**, *10*, 1–67.

- (2) Beck, M. W.; Pithadia, A. S.; DeToma, A. S.; Korshavn, K. J.; Lim, M. H. *Ligand Design in Medicinal Inorganic Chemistry*; Wiley: New York, 2014; Chapter 10.
- (3) Barnham, K. J.; Bush, A. I. *Chem. Soc. Rev.* **2014**, *43*, 6727–6749.
- (4) Que, E. L.; Domaille, D. W.; Chang, C. J. *Chem. Rev.* **2008**, *108*, 1517–1549.
- (5) Kepp, K. P. *Chem. Rev.* **2012**, *112*, 5193–5239.
- (6) Jakob-Roetne, R.; Jacobsen, H. *Angew. Chem. Int. Ed.* **2009**, *48*, 3030–3059.
- (7) Sashidhara, K. V.; Modukuri, R. K.; Jadiya, P.; Rao, K. B.; Sharma, T.; Haque, R.; Singh, D. K.; Banerjee, D.; Siddiqi, M. I.; Nazir, A. *ACS Med Chem Lett* **2014**, *5*, 1099–1103.
- (8) Devos, D.; Moreau, C.; Devedjian, J. C.; Kluza, J.; Petrault, M.; Laloux, C.; Jonneaux, A.; Ryckewaert, G.; Garçon, G.; Rouaix, N. Duhamel, A.; Jissendi, P.; Dujardin, K.; Auger, F.; Ravasi, L.; Hopes, L.; Grolez, G.; Firdaus, W.; Sablonnière, B.; Strubi-Vuillaume, I.; Zahr, N.; Destée, A.; Còrvol, J.-C.; Pörtl, D.; Leist, M.; Rose, C.; Defebvre, L.; Marchetti, P.; Cabantchik, Z. I.; Bordet, R. *Antioxid. Redox Signaling* **2014**, *21*, 195–210.
- (9) Bush, A. I.; Tanzi, R. E. *Neurotherapeutics* **2008**, *5*, 421–432.
- (10) Nguyen, T.; Hamby, A.; Massa, S. M.; Palmiter, R. D. *Proc. Natl. Sci. Acad. U.S.A.* **2005**, *102*, 11840–11845.
- (11) Kaur, D.; Yantiri, F.; Rajagopalan, S.; Kumar, J.; Mo, J. Q.; Boonplueang, R.; Viswanath, V.; Jacobs, R.; Yang, L.; Beal, M. F.; DiMonte, D.; Volitaskis, I.; Ellerby, L.; Cherny, R. A.; Bush, A. I.; Andersen J. K. *Neuron* **2003**, *37*, 899–909.
- (12) Rauk, A. *Chem. Soc. Rev.* **2009**, *38*, 2698–2715.
- (13) Savelieff, M. G.; Lee, S.; Liu, Y.; Lim, M. H. *ACS Chem. Biol.* **2013**, *8*, 856–865.
- (14) Rauk, A. *Dalton Trans.* **2008**, 1273–1282.
- (15) DeToma, A. S.; Salamekh, S.; Ramamoorthy, A.; Lim, M. H. *Chem. Soc. Rev.* **2012**, *41*, 608–621.
- (16) Faller, P.; Hureau, C.; Berthoumieu, O. *Inorg. Chem.* **2013**, *52*, 12193–12206.
- (17) Pithadia, A. S.; Lim, M. H. *Curr. Opin. Chem. Biol.* **2012**, *16*, 67–73.
- (18) Köpke, E.; Tung, Y.-C.; Shaikh, S.; Alonso, A. D. C.; Iqbal, K.; Grundke-Iqbal, I. *J. Biol. Chem.* **1993**, *268*, 24374–24384.
- (19) Yamamoto, A.; Shin, R.-W.; Hasegawa, K.; Naiki, H.; Sato, H.; Yoshimasu, F.; Kitamoto, T. *J. Neurochem.* **2002**, *82*, 1137–1147.
- (20) Scott, L. E.; Orvig, C. *Chem. Rev.* **2009**, *109*, 4885–4910.
- (21) Bolognin, S.; Messori, L.; Zatta, P. *Neuromolecular Med.* **2009**, *11*, 223–238.
- (22) Lovell, M. A.; Robertson, J. D.; Teesdale, W. J.; Campbell, J. L.; Markesbery, W. R. *J. Neurol. Sci.* **1998**, *158*, 47–52.

- (23) Viles, J. H. *Coord. Chem. Rev.* **2012**, *256*, 2271–2284.
- (24) Solomonov, I.; Korkotian, E.; Born, B.; Feldman, Y.; Bitler, A.; Rahimi, F.; Li, H.; Bitan, G.; Sagi, I. *J. Biol. Chem.* **2012**, *287*, 20555–20564.
- (25) Savelieff, M. G.; DeToma, A. S.; Derrick, J. S.; Lim, M. H. *Acc. Chem. Res.* **2014**, *47*, 2475–2482.
- (26) Hamaguchi, T.; Ono, K.; Yamada, M. *Cell. Mol. Life Sci.* **2006**, *63*, 1538–1552.
- (27) Cheng, B.; Gong, H.; Xiao, H.; Petersen, R. B.; Zheng, L.; Huang, K. *Biochim. Biophys. Acta* **2013**, *1830*, 4860–4871.
- (28) Valensin, D.; Gabbiani, C.; Messori, L. *Coord. Chem. Rev.* **2012**, *256*, 2357–2366.
- (29) Panza, F.; Solfrizzi, V.; Frisardi, V.; Capurso, C.; D'Introno, A.; Colacicco, A. M.; Vendemiale, G.; Capurso, A.; Imbimbo, B. P. *Drugs Aging* **2009**, *26*, 537–555.
- (30) Wang, Q.; Yu, X.; Li, L.; Zheng, J. *Curr. Pharm. Des.* **2014**, *20*, 1223–1243.
- (31) Walke, G. R.; Rapole, S.; Kulkarni, P. P. *Inorg. Chem.* **2014**, *53*, 10003–10005.
- (32) Hureau, C.; Faller, P. *Dalton Trans.* **2014**, *43*, 4233–4237.
- (33) Kenche, V. B.; Hung, L. W.; Perez, K.; Volitakes, I.; Ciccotosto, G.; Kwok, J.; Critch, N.; Sherratt, N.; Cortes, M.; Lal, V.; Masters, C. L.; Murakami, K.; Cappai, R.; Adlard, P. A.; Barnham, K. J. *Angew. Chem. Int. Ed.* **2013**, *52*, 3374–3378.
- (34) Collin, F.; Sasaki, I.; Eury, H.; Faller, P.; Hureau, C. *Chem. Commun.* **2013**, *49*, 2130–2132.
- (35) Xue, W.-F.; Homans, S. W.; Radford, S. E. *Proc. Natl. Acad. Sci. U. S. A.* **2008**, *105*, 8926–8931.
- (36) Strooper, B. D.; Annaert, W.; Cupers, P.; Saftig, P.; Craessaerts, K.; Mumm, J. S.; Schroeter, E. H.; Schrijvers, V.; Wolfe, M. S.; Ray, W. J.; Goate, A.; Kopan, R. *Nature* **1999**, *398*, 518–522.
- (37) Fülöp, L.; Mándity, I. M.; Juhász, G.; Szegedi, V.; Hetényi, A.; Wéber, E.; Bozsó, Z.; Simon, D.; Benkő, M.; Király, Z.; Martinek, T. A. *PLoS One* **2012**, *7*, e39485.
- (38) Imamura, Y.; Umezawa, N.; Osawa, S.; Shimada, N.; Higo, T.; Yokoshima, S.; Fukuyama, T.; Iwatsubo, T.; Kato, N.; Tomita, T.; Higuchi, T. *J. Med. Chem.* **2013**, *56*, 1443–1454.
- (39) Kimura, T.; Shuto, D.; Kasai, S.; Liu, P.; Hidaka, K.; Hamada, T.; Hayashi, Y.; Hattori, C.; Asai, M.; Kitazume, S.; Saido, T. C.; Ishiura, S.; Kiso, Y. *Bioorg. Med. Chem. Lett.* **2004**, *14*, 1527–1531.
- (40) Kimura, T.; Shuto, D.; Hamada, Y.; Igawa, N.; Kasai, S.; Liu, P.; Hidaka, K.; Hamada, T.; Hayashi, Y.; Kiso, Y. *Bioorg. Med. Chem. Lett.* **2005**, *15*, 211–215.
- (41) Lee, H. J.; Korshavn, K. J.; Kochi, A.; Derrick, J. S.; Lim, M. H. *Chem. Soc. Rev.* **2014**, *43*, 6672–6682.

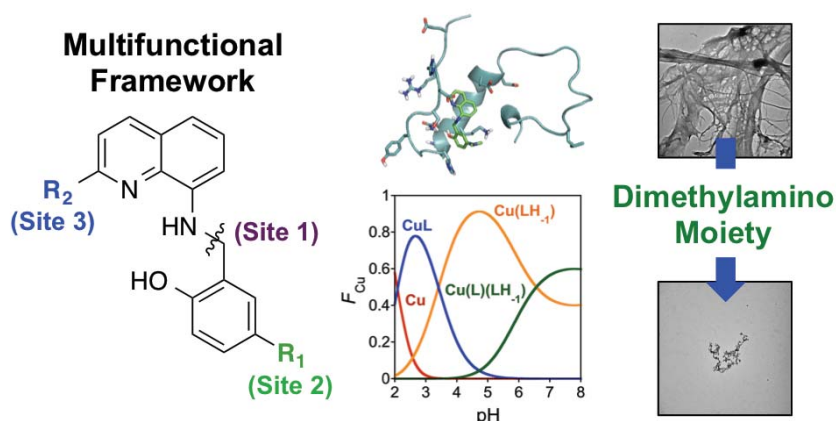
- (42) Barnham, K. J.; Kenche, V. B.; Ciccotosto, G. D.; Smith, D. P.; Tew, D. J.; Liu, X.; Perez, K.; Cranston, G. A.; Johanssen, T. J.; Volitakis, I.; Bush, A. I.; Masters, C. L.; White, A. R.; Smith, J. P.; Cherny, R. A.; Cappai, R. *Proc. Natl. Acad. Sci. U.S.A.* **2008**, *105*, 6813–6818.
- (43) Yankner, B. A. *Neuron* **1996**, *16*, 921–932.
- (44) Lorenzo, A.; Yankner, B. A. *Proc. Natl. Acad. Sci. U.S.A.* **1994**, *91*, 12243–12247.
- (45) Bolognin, S.; Drago, D.; Messori, L.; Zatta, P.; *Med. Res. Rev.* **2009**, *29*, 547–570.
- (46) Gaeta, A.; Hider, R. C. *Br. J. Pharmacol.* **2005**, *146*, 1041–1059.
- (47) Zheng, H.; Youdim, M. B.; Fridkin, M. *J. Med. Chem.* **2009**, *52*, 4095–4098.
- (48) Liu, G.; Men, P.; Harris, P. L. R.; Rolston, R. K.; Perry, G.; Smith, M. A. *Neurosci. Lett.* **2006**, *406*, 189–193.
- (49) Liu, G.; Men, P.; Kudo, W.; Perry, G.; Smith, M. A. *Neurosci. Lett.* **2009**, *455*, 187–190.
- (50) Gabathuler, R. *Neurobiol. Dis.* **2010**, *37*, 48–57.
- (51) Clark, D. E.; Pickett, S. D. *Drug Discovery Today* **2000**, *5*, 49–58.
- (52) Perez, L. R.; Franz, K. J. *Dalton Trans.* **2010**, *39*, 2177–2187.
- (53) Lipinski, C. A.; Lombardo, F.; Dominy, B. W.; Feeney, P. J. *Adv. Drug Delivery Rev.* **2001**, *46*, 3–26.
- (54) Lee, S.; Zheng, X.; Krishnamoorthy, J.; Savelieff, M. G.; Park, H. M.; Brender, J. R.; Kim, J. H.; Derrick, J. S.; Kochi, A.; Lee, H. J.; Kim, C.; Ramamoorthy, A.; Bowers, M. T.; Lim, M. H. *J. Am. Chem. Soc.* **2014**, *136*, 299–310.
- (55) Wu, W.-H.; Lei, P.; Liu, Q.; Hu, J.; Gunn, A. P.; Chen, M.-S.; Rui, Y.-F.; Su, X.-Y.; Xie, Z.-P.; Zhao, Y.-F.; Bush, A. I.; Li, Y.-M. *J. Biol. Chem.* **2008**, *283*, 31657–31664.
- (56) Dickens, M. G.; Franz, K. J. *ChemBioChem* **2010**, *11*, 59–62.
- (57) Ritchie, C. W.; Bush, A. I.; Mackinnon, A.; Macfarlane, S.; Mastwyk, M.; MacGregor, L.; Kiers, L.; Cherny, R.; Li, Q.-X.; Tammer, A.; Carrington, D.; Mavros, C.; Volitakis, I.; Xilinas, M.; Ames, D.; Davis, S.; Beyreuther, K.; Tanzi, R. E.; Masters, C. L. *Arch. Neurol.* **2003**, *60*, 1685–1691.
- (58) Caragounis, A.; Du, T.; Filiz, G.; Laughton, K. M.; Volitakis, I.; Sharples, R. A.; Cherny, R. A.; Masters, C. L.; Drew, S. C.; Hill, A. F.; Li, Q.-X.; Crouch, P. J.; Barnham, K. J.; White, A. R. *Biochem. J.* **2007**, *407*, 435–450.
- (59) Cherny, R. A.; Atwood, C. S.; Xilinas, M. E.; Gray, D. N.; Jones, W. D.; McLean, C. A.; Barnham, K. J.; Volitakis, I.; Fraser, F. W.; Kim, Y.-S.; Huang, X.; Goldstein, L. E.; Moir, R. D.; Lim, J. T.; Beyreuther, K.; Zheng, H.; Tanzi, R. E.; Masters, C. L.; Bush, A. I. *Neuron* **2001**, *30*, 665–676.

- (60) Filiz, G.; Caragounis, A.; Bica, L.; Du, T.; Masters, C. L.; Crouch, P. J.; White, A. R. *Int. J. Biochem. Cell. Biol.* **2008**, *40*, 1030–1042.
- (61) Mancino, A. M.; Hindo, S. S.; Kochi, A.; Lim, M. H. *Inorg. Chem.* **2009**, *48*, 9596–9598.
- (62) Bareggi, S. R.; Cornelli, U. *CNS Neurosci. Ther.* **2012**, *18*, 41–46.
- (63) Relkin, N. R. *Lancet Neurol.* **2008**, *7*, 762–763.
- (64) Adlard, P. A.; Cherny, R. A.; Finkelstein, D. I.; Gautier, E.; Robb, E.; Cortes, M.; Volitakis, I.; Liu, X.; Smith, J. P.; Perez, K.; Laughton, K.; Li, Q.-X.; Charman, S. A.; Nicolazzo, J. A.; Wilkins, S.; Deleva, K.; Lynch, T.; Kok, G.; Ritchie, C. W.; Tanzi, R. E.; Cappai, R.; Masters, C. L.; Barnham, K. J.; Bush, A. I. *Neuron* **2008**, *59*, 43–55.
- (65) Youdim, M. B. H. *Exp. Neurobiol.* **2010**, *19*, 1–14.
- (66) Rodríguez-Rodríguez, C.; Telpoukhovskaia, M.; Orvig, C. *Coord. Chem. Rev.* **2012**, *256*, 2308–2332.
- (67) Munoz-Torrero, D. *Curr. Med. Chem.* **2008**, *15*, 2433–2455.
- (68) Choi, J.-S.; Braymer, J. J.; Nanga, R. P. R.; Ramamoorthy, A.; Lim, M. H. *Proc. Natl Acad. Sci. U.S.A.* **2010**, *107*, 21990–21995.
- (69) Geldenhuys, W. J.; Ko, K. S.; Stinnett, H.; Van der Schyf, C. J.; Lim, M. H. *Med. Chem. Commun.* **2011**, *2*, 1099–1103.
- (70) Beck, M. W.; Oh, S. B.; Kerr, R. A.; Lee, H. J.; Kim, S. H.; Kim, S.; Jang, M.; Ruotolo, B. T.; Lee, J.-Y.; Lim, M. H. *Chemi. Sci.* **2015**, *6*, 1879–1886.
- (71) Huang, L.; Lu, C.; Sun, Y.; Mao, F.; Luo, Z.; Su, T.; Jiang, H.; Shan, W.; Li, X. *J. Med. Chem.* **2012**, *55*, 8483–8492.
- (72) Zheng, H.; Gal, S.; Weiner, L. M.; Bar-Am, O.; Warshawsky, A.; Fridkin, M.; Youdim, M. B. H. *J. Neurochem.* **2005**, *95*, 68–78.
- (73) Kupersmidt, L.; Amit, T.; Bar-Am, O.; Youdim, M. B. H.; Weinreb, O. *Antioxid. Redox Signaling* **2012**, *17*, 860–877.
- (74) Scott, L. E.; Telpoukhovskaia, M.; Rodríguez-Rodríguez, C.; Merkel, M.; Bowen, M. L.; Page, B. D. G.; Green, D. E.; Storr, T.; Thomas, F.; Allen, D. D.; Lockman, P. R.; Patrick, B. O.; Adam, M. J.; Orvig, C. *Chem. Sci.* **2011**, *2*, 642–648.
- (75) Schugar, H.; Green, D. E.; Bowen, M. L.; Scott, L. E.; Storr, T.; Böhmerle, K.; Thomas, F.; Allen, D. D.; Lockman, P. R.; Merkel, M.; Thompson, K. H.; Orvig, C. *Angew. Chem. Int. Ed.* **2007**, *46*, 1716–1718.
- (76) Hernandez, F.; Lucas, J. J.; Avila, J. J. *Alzheimers Dis.* **2013**, *33*, S141–S144.
- (77) Medeiros, R.; Baglietto-Vargas, D.; LaFerla, F. M. *CNS Neurosci. Ther.* **2011**, *17*, 514–524.

- (78) Takashima, A. *J. Alzheimers Dis.* **2009**, *17*, 729–736.
- (79) Huang, H.-C.; Jiang, Z.-F. *J. Alzheimers Dis* **2009**, *16*, 15–27.
- (80) Guo, J.-P.; Arai, T.; Miklossy, J.; McGeer, P. L. *Proc. Natl. Acad. Sci. U.S.A.* **2006**, *103*, 1953–1958.
- (81) Soragni, A.; Zambelli, B.; Mukrasch, M. D.; Biernat, J.; Jeganathan, S.; Griesinger, C.; Ciurli, S.; Mandelkow, E.; Zweckstetter, M. *Biochemistry* **2008**, *47*, 10841–10851.
- (82) Ma, Q.-F.; Li, Y.-M.; Du, J.-T.; Kanazawa, K.; Nemoto, T.; Nakanishi, H.; Zhao, Y.-F. *Biopolymers* **2005**, *79*, 74–85.
- (83) Ma, Q.; Li, Y.; Du, J.; Liu, H.; Kanazawa, K.; Nemoto, T.; Nakanishi, H.; Zhao, Y. *Peptides* **2006**, *27*, 841–849.
- (84) Zhou, L.-X.; Du, J.-T.; Zeng, Z.-Y.; Wu, W.-H.; Zhao, Y.-F.; Kanazawa, K.; Ishizuka, Y.; Nemoto, T.; Nakanishi, H.; Li, Y.-M. *Peptides* **2007**, *28*, 2229–2234.
- (85) Yamamoto, A.; Shin, R.-W.; Hasegawa, K.; Naiki, H.; Sato, H.; Yoshimasu, F.; Kitamoto, T. *J. Neurochem.* **2002**, *82*, 1137–1147.
- (86) Su, X.-Y.; Wu, W.-H.; Huang, Z.-P.; Hu, J.; Lei, P.; Yu, C.-H.; Zhao, Y.-F.; Li, Y.-M. *Biochem. Biophys. Res. Commun.* **2007**, *358*, 661–665.
- (87) Golde, T. E.; Petrucelli, L.; Lewis, J. *Exp. Neurol.* **2010**, *223*, 252–266.
- (88) Medina, M.; Avila, J. *Biochem. Pharmacol.* **2014**, *88*, 540–547.
- (89) Ballatore, C.; Brunden, K. R.; Hurn, D. M.; Trojanowski, J. Q.; Lee, V. M.-Y.; Smith, III, A. B. *J. Med. Chem.* **2012**, *55*, 8979–8996.
- (90) Li, P.-K.; Pandit, B.; Sackett, D. L.; Hu, Z.; Zink, J.; Zhi, J.; Freeman, D.; Robey, R. W.; Werbovetz, K.; Lewis, A.; Li, C. *Mol. Cancer Ther.* **2006**, *5*, 450–456.
- (91) Brunden, K. R.; Trojanowski, J. Q.; Smith, A. B. 3rd, Lee, V. M.-Y.; Ballatore, C. *Bioorg. Med. Chem.* **2014**, *22*, 5040–5049.
- (92) Michaelis, M. L.; Ansar, S.; Chen, Y.; Reiff, E. R.; Seyb, K. I.; Himes, R. H.; Audus, K. L.; Georg, G. I. *J. Pharmacol. Exp. Ther.* **2005**, *312*, 659–668.
- (93) Amos, L. A.; Löwe, J. *Chem. Biol.* **1999**, *6*, R65–R69.
- (94) Connelly, S.; Choi, S.; Johnson, S. M.; Kelly, J. W.; Wilson, I. A. *Curr. Opin. Struct. Biol.* **2010**, *20*, 54–62.

Chapter 2.

Importance of the Dimethylamino Functionality on a Multifunctional Framework for Regulating Metals, Amyloid- β , and Oxidative Stress in Alzheimer's Disease



The results presented in this chapter were previously published (Derrick, J. S.; Kerr, R. A.; Korshavn, K. J.; McLane, M. J.; Kang, J.; Nam, E.; Ramamoorthy, A.; Ruotolo, B. T.; Lim, M. H. *Inorg. Chem.*, **2016**, 55, 5000–5013). I thank Professor Brandon T. Ruotolo and Dr. Richard A. Kerr for the nESI-IM-MS studies as well as Professor Ayyalusamy Ramamoorthy and Kyle J. Korshavn for the HMQC NMR data. Juhye Kang and Eunju Nam conducted cell culture experiments and Michael J. McLane assisted with some of the synthesis and the docking and metal binding experiments. I synthesized and characterized all the compounds, performed the biological assays, gel/Western blot, TEM, and metal binding experiments. I also handled the manuscript writing with the assistance of Professor Lim.

2.1. Introduction

The discovery of effective therapeutic strategies to combat Alzheimer's disease (AD), the most common form of dementia, have yet to be identified, which is most likely a result of the disease's complex and multifaceted pathology.¹⁻¹⁰ For example, some pathological features being actively investigated include: misfolded and aggregated proteins (*i.e.*, amyloid- β (A β) and tau), metal ion dyshomeostasis and miscompartmentalization, oxidative stress, excitotoxicity, neuroinflammation, and mitochondrial damage.^{1-6,11,12} Furthermore, the interconnections between many of these pathological factors, such as A β , metal ions, and reactive oxygen species (ROS), make the elucidation of a comprehensive molecular-level understanding of AD etiology extremely challenging.^{1-4,6-9,13,14} One approach to address the inherently complex multifaceted nature of AD is to utilize multifunctional compounds able to preferentially modulate the activities of multiple targets simultaneously. This strategy has been increasing in prevalence within the literature with common targets, including A β , tau, various neuroreceptors (*e.g.*, cholinergic, glutamatergic, and dopaminergic receptors), and enzymes (*e.g.*, acetylcholinesterase, monoamine oxidase).^{1,15-22} Unfortunately, a majority of the current multifunctional molecules are developed by slightly modifying existing drugs or known molecular scaffolds (*e.g.*, tacrine, coumarin, curcumin).^{1,15-22} Such a tactic is often costly and time consuming since it frequently involves the high-throughput screening of many structural derivatives, most of which fail to be selected for further analysis.

Rather than modifying familiar frameworks, we have recently reported that novel multifunctional AD agents can be generated through the use of an incorporation approach to rational ligand design.^{23,24} Initial studies with a multifunctional ligand (**ML**) identified the feasibility of designing a single molecular entity that can control metal-free and metal-induced A β aggregation, toxicity engendered by metal-free A β and metal-A β , and metal-mediated ROS generation, as well as scavenge free radicals, overall validating **ML**'s structure-based design strategy.^{12,23,24} Further progress toward the production of more diverse and improved multifunctional reagents is dependent on the recognition of critical pharmacophores that can be employed as figurative 'building blocks' to engineer next-generation ligands through such a rational design approach. Structure-reactivity studies, using individual components within a complex molecule and structurally modified molecules, can provide the information to determine the chemical functionalities that may impart the desired reactivities.

Toward this goal, we have prepared a series of aminoquinoline (**AQ**) derivatives (*i.e.*, **AQ1-4**, **AQP1-4**, **AQDA1-3**; Figure 2.1) based on the framework of **ML** in order to discern a structure-reactivity understanding of **ML**'s multifunctionality. Our *in vitro* investigations have proposed the dimethylamino functionality of **ML** to be critical toward its ability to modulate the aggregation pathways of metal-free

A β and metal–A β . Two-dimensional (2D) NMR studies have shown that functionalization of the aminoquinoline moiety is capable of shifting the preferred region of interaction along the sequence of A β . In addition, the slight modifications to **ML**'s metal binding site are also indicated to direct the derivatives' ability to bind Cu(II) and Zn(II), control reactive oxygen species (ROS) formation, and alter Cu(II)–/Zn(II)–A β aggregation. The overall structural variation of **ML** also tuned its capability to scavenge free radicals. Mass spectrometric studies further illustrate the importance of the metal binding affinity of this series of small molecules in regulating metal–A β aggregation and potentially suggest larger, higher-order oligomers as the interacting species. Similar to **ML**, our structural derivatives are also observed to be potentially suitable in biological systems since they are moderately water soluble and potentially possess the ability to penetrate the blood-brain barrier (BBB). Overall, our studies highlight the importance of the dimethylamino moiety for imparting reactivity toward AD-relevant targets (*e.g.*, metals, A β , metal–A β) yet further studies are still warranted to assess its transferability to other molecular scaffolds.

2.2. Results and Discussion

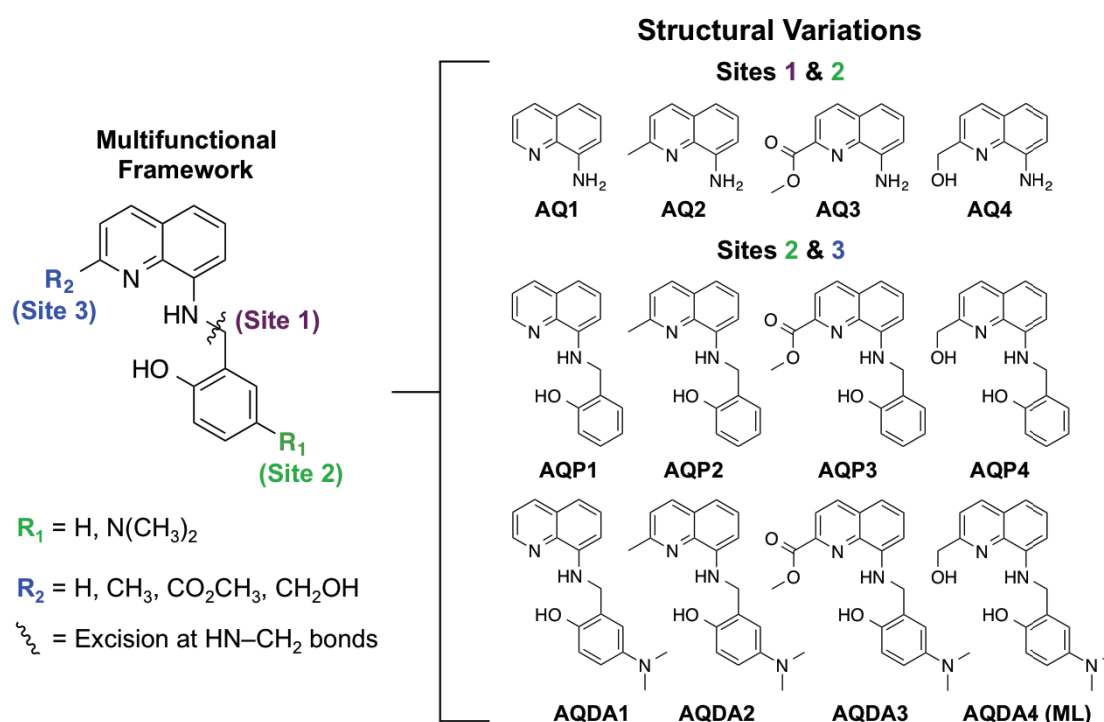


Figure 2.1. Structural variations on a multifunctional ligand (**ML**) framework. Modifications were performed on the multimodal scaffold to identify a structure-reactivity understanding of **ML**'s multifunctionality as well as to tune its metal binding characteristics. The quinoline portion of the

structure was examined by cleavage of the HN–CH₂ bond (site 1, purple) and modulating the functionalities at the R₂ position (site 3, blue). Furthermore, simultaneous structural alterations at the R₁ and R₂ positions (sites 2 and 3, green and blue, respectively) allowed the role of the dimethylamino group and the 4-(dimethylamino)phenol in **ML**'s activities to be illuminated.

2.2.1. Design Rationale and Preparation for Structural Modifications to a Multifunctional Framework

A series of aminoquinoline (**AQ**) derivatives based on our previously reported multifunctional ligand (**ML**) were generated to (i) develop a structure-reactivity understanding of **ML**'s multifaceted reactivity toward metal-free A β , metal–A β , ROS, and free radicals and (ii) reduce its relatively high binding affinity for Cu(II) and Zn(II) (*i.e.*, dissociation constants for Cu(II) and Zn(II) in the picomolar and nanomolar range, respectively) that may potentially interfere with biologically essential metalloproteins.²³ The **AQ** derivatives were obtained by subjecting **ML** to modifications at three sites (Figure 2.1). First, in order to determine the significance of the phenol or 4-(dimethylamino)phenol moieties in **ML**'s activities, **AQ1-4** were prepared by excision of the HN–(CH₃)₂ bond (site 1, Figure 2.1). The role of the dimethylamino moiety in directing **ML**'s multifunctionality was also evaluated by modifying site 2 through installation of a hydrogen atom (**AQP1-4**) or a dimethylamino group (**AQDA1-4**) (Figure 2.1). Further modifications to the metal binding site (site 3) from a hydrogen atom (in **AQ1**, **AQP1**, and **AQDA1**) or a methyl group (in **AQ2**, **AQP2**, and **AQDA2**) to an ester (in **AQ3**, **AQP3**, and **AQDA3**) or an alcohol moiety (in **AQ4**, **AQP4**, and **ML**) allowed us to examine the difference in denticity and electronics of the ligands (Figure 2.1). Similar to **ML**, all **AQ** derivatives were also designed to adhere to Lipinski's rules and calculated logBB values for potential drug-likeness and BBB permeability (Tables 2.1 and 2.2).^{23,25,26}

Table 2.1. Values (MW, clogP, HBA, HBD, PSA, logBB, and –logP_e) of **AQDA1-3** and **ML**.^a

Calculation	AQDA1	AQDA2	AQDA3	ML ^b	Permeability rules
MW	293	307	351	396	≤ 450
clogP	3.15	3.65	2.91	2.57	≤ 5.0
HBA	4	4	6	5	≤ 10
HBD	2	2	2	3	≤ 5
PSA	48.4	48.4	74.7	68.6	≤ 90 Å ²
logBB	–0.107	–0.323	–0.533	–0.496	< –1.0 (poor distribution)
–logP _e	4.30 ± 0.01	4.30 ± 0.01	4.30 ± 0.01	4.50 ± 0.01	–logP _e < 5.4 (CNS+) –logP _e > 5.7 (CNS–)
CNS+/- prediction	CNS+	CNS+	CNS+	CNS+	CNS+; CNS–

Table 2.2. Values (MW, $clogP$, HBA, HBD, PSA, $\log BB$, and $-\log P_e$) of **AQ1-AQ4** and **AQP1-AQP4**.^a

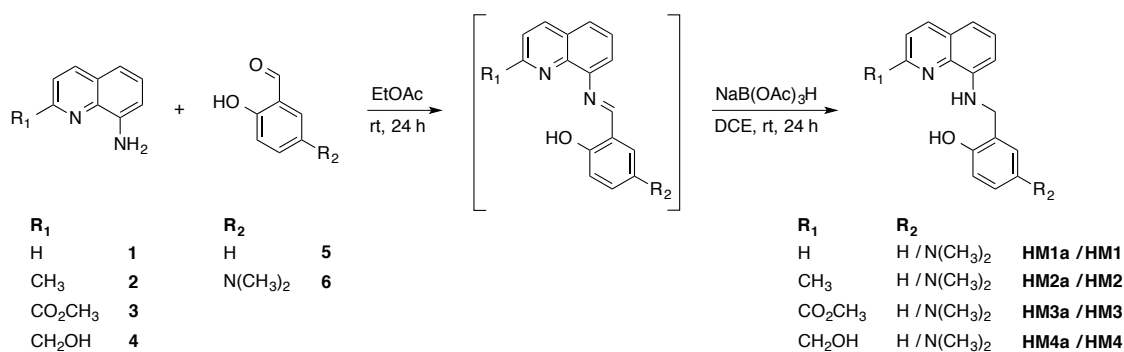
Calculation	AQ1	AQ2	AQ3	AQ4	AQP1	AQP2	AQP3	AQP4	Permeability rules
MW	144	158	186	174	250	264	308	280	≤ 450
$clogP$	1.48	1.98	1.74	0.89	2.99	3.49	2.75	2.40	≤ 5.0
HBA	2	2	3	3	3	3	5	4	≤ 10
HBD	2	2	2	3	2	2	2	3	≤ 5
PSA	38.9	38.9	60.0	59.1	45.1	45.1	71.5	65.4	$\leq 90 \text{ \AA}^2$
$\log BB$	-0.221	-0.136	-0.434	-0.610	-0.084	-0.008	-0.501	-0.473	< -1 (poor distribution)
$-\log P_e$	4.20 ± 0.01	4.20 ± 0.01	4.30 ± 0.01	4.70 ± 0.01	4.40 ± 0.01	4.20 ± 0.01	5.05 ± 0.08	4.50 ± 0.01	$-\log P_e < 5.4$ (CNS+)
									$-\log P_e > 5.7$ (CNS-)
CNS +/- Prediction	CNS +	CNS +	CNS +	CNS +	CNS +	CNS +	CNS +	CNS +	CNS +

^aMW, molecular weight; $clogP$, calculated logarithm of the octanol-water partition coefficient; HBA, hydrogen bond acceptor atoms; HBD, hydrogen bond donor atoms; PSA, polar surface area; $\log BB = -0.0148 \times PSA + 0.152 \times clogP + 0.139$ ($\log BB < -1.0$ poorly distributed in the brain); $-\log P_e$ values, determined using the PAMPA-BBB assay, were calculated by the PAMPA 9 explorer software V. 3.5. Prediction of compound's ability to penetrate the central nervous system (CNS) on the basis of literature values. Compounds categorized as CNS+ possess the potential ability to penetrate the BBB while those categorized as CNS- are expected to have poor BBB permeability. ^bReference 23.

Synthetically, the structural derivatives were obtained *via* synthetic routes analogous to the one previously reported for **ML**.^{23,27-30} Starting from 2-methyl-8-nitroquinoline, the **AQ** derivatives, **AQ3** and **AQ4**, were produced through a multi-step reaction (**AQ1** and **AQ2** were commercially available).³¹ First, the nitro precursor compound, methyl 8-nitroquinoline-2-carboxylate, was prepared by bromination of 2-methyl-8-nitroquinoline followed by hydrolysis in 20% sulfuric acid to afford 8-nitroquinoline-2-carboxylic acid. 8-nitroquinoline-2-carboxylic acid was then methylated with trimethylsilyldiazomethane ($\text{Me}_3\text{SiCHN}_2$), a safer alternative to diazomethane, to produce the precursor (*i.e.*, methyl 8-nitroquinoline-2-carboxylate) to **AQ3** and **AQ4**. Hydrogenation of methyl 8-nitroquinoline-2-carboxylate in the presence of 10% palladium on carbon provided **AQ3** at a modest yield (*ca.* 50%). Further reduction of **AQ3** with sodium borohydride (NaBH_4) generated **AQ4**. The derivatives containing an aminoquinoline and phenol (*i.e.*, **AQP1-4**) or a 4-(dimethylamino)phenol (*i.e.*, **AQDA1-3**) were constructed by a Schiff base condensation reaction of **AQ1-4** with either salicylaldehyde (for **AQP1-3**) or 4-(dimethylamino)-2-

hydroxybenzaldehyde (for **AQDA1-3**) followed by the reduction of the resultant imine with sodium triacetoxyborohydride as shown in Scheme 2.1.

Scheme 2.1. Synthetic routes to **AQ**, **AQP**, and **AQDA** derivatives.



2.2.2. Effect of AQ Derivatives on Metal-Free and Metal-Induced A β Aggregation

In order to determine the effect of structural modifications on the ability of **AQ** derivatives to modulate A β aggregation in both the absence and presence of metal ions [Cu(II) and Zn(II)], gel electrophoresis with Western blotting (gel/Western blot) utilizing an anti-A β antibody (6E10) and transmission electron microscopy (TEM) were performed to analyze the molecular weight (MW) distribution and morphological change of the resultant A β species, respectively. Two experiments were conducted to determine (i) the ability of the derivatives to prevent the formation of fibrillar aggregates (inhibition experiment, Figures 2.2a and 2.3a) and (ii) to dismantle preformed A β aggregates into smaller species (disaggregation experiment, Figures 2.6a and 2.7a). Generally, under the experimental conditions employed herein, compound-free A β samples with and without metal ions assemble into a distribution of large aggregates that are too big to penetrate into the gel matrix, which yields very little smearing in the gel/Western blots, but can be visualized *via* TEM.^{23,31,32} The administration of compounds, capable of interacting with A β , inhibiting the formation of high MW aggregates, and/or disassembling preformed aggregates, typically generates a distribution of smaller-sized A β species that can enter into the gel and produce a substantial amount of streaking compared to the samples containing only A β .^{23,31,32}

In the inhibition experiments, only the derivatives containing the 4-(dimethylamino)phenol moiety (*i.e.*, **AQDA1-3**) were able to modulate the MW distribution of metal-free A β_{40} and Zn(II)-A β_{40} (Figure 2.2b, 3rd column, lanes 1–3). In the case of Cu(II)-A β_{40} , only one compound without the 4-(dimethylamino)phenol, **AQP1**, in addition to **AQDA1-3**, produced detectable smearing in the high MW region of the gel/Western blot (> 100 kDa; Figure 2.2b, 2nd column, lane 1). The reactivity of **AQP1** for

Cu(II)-A β_{40} may be a result of its relatively high binding affinity for Cu(II) compared to that of the other multifunctional derivatives (*vide infra*). The inhibitory reactivity of **AQDA1-AQDA3** toward metal-free and metal-treated A β_{40} also appeared to be time dependent. Longer, darker bands (*ca.* 4-260 kDa) were detected on the gel/Western blot following later incubation periods (*i.e.*, 24 h) of metal-free A β_{40} and metal-A β_{40} with **AQP1** or **AQDA1-AQDA3** (Figure 2.2b).

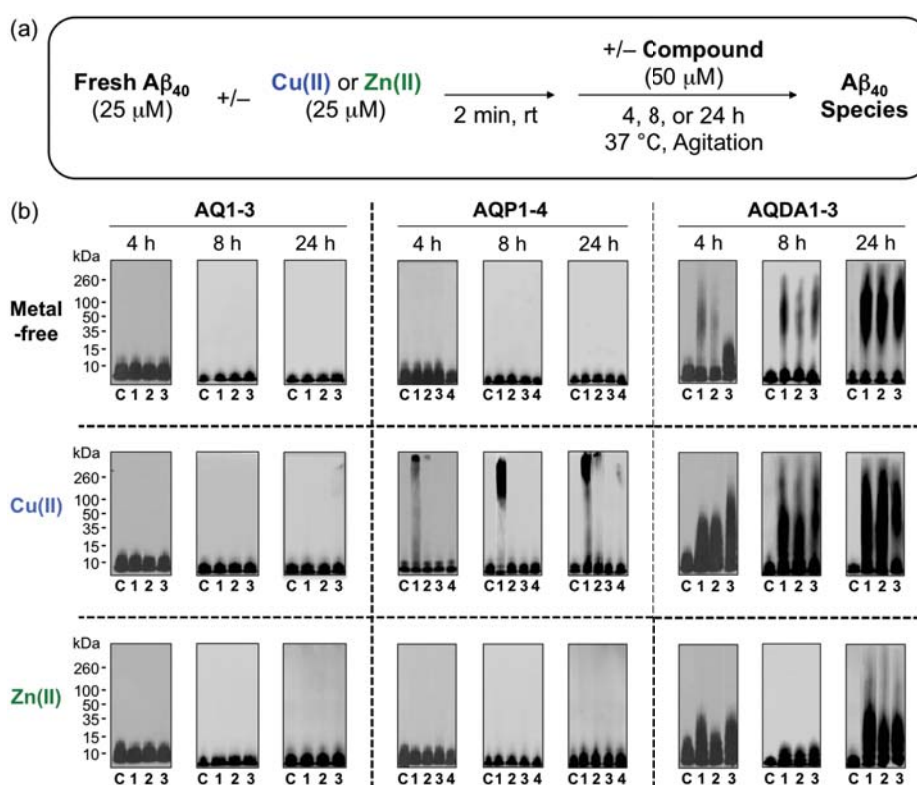


Figure 2.2. Ability of compounds (**AQ1-3**, **AQP1-4**, and **AQDA1-3**) to control the formation of A β_{40} aggregates in the absence and presence of metal ions [Cu(II) and Zn(II)]. (a) Scheme of the inhibition experiments. (b) Visualization of the resultant A β species from the inhibition experiments by gel/Western blot utilizing an anti-A β antibody (6E10). Experimental conditions: [A β_{40}] = 25 μ M; [CuCl₂ or ZnCl₂] = 25 μ M; [compound] = 50 μ M; incubated for 4, 8, and 24 h; pH 7.4 (for metal-free and Zn(II) experiments) or 6.6 (for Cu(II) experiments); 37 °C; constant agitation. The control lane (without compound treatment) is identified by the letter “C”, and the lane number refers to the specific compound within each small molecule group (*i.e.*, **AQ**, **AQP**, **AQDA**).

AQ derivatives also had a similar aptitude for inhibiting the self-assembly of the more aggregation-prone isoform, A β_{42} .^{6,11,12} Only **AQDA1-3** with the 4-(dimethylamino)phenol functionality perturbed the MW distribution of the resultant metal-free and metal-induced A β_{42} aggregates different from that of the control samples (Figure 2.3b, 3rd column, lanes 1-3). Unlike in the A β_{40} conditions, **AQP1** was not

indicated to significantly ameliorate the aggregation of Cu(II)-A β_{42} , which might be a result of the faster aggregation thus limiting the interaction with Cu(II) surrounded by A β_{42} (Figure 2.3b, 2nd column, lane 1). TEM images of metal-free and metal-bound A β_{40} and A β_{42} samples treated with **AQDA1-3** revealed a shift from the large A β aggregates and fibrils found in the compound-untreated samples of metal-free and metal-bound A β toward morphologies that are much smaller and more amorphous (Figure 2.4 for A β_{42} ; Figure 2.5 for A β_{40}). Consistent with the gel/Western blot findings, the aminoquinoline derivative, **AQ1**, and aminoquinolinephenol derivative, **AQP1**, were not observed to significantly alter the size or morphology of metal-free A β or Zn(II)-A β (Figures 4 and S3). Some smaller and more unstructured aggregates, however, were identified in the Cu(II)-A β_{40} inhibition samples incubated with **AQP1** (Figure 2.5, middle column, inset).

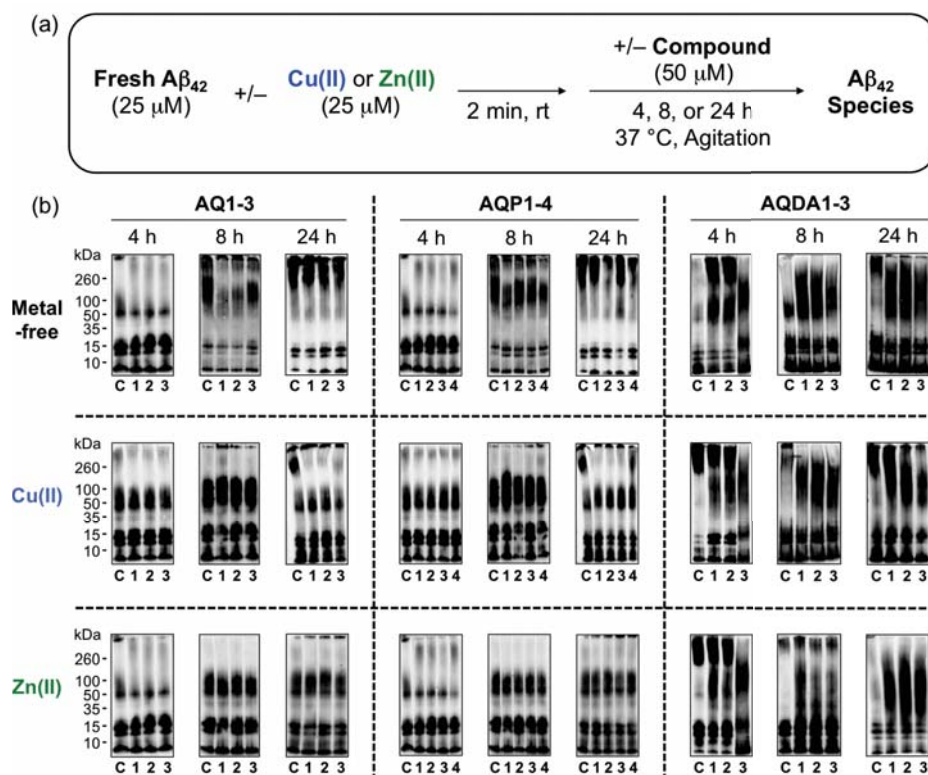


Figure 2.3. Capability of compounds (**AQ1-3**, **AQP1-4**, and **AQDA1-3**) to inhibit the formation of A β_{42} aggregates in the absence and presence of metal ions [Cu(II) and Zn(II)]. (a) Scheme of the inhibition experiments. (b) Visualization of the resultant A β species from the inhibition experiments by gel/Western blot utilizing an anti-A β antibody (6E10). Experimental conditions: [A β_{42}] = 25 μ M; [CuCl₂ or ZnCl₂] = 25 μ M; [compound] = 50 μ M; incubation for 4, 8, and 24 h; pH 7.4 (for metal-free and Zn(II) experiments) or 6.6 (for Cu(II) experiments); 37 °C; constant agitation. The control lane (without compound treatment) is identified by the letter “C”, and the lane number refers to the specific compound within each small molecule group (*i.e.*, **AQ**, **AQP**, **AQDA**).

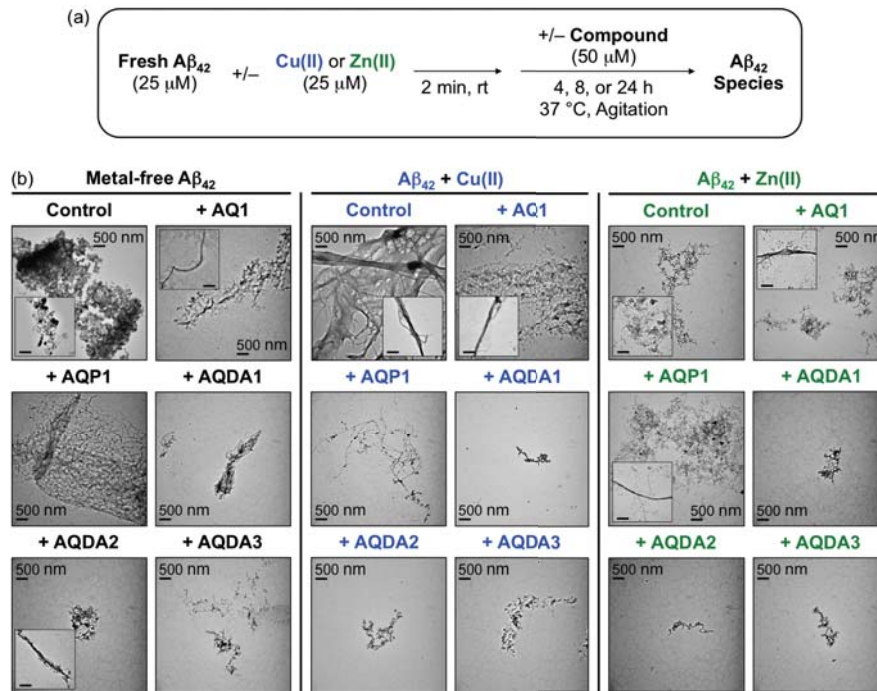


Figure 2.4. Morphologies of the resultant metal-free A β_{42} and metal–A β_{42} aggregates upon treatment with AQ1, AQP1, and AQDA1-3. (a) Scheme of the inhibition experiments. (b) TEM images for the A β_{42} samples (24 h incubation). Insets represent the minor species.

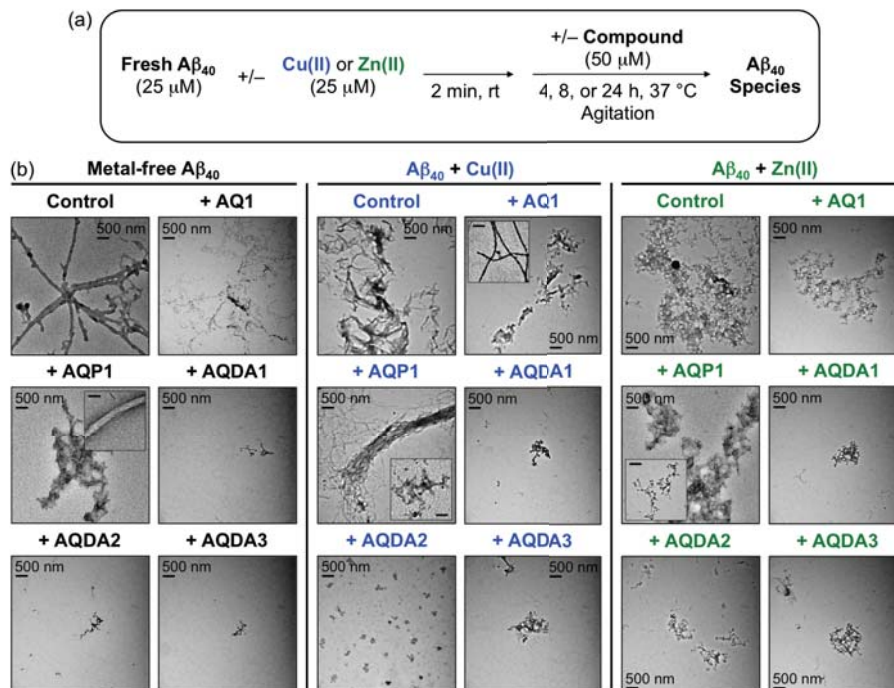


Figure 2.5. Morphologies of the resultant metal-free and metal–associated A β aggregates. (a) Scheme of the inhibition experiments upon treatment with AQ1, AQP1, and AQDA1-3. (b) TEM images for the A β_{40} samples (24 h incubation). Insets represent the minor species.

We also evaluated the capacity of the multifunctional derivatives to interact with and degrade preformed $A\beta_{40}$ and $A\beta_{42}$ aggregates (*i.e.*, disaggregation experiments; Figures 2.6a and 2.7a). The disaggregation experiments showed similar trends as those observed in the inhibition studies. Only compounds with the 4-(dimethylamino)phenol moiety (**AQDA1-3**) were able to disassemble preformed metal-free $A\beta_{40}/A\beta_{42}$ and metal- $A\beta_{40}/A\beta_{42}$ aggregates (Figures 2.6b, and 2.7b, 3rd column, lanes 1–3). Consistent with the observations from the Cu(II)- $A\beta_{40}$ inhibition experiment, **AQP1** also presented an ability to generate a distribution of smaller MW species only under $A\beta_{40}$ conditions; however, the bands appeared at a higher MW region (*i.e.*, 100–260 kDa), relative to the compounds containing the 4-(dimethylamino)phenol moiety which produced a more disperse MW range of aggregates (*i.e.*, *ca.* 4–260 kDa). Overall, our *in vitro* gel/Western blot and TEM studies suggest the 4-(dimethylamino)phenol functionality as a critical moiety for the anti-amyloidogenic properties of **ML**.

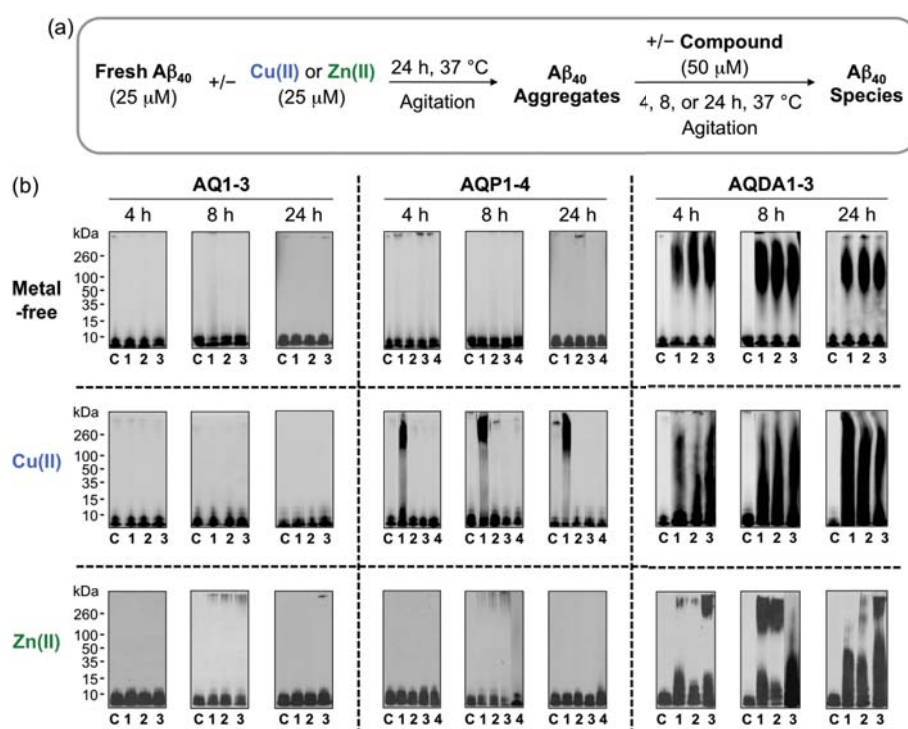


Figure 2.6. Ability of compounds (**AQ1-3**, **AQP1-4**, and **AQDA1-3**) to reverse preformed $A\beta_{40}$ aggregates in the absence and presence of metal ions [Cu(II) and Zn(II)]. (a) Scheme of the disaggregation experiments. (b) Visualization of the resultant $A\beta$ species from the disaggregation experiments by gel/Western blot utilizing an anti- $A\beta$ antibody (6E10). Experimental conditions: $[A\beta_{40}] = 25 \mu\text{M}$; $[\text{CuCl}_2 \text{ or } \text{ZnCl}_2] = 25 \mu\text{M}$; [compound] = 50 μM ; incubation for 4, 8, and 24 h; pH 7.4 (for metal-free and Zn(II) experiments) or 6.6 (for Cu(II) experiments); 37 °C; constant agitation. The control lane (without compound treatment) is identified by the letter “C”, and the lane number refers to the specific compound within each chemical group (*i.e.*, **AQ**, **AQP**, **AQDA**).

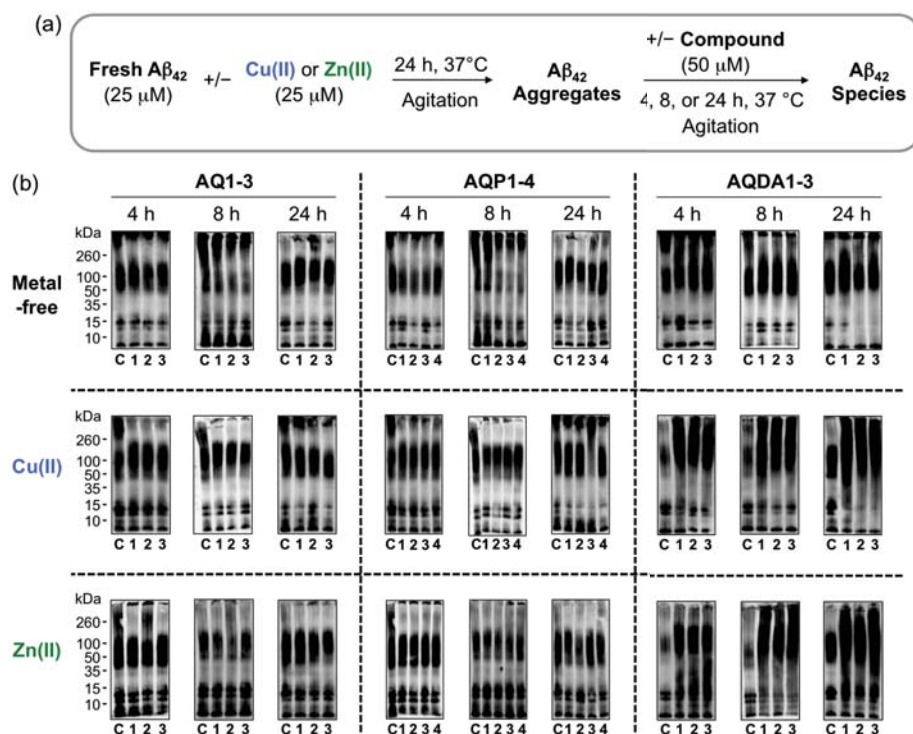


Figure 2.7. Capability of compounds (AQ1-3, AQP1-4, and AQDA1-3) to reverse preformed $A\beta_{42}$ aggregates in the absence and presence of metal ions [Cu(II) and Zn(II)]. (a) Scheme of the disaggregation experiments. (b) Visualization of the resultant $A\beta$ species from the disaggregation experiments by gel/Western blot utilizing an anti- $A\beta$ antibody (6E10). Experimental conditions: $[A\beta_{42}] = 25 \mu\text{M}$; $[\text{CuCl}_2 \text{ or } \text{ZnCl}_2] = 25 \mu\text{M}$; [compound] $50 \mu\text{M}$; incubation for 4, 8, and 24 h; pH 7.4 (for metal-free and Zn(II) experiments) or 6.6 (for Cu(II) experiments); $37 \text{ }^\circ\text{C}$; constant agitation. The control lane (without compound treatment) is identified by the letter “C”, and the lane number refers to the specific compound within each chemical group (*i.e.*, AQ, AQP, AQDA).

2.2.3. Direct Interaction Between Soluble Metal-Free $A\beta$ and AQ Derivatives

In order to elucidate the potential binding regions between $A\beta_{40}$ and the AQ derivatives, 2D band-Selective Optimized Flip-Angle Short Transient Heteronuclear Multiple Quantum Coherence (SOFAST-HMQC) NMR was employed.^{23,31} Chemical shift perturbation (CSP) is indicative of an altered electronic environment around the assigned residue which is likely the result of interaction with the derivatives (Figures 2.8 and 2.9). Despite the various chemical alterations to the ML framework investigated herein, there are two primary structural regions of $A\beta$ that show interaction with the AQ derivatives observed by NMR. Compounds altered either the N-terminal residues near the metal binding site of $A\beta_{40}$ (*i.e.*, predominantly E11 and V12) or the central hydrophobic residues within the self-recognition sequence (LVFFA).^{7,8,11,12} It was previously demonstrated that ML predominantly perturbs V12 and Q15, suggesting that the N-terminal contacts may be partially responsible for its efficacy and desirable for future chemical tools.²³

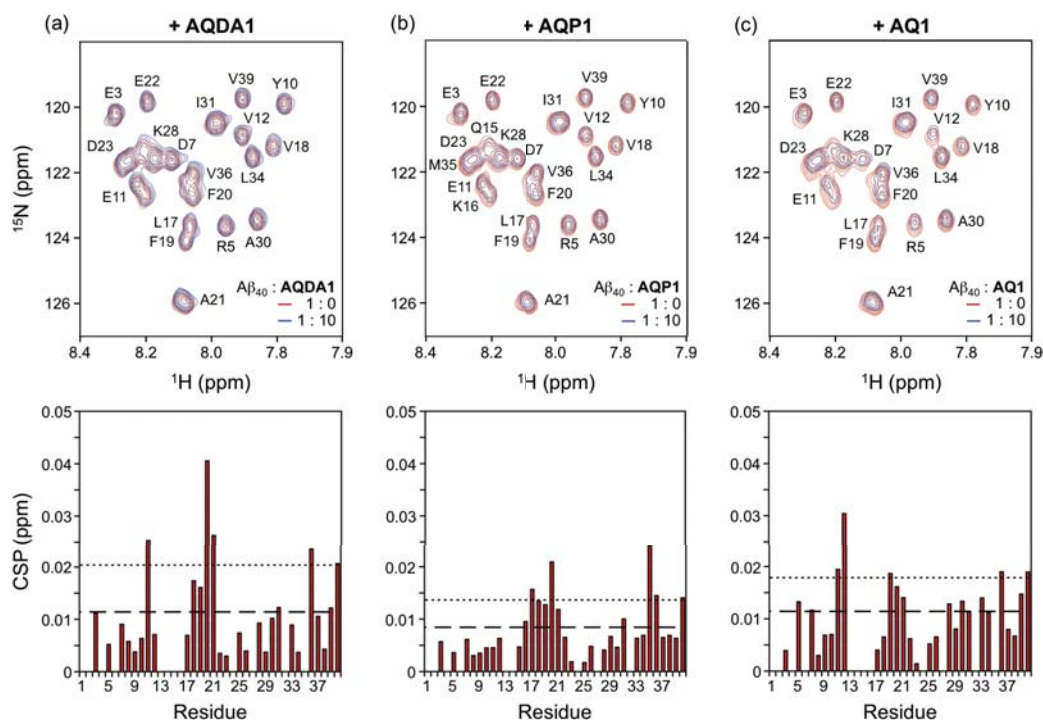


Figure 2.8. Interactions of **AQ1**, **AQP1**, and **AQDA1** with monomeric $A\beta_{40}$, monitored by SOFAST-HMQC NMR. (a-c) SOFAST-HMQC NMR spectra (zoomed in view from 7.9 to 8.4 ppm; top) and chemical shift perturbations (CSPs) (bottom) of $A\beta_{40}$ upon treatment with (a) **AQDA1**, (b) **AQP1**, or (c) **AQ1**. Two horizontal lines represent the average chemical shift (dashed line) plus one standard deviation (dotted line). Residues which show no CSP are the result of unresolved peaks in the spectra.

Of the **AQ** derivatives studied by NMR, both **AQ1** and **AQ2** have CSP profiles most similar to **ML** (Figures 2.8 and 2.9). These molecules are not shown to have any **ML**-like anti-amyloidogenic activity, which suggests that simply targeting the N-terminal metal binding site (in particular, metal binding residues H6, H13, and H14) is insufficient for such function. Predictably, the addition of the phenol group (shown in **AQP1**, **AQP2**, and **AQP4**) shifted the preferred interaction toward the more nonpolar and aromatic residues. Of these three compounds, only **AQP4** demonstrated any interaction with N-terminal residues (E11; Figure 2.9d). Additionally, only **AQP1** was observed to effectively modulate Cu(II)- $A\beta_{40}$ aggregation, which is likely associated with the relatively high affinity of **AQP1** for Cu(II) (*vide infra*). Combined, these results further imply that anti-amyloidogenic activity is not as much a function of simply where on the monomer a compound binds but rather a function of a compound's interaction site(s) and its ability to interact with other components of the system.

The addition of the 4-(dimethylamino)phenol, instead of the phenol group, had a slightly unexpected result. While the added aromaticity promoted interactions of **AQDA1-3** with the central self-recognition sequence (like **AQP1** and **AQP2**), it also maintained contacts with more N-terminal residues (E11 and

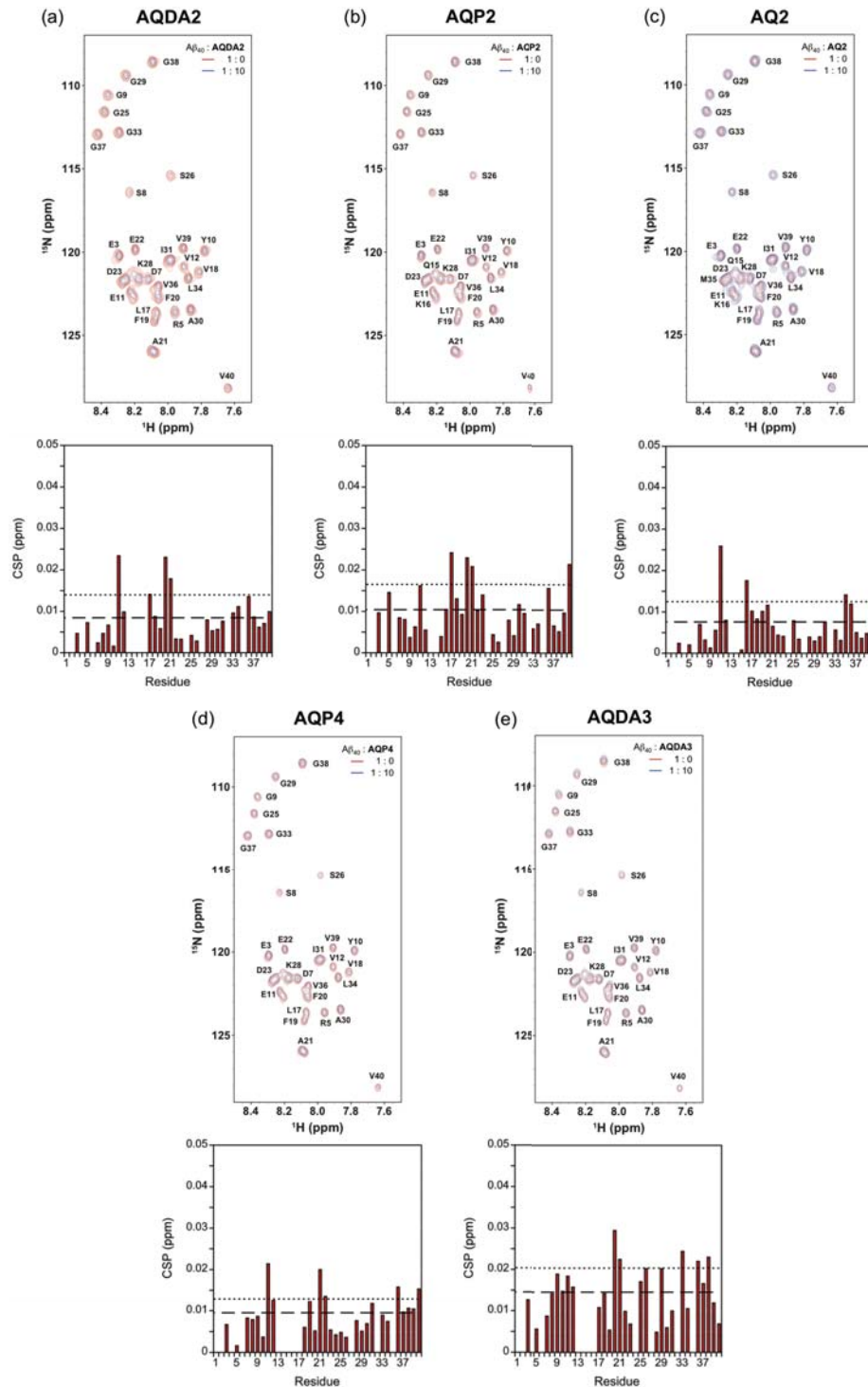


Figure 2.9. Interactions of AQDA2, AQP2, AQ2, AQP4, and AQDA3 with monomeric $A\beta_{40}$, monitored by SOFAST-HMQC NMR. (a-e) SOFAST-HMQC NMR spectra (top) and chemical shift perturbations (CSPs) (bottom) of $A\beta_{40}$ upon treatment with (a) AQDA2, (b) AQP2, (c) AQ2, (d) AQP4, and (e) AQDA3. Two horizontal lines represent the average chemical shift (dashed line) plus one standard deviation (dotted line). Residues which show no CSP are the result of unresolved peaks in the spectra.

V12) by **AQDA1** and **AQDA2** which was similar to the interactions observed in both the nonreactive **AQ1** and **AQ2**, along with the functional parent, **ML** (Figures 2.8 and 2.9). In addition, like **ML**, it is possible that having the slightly polar dimethylamino moiety on the framework appended to the added hydrophobicity of the phenol group remedies the shift toward hydrophobic residues seen for the **AQP** compounds. The dimethylamino functionality is indicated to be a moiety that is able to tune the interaction of hydrophobic compounds toward more polar peptide regions, functioning as a chemical rheostat. It is also coupled with consistent reactivity against $A\beta$. Thus, having modest hydrophilicity (in this case, instilled by the dimethylamino functionality) may promote the anti-amyloidogenic activity of the compounds, as observed in both **ML** and the **AQDA** derivatives.

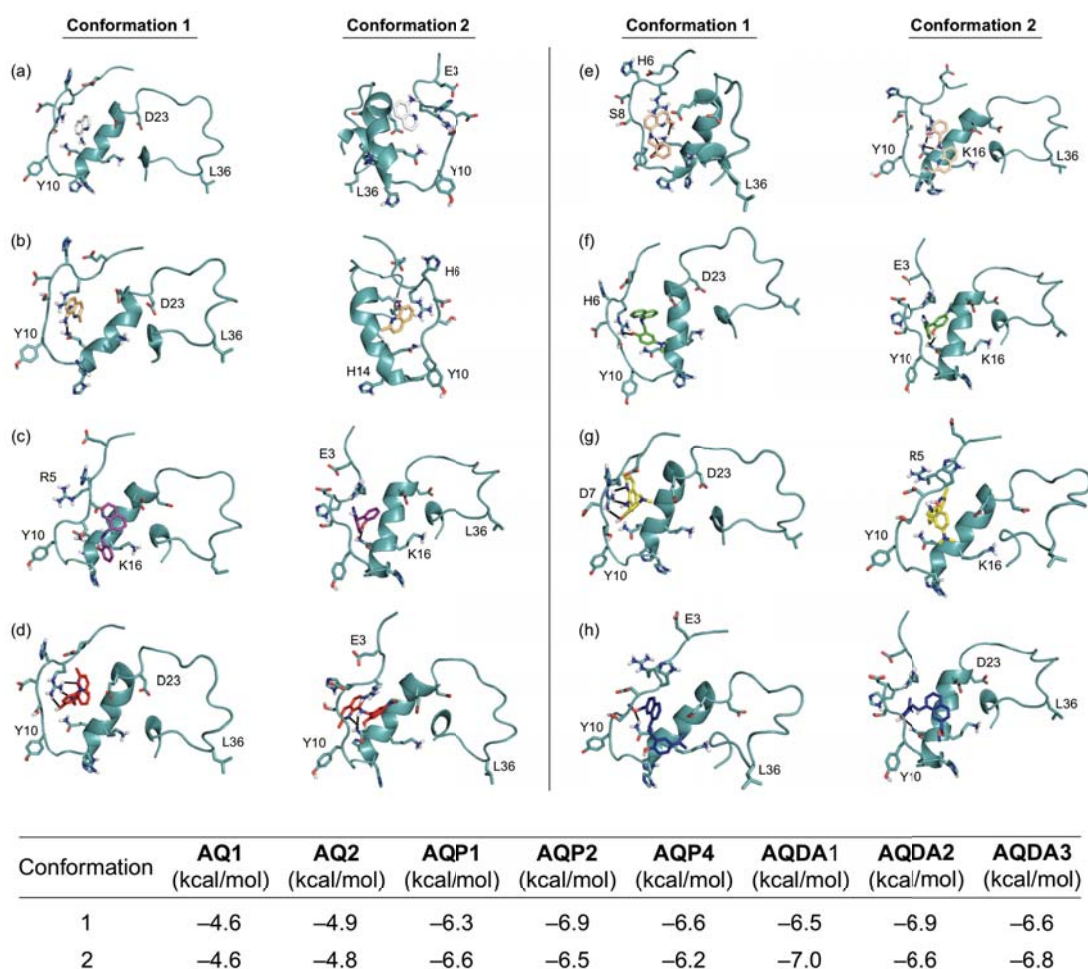


Figure 2.10. Docking studies of **AQ** derivatives with $A\beta_{40}$ monomer. Top: The two lowest energy cartoon conformations of (a) **AQ1**, (b) **AQ2**, (c) **AQP1**, (d) **AQP2**, (e) **AQP4**, (f) **AQDA1**, (g) **AQDA2**, and (h) **AQDA3** with $A\beta_{40}$ (PDB 2LFM) by AutoDock Vina. Hydrogen bonding is indicated with dashed lines (2.0-2.7 Å). Bottom: Summary of calculated binding energies of the **AQ** series to each $A\beta$ conformation.

The interactions between A β and the **AQ** derivatives examined by 2D NMR were further visualized and probed by docking studies that were performed employing AutoDock Vina⁴⁶ and the previously reported NMR structure of monomeric A β ₄₀ (PDB 2LFM)⁴³ (Figure 2.10). The docking results showed that for most conformations of A β , the ligands bound almost exclusively in the pocket formed by the folding of the N-terminal random coil and α -helix and their adducts with the peptide were stabilized by nonspecific and/or direct intermolecular interactions (*e.g.*, hydrogen bonding, π - π stacking). These interactions had calculated binding energies ranging from -7.0 to -4.6 kcal/mol (Figure 2.10). Similar to the findings from our 2D NMR experiments, the **AQP** derivatives (**AQP1**, **AQP2**, and **AQP4**) containing the more hydrophobic phenol functionality were observed to penetrate more deeply into the N-terminal pocket and appeared to interact more tightly with the central self-recognition sequence. Conversely, **AQ1** and **AQ2** appeared to dock more toward the N-terminal residues while the derivatives equipped with the 4-(dimethylamino)phenol functionality (**AQDA1-3**) showed a tendency to maintain both close interaction with the N-terminal residues, mostly by hydrogen bonding, while simultaneously establishing close contacts with the α -helical central hydrophobic region. Overall, these docking findings support the 2D NMR investigations that identified the aptitude of the dimethylamino functionality to tune the interaction of hydrophobic compounds toward the N-terminal hydrophilic residues.

2.2.4. Analysis of AQ Derivatives Incubated with A β ₄₀ by Ion Mobility–Mass Spectrometry

To further explore the interactions between A β ₄₀ and the **AQ** derivatives studied herein, we applied nano-electrospray–ionization mass spectrometry (nESI–MS) combined with ion mobility–mass spectrometry (IM–MS), optimized for the detection of non-covalent protein complexes.^{33,34} The MS data presented in Figure 2.11 highlight that among the multifunctional derivatives, only **AQP1** and **AQP4** were capable of binding Cu(II)-treated A β ₄₀. While no other small molecules were observed to form complexes with Cu(II)-associated A β ₄₀, a notable and replicable reduction in the total Cu(II)-bound A β species was identified upon incubation with many of the ligands studied (**AQP1**, **AQDA1**, **AQDA2**, and **ML**), when compared to the baseline levels prior to small molecule incubation supporting their metal chelation activity (Figure 2.12). In the absence of a source of Cu(II), no ligand binding was observed (data not shown).

To gain further insight into the structures of the complexes between Cu(II)-treated A β ₄₀ and the **AQ** derivatives, we measured and compared the IM arrival time distributions for these complexes (Figure 2.11 i; see Table 2.3 for the supporting collisional cross-section (CCS) data). Our results indicate that **AQP1** and **AQP4** binding to Cu(II)-treated A β leads to a distinct conformation shift when compared to the

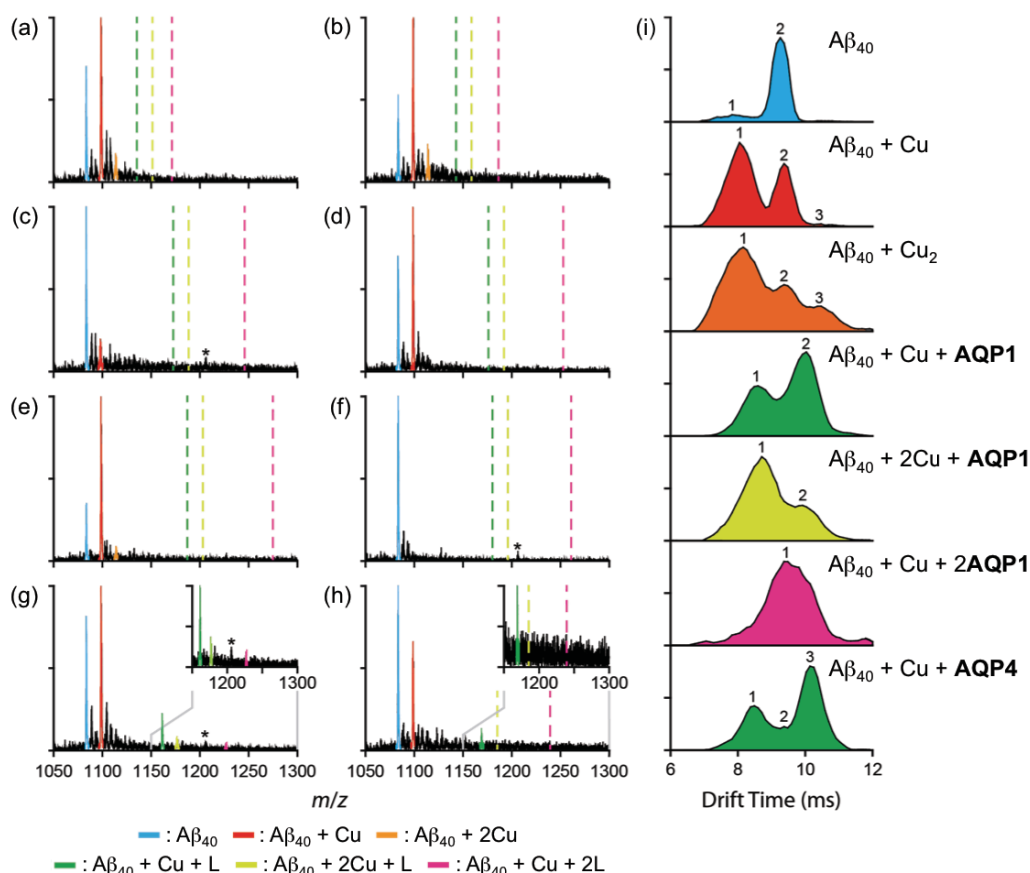


Figure 2.11. Mass spectrometric and ion mobility–mass spectrometric analyses of **AQ1**, **AQ4**, **AQP1**, **AQP4**, **AQDA1-3**, and **ML** upon addition of $CuCl_2$. MS spectra of (a) **AQ1**, (b) **AQ4**, (c) **AQDA1**, (d) **AQDA2**, (e) **AQDA3**, (f) **ML**, (g) **AQP1**, and (h) **AQP4**. (i) IM-MS drift time analysis. Collision cross section data for all ion mobility data sets are presented in Table 2.3. L = ligand (*i.e.*, **AQ1**, **AQ4**, **AQDA1-3**, **ML**, **AQP1**, **AQP4**). *Indicates a contaminant refractory to our purification methods.

Table 2.3. Calculated collision cross section data from observed 4^+ ligated $A\beta_{40}$ species.

	Conformational Specie (\AA^2)		
	1	2	3
$[A\beta_{40}]$	659.26 +/- 32.63	718.16* +/- 38.04	–
$[A\beta_{40}][Cu]$	666.24* +/- 28.38	732.57 +/- 30.91	790.53 +/- 40.73
$[A\beta_{40}][Cu]_2$	657.89* +/- 25.87	734.80 +/- 28.02	791.46 +/- 24.61
$[A\beta_{40}][AQP1][Cu]$	691.67 +/- 30.20	765.43* +/- 29.04	–
$[A\beta_{40}][AQP1][Cu]_2$	695.53* +/- 45.81	760.59 +/- 38.12	–
$[A\beta_{40}][AQP1]_2[Cu]$	741.25* +/- 23.91	–	–
$[A\beta_{40}][AQP4][Cu]$	684.80 +/- 33.49	730.43 +/- 34.00	773.84* +/- 30.13

*Indicates the dominant structural species observed.

compound-untreated metal-free and metal-bound $A\beta$ states. In particular, close analysis of the IM drift time presents a slight perturbation of the $Cu(II)$ – $A\beta_{40}$ conformations toward more expanded conformers

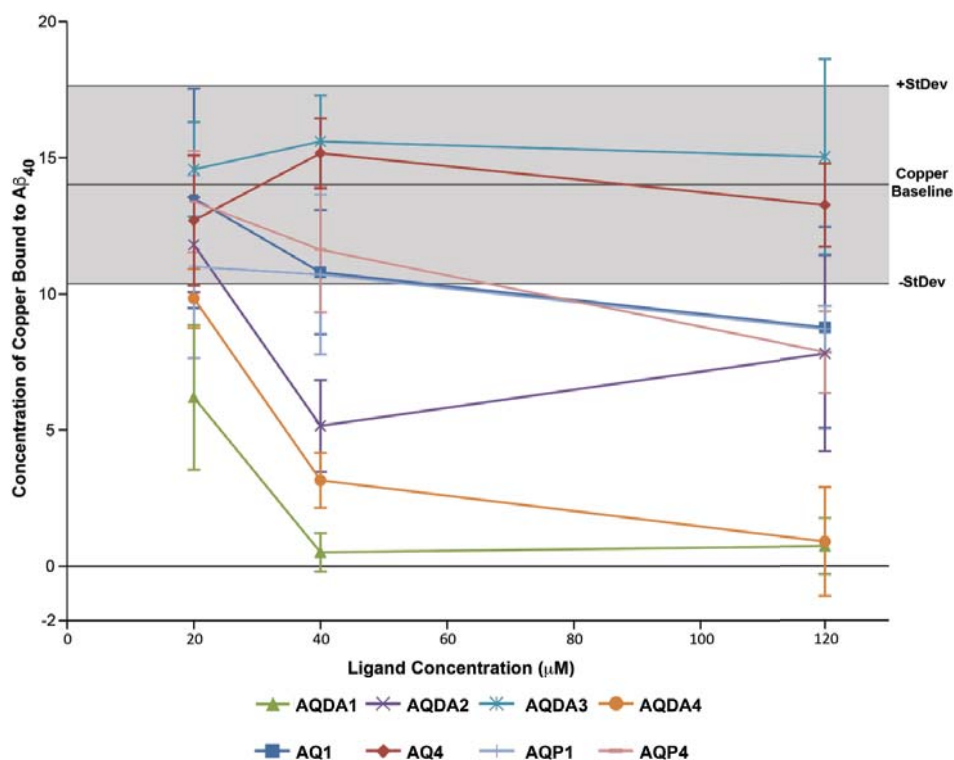


Figure 2.12. Analysis of the amount of copper-bound $A\beta_{40}$ as a function of ligand concentration. Compared to baseline levels of metal-bound $A\beta_{40}$, **AQDA1**, **AQDA2**, **ML**, and **AQP1** are all shown to be capable of reducing the concentration of Cu(II)-associated peptide species.

compared to compound-free Cu(II)-associated $A\beta_{40}$. These data contrast the results for previously studied small molecules which induced conformational compaction upon co-incubation with $A\beta$.^{31,32,35} Such a difference in the conformations generated upon **AQP1** treatment (*i.e.*, the more expanded structures compared to the compaction observed previously)^{31,32,35} may suggest that **AQP1**'s ability to alter the $A\beta_{40}$ aggregation pathway in the presence of Cu(II) may be directed mainly by its metal chelation properties rather than its induction of structural alteration of $A\beta$. A metal chelation dependence would also further validate why **AQP4** [the compound which binds Cu(II) much weaker than **AQP1** (*vide infra*)] does not modulate the aggregation of copper-bound $A\beta_{40}$ *in vitro*.

On the basis of the absence of any observable $A\beta$ -ligand complexes for the **AQ** derivatives equipped with the 4-(dimethylamino)phenol functionality (*i.e.*, **AQDA1**, **AQDA2**, **AQDA3**), two mechanisms are proposed to rationalize the activities of these molecules as $A\beta$ modulators. First, these remaining small molecules may target larger, higher-order oligomers that are too transient for IM-MS detection under the conditions used herein. While the analyses of the interactions between small molecules, such as these, and $A\beta$ dimers are technically possible, the presence of Cu-based salt cluster chemical noise has prevented

this analysis.³⁵ Second, **AQDA1**, **AQDA2**, and **ML** are shown to sequester Cu(II) from A β , and thus our data suggests the contribution of the ligands' metal chelation properties toward its control of metal-induced A β aggregation.

2.2.5. Metal Binding Properties of AQ Derivatives

UV-visible (UV-vis) and ¹H NMR spectroscopy were first employed in order to probe the effects of structural modifications on the metal binding properties of the multifunctional derivatives. Upon co-incubation of the ligands with increasing amounts of CuCl₂ or ZnCl₂ (Figures 2.13 and 2.14) new optical bands and/or changes in the absorbance intensity were observed. Decreases in the absorbance of the peaks at *ca.* 250/340 (for **AQ1**) and 250/400 nm (for **AQ3**) followed by the growth of new bands at *ca.* 300 and/or 450 nm (for **AQ1-3**) were discernable as CuCl₂ was titrated into solution (Figure 2.13a-c). **AQ** derivatives augmented with phenols (*i.e.*, **AQP1-4**) produced new peaks at *ca.* 320 and 430 nm in the presence of CuCl₂ (Figure 2.13d-g), while the compounds with the 4-(dimethylamino)phenol moiety (*i.e.*, **AQDA1-3**) generated new optical bands at *ca.* 380 and 470 nm (Figure 2.13h-j).

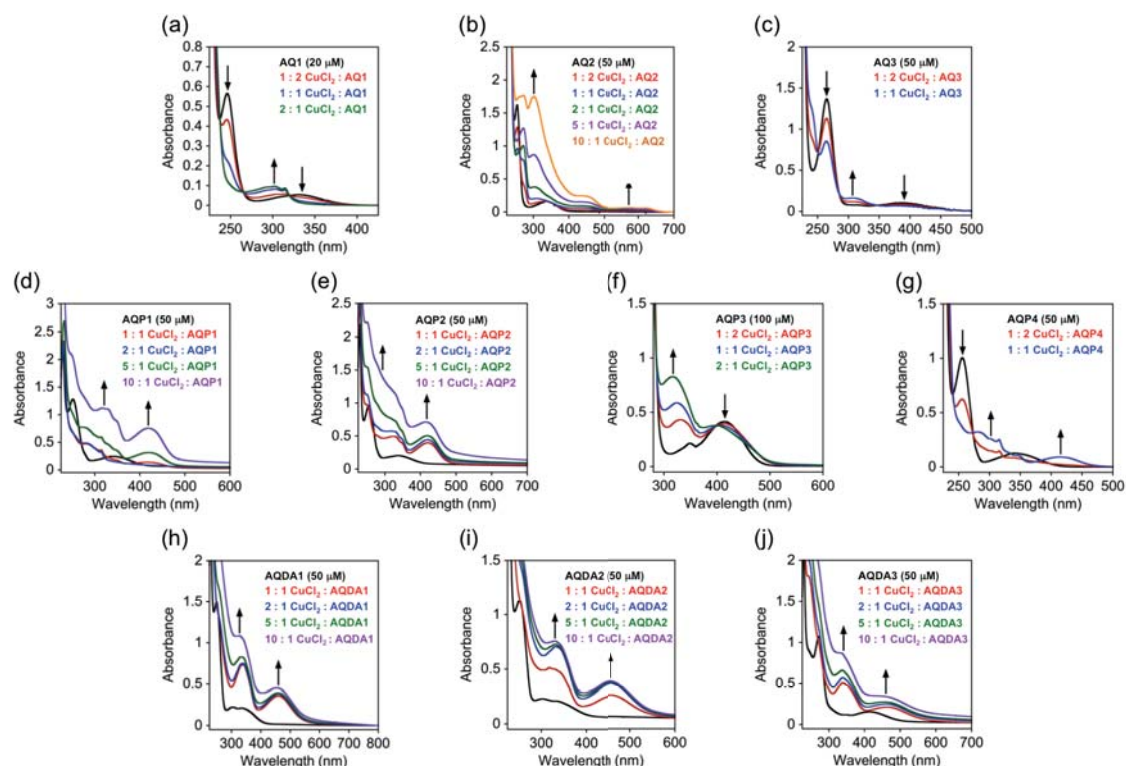


Figure 2.13. Cu(II) binding studies of **AQ1-3**, **AQP1-4**, and **AQDA1-3**. (a-j) UV-vis spectra of ligands [(a) **AQ1**, (b) **AQ2**, (c) **AQ3**, (d) **AQP1**, (e) **AQP2**, (f) **AQP3**, (g) **AQP4**, (h) **AQDA1**, (i) **AQDA2**, and (j) **AQDA3**; black lines] with the addition of increasing amounts of CuCl₂ (colored lines; 30 min

incubation; room temperature). Experimental conditions: for **AQ1** and **AQ3**, [M(II)]:[L] = 1:2, 20 mM HEPES, pH 7.4, 150 mM NaCl; for **AQ2**, [M(II)]:[L] = 1:2, CH₃CN; for **AQP1-2**, [M(II)]:[L] = 1:1, 20 mM HEPES, pH 7.4, 150 mM NaCl; for **AQP3**, [M(II)]:[L] = 1:2, CH₃CN; for **AQP4**, [M(II)]:[L] = 1:2, 20 mM HEPES, pH 7.4, 150 mM NaCl; for **AQDA1-3**, [M(II)]:[L] = 1:1, 20 mM HEPES, pH 7.4, 150 mM NaCl.

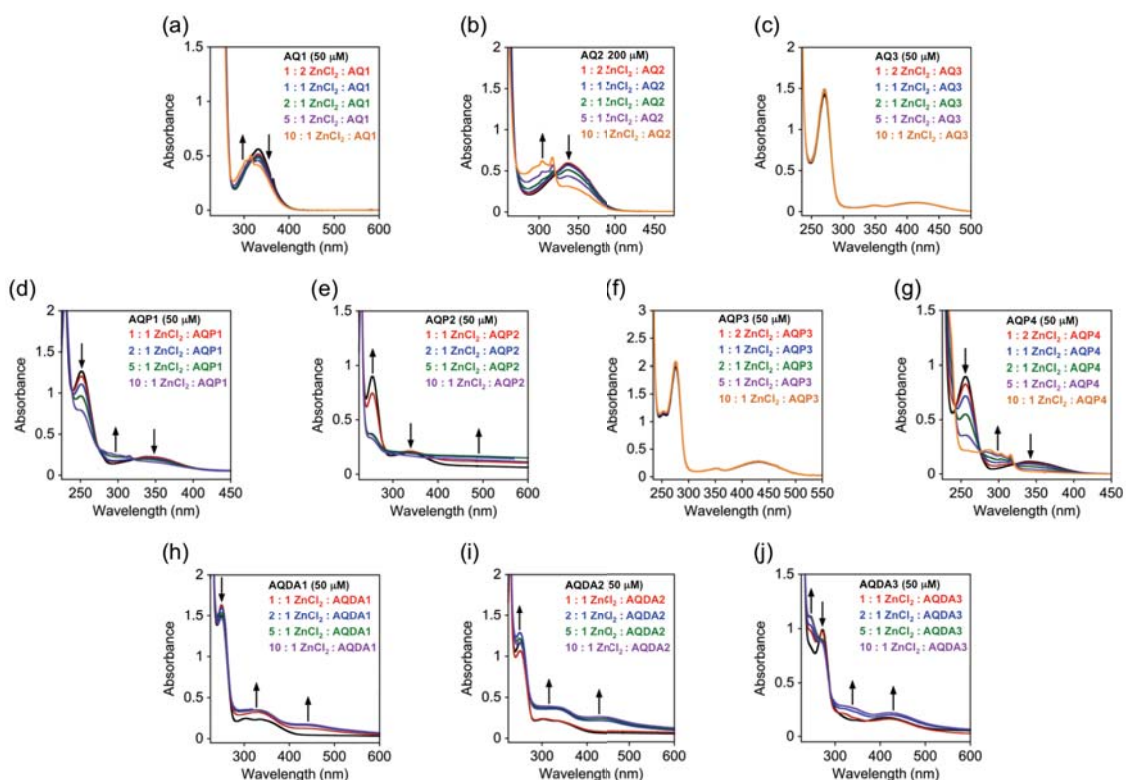


Figure 2.14. Zn(II) binding experiments. (a-j) UV-vis spectra of [(a) **AQ1**, (b) **AQ2**, (c) **AQ3**, (d) **AQP1**, (e) **AQP2**, (f) **AQP3**, (g) **AQP4**, (h) **AQDA1**, (i) **AQDA2**, and (j) **AQDA3**; black lines] with the addition of increasing amounts of ZnCl₂ (colored lines; 30 min incubation; room temperature). Experimental conditions: for **AQ1**, [M(II)]:[L] = 1:2, 20 mM HEPES, pH 7.4, 150 mM NaCl; for **AQ2**, [M(II)]:[L] = 1:2, CH₃CN; for **AQ3**, [M(II)]:[L] = 1:2, EtOH; for **AQP1-2**, [M(II)]:[L] = 1:1, 20 mM HEPES, pH 7.4, 150 mM NaCl; for **AQP3**, [M(II)]:[L] = 1:2, EtOH; for **AQP4**, [M(II)]:[L] = 1:2, 20 mM HEPES, pH 7.4, 150 mM NaCl; for **AQDA1-3**, [M(II)]:[L] = 1:1, 20 mM HEPES, pH 7.4, 150 mM NaCl.

Administration of ZnCl₂ into solutions of **AQ** derivatives resulted in less noticeable spectral changes when compared to the CuCl₂ results (Figure 2.14). Optical shifts from *ca.* 350 to 300 nm were detected upon increased addition of ZnCl₂ to solutions of **AQ1** and **AQ2** (Figure 2.14a,b). Incubation of **AQP1**, **AQP2**, and **AQP4** with ZnCl₂ caused various spectral changes at *ca.* 250, 300, and 350 nm (Figure 2.14d,e,g). Similar to the CuCl₂ experiments, the ZnCl₂ binding peaks for the derivatives containing the 4-(dimethylamino)phenol functionality were relatively red-shifted compared to the **AQP** derivatives (*i.e.*, new peaks growing in at *ca.* 350 and 450 nm; Figure 2.14h-j). No significant changes in the UV-vis

spectra could be identified for **AQ3** and **AQP3** under the experimental conditions employed; therefore, ^1H NMR spectroscopy was utilized to further probe their Zn(II) binding. Introduction of 3.5 equiv of ZnCl_2 to a CD_3CN solution of **AQ3** induced a slight downfield chemical shift of the quinoline protons, demonstrating the potential involvement of the nitrogen donor atoms from the primary amine and quinoline ring in Zn(II) coordination (Figure 2.15). No significant chemical shifts were observed when ZnCl_2 was added to a solution of **AQP3**; however, this is most likely a result of its limited solubility under the experimental conditions. Overall, our UV-vis and NMR studies indicate the ability of the structural derivatives of **ML** to bind both Cu(II) and Zn(II).

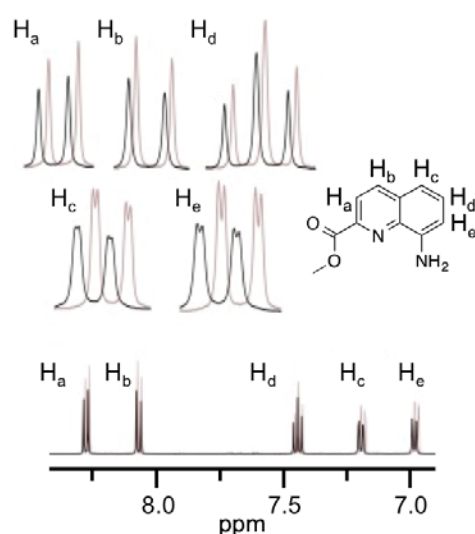


Figure 2.15. Zn(II) binding studies, measured by ^1H NMR. ^1H NMR spectra of **AQ3** (red) with 3.5 equiv of ZnCl_2 (black) were obtained at room temperature. Experimental conditions: CD_3CN ; $[\text{AQ3}] = 5 \text{ mM}$; $[\text{ZnCl}_2] = 17.5 \text{ mM}$; 10 min incubation. Note that Zn(II) binding to **AQP3** could not be determined due to limited solubility under experimental conditions.

In order to comprehend the solution speciation of the **AQ** derivatives in the absence and presence of Cu(II) and attempt to determine the effects of structural variations on the Cu(II) binding affinity of our ligands, UV-vis variable-pH titration experiments were conducted. First, spectrophotometric titrations of the ligands (*i.e.*, **AQP1**, **AQP4**, **AQDA1-3**) were used to estimate the acidity constants ($\text{p}K_{\text{a}}$) [see Figure 2.16; for **AQP1**, $\text{p}K_{\text{a}2} = 3.67(4)$, $\text{p}K_{\text{a}3} = 9.92(6)$; for **AQP4**, $\text{p}K_{\text{a}2} = 3.78(8)$, $\text{p}K_{\text{a}3} = 10.11(8)$; for **AQDA1**, $\text{p}K_{\text{a}1} = 3.72(9)$, $\text{p}K_{\text{a}2} = 6.61(5)$, $\text{p}K_{\text{a}3} = 8.99(6)$; for **AQDA2**, $\text{p}K_{\text{a}1} = 3.21(9)$, $\text{p}K_{\text{a}2} = 4.82(6)$, $\text{p}K_{\text{a}3} = 7.69(4)$; for **AQDA3**, $\text{p}K_{\text{a}1} = 2.30(8)$, $\text{p}K_{\text{a}2} = 3.82(3)$, $\text{p}K_{\text{a}3} = 6.73(5)$]. The solution speciation diagrams depict the presence of three species for the phenol derivatives, **AQP1** and **AQP4** (anionic, neutral, and monoprotonated species; LH_1 , L, and LH), and predict the neutral ligand (L) predominately being present at the physiological pH (*i.e.*, 7.4; Figure 2.16a,b). Due to the protonation of the dimethylamino group,

AQDA derivatives contain an additional diprotonated species (LH_2) in the pH range examined and exist in a mixture of neutral and cationic (for **AQDA1**) or anionic and neutral (for **AQDA2** and **AQDA3**) species (Figure 2.16c-e). Overall, the relative abundance of the neutral form of the ligands at pH 7.4 (*ca.* 100% for **AQP1** and **AQP4**; *ca.* 50% for **AQDA1-3**) may explain their potential BBB penetration, as suggested by Lipinski's rules, the PAMPA-BBB assay, and calculated logBB values (Tables 2.1 and 2.2).

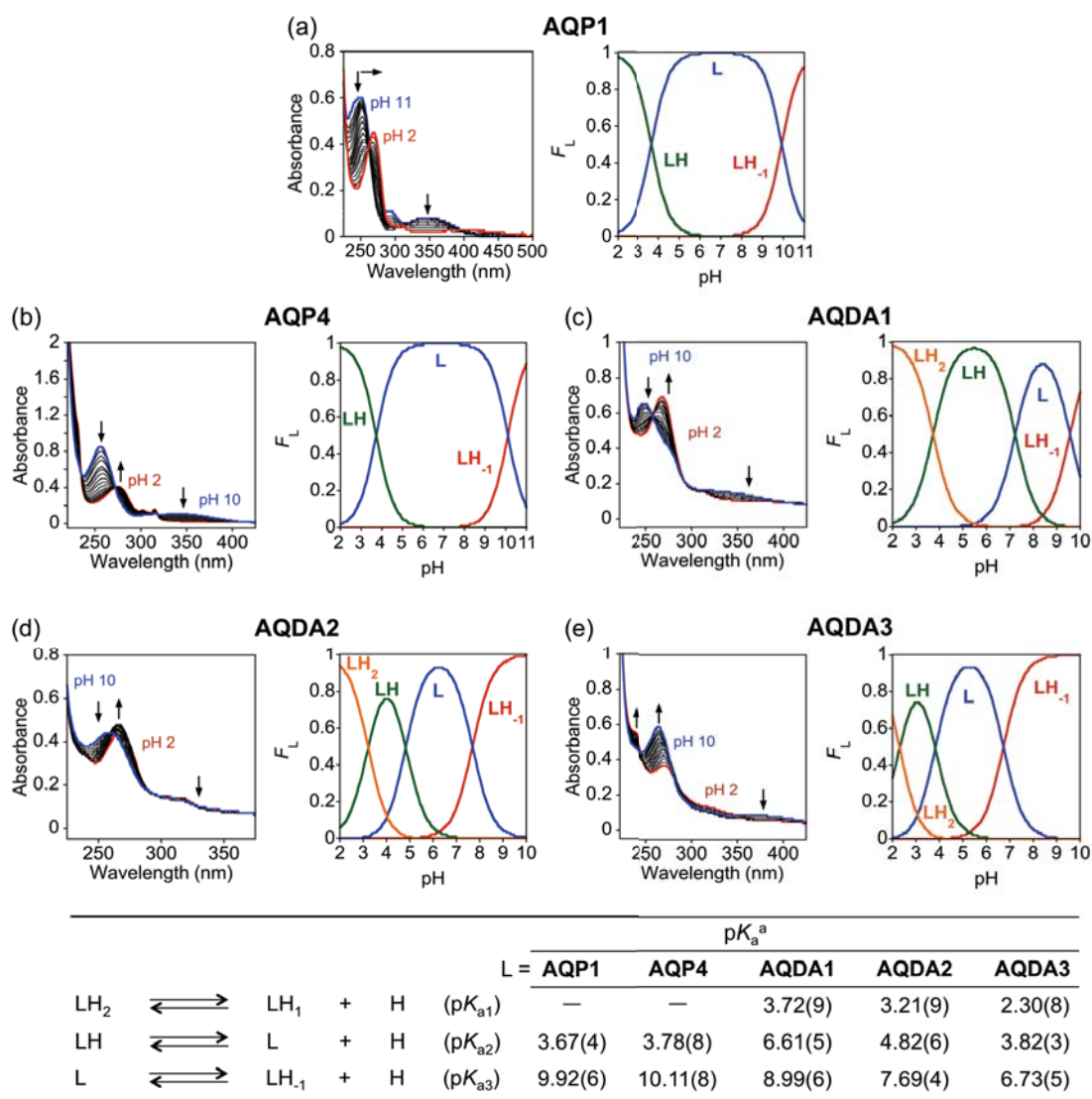


Figure 2.16. Solution speciation studies of **AQP1**, **AQP4**, and **AQDA1-3**. UV-vis variable-pH titration spectra (left) and solution speciation diagrams (right) of (a) **AQP1** (pH 2–11), (b) **AQP4** (pH 2–11), (c) **AQDA1** (pH 2–10), (d) **AQDA2** (pH 2–10), and (e) **AQDA3** (pH 2–10) (F_L = fraction of species at given pH). Acidity constants (pK_a) of L ($L = \text{AQP1, AQP4, and AQDA1-3}$) are summarized in the table. Experimental conditions: $[L] = 50 \mu\text{M}$ ($L = \text{AQP4 or AQDA1}$) or $25 \mu\text{M}$ ($L = \text{AQP1, AQDA2, and AQDA3}$); $I = 0.10 \text{ M NaCl}$; room temperature. Charges are omitted for clarity. ^aThe error in the last digit is shown in the parentheses.

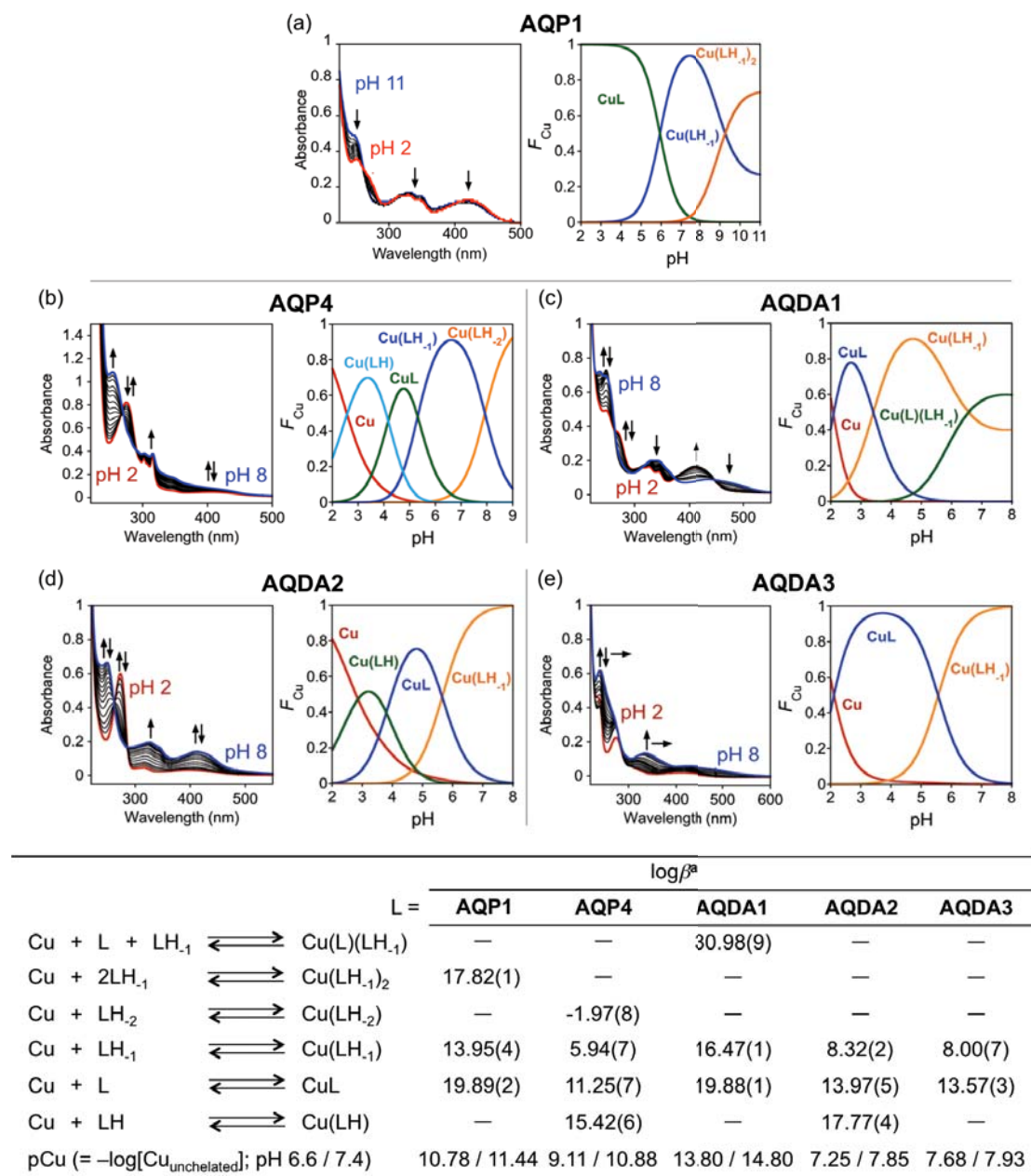


Figure 2.17. Solution speciation studies of **AQP1**, **AQP4**, and **AQDA1-3** in the presence of **Cu(II)**. UV-vis variable-pH titration spectra (left) and solution speciation diagrams (right) of (a) **AQP1**, (b) **AQP4**, (c) **AQDA1**, (d) **AQDA2**, and (e) **AQDA3** upon incubation with **Cu(II)** (F_{Cu} = fraction of species at given pH). Stability constants ($\log \beta$) of **Cu(II)**-**L** complexes (**L** = **AQP1**, **AQP4**, and **AQDA1-3**) are summarized in the table. Charges are omitted for clarity. ^a The error in the last digit is shown in parentheses. Experimental conditions: [**AQP1**] = 25 μM , [**CuCl**₂] = 12.5 μM , pH 2–11 (titrated from basic to acidic); [**AQP4**] = 100 μM , [**CuCl**₂] = 50 μM , pH 2–9 (titrated from basic to acidic); [**AQDA1**] = 25 μM , [**CuCl**₂] = 12.5 μM , pH 2–8 (titrated from basic to acidic); [**AQDA2**] = 25 μM , [**CuCl**₂] = 12.5 μM , pH 2–8 (titrated from acidic to basic); [**AQDA3**] = 25 μM , [**CuCl**₂] = 12.5 μM , pH 2–8 (titrated from acidic to basic); incubated for 1 h; I = 0.10 M NaCl; room temperature.

Once pK_a values were obtained for the ligands of interest, solution speciation experiments in the presence of CuCl_2 were carried out to determine if structural modifications to **ML**'s framework at sites 2 and 3 could alter its high apparent dissociation constant for Cu(II) (picomolar K_d at pH 7.4), while still maintaining competitive metal binding with $\text{A}\beta$ (*e.g.*, nanomolar range).^{7,9,11,12,23} Based on the stability constants ($\log\beta$) and values of $p\text{Cu}$ ($p\text{Cu} \approx -\log[\text{Cu}_{\text{unchelated}}]$) (Figure 2.17), the approximate dissociation constants ($K_d = [\text{Cu}_{\text{unchelated}}]$) for the multifunctional derivatives were determined. As summarized in the table in Figure 2.17, the more inert Cu(II) –ligand complexes were shown in the order of **AQDA1**, **AQP1**, **AQP4**, **AQDA3**, and **AQDA2**. Interestingly, the tridentate ligands, **AQDA1** and **AQP1**, with hydrogen atoms in the R_2 position, presented the strongest affinity for Cu(II) compared to the other tetradentate ligands measured herein (*i.e.*, **AQP4**, **AQDA3**), thus possibly explaining the ability of **AQP1** to modulate the aggregation of Cu(II) – $\text{A}\beta_{40}$ (Figures 2.2 and 2.6). This trend may be explained by the ability of **AQDA1** and **AQP1** to form 1:2 complexes [$\text{Cu(II)}:\text{ligand}$] in addition to the 1:1 stoichiometry observed for the other derivatives (Figure 2.17a,c).²⁷ Comparison of the apparent K_d values of **AQDA1** with **AQP1** and **ML** with **AQP4** indicates that the dimethylamino functionality slightly increases the metal binding affinity, as would be expected with the installation of an electron donating group located *para* to the oxygen donor atom of the phenol. **AQDA2** and **AQDA3** were determined to have larger K_d values [lower binding affinity for Cu(II)] than **ML**. The slightly smaller K_d of **AQDA3** for Cu(II) , compared to **AQDA2**, is most likely due to the weak contribution from the ester functionality. Overall, tuning metal binding strengths of the multifunctional derivatives is able to be accomplished through structural modifications at the R_1 and R_2 positions.

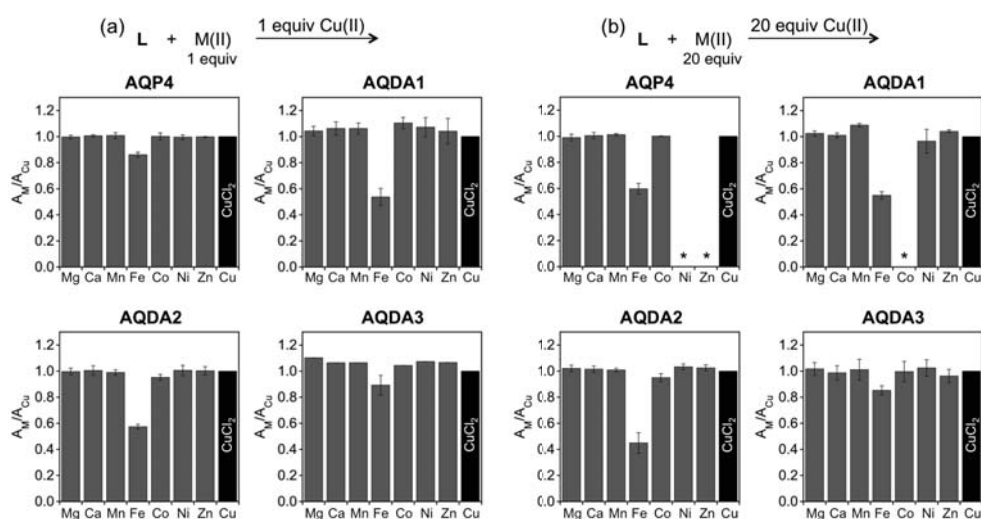


Figure 2.18. Metal selectivity of **AQP4** and **AQDA1-3** for Cu(II) over other biologically relevant divalent metal ions. Gray bars represent the subsequent addition of CuCl₂ (50 μM) to solutions containing ligand (50 μM) with (a) 1 equiv or (b) 20 equiv of the other divalent metal ions (MgCl₂, CaCl₂, MnCl₂, FeCl₂, CoCl₂, NiCl₂, and ZnCl₂). The absorbance wavelengths of **AQP4**, **AQDA1**, **AQDA2**, and **AQDA3** used to calculate A_M/A_{Cu} are listed as follows: 290 nm, 449 nm, 449 nm, and 338 nm, respectively. *Due to similar optical bands of the ligand upon binding to Cu(II) and the other metal ions, accurate metal ion selectivity cannot be obtained.

Competition reactions, monitored by UV-vis, were also conducted to examine the selectivity of **AQP4** and **AQDA1-3** for Cu(II) over other biologically relevant divalent metal ions [*i.e.*, Mg(II), Ca(II), Mn(II), Fe(II), Co(II), Ni(II), Zn(II)]. As shown in Figure 2.18, in the presence of equimolar (Figure 2.18a) or excess metal ions (20 equiv; Figure 2.18b), the ligands still exhibited spectral changes consistent with the formation of Cu(II) complexes. Fe(II) did appear to competitively interact with **AQP4**, **AQDA1**, and **AQDA2**, especially at excess concentrations. It is also worth noting that the exact quantification of the selectivity for Cu(II) over Ni(II) and Zn(II) for **AQP4** and Co(II) for **AQDA1** could not be determined due to the optical overlap of their respective metal binding bands, but the overall spectral changes were suggestive of preferential binding to Cu(II) (Figure 2.18). Collectively, these results present that **AQ** derivatives can competitively bind to Cu(II) over other biologically available divalent metal ions and that their metal affinities can be modulated through structural modifications.

2.2.6. Biological Properties: ROS Formation Control, Free Radical Scavenging Capacity, and Cytotoxicity

The extent to which structural modifications affect the biological properties of our multifunctional derivatives was also investigated. The ability to control the redox cycling between Cu(I) and Cu(II) in order to reduce ROS production through Fenton-like chemistry was first analyzed by the 2-deoxyribose assay, which measures the capacity of ligands to control the formation of copper-catalyzed hydroxyl radicals.^{23,36} As depicted in Figure 2.19a, copper-mediated generation of hydroxyl radicals was most significantly reduced upon treatment with **AQDA1**. Relative to **AQDA1**, the other derivatives evaluated showed very little aptitude to attenuate hydroxyl radical formation, possibly due to their binding properties, including weaker binding affinity for Cu(II) compared that of **AQDA1** or **ML**. Still, **ML** appeared to be about twice as efficient at controlling the formation of hydroxyl radicals relative to **AQDA1** (A/A_0 of *ca.* 0.40 for **AQDA1**; A/A_0 of *ca.* 0.20 for **ML**).²³ The enhanced ROS formation control of **ML** is most likely due to its tetradentate metal binding center, which can easily accommodate the preferred square planar geometry of Cu(II) but prohibit the generation of linear or tetrahedral geometries favored by Cu(I). In fact, based on crystallographic data reported for **AQP1**, **AQDA1** may be able to facilitate a tetrahedral copper-binding mode depending on the metal-to-ligand stoichiometry and

the pH of the solution.²⁷

In order to evaluate the antioxidant capacity of the **AQ** derivatives, the Trolox equivalent antioxidant capacity (TEAC) assay which measures the ability of the multifunctional derivatives to quench preformed ABTS cation radicals (ABTS^{•+}; ABTS = 2,2'-azino-bis(3-ethylbenzothiazoline-6-sulfonic acid)^{15,37} was performed using lysates of human neuroblastoma SK-N-BE(2)-M17 cells. Cell lysates was utilized in order to get a more accurate measure of the antioxidant capacity of the **AQ** derivatives in a more biologically relevant heterogeneous environment. As shown in Figure 2.19b, the compounds containing the phenol or 4-(dimethylamino)phenol functionalities were able to scavenge free radicals about two times more effectively than that of the water-soluble vitamin E analog, Trolox. These findings are in-line with the known antioxidant properties of phenols.³⁸⁻⁴⁰ The most efficient antioxidants, **AQDA1** and **AQDA2**, were still less active than **ML** which was determined to be *ca.* 2.5 times as effective as Trolox,²³ indicating that the primary alcohol in the R₂ position may contribute to the antioxidant activity of **ML**. In addition, an ester at the R₂ site appeared to reduce both abilities of the compounds to control ROS generation and scavenge free radicals relative to those of the other multifunctional derivatives (Figure 2.19a,b).

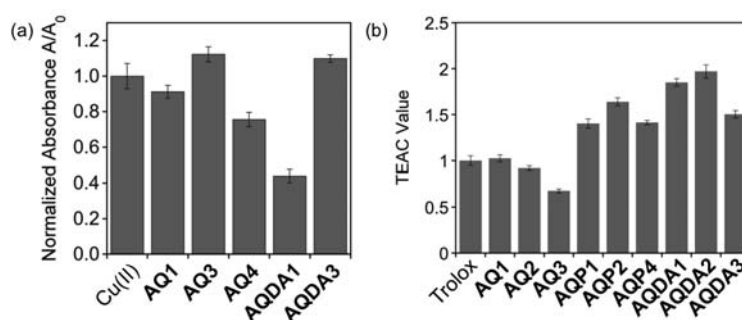


Figure 2.19. Biological activities of small molecules. (a) Inhibitory activity of **AQ1**, **AQ3**, **AQ4**, **AQDA1**, and **AQDA3** toward Cu-mediated ROS formation as determined by the 2-deoxyribose assay. The absorbance values are normalized to the ligand-free condition ($[\text{CuCl}_2] = 10 \mu\text{M}$; $[\text{ligand}] = 125 \mu\text{M}$). (b) Antioxidant activity of **AQ1-3**, **AQP1**, **AQP2**, **AQP4**, and **AQDA1-3**, identified by the TEAC assay using cell lysates. The TEAC values are relative to that of the vitamin E analogue, Trolox (6-hydroxy-2,5,7,8-tetramethylchroman-2-carboxylic acid).

Finally, the MTT assay [MTT = 3-(4,5-dimethyl-2-thiazolyl)-2,5-diphenyl-2H-tetrazolium bromide] was employed to evaluate the toxicity of the **AQ** derivatives in the mouse Neuro-2a (N2a) neuroblastoma cell line with and without CuCl_2 and ZnCl_2 (Figures 2.20). Cell viability of *ca.* 80% was measured for N2a cells treated with 5 μM of the **AQ** derivatives in the absence and presence of metal ions (CuCl_2 or ZnCl_2) (Figure 2.20a,b). A little more fluctuation in cell viability was observed upon increasing the

concentration of compound to 10 μM with and without of metal ions, but still most derivatives appeared to retain values around *ca.* 75-85% (Figure 2.20c,d). In particular, with the exception of **ML**, the multifunctional derivatives containing the 4-(dimethylamino)phenol functionality are indicated to be relatively more cytotoxic. Overall, our cell studies suggest that the structural variations of a framework may also trigger its differing levels of toxicity in living cells.

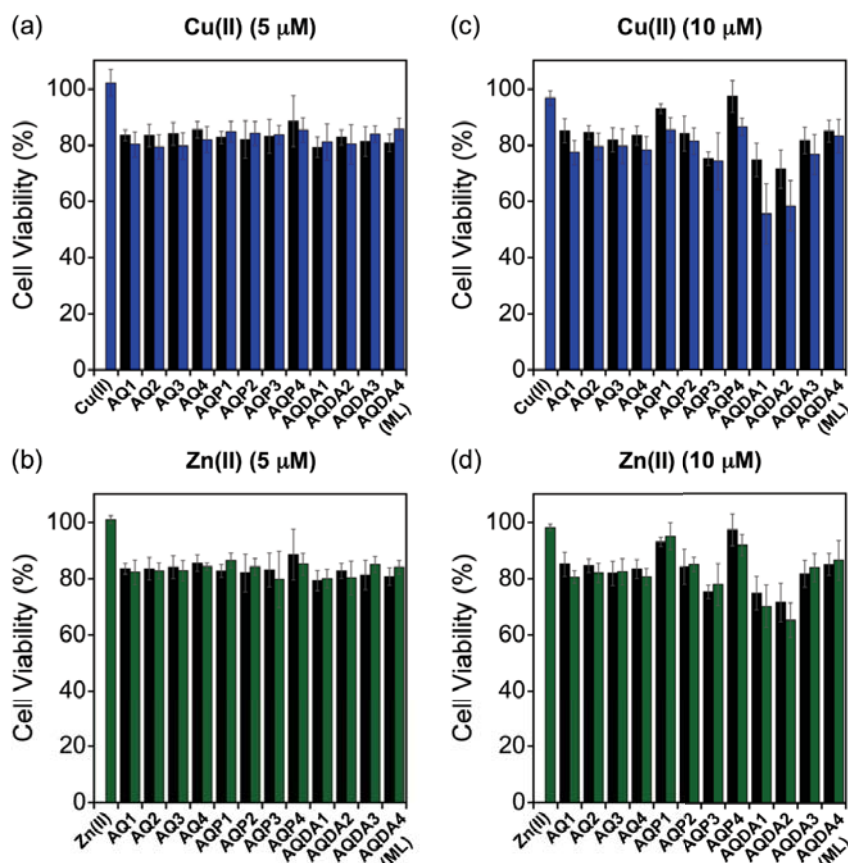


Figure 2.20. Cell viability of **AQ1-4**, **AQP1-4**, **AQDA1-3**, and **ML** in N2a cells in the absence and presence of Cu(II) and Zn(II). (a) Cu(II):ligand (1:1) (5 μM), (b) Zn(II):ligand (1:1) (5 μM), (c) Cu(II):ligand (1:1) (10 μM), and (d) Zn(II):ligand (1:1) (10 μM). Cell viability (%) was determined by the MTT assay compared to cells treated with DMSO only (1% v/v) [MTT = 3-(4,5-dimethyl-2-thiazolyl)-2,5-diphenyl-2H-tetrazolium bromide]. Black, blue, and green bars indicate cell viability upon incubation with ligand only and ligand with CuCl₂ or ZnCl₂, respectively.

2.3. Conclusions

A series of derivatives, **AQ1-4**, **AQP1-4**, and **AQDA1-3**, were developed based on the structural framework of the multifunctional ligand, **ML**, in order to tune its affinity for Cu(II) and to establish a structure-reactivity understanding of **ML**'s activities to modulate metal-free

and metal-bound A β aggregation, control metal-mediated ROS formation, and scavenge free radicals. Only compounds augmented with the dimethylamino functionality displayed noticeable modulation of both metal-free and metal-treated A β aggregation *in vitro*, with the exception of **AQP1** which exhibited its ability to regulate the aggregation of Cu(II)–A β ₄₀, which was most likely aided by its metal chelating properties (*i.e.*, pCu = 11.44 at pH 7.4). Based on NMR investigations, this dimethylamino moiety appears to act to control the distribution of the compounds' interaction with the N-terminal metal-binding region and/or the central self-recognition sequence of A β ₄₀. **ML** was previously found to preferentially target the polar N-terminal residues, which suggests that the dimethylamino group is at least partly responsible for A β interaction.²³ Favoring these interactions may be important for directing the formation of stable ternary complexes of A β –metal–ligand. Under our MS and IM–MS conditions, only noncovalent interactions between A β and **AQP1** or **AQP4** when Cu(II) was present with slight structural elongation were observed, rather than compaction of the peptide which has been previously reported for other inhibitors.^{31,32,35} Preferential transient interactions with higher-order oligomers that cannot easily be detected by IM–MS may explain the absence of complexation peaks in the **AQDA1-3**-treated samples that most noticeably perturbed metal-free and metal-treated A β aggregation *in vitro*. Structural modifications to **ML** also had drastic effects on its metal binding properties, ROS formation control, and free radical scavenging capacity. Substitution of the primary alcohol on **ML** with a hydrogen atom allowed for the formation of 1:1 and 1:2 (metal:ligand) complexes, providing a higher binding affinity for Cu(II) with respect to the other **AQ** derivatives. Structural variations also had impacts on compounds' abilities to control ROS formation and scavenge free radicals. **AQDA1**, with a hydrogen atom at the R₂ site, was indicated to be the most efficient at controlling the generation of hydroxyl radicals, while the compounds containing the phenol or 4-(dimethylamino)phenol groups (**AQP1-4** or **AQDA1-3** and **ML**) were much more potent antioxidants with respect to their **AQ** counterparts (**AQ1-4**). Conversely, the endowment with an ester, shown in **AQ3**, **AQP3**, or **AQDA3**, appeared to negatively alter the capacity to inhibit ROS generation and scavenge free radicals. Overall, by employing a series of **AQ** derivatives, a relationship between structures of the small molecules and reactivities toward targets found in AD (*e.g.*, metal-free A β /metal–A β , metals, ROS) was established. These structure-reactivity insights, gleaned through our studies, may aid in further

design of more sophisticated multifunctional ligands, especially once the degree of transferability of these studies have been determined.

2.4. Experimental Section

2.4.1. Materials and Methods

All reagents were purchased from commercial suppliers and used as received unless otherwise noted. A β ₄₀ and A β ₄₂ were purchased from Anaspec (A β ₄₂ = DAEFRHDSGYEVHHQKLVFFAEDVGSNKGAIIGLMVGGVVIA; Fremont, CA, USA). NMR and mass spectrometric analysis of small molecules were conducted on a 400 MHz Varian NMR spectrometer and a Micromass LCT Electrospray Time-of-Flight (TOF) mass spectrometer, respectively. Trace metal contamination was removed from buffers and solutions used for metal binding and A β experiments (*vide infra*) by treating with Chelex overnight (Sigma-Aldrich, St. Louis, MO, USA). Optical spectra were recorded on an Agilent 8453 UV-visible (UV-vis) spectrophotometer. TEM images were taken using a JEOL JEM-2100 transmission electron microscope (UNIST Central Research Facilities, Ulsan National Institute of Science and Technology, Ulsan, Republic of Korea). Absorbance values for biological assays, including cell viability assay, PAMPA-BBB, 2-deoxyribose assay, and TEAC assay, were measured on a Molecular Devices SpectraMax 190 microplate reader (Sunnyvale, CA, USA). Ion Mobility–Mass Spectrometry experiments investigating the interaction of **AQ** derivatives with A β in the absence and presence of Cu(II) were acquired using a Quadrupole-Ion Mobility-TOF (Q-IM-TOF) mass spectrometer (Waters Synapt G2, Milford, MA, USA) equipped with a nano-electrospray ionization (nESI) source. NMR studies of small molecules with A β were performed on a 600 MHz Bruker NMR spectrometer (University of Michigan, Ann Arbor, MI, USA).

2.4.2. Syntheses

The compounds, quinolin-8-amine (**AQ1**) and 2-methylquinolin-8-amine (**AQ2**), were purchased from TCI chemicals. 5-(Dimethylamino)-2-hydroxybenzaldehyde (**DHB**),²⁸ methyl 8-aminoquinoline-2-carboxylate (**AQ3**),^{29,31} (8-aminoquinolin-2-yl)methanol (**AQ4**),^{29,31} 2-((quinolin-8-ylamino)methyl)phenol (**AQP1**),^{29,30} and 4-(dimethylamino)-2-(((2-(hydroxymethyl)quinolin-8-yl)amino)methyl)phenol (**ML**)²³ were prepared by adapting previously reported methods.

2.4.3. Preparation of 2-(((2-Methylquinolin-8-yl)amino)methyl)phenol (**AQP2**)

To a solution of dry ethyl acetate (16 mL) was added 2-methylquinolin-8-amine (**AQ2**) (300 mg, 1.89 mmol). Salicylaldehyde (198 μ L, 1.89 mmol) was slowly added to the reaction mixture. The reaction mixture was then protected from the light and allowed to stir overnight for 24 h. After 24 h, the reaction mixture was concentrated and dried. To a solution of dichloroethane (16 mL) was added sodium triacetoxyborohydride (804 mg, 3.78 mmol). The sodium triacetoxyborohydride solution was then slowly added to the dried reaction mixture and allowed to stir for 48 h (protected from the light). After 48 h, the reaction mixture was concentrated and purified by column chromatography (Al_2O_3 , 1:10 ethyl acetate (EtOAc)/hexanes (Hx), $R_f = 0.23$) to yield the final product (light yellow powder, 241 mg, 0.912 mmol, 48%). ^1H NMR (400 MHz, $(\text{CD}_3)_2\text{SO}$) / δ (ppm): 2.62 (3H, s), 4.41 (2H, d, $J = 4.0$ Hz), 6.57 (1H, d, $J = 8.0$ Hz), 6.68 (2H, m), 6.81 (1H, d, $J = 8.0$ Hz), 6.96 (1H, d, $J = 8.0$ Hz), 7.03 (1H, t, $J = 8.0$ Hz), 7.18 (2H, m), 7.34 (1H, d, $J = 8.0$ Hz), 8.05 (1H, d, $J = 8.0$), 9.07 (1H, s). ^{13}C NMR (100 MHz, $(\text{CD}_3)_2\text{SO}$) / δ (ppm): 25.3, 42.1, 105.2, 113.6, 115.4, 119.2, 122.7, 125.7, 126.7, 127.1, 128.2, 136.6, 137.3, 144.2, 155.6, 155.7. HRMS Calcd for $\text{C}_{17}\text{H}_{17}\text{N}_2\text{O}$ $[\text{M}+\text{H}]^+$, 265.1341; found 256.1331.

2.4.4. Preparation of Methyl 8-((2-hydroxybenzyl)amino)quinoline-2-carboxylate (**AQP3**)

A solution of methyl 8-aminoquinoline-2-carboxylate (**AQ3**) (100 mg, 0.494 mmol) was utilized to prepare **AQP3** following an identical procedure as the one described for **AQP2**. **AQP3** was purified by column chromatography (SiO_2 , 1:5 EtOAc/dichloromethane (DCM), $R_f = 0.72$) to yield the final product (yellow-orange powder, 79.3 mg, 0.257 mmol, 52%). ^1H NMR (400 MHz, $(\text{CD}_3)_2\text{SO}$) / δ (ppm): 3.91 (3H, s), 4.46 (2H, s), 6.67 – 6.70 (2H, m), 6.82 (1H, d, $J = 8.0$ Hz), 7.02 (1H, t, $J = 8.0$ Hz), 7.07 (1H, d, $J = 8.0$ Hz), 7.19 (1H, d, $J = 8.0$ Hz), 7.41 (1H, t, $J = 8.0$ Hz), 8.04 (1H, d, $J = 12.0$ Hz), 8.34 (1H, d, $J = 12.0$ Hz), 9.66 (1H, s). ^{13}C NMR (100 MHz, $(\text{CD}_3)_2\text{SO}$) / δ (ppm): 40.3, 53.0, 105.8, 113.2, 115.5, 119.3, 121.6, 125.2, 128.4, 129.0, 130.8, 137.1, 137.7, 144.3, 145.5, 155.7, 165.6. HRMS Calcd for $\text{C}_{18}\text{H}_{17}\text{N}_2\text{O}_3$ $[\text{M}+\text{H}]^+$, 309.1239; found 309.1231

2.4.5. Preparation of 2-(((2-(Hydroxymethyl)quinolin-8-yl)amino)methyl)phenol (**AQP4**)

A solution of (8-aminoquinolin-2-yl)methanol (**AQ4**) (100 mg, 0.574 mmol) was utilized to prepare **AQP4** following an identical procedure as the one described for **AQP2**. **AQP4** was purified by column chromatography (SiO_2 , 1:1 EtOAc/Hx, $R_f = 0.50$) to yield the final product (light brown powder, 64.8 mg, 0.231 mmol, 40%). ^1H NMR (400 MHz, $(\text{CD}_3)_2\text{SO}$) / δ (ppm): 4.41 (2H, d, $J = 8.0$ Hz), 4.70 (2H, d, $J = 8.0$ Hz), 5.45 (1H, t, $J = 8.0$ Hz), 6.55 (1H, d, $J = 8.0$ Hz), 6.67 (1H, t, $J = 8.0$ Hz), 6.81 (1H, d, $J = 8.0$ Hz), 6.92 (1H, t, $J = 8.0$ Hz), 6.95 – 7.04 (2H, m), 7.16 (1H, d, $J = 8.0$ Hz), 7.22 (1H, t, $J = 8.0$ Hz), 7.53 (1H, d, $J = 8.0$ Hz), 8.15 (1H, d, $J = 12.0$ Hz), 9.56 (1H, s). ^{13}C NMR (100 MHz, $(\text{CD}_3)_2\text{SO}$) / δ (ppm):

41.9, 65.2, 105.2, 113.5, 115.4, 119.2, 119.6, 125.7, 127.5, 127.7, 128.1, 136.7, 136.9, 144.6, 155.6, 158.9. HRMS Calcd for $C_{17}H_{17}N_2O_2 [M+H]^+$, 281.1290; found 281.1280.

2.4.6. Preparation of 4-(Dimethylamino)-2-((quinolin-8-ylamino)methyl)phenol (AQDA1)

To a solution of dry EtOAc (5.0 mL) was added quinolin-8-amine (**AQ1**) (100 mg, 0.694 mmol). 5-(Dimethylamino)-2-hydroxybenzaldehyde (**DHB**) (115 mg, 0.694 mmol) was slowly added to the reaction mixture. The reaction mixture was then protected from the light and allowed to stir overnight for 24 h. After 24 h, the reaction mixture was concentrated and dried. To a solution of DCE (5.0 mL) was added sodium triacetoxyborohydride (212 mg, 1.39 mmol). The sodium triacetoxyborohydride solution was then slowly added to the dried reaction mixture and allowed to stir for 24 h (protected from the light). After 24 h, the reaction mixture was concentrated and dissolved in dry methanol. Sodium borohydride (150 mg, 3.97 mmol) was added to the reaction mixture at 0 °C and allowed to stir for 2 h. After 2 h, the reaction mixture was quenched with sodium bicarbonate and H_2O , extracted with DCM (3x), and purified by column chromatography (SiO_2 , 1:1 EtOAc/Hx, $R_f = 0.43$). The solid was recrystallized in DCM/Hx to afford the final product (light brown powder, 140 mg, 0.479 mmol, 69%). 1H NMR (400 MHz, $(CD_3)_2SO$) / δ (ppm): 2.63 (6H, s), 4.36 (2H, d, $J = 4.0$ Hz), 6.49 (1H, dd, $J = 8.0$ Hz, $J = 4.0$ Hz), 6.66 – 6.69 (2H, m), 6.74 (1H, d, $J = 4.0$ Hz), 6.79 (1H, t, $J = 8.0$ Hz), 7.01 (1H, d, $J = 8.0$ Hz), 7.29 (1H, t, $J = 8.0$ Hz), 7.46 (1H, dd, $J = 8.0$ Hz, $J = 4.0$ Hz), 8.16 (1H, dd, $J = 6.8$ Hz, $J = 8.4$ Hz), 8.69 (1H, dd, $J = 2.4$ Hz, $J = 4.0$ Hz), 8.83 (1H, s). ^{13}C NMR (100 MHz, $(CD_3)_2SO$) / δ (ppm): 41.8, 42.7, 105.2, 113.6, 113.7, 115.4, 116.0, 122.1, 125.9, 128.2, 128.7, 136.4, 138.0, 144.8, 145.0, 147.3, 147.6. HRMS Calcd for $C_{18}H_{19}N_3NaO [M+Na]^+$, 316.1426; found 316.1418.

2.4.7. Preparation of 4-(Dimethylamino)-2-(((2-methylquinolin-8-yl)amino)methyl)phenol (AQDA2)

A solution of 2-methylquinolin-8-amine (**AQ2**) (100 mg, 0.632 mmol) was utilized to prepare **AQDA2** following an identical procedure as the one described for **AQDA1**. **AQDA2** was purified by column chromatography (SiO_2 , 1:3 EtOAc/Hx, $R_f = 0.33$). The solid was recrystallized in EtOAc/Hx to afford the final product (light brown powder, 83.5 mg, 0.272 mmol, 43%). 1H NMR (400 MHz, $(CD_3)_2SO$) / δ (ppm): 2.63 (3H, s), 2.68 (6H, s), 4.38 (2H, d, $J = 8.0$ Hz), 6.53 (1H, dd, $J = 4.0$ Hz, $J = 8.0$ Hz), 6.64 (1H, t, $J = 8.0$ Hz), 6.68–6.73 (2H, m), 6.77 (1H, d, $J = 8.0$ Hz), 7.00 (1H, d, $J = 8.0$ Hz), 7.25 (1H, t, $J = 8.0$ Hz), 7.36 (1H, d, $J = 8.0$ Hz), 8.07 (1H, d, $J = 8.0$ Hz), 8.86 (1H, s). ^{13}C NMR (100 MHz, $(CD_3)_2SO$) / δ (ppm): 25.3, 41.9, 43.0, 105.4, 113.6, 113.7, 115.4, 116.0, 122.6, 125.9, 126.7, 127.1, 136.6, 137.4, 144.5, 144.8, 147.6, 155.6. HRMS Calcd for $C_{19}H_{22}N_3O [M+H]^+$, 308.1763 found 308.1762.

2.4.8. Preparation of Methyl 8-((5-(dimethylamino)-2-hydroxybenzyl)amino)quinoline-2-carboxylate (AQDA3)

To a solution of dry EtOAc (15 mL) was added methyl 8-aminoquinoline-2-carboxylate (**AQ3**) (100 mg, 0.494 mmol). 5-(Dimethylamino)-2-hydroxybenzaldehyde (**DHB**) (82.6 mg, 0.494 mmol) was slowly added to the reaction mixture. The reaction mixture was then protected from the light and allowed to stir overnight for 24 h. After 24 h, the reaction mixture was concentrated and dried. To a solution of DCE (15 mL) was added sodium triacetoxyborohydride (209 mg, 0.988 mmol). The sodium triacetoxyborohydride solution was then slowly added to the dried reaction mixture and allowed to stir for 24 h (protected from the light). After 24 h, the reaction mixture was concentrated and purified by column chromatography (SiO₂, 1:1 EtOAc/Hx, $R_f = 0.16$). The solid was recrystallized in EtOAc/Hx to afford the final product (yellow powder, 111 mg, 0.316 mmol, 64%). ¹H NMR (400 MHz, (CD₃)₂SO) / δ (ppm): 2.69 (6H, s), 3.99 (3H, s), 4.43 (2H, d, $J = 4.0$ Hz), 6.55 (1H, dd, $J = 9.0$ Hz, $J = 3.0$ Hz), 6.71 – 6.82 (4H, m), 7.13 (1H, d, $J = 8.0$ Hz), 7.47 (1H, t, $J = 8.0$ Hz), 8.06 (1H, d, $J = 8.0$ Hz), 8.38 (1H, d, $J = 9.0$ Hz), 8.92 (1H, s). ¹³C NMR (100 MHz, (CD₃)₂SO) / δ (ppm): 41.4, 42.4, 52.6, 105.6, 112.8, 113.4, 114.9, 115.7, 121.1, 124.9, 129.6, 130.4, 136.7, 137.2, 143.8, 144.3, 145.3, 147.2, 165.2. HRMS Calcd for C₂₀H₂₂N₃O₃ [M+H]⁺, 352.1661; found 352.1658.

2.4.9. A β Aggregation Experiments

All experiments were performed according to previously published methods.^{23,31,32,35} Prior to experiments, A β ₄₀ or A β ₄₂ was dissolved in ammonium hydroxide (NH₄OH, 1% v/v, aq), aliquoted, lyophilized overnight, and stored at –80 °C. For experiments described herein, a stock solution of A β was prepared by dissolving the lyophilized peptide in 1% NH₄OH (10 μ L) and diluting with ddH₂O. The concentration of the solution was determined by measuring the absorbance of the solution at 280 nm ($\epsilon = 1450$ M⁻¹cm⁻¹ for A β ₄₀ and $\epsilon = 1490$ M⁻¹cm⁻¹ for A β ₄₂). The peptide stock solution was diluted to a final concentration of 25 μ M in the Chelex-treated buffered solution containing HEPES [20 μ M; pH 7.4 (for metal-free and Zn(II) samples) pH 6.6 (for Cu(II) samples) and NaCl (150 μ M)]. For the inhibition studies,^{23,31,32,35} compound (final concentration 50 μ M, 1% v/v DMSO) was added to the sample of A β (25 μ M) in the absence and presence of a metal chloride salt (CuCl₂ or ZnCl₂; 25 μ M) followed by the incubation at 37 °C with constant agitation for 4, 8, and 24 h. For the disaggregation studies, A β with and without metal ions was incubated for 24 h at 37 °C with constant agitation prior to treatment with compound (50 μ M). The resulting samples containing A β , a metal chloride salt, and a compound were incubated at 37 °C with constant agitation for 4, 8, and 24 h.

2.4.10. Gel Electrophoresis with Western Blotting

The samples from the inhibition and disaggregation experiments were analyzed by gel electrophoresis with Western blot using anti-A β antibody (6E10).^{23,31,32,35} Each sample (10 μ L) was separated on a 10–20% Tris-tricine gel (Invitrogen, Grand Island, NY, USA). Following separation, the proteins were transferred onto nitrocellulose, which was blocked with bovine serum albumin (BSA, 3% w/v, RMBIO, Missoula, MT, USA) in Tris-buffered saline (TBS) containing 0.1% Tween-20 (TBS-T) for 4 h at room temperature. The membranes were incubated with antibody (6E10, 1:2000, Covance, Princeton, NJ, USA) in a solution of 2% BSA (w/v in TBS-T) overnight at 4 °C. After washing, the horseradish peroxidase-conjugated goat antimouse secondary antibody (1:5000) in 2% BSA was added for 1 h at room temperature. ThermoScientific SuperSignal West Pico Chemiluminescent Substrate (Thermo Scientific, Rockford, IL, USA), Biosesang ECL Plus kit (Biosesang, Gyeonggi-do, Republic of Korea), or a homemade ECL kit⁴¹ was used to visualize the results on a ChemiDoc MP Imaging System (Bio-Rad, Hercules, CA, USA).

2.4.11. Transmission Electron Microscopy (TEM)

Samples for TEM were prepared according to previously reported methods.^{23,31,32,35} Glow-discharged grids (Formar/Carbon 300-mesh, Electron Microscopy Sciences, Hatfield, PA, USA) were treated with A β samples from the inhibition and disaggregation experiments (5 μ L) for 2 min at room temperature. Excess sample was removed using filter paper followed by washing three times with ddH₂O. Each grid was incubated with uranyl acetate (1% w/v ddH₂O, 5 μ L, 1 min). Upon removal of excess uranyl acetate with filter paper, the grids were dried for at least 30 min at room temperature before measurement. Images from each sample were taken on a JEOL JEM-2100 transmission electron microscope (UNIST Central Research Facilities, Ulsan National Institute of Science and Technology, Ulsan, Republic of Korea) at 120 kV and 25,000x magnification.

2.4.12. 2D NMR Experiments

The interactions of A β ₄₀ monomer with AQ derivatives was interrogated by 2D band-Selective Optimized Flip-Angle Short Transient Heteronuclear Multiple Quantum Coherence (SOFAST-HMQC) NMR at 10 °C.⁴² Uniformly ¹⁵N-labeled A β ₄₀ (rPeptide, Bogart, GA, USA) was dissolved in 1% NH₄OH and lyophilized to ensure the absence of preformed aggregates. The peptide was re-dissolved in 3 μ L of DMSO-*d*₆ (Cambridge Isotope, Tewksbury, MA, USA) and diluted by buffer to a final peptide concentration of 80 μ M (20 mM PO₄, pH 7.4, 5 mM NaCl, 7% v/v D₂O). Each spectrum was obtained using 64 complex *t*₁ points and a 0.1 sec recycle delay on a Bruker Avance 600 MHz spectrometer

equipped with a cryoprobe. The data were processed using TOPSPIN 2.1 (Bruker) and assignment was performed using SPARKY 3.1134 using published assignments as a guide.⁴³⁻⁴⁵ Chemical shift perturbation (CSP) was calculated using the following equation:

$$\Delta\delta_{NH} = \sqrt{\Delta\delta_H^2 + \left(\frac{\Delta\delta_N}{5}\right)^2}$$

2.4.13. Docking Studies

Flexible ligand docking studies for **AQ** derivatives against the A β ₄₀ monomer from previously determined aqueous solution NMR structure (PDB 2LFM)⁴³ were conducted using AutoDock Vina.⁴⁶ 10 conformations were selected from 20 conformations within the Protein Databank (PDB) file (1, 3, 5, 8, 10, 12, 13, 16, 17, and 20). The MMFF94 energy minimization in ChemBio3D Ultra 11.0 was used to optimize the ligand structures for docking studies. The structural files of the **AQ** derivatives and the peptide were generated by AutoDock Tools and imported into PyRx,⁴⁷ which were used to run AutoDock Vina.⁴⁶ The search space dimensions were set to contain the entire peptide. The exhaustiveness for the docking runs was set to 1024. Docked poses of the ligand with A β were visualized using Pymol.

2.4.14. Ion Mobility–Mass Spectrometry

All nano-electrospray ionization MS (nESI–MS) combined with ion mobility-mass spectrometry (IM–MS) experiments were carried out on a Synapt G2 (Waters, Milford, MA).^{48,49} Samples were ionized using a nano-electrospray source operated in positive ion mode. MS instrumentation was operated at a backing pressure of 2.7 mbar and sample cone voltage of 40 V. Aliquots of A β ₄₀ peptides (final concentration, 20 μ M) were sonicated for 5 sec prior to pre-incubation with or without a source of Cu(II) (copper(II) acetate, 20 μ M) at 37 °C for 10 min. After pre-incubation, samples were titrated with or without ligand (**AQ1**, **AQ4**, **AQP1**, **AQP4**, **AQDA1-3**, or **ML**; final concentrations: 20, 40, 80, and 120 μ M) and incubated at 37 °C for 30 min prior to analysis. Solution conditions were 100 mM ammonium acetate (pH 7.5) with 1% v/v DMSO. For control purposes, all data are compared to incubations of A β ₄₀ peptides with **EGCG** under the same conditions.³⁵ Collision cross-section (CCS) measurements were externally calibrated using a database of known values in helium, with values for proteins that bracket the likely CCS and ion mobility values of the unknown ions.^{34,50} CCS values are the mean average of five replicates with errors reported as the least square product. This least square analysis combines inherent calibrant error from drift tube measurements (3%),⁵⁰ calibration curve error, and twice the replicate

standard deviation error. Determination of the amount of Cu(II) bound to A β ₄₀ was calculated using the total ion count extracted from the peak of interest at its full width half maximum using methods previously described.⁵¹ All other conditions are consistent with previously published methods.³²

2.4.15. Metal Binding Experiments

Metal binding properties of **AQ1-3**, **AQP1-4**, and **AQDA1-3** were investigated by UV-vis and ¹H NMR. UV-vis experiments were carried out in acetonitrile (for **AQ2** and **AQP3**) or a Chelex-treated buffered solution containing 20 mM HEPES, pH 7.4, and 150 mM NaCl. To a solution of ligand, CuCl₂ or ZnCl₂ was titrated up to 10 equiv at room temperature. The solutions were allowed to equilibrate before further addition of CuCl₂ or ZnCl₂. Zn(II) binding to **AQ3** was probed by ¹H NMR by slowly titrating up to 3.5 equiv of ZnCl₂ (17.5 mM) at room temperature in CD₃CN. To examine the metal selectivity of **AQP4** and **AQDA1-3** for Cu(II), 1 or 20 equiv of MgCl₂, CaCl₂, MnCl₂, FeCl₂, CoCl₂, NiCl₂, and ZnCl₂ were first treated to a solution containing 50 μ M ligand (**AQP4** and **AQDA1-3**). The spectra were recorded after 10 min incubation at room temperature. The Fe(II) samples were prepared in an anaerobic N₂-filled glove box. CuCl₂ (50 μ M) was then added to a solution of compound and a divalent metal chloride salt. The spectra were taken after an additional 10 min incubation period at room temperature. Quantification of metal selectivity was calculated by comparing and normalizing the absorption values of metal–ligand complexes at 290 (for **AQP4**), 440 (for **AQDA1** and **AQDA2**), and 338 nm (for **AQDA3**) to the absorption at these wavelengths before and after the addition of CuCl₂ (A_M/A_{Cu}).

2.4.16. Solution Speciation Studies

The p*K*_a values for **AQP1**, **AQP4**, and **AQDA1-3** were determined through UV-vis variable-pH titrations based on a previously reported procedure.^{23,31,32,35} To obtain p*K*_a values for the ligands (50 μ M for **AQP4** or **AQDA1**; 25 μ M for **AQP1**, **AQDA2**, or **AQDA3**), HCl was titrated into the speciation solution (100 mM NaCl, pH 12, 10 mM NaOH) in small aliquots to obtain at least 30 spectra in the range of pH 2–11 (for **AQP1** and **AQP4**) or pH 2–10 (for **AQDA1-3**). In addition, to investigate Cu(II) binding to the ligands at various pHs, small aliquots of HCl were titrated into the solutions containing a ligand and a metal chloride salt [[M(II)]:[L] = 1:2; [CuCl₂] = 50 (for **AQP4**), 12.5 (for **AQDA1** and **AQDA2**), and 25 μ M (for **AQP1** and **AQDA3**)]. At least 30 spectra were measured over the range of pH 2–8. The acidity and stability constants were calculated by using the HypSpec program (Protonic Software, Leeds, UK).^{52,53}

2.4.17. 2-Deoxyribose Assay

The ability of **AQ1**, **AQ3**, **AQ4**, **AQDA1**, and **AQDA3** to suppress the generation of hydroxyl radicals was determined by the 2-deoxyribose assay. The assay was performed based on previously reported methods.^{23,36} Chelexed solutions were used, and reactions (total volume, 200 μ L) were prepared by mixing, in the following order, buffer (50 mM NaH_2PO_4 , pH 7.4), ligand (125 μ M), CuCl_2 (10 μ M), 2-deoxy-D-ribose (15 mM), H_2O_2 (200 μ M), and sodium ascorbate (2 mM) and allowed to react for 1 h at 37 $^\circ\text{C}$ with constant agitation. The reactions were quenched upon addition of trichloroacetic acid (200 μ L of 2.8% m/v) and 2-thiobarbituric acid (200 μ L of 1% w/v). After quenching, the reactions were heated at 100 $^\circ\text{C}$ for 20 min, then allowed to cool for 5 min prior to measurement of their absorbance values at 532 nm. Samples without ligand were prepared as a control. Experiments were performed in triplicates. Normalized absorbance values (A/A_0) were calculated by taking the absorbance (A) and dividing by the absorbance of the control (A_0).

2.4.18. Trolox Equivalent Antioxidant Capacity (TEAC) Assay

The antioxidant activity of **AQ1-3**, **AQP1-2**, **AQP4**, and **AQDA1-3** was determined by the TEAC assay using human neuroblastoma SK-N-BE(2)-M17 (M17) cell lysates and was conducted according to a protocol of the antioxidant assay kits purchased from Cayman Chemical Company (Ann Arbor, MI, USA) with minor modifications. The cell line purchased from ATCC (Manassas, VA, USA) was maintained in media containing 1:1 minimum Essential Media (MEM, GIBCO) and Ham's F12K Kaighn's Modification Media (F12K, GIBCO), 10% (v/v) fetal bovine serum (FBS, GIBCO), 100 U/mL penicillin (GIBCO), and 100 mg/mL streptomycin (GIBCO). The cells were grown and maintained at 37 $^\circ\text{C}$ in a humidified atmosphere with 5% CO_2 . The cells were seeded in a 6 well plate and grown to approximately 80-90% confluence. Cell lysates were prepared following a previously reported method with modifications.⁵⁴ M17 cells were washed once with cold PBS (pH 7.4, GIBCO) and harvested by gently pipetting off adherent cells with cold PBS. A cell pellet was generated by centrifugation (2,000 g for 10 min at 4 $^\circ\text{C}$). This cell pellet was sonicated on ice (5 sec pulses five times with 20 sec intervals between each pulse) in 2 mL of cold Assay Buffer [5 mM potassium phosphate (pH 7.4) containing 0.9% NaCl and 0.1% glucose]. The cell lysates were centrifuged at 10,000 g for 10 min at 4 $^\circ\text{C}$. The supernatant was removed and stored on ice until use. To a standard sample 96 microplate, 10 μ L of the supernatant cell lysates was delivered followed by addition of compound, metmyoglobin (2.5 μ M), ABTS (165 μ M), and H_2O_2 (82.4 μ M) in order. Compound concentration ranges utilized were as follows: Trolox (45, 90, 135, 180, 225, and 330 μ M); **AQ1**, **AQ3**, **AQP4**, **AQDA1**, and **AQDA2** (30, 50, 70, 90, 110, and 135 μ M); **AQ2** (30, 70, 110, 150, 190, and 255 μ M); **AQP1** and **AQP2** (20, 40, 60, 80, 100, and 120

μM); **AQDA3** (30, 60, 90, 120, 150, and 180 μM). After 5 min incubation at room temperature on a shaker, absorbance values at 750 nm were recorded. The percent inhibition was calculated according to the measured absorbance (% inhibition = $(A_0 - A)/A_0$, where A_0 is the absorbance of the supernatant of cell lysates) and was plotted as a function of compound concentration. The TEAC value of ligands was calculated as a ratio of the slope of the standard curve of the compound to that of Trolox. The measurements were conducted in triplicate.

2.4.19. Parallel Artificial Membrane Permeability Adapted for the Blood-Brain Barrier (PAMPA-BBB) Assay

PAMPA-BBB experiments were carried out using the PAMPA Explorer kit (pION Inc., Billerica, MA, USA) with modifications to previously reported protocols.^{23,25,26,55} Each stock solution was diluted with Prisma HT buffer (pH 7.4, pION) to a final concentration of 25 μM (1% v/v final DMSO concentration). The resulting solution was added to wells of the donor plate (200 μL , 12 replicates). BBB-1 lipid formulation (5 μL , pION) was used to coat the polyvinylidene fluoride (PVDF, 0.45 mM) filter membrane on the acceptor plate. This acceptor plate was placed on top of the donor plate forming a sandwich. Brain sink buffer (BSB, 200 μL , pION) was added to each well of the acceptor plate. The sandwich was incubated for 4 h at ambient temperature without stirring. UV-vis spectra of the solutions in the reference, acceptor, and donor plates were measured using a microplate reader. The PAMPA Explorer software v. 3.5 (pION) was used to calculate $-\log P_e$ for each compound. CNS \pm designations were assigned by comparison to compounds that were identified in previous reports.^{25,26,55}

2.4.20. Cell Viability Measurements

The mouse Neuro-2a (N2a) neuroblastoma cell line was purchased from the American Type Cell Collection (ATCC, Manassas, VA, USA). Cells were maintained in media containing 1:1 DMEM (GIBCO, Grand Island, NY, USA) and opti-MEM (GIBCO), supplemented with 5% (v/v) fetal bovine serum (FBS; GIBCO), 1% (v/v) L-glutamine (GIBCO), 100 U/mL penicillin, and 100 mg/mL streptomycin (GIBCO). The cells were grown and maintained at 37 °C in a humidified atmosphere with 5% CO₂. Cell viability upon treatment of compounds was determined by the MTT assay [MTT = 3-(4,5-dimethyl-2-thiazolyl)-2,5-diphenyl-2H-tetrazolium bromide, Sigma-Aldrich]. N2a cells were seeded in a 96 well plate (15,000 cells in 100 μL per well). The cells were treated with compounds (5 or 10 μM , 1% v/v final DMSO concentration) with or without CuCl₂ or ZnCl₂ (5 or 10 μM), and incubated for 24 h with the cells. After incubation, MTT [25 μL ; 5 mg / mL in phosphate buffered saline (PBS, pH 7.4, GIBCO)] was added to each well and the plate was incubated for 4 h at 37 °C. Formazan produced by the cells was

solubilized using an acidic solution of *N,N*-dimethylformamide (DMF, 50%, v/v aq) and sodium dodecyl sulfate (SDS, 20%, w/v) overnight at room temperature in the dark. The absorbance was measured at 600 nm using a microplate reader. Cell viability was calculated relative to cells treated with an equivalent amount of DMSO. All Experiments were performed in triplicate.

2.5. Acknowledgments

This work was supported by the University of Michigan Protein Folding Disease Initiative (to A.R., B.T.R., and M.H.L.) and the National Research Foundation of Korea (NRF) grant funded by the Korean government [NRF-2014S1A2A2028270 (to M.H.L. and A.R.); NRF-2014R1A2A2A01004877 (to M.H.L.)]; the 2016 Research Fund (Project Number 1.160001.01) of Ulsan National Institute of Science and Technology (UNIST). J.K. thanks the support from the Global Ph.D. fellowship program through the National Research Foundation of Korea (NRF) funded by the Ministry of Education (NRF-2015HIA2A1030823).

2.6. References

- (1) Guzior, N.; Wieckowska, A.; Panek, D.; Malawska, B. *Curr. Med. Chem.* **2015**, *22*, 373–404.
- (2) Perez, L. R.; Franz, K. J. *Dalton Trans.* **2010**, *39*, 2177–2187.
- (3) Zatta, P.; Drago, D.; Bolognin, S.; Sensi, S. L. *Trends Pharmacol. Sci.* **2009**, *30*, 346–355.
- (4) Duce, J. A.; Bush, A. I. *Prog. Neurobiol.* **2010**, *92*, 1–18.
- (5) Haass, C.; Selkoe, D. J. *Nat. Rev. Mol. Cell Biol.* **2007**, *8*, 101–112.
- (6) Jakob-Roetne, R.; Jacobsen, H. *Angew. Chem. Int. Ed.* **2009**, *48*, 3030–3059.
- (7) Scott, L. E.; Orvig, C. *Chem. Rev.* **2009**, *109*, 4885–4910.
- (8) Miller, Y.; Ma, B.; Nussinov, R. *Chem. Rev.* **2010**, *110*, 4820–4838.
- (9) Telpoukhovskaia, M. A.; Orvig, C. *Chem. Soc. Rev.* **2013**, *42*, 1836–1846.
- (10) Jensen, M.; Canning, A.; Chiha, S.; Bouquerel, P.; Pedersen, J. T.; Østergaard, J.; Cuvillier, O.; Sasaki, I.; Hureau, C.; Faller, P. *Chem. Eur. J.* **2012**, *18*, 4836–4839.
- (11) Kepp, K. P. *Chem. Rev.* **2012**, *112*, 5193–5239.
- (12) Derrick, J. S.; Lim, M. H. *ChemBioChem* **2015**, *16*, 887–898.
- (13) Corbett, A.; Pickett, J.; Burns, A.; Corcoran, J.; Dunnett, S. B.; Edison, P.; Hagan, J. J.; Holmes, C.; Jones, E.; Katona, C.; Kearns, I.; Kehoe, P.; Mudher, A.; Passmore, A.; Shepherd, N.; Walsh, F.; Ballard, C. *Nat. Rev. Drug Discovery* **2012**, *11*, 833–846.
- (14) Rodríguez-Rodríguez, C.; Telpoukhovskaia, M.; Orvig, C. *Coord. Chem. Rev.* **2012**, *256*, 2308–2332.

- (15) Schugar, H.; Green, D. E.; Bowen, M. L.; Scott, L. E.; Storr, T.; Bohmerle, K.; Thomas, F.; Allen, D. D.; Lockman, P. R.; Merkel, M.; Thompson, K. H.; Orvig, C. *Angew. Chem. Int. Ed.* **2007**, *46*, 1716–1718.
- (16) Lincoln, K. M.; Offutt, M. E.; Hayden, T. D.; Saunders, R. E.; Green, K. N. *Inorg. Chem.* **2014**, *53*, 1406–1416.
- (17) Lincoln, K. M.; Gonzalez, P.; Richardson, T. E.; Julovich, D. A.; Saunders, R.; Simpkins, J. W.; Green, K. N. *Chem. Commun.* **2013**, *49*, 2712–2714.
- (18) Lincoln, K. M.; Richardson, T. E.; Rutter, L.; Gonzalez, P.; Simpkins, J. W.; Green, K. N. *ACS Chem. Neurosci.* **2012**, *3*, 919–927.
- (19) Otto, R.; Penzis, R.; Gaube, F.; Adolph, O.; Foehr, K. J.; Warncke, P.; Robaa, D.; Appenroth, D.; Fleck, C.; Enzensperger, C.; Lehmann, J.; Winckler, T. *J. Med. Chem.* **2015**, *58*, 6710–6715.
- (20) Telpoukhovskaia, M. A.; Cawthray, J. F.; Rodríguez-Rodríguez, C.; Scott, L. E.; Page, B. D.; Patrick, B. O.; Orvig, C. *Bioorg. Med. Chem. Lett.* **2015**, *25*, 3654–3657.
- (21) Storr, T.; Merkel, M.; Song-Zhao, G. X.; Scott, L. E.; Green, D. E.; Bowen, M. L.; Thompson, K. H.; Patrick, B. O.; Schugar, H. J.; Orvig, C. *J. Am. Chem. Soc.* **2007**, *129*, 7453–7463.
- (22) Wang, Z.; Wang, Y.; Li, W.; Mao, F.; Sun, Y.; Huang, L.; Li, X. *ACS Chem. Neurosci.* **2014**, *5*, 952–962.
- (23) Lee, S.; Zheng, X.; Krishnamoorthy, J.; Savelieff, M. G.; Park, H. M.; Brender, J. R.; Kim, J. H.; Derrick, J. S.; Kochi, A.; Lee, H. J.; Kim, C.; Ramamoorthy, A.; Bowers, M. T.; Lim, M. H. *J. Am. Chem. Soc.* **2014**, *136*, 299–310.
- (24) Savelieff, M. G.; DeToma, A. S.; Derrick, J. S.; Lim, M. H. *Acc. Chem. Res.* **2014**, *47*, 2475–2482.
- (25) Di, L.; Kerns, E. H.; Fan, K.; McConnell, O. J.; Carter, G. T. *Eur. J. Med. Chem.* **2003**, *38*, 223–232.
- (26) Avdeef, A.; Bendels, S.; Di, L.; Faller, B.; Kansy, M.; Sugano, K.; Yamauchi, Y. *J. Pharm. Sci.* **2007**, *96*, 2893–2909.
- (27) Lim, M. H.; Wang, B. A.; Pitcock, W. H.; Mokshagundam, D.; Baik, M.-H.; Lippard, S. J. *J. Am. Chem. Soc.* **2006**, *128*, 14364–14373.
- (28) Waibel, M.; Hasserodt, J. *Tetrahedron Lett.* **2009**, *50*, 2767–2769.
- (29) Roth, R.; Erlenmeyer, H. *Helv. Chim. Acta* **1954**, *37*, 1064–1068.
- (30) Shaffer, K. J.; Davidson, R. J.; Burrell, A. K.; McCleskey, T. M.; Plieger, P. G. *Inorg. Chem.* **2013**, *52*, 3969–3975.
- (31) Derrick, J. S.; Kerr, R. A.; Nam, Y.; Oh, S. B.; Lee, H. J.; Earnest, K. G.; Suh, N.; Peck, K. L.;

- Ozbil, M.; Korshavn, K. J.; Ramamoorthy, A.; Prabhakar, R.; Merino, E. J.; Shearer, J.; Lee, J.-Y.; Ruotolo, B. T.; Lim, M. H. *J. Am. Chem. Soc.* **2015**, *137*, 14785–14797.
- (32) Beck, M. W.; Oh, S. B.; Kerr, R. A.; Lee, H. J.; Kim, S. H.; Kim, S.; Jang, M.; Ruotolo, B. T.; Lee, J.-Y.; Lim, M. H. *Chem. Sci.* **2015**, *6*, 1879–1886.
- (33) Hernandez, H.; Robinson, C. V. *Nat. Protoc.* **2007**, *2*, 715–726.
- (34) Ruotolo, B. T.; Benesch, J. L. P.; Sandercock, A. M.; Hyung, S.-J.; Robinson, C. V. *Nat. Protoc.* **2008**, *3*, 1139–1152.
- (35) Hyung, S.-J.; DeToma, A. S.; Brender, J. R.; Lee, S.; Vivekanandan, S.; Kochi, A.; Choi, J.-S.; Ramamoorthy, A.; Ruotolo, B. T.; Lim, M. H. *Proc. Natl. Acad. Sci. U.S.A.* **2013**, *110*, 3743–3748.
- (36) Charkoudian, L. K.; Pham, D. M.; Franz, K. J. *J. Am. Chem. Soc.* **2006**, *128*, 12424–12425.
- (37) Re, R.; Pellegrini, N.; Proteggente, A.; Pannala, A.; Yang, M.; Rice-Evans, C. *Free Radical Biol. Med.* **1999**, *26*, 1231–1237.
- (38) Puskullu, M. O.; Tekiner, B.; Süzen, S. *Mini Rev. Med. Chem.* **2013**, *13*, 365–372.
- (39) Havsteen, B. H. *Pharmacol. Ther.* **2002**, *96*, 67–202.
- (40) Rice-Evans, C.; Miller, N. J.; Paganga, G. *Free Radical Biol. Med.* **1996**, *20*, 933–956.
- (41) Mruk, D. D.; Cheng, C. Y. *Spermatogenesis* **2011**, *1*, 121–122.
- (42) Schanda, P.; Brutscher, B. *J. Am. Chem. Soc.* **2005**, *127*, 8014–8015.
- (43) Vivekanandan, S.; Brender, J. R.; Lee, S. Y.; Ramamoorthy, A., *Biochem. Biophys. Res. Commun.* **2011**, *411*, 312–316.
- (44) Yoo, S. I.; Yang, M.; Brender, J. R.; Vivekanandan, S.; Sun, K.; Joo, N. E.; Jeong, S.-H.; Ramamoorthy, A.; Kotov, N. A. *Angew. Chem. Int. Ed.* **2011**, *50*, 5110–5115.
- (45) Fawzi, N. L.; Ying, J.; Torchia, D. A.; Clore, G. M. *J. Am. Chem. Soc.* **2010**, *132*, 9948–9951.
- (46) Trott, O.; Olson, A. J. *J. Comput. Chem.* **2010**, *31*, 455–461
- (47) Wolf, C. K. *Chem. Eng. News*, **2009**, *87*, 31.
- (48) Giles, K.; Williams, J. P.; Campuzano, I. *Rapid Commun. Mass Spectrom.* **2011**, *25*, 1559–1566.
- (49) Zhong, Y.; Hyung, S.-J.; Ruotolo, B. T., *Analyst* **2011**, *136*, 3534–3541.
- (50) Bush, M. F.; Hall, Z.; Giles, K.; Hoyes, J.; Robinson, C. V.; Ruotolo, B. T. *Anal. Chem.* **2010**, *82*, 9557–9565.
- (51) Soper, M. T.; DeToma, A. S.; Hyung, S.-J.; Lim, M. H.; Ruotolo, B. T. *Phys. Chem. Chem. Phys.* **2013**, *15*, 8952–8961.
- (52) Gans, P.; Sabatini, A.; Vacca, A. *Ann. Chim.* **1999**, *89*, 45–49.
- (53) Alderighi, L.; Gans, P.; Lenco, A.; Peters, D.; Sabatini, A.; Vacca, A. *Coord. Chem. Rev.* **1999**,

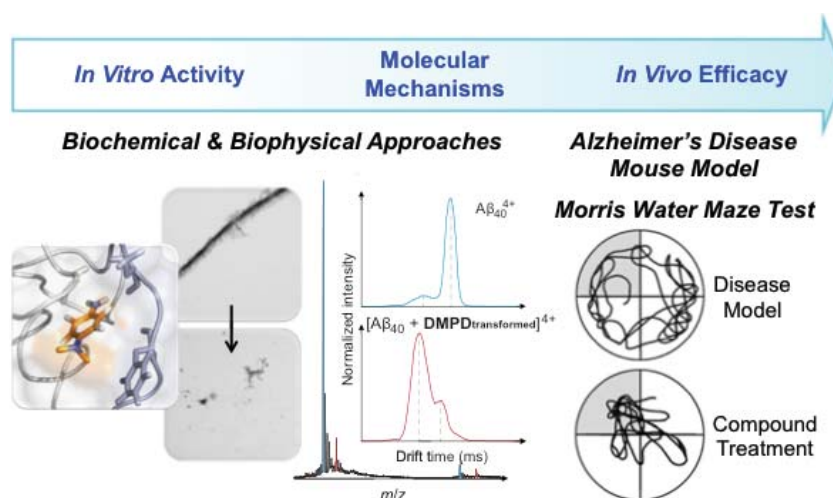
184, 311–318.

(54) Spencer, V. A.; Sun, J.-M.; Li, L.; Davie, J. R. *Methods* **2003**, *31*, 67–75.

(55) *BBB Protocol and Test Compounds*; pION Inc.: Woburn, MA, 2009.

Chapter 3.

A Redox-Active, Compact Molecule for Cross-Linking Amyloidogenic Peptides into Nontoxic, Off-Pathway Aggregates: *In Vitro* and *In Vivo* Efficacy and Molecular Mechanisms



The results presented in this chapter were previously published (Derrick, J. S.; Kerr, R. A.; Nam, Y.; Oh, S. B.; Lee, H. J.; Earnest, K. G.; Suh, N.; Peck, K. L.; Ozbil, M.; Korshavn, K. J.; Ramamoorthy, A.; Prabhakar, R.; Merino, E. J.; Shearer, J.; Lee, J.-Y.; Ruotolo, B. T.; Lim, M. H. *J. Am. Chem. Soc.*, **2015**, *137*, 14785–14797). I thank Professor Brandon T. Ruotolo and Dr. Richard A. Kerr for the MS studies, Professor Joo-Yong Lee, Shin Bi Oh, and Nayoung Suh for *in vivo* analysis, Professor Jason Shearer and Kristy L. Peck for XAS measurements, Professor Merino and Kaylin G. Earnest for metabolic stability assessment, Professor Prabhakar and Dr. Mehmet Ozbil for molecular dynamics simulations, and Professor Ayyalusamy Ramamoorthy and Kyle J. Korshavn for 2D NMR assistance. Younwoo Nam and Hyuck Jin Lee were involved in the gel/Western blot, UV-vis, and TEM experiments. I was instrumental in the design and performance of experiments as well as the writing of the manuscript with the assistance of Professor Lim.

3.1. Introduction

Alzheimer's disease (AD), the most common form of all neurodegenerative diseases, has continued to expand in prevalence and remains unabated due to an inadequate understanding of disease pathology, which has significantly impaired efforts to establish effective strategies against the disorder.¹⁻⁴ As such, fatalities resulting from this deadly malady have continued to increase to the point where today, almost one third of every senior citizen will be affected by AD or a related form of dementia.⁵ The costs associated with providing the long-term care and resources required by those suffering from AD have also reached staggering levels. This year alone, AD will cost the United States 226 billion dollars, and without intervention, this figure is expected to reach 1.1 trillion by 2050.⁵ Therefore, it is clear that if this trend is to be suppressed, we must develop a more detailed, molecular-level understanding of the convoluted and multilayered pathology of AD, which will then be able to provide the foundation toward the generation of new strategies against the disease.

Illumination of the molecular mechanisms underlying AD is further obstructed by the absence of completely accurate model systems from which to study the ailment. For example, *in vitro* analyses often require the experimentalist to narrow the scope of their study to a few potential players (*e.g.*, misfolded proteins) and often deviate from physiological relevancy.¹⁻⁴ Similarly, *in vivo* studies are limited by the absence of accurate models that fully mimic human AD.⁶ Due to these inherent complexities along with the impossibility of addressing every potential factor contributing toward neuronal death in a single report, we have chosen to focus our investigation on the amyloid- β (A β) peptide, a hallmark of the disease which is known to aggregate to form characteristic senile plaques, and its interplay with metal ions [*e.g.*, Cu(II), Zn(II)].^{1-4,7-14} Metal ions were incorporated into our studies because of their extensively explored involvement in the facilitation of A β aggregation pathways and generation of reactive oxygen species (ROS) *via* Fenton-like reactions *in vitro*.^{2-4,7-14} It is important, however, that we specify that by focusing our analysis on the aggregation and interaction of A β and metal ions, we are not implying that these are the sole causes of the disorder.

The evidence suggesting that A β is implicated in the pathology of AD is incontrovertible.^{1-4,7-14} For example, A β oligomer load has been closely correlated with cognitive impairment and behavioral tests in transgenic AD mouse models.^{1,3} Furthermore, multiple cell and transgenic mouse studies have clearly identified A β as a contributor to the diminished mitochondrial function observed in AD.³ A β has also been indicated to induce kinases responsible for the phosphorylation of tau protein and the subsequent destabilization of microtubules.³ These findings are only a small number of the available reports that implicate A β in AD. The mechanisms by which A β may induce cellular death, however, have not been fully understood. In order to advance our understanding of these pathways, the use of chemical tools,

capable of elucidating the mechanism of these processes at the molecular level, will be of indispensable value.^{2,4,14-22}

To this end, we present a redox-active, compact amine derivative, **DMPD** (*N,N*-dimethyl-*p*-phenylenediamine; Figure 3.2a), as a novel chemical tool for redirecting both metal-free A β and metal-A β peptides into nontoxic, off-pathway peptide aggregates, *via* an approach mediated by intramolecular crosslinks between compound and peptide. Our strategy, the generation of covalently linked adducts composed of aggregation-prone peptides, was inspired by a recent study suggesting a covalent bond between catechol-type flavonoids and A β .^{23,24} In a previous report, a well-known, redox-active compound, **DMPD**,²⁵⁻²⁷ was indicated as a potential molecule of interest, among many others, in a brief calculation focused screening method and a fluorescence-based assay [*i.e.*, thioflavin-T (ThT) assay].²⁸ Unfortunately, in addition to spectral interference between **DMPD** and ThT, making results of the assay inconclusive, the report did not present whether **DMPD** influences the A β aggregation pathways with elucidation of a mechanistic understanding of its activity with the peptide.²⁸ Through our present studies, we demonstrate the ability of **DMPD** to redirect both metal-free and metal-induced A β aggregation pathways and consequently produce less toxic, off-pathway amorphous aggregates. Biophysical analyses and molecular dynamics (MD) simulations indicate molecular-level interactions of **DMPD** with both metal-free A β and metal-A β *in vitro* as well as its potential mechanism, based on the formation of intramolecular crosslinks between transformed **DMPD** and A β , for redirecting the peptide aggregation. Finally, the efficacy of our approach in biological settings [*e.g.*, living cells, *in vivo* (*i.e.*, the AD 5 \times FAD mouse model)²⁹] was investigated. Treatment with **DMPD** mitigates A β -/metal-A β -induced toxicity in living cells and reduces the overall cerebral amyloid levels in 5 \times FAD mice. Additionally, cognitive defects of 5 \times FAD mice, as evaluated by the Morris water maze task, are significantly improved upon **DMPD** administration. Taken together, our *in vitro* and *in vivo* studies of a redox-active small molecule, along with the molecular-level mechanistic elucidation, illustrate that the strategy to generate A β -small molecule adducts could be an effective tactic to control and promote the formation of relatively less toxic, off-pathway aggregates.

3.2. Results and Discussion

3.2.1. Rational Selection of DMPD Toward Redirecting Both Metal-free and Metal-induced A β Aggregation *In Vitro* and in Biological Systems

Although **DMPD** is a compact, simple compound, its structure (Figure 3.2a) includes moieties, suggested to be potentially essential for interactions with metal-free A β , metal-A β , and metal ions.^{2,4,14-16}

Table 3.1. Brain uptake and antioxidant properties of **DMPD**.

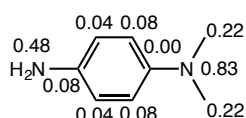
Calculation ^a	DMPD	Lipinski's rules and others
MW	136	≤ 450
clogP	1.08	≤ 5.0
HBA	2	≤ 10
HBD	2	≤ 5
PSA	29.3	≤ 90
logBB	-0.139	> 3.0 (readily) < -1.0 (poorly)
PAMPA-BBB assay		
logP _e ^b	5.0 ± 0.2 (CNS+)	-logP _e < 5.4 (CNS+) -logP _e > 5.7 (CNS-)
TEAC assay	DMPD	Trolox
Value ^c	1.05 (±0.04)	1.00 (±0.02)

^aMW, molecular weight; clogP, calculated logarithm of the octanol–water partition coefficient; HBA, hydrogen bond acceptor atoms; HBD, hydrogen bond donor atoms; PSA, polar surface area; logBB = $-0.0148 \text{ \AA} \times \text{PSA} + 0.152 \text{ \AA} \times \text{clogP} + 0.139$ (logBB > 3.0, readily crosses BBB; logBB < -1.0, poorly distributed to the brain); -logP_e values were determined using the Parallel Artificial Membrane Permeability Assay (PAMPA), and average -logP_e values were then calculated by the PAMPA 9 Explorer software v. 3.5. ^bPrediction of a compound's ability to penetrate the central nervous system (CNS) on the basis of literature values. Compounds categorized as CNS+ possess the ability to penetrate the BBB and are available in the CNS. Compounds assigned as CNS- have poor permeability through the BBB; therefore, their bioavailability into the CNS is considered to be minimal. ^cAntioxidant activity of **DMPD**, identified by the TEAC assay in EtOH. The TEAC value is relative to a vitamin E analogue, Trolox (6-hydroxy-2,5,7,8-tetramethylchroman-2-carboxylic acid).

The overall redox and structural characteristics of **DMPD** could indicate its direct interactions with both metal-free Aβ or metal–Aβ, as well as its subsequent ability to redirect peptide aggregation pathways *via* the generation of covalently linked adducts between compound and Aβ, as previously presented for catechol-type flavonoids.^{23,24} In addition, **DMPD** is shown to be biologically compatible based on our investigations. First, **DMPD** is potentially blood-brain barrier permeable and has antioxidant activity similar to that of a water-soluble vitamin E analogue, Trolox (Table 3.1). Secondly, as presented in Figure 3.1, in phosphate buffered saline (PBS), **DMPD** is relatively stable with an approximate half-life (*t*_{1/2}) of one day. Addition of hydrogen peroxide, however, leads to oxidation of **DMPD** (its cationic radical²⁵⁻²⁷) with a *t*_{1/2} value of 55 min. Lastly, **DMPD** has relative metabolic stability. Using FAME software,³⁰ the sites of metabolism were predicted showing the alkylate aniline nitrogen as a site of metabolism reaction

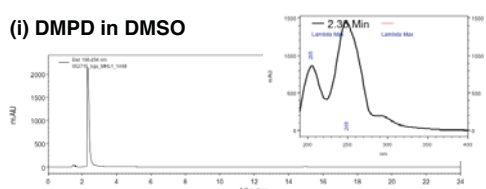
(Figure 3.1a). The metabolic stability of **DMPD** was also further analyzed employing human liver microsomes. We observed classic enzyme kinetics showing that the metabolic processing is between 30 min and 120 min [$t_{1/2} = 107$ min ($[\text{DMPD}] = 0.5$ mM); V_{\max} , *ca.* 22.9 nM/min; K_M , *ca.* 2.07 mM; Figure 3.1]. Overall, **DMPD** is indicated to have moderate metabolic stability, as well as could be administered for its applications *in vivo* since its concentration would be much lower than the 2.07 mM K_M for liver microsomes.

(a) FAME calculation of **DMPD**^a

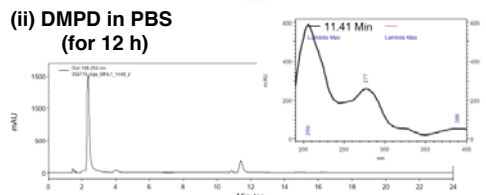


(b) Stability of **DMPD** in solution

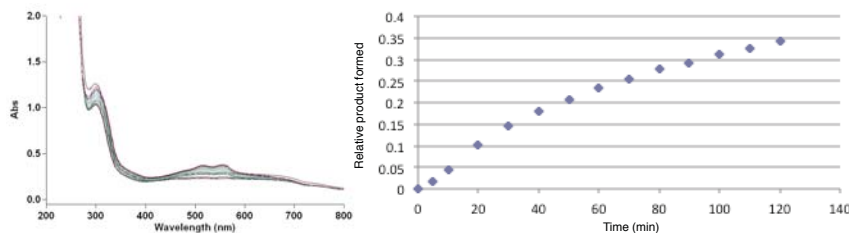
(i) **DMPD** in DMSO



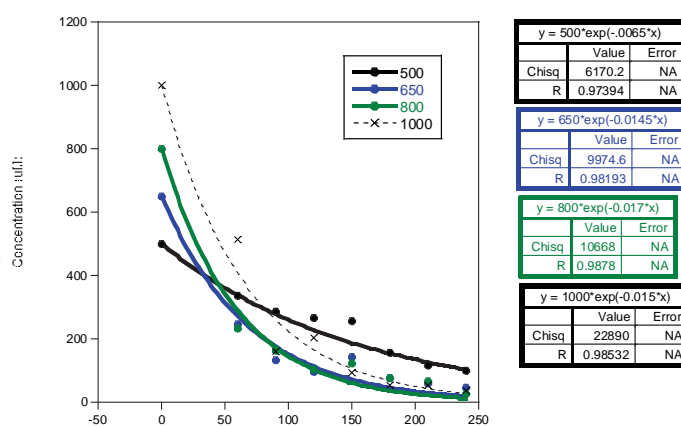
(ii) **DMPD** in PBS (for 12 h)



(c) Oxidation of **DMPD** by hydrogen peroxide in PBS



(d) Degradation of **DMPD** in liver microsomes



Lineweaver-Burk analysis

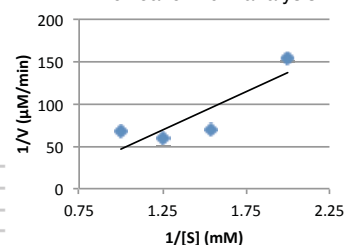


Figure 3.1. Solution and metabolic stability of **DMPD**. (a) FAME calculation of **DMPD**. ^aPredicts the sites of metabolism, the atom where a metabolic reaction is initiated. The number reported is the probability of each atom being a site of metabolism. Therefore, the closer the number is to one, the more likely that atom is a site of metabolism [see Kirchmair, J. *et al.*, *J. Chem. Inf. Model* **2013**, *53*, 2896–2907]. (b) Stability of **DMPD** in DMSO and PBS. **DMPD** is shown to be degraded by *ca.* 20% in PBS for 12 h. (c) Oxidation of **DMPD** by hydrogen peroxide (H_2O_2) in PBS ($t_{1/2} = 55$ min). Conditions: **DMPD** (0.5 mM); H_2O_2 (5 mM); pseudo-first order kinetics. (d) Metabolic stability of **DMPD** using liver microsomes. Based on Lineweaver–Burk analysis, the values of V_{\max} and K_M (*ca.* 22.9 nM/min and *ca.* 2.07 mM, respectively) are obtained.

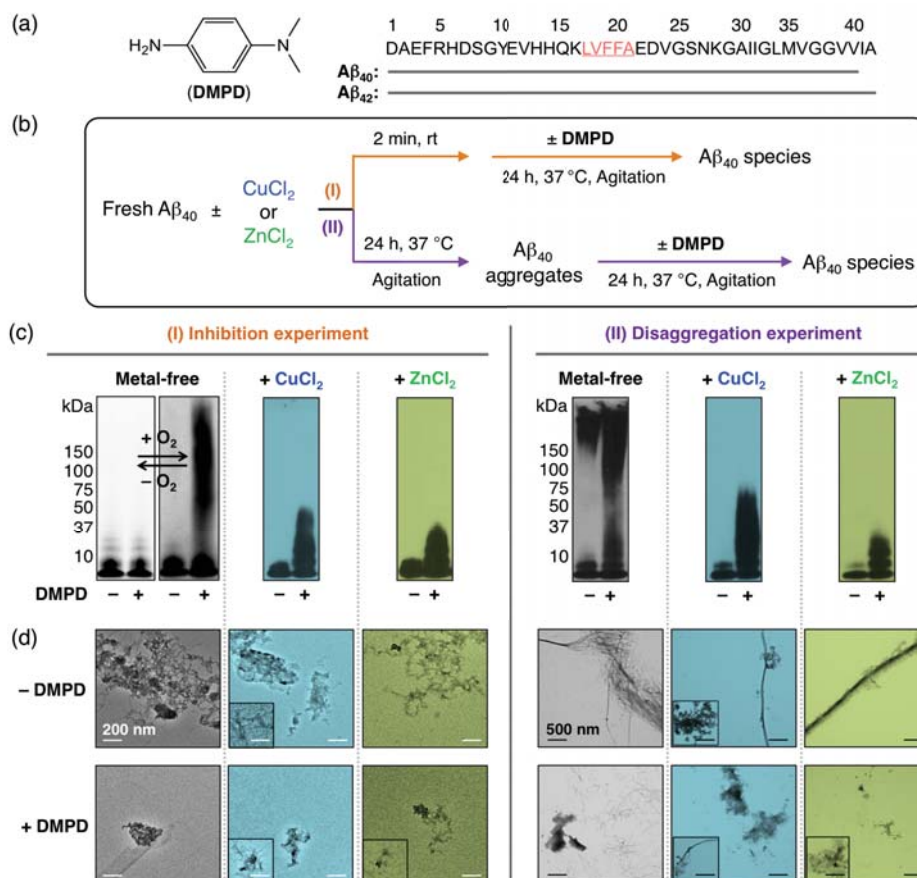


Figure 3.2. Effects of **DMPD** toward metal-free/metal-induced $A\beta_{40}$ aggregation *in vitro*. (a) Chemical structure of **DMPD** (N,N -dimethyl- p -phenylenediamine) and amino acid sequence of $A\beta$ (the self recognition site is underlined and highlighted in red). (b) Scheme of the (I) inhibition or (II) disaggregation experiments. The metal-free samples were prepared in both the absence (left) and presence (right) of O_2 . (c) Analyses of the resultant $A\beta$ species from (I) and (II) by gel electrophoresis with Western blotting (gel/Western blot) using an anti- $A\beta$ antibody (6E10). For the experiment (I), the samples containing metal-free $A\beta_{40}$ were prepared under anaerobic (left, white background) and aerobic (right, gray background) conditions. Conditions: $A\beta$ (25 μ M); $CuCl_2$ or $ZnCl_2$ (25 μ M); **DMPD** (50 μ M); 24 h; pH 6.6 (for Cu(II) experiments) or pH 7.4 (for metal-free and Zn(II) experiments); 37 °C; constant agitation. (d) TEM images of the $A\beta_{40}$ samples prepared under aerobic conditions (from (c)). Inset: Minor species from TEM measurements. White and black scale bars indicate 200 and 500 nm, respectively.

3.2.2. Effects of DMPD on Both Metal-Free and Metal-Induced $A\beta$ Aggregation *In Vitro*

The influence of **DMPD** on the aggregation of both $A\beta_{40}$ and $A\beta_{42}$ was probed in the absence and presence of metal ions [*i.e.*, Cu(II), Zn(II)]. Gel electrophoresis with Western blotting (gel/Western blot) using an anti- $A\beta$ antibody (6E10) and transmission electron microscopy (TEM) were employed to analyze the molecular weight (MW) distribution and morphological change of the resultant $A\beta$ species, respectively (Figures 3.2c,d, 3.3, and 3.4).^{18-22,31} As depicted in Figure 3.2b and Figure 3.3a, two different

experiments were conducted to assess whether **DMPD** can either inhibit the formation of metal-free/-treated A β aggregates (**I**: inhibition experiment) or disassemble preformed metal-free/-associated A β aggregates (**II**: disaggregation experiment). Generally, small molecules able to inhibit the formation of A β fibrils or disassemble preformed A β aggregates will generate a distribution of smaller A β species that can penetrate into the gel matrix and will produce a significant amount of smearing compared to compound-free controls. A β samples without treatment with compounds contain large A β aggregates (*i.e.*, mature fibrils), which can be observed by TEM, but are too big to enter the gel matrix (restricted to the entrance where the sample is loaded) and therefore do not produce smearing or bands in the gel/Western blot.

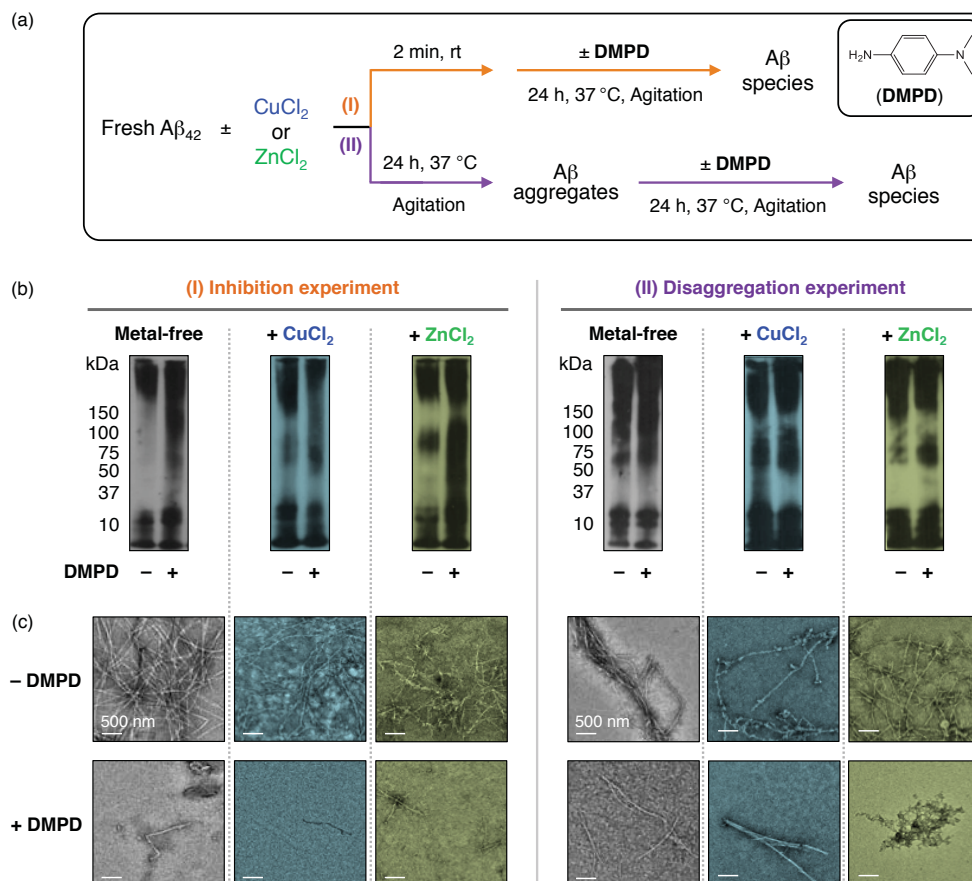


Figure 3.3. Effects of **DMPD** on metal-free and metal-induced A β ₄₂ aggregation. (a) Scheme of **(I)** inhibition and **(II)** disaggregation experiments. (b) Analyses of the resultant A β species from **I** and **II** by gel/Western blot using an anti-A β antibody (6E10). Conditions: A β (25 μ M); CuCl₂ or ZnCl₂ (25 μ M); **DMPD** (50 μ M); 24 h; pH 6.6 (for Cu(II) experiments) or pH 7.4 (for metal-free and Zn(II) experiments); 37 °C; constant agitation. (c) TEM images of the A β ₄₂ samples from (b). White scale bars indicate 500 nm.

In the inhibition experiment (I, Figure 3.2b), different MW distributions were observed for **DMPD**-treated $A\beta_{40}$ with and without metal ions compared to the untreated analogs. TEM images revealed the generation of small amorphous $A\beta$ aggregates with respect to the large clusters of fibrils generated in the absence of **DMPD** (Figure 3.2c,d). **DMPD** exhibited a similar ability to inhibit aggregate formation with $A\beta_{42}$ (Figure 3.3b). In the disaggregation experiment (II, Figure 3.2b), **DMPD** indicated more noticeable effects on the transformation of preformed metal-free $A\beta_{40}$ and metal- $A\beta_{40}$ aggregates than for the $A\beta_{42}$ conditions visualized by gel/Western blot (Figure 3.2c, right and Figure 3.3b, right); however, the generation of shorter, more dispersed fibrils, relative to the **DMPD**-untreated $A\beta_{42}$ controls, was indicated by TEM (Figure 3.3b,c). Moreover, in order to determine the effect of **DMPD** on $A\beta$ aggregation in a heterogeneous *in vitro* environment, the inhibition experiment was performed in a cell culture medium. Upon treatment of **DMPD** to $A\beta_{40}$ in a cell culture medium, a distinguishable variation in the MW distribution of $A\beta$ species was still observed (Figure 3.4), but this distribution was different from that shown in a buffered solution (Figure 3.2c, left). Therefore, these results support that the small monodentate ligand, **DMPD**, is able to redirect both metal-free $A\beta$ and metal- $A\beta$ species into off-pathway, relatively smaller and/or less structured peptides aggregates, which has been suggested to be less toxic,^{16,20,21} in a buffered solution and a heterogeneous matrix.

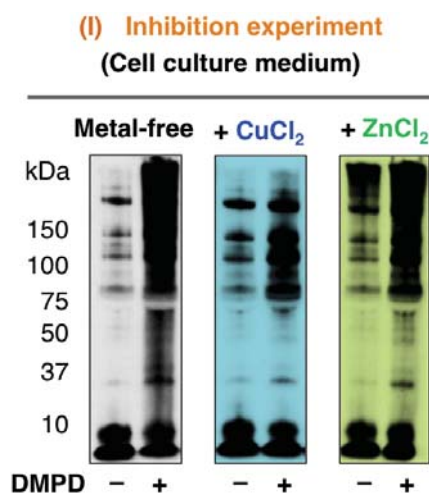


Figure 3.4. Effect of **DMPD** toward metal-free and metal-induced $A\beta_{40}$ aggregation in a cell culture medium. Gel/Western blot analyses of the resultant $A\beta_{40}$ species upon treatment with **DMPD** in a cell culture medium containing 1:1 Minimum Essential Media (MEM) and Ham's F12K Kaighn's Modification Media (F12K), 10% (v/v) fetal bovine serum (FBS), 100 U/mL penicillin, and 100 mg/mL streptomycin. Conditions: $A\beta$ (25 μ M); $CuCl_2$ or $ZnCl_2$ (25 μ M); **DMPD** (50 μ M); 24 h; 37 °C; constant agitation. The experimental scheme is depicted in Figure 3.2b.

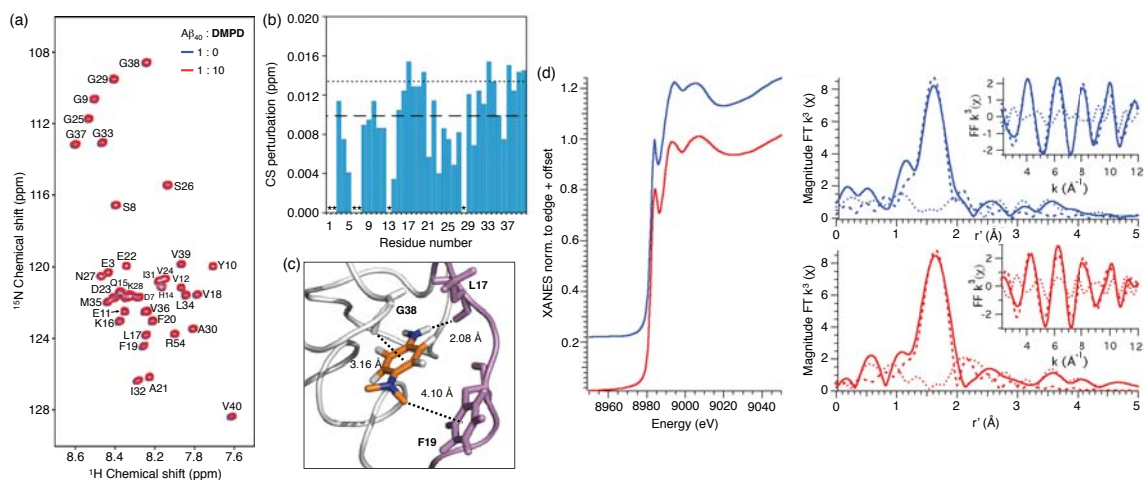


Figure 3.5. Interactions of **DMPD** with monomeric A β and fibrillar Cu(II)-A β , observed by 2D NMR spectroscopy and Cu K-edge X-ray absorption spectroscopy, respectively. (a) 2D ^1H - ^{15}N SOFAST-HMQC NMR investigation of **DMPD** with ^{15}N -labeled A β_{40} . (b) Chemical shift perturbations (CSPs) of A β_{40} were determined upon addition of **DMPD** (A β : **DMPD** = 1 : 10). On the chemical shift plot, the dashed and dotted lines represent the average CSP and one standard deviation above the average, respectively. Relatively noticeable CSPs were observed around the hydrophobic residues of the peptide. *Residues could not be resolved for analysis. (c) Molecular dynamics (MD) simulations of the A β_{40} -**DMPD** complex. **DMPD** and A β_{40} are shown to interact directly with the hydrophobic region of the A β_{40} monomer in its lowest energy conformation (see Figure 3.6). The chemical structure of **DMPD** is colored as follows: Carbon, orange; hydrogen, white; nitrogen, blue. The self-recognition site of A β_{40} is highlighted in light violet. (d) Left: X-ray absorption near edge structure (XANES) region of the Cu K-edge X-ray absorption spectrum of **DMPD**-incubated Cu(I)- (red) and Cu(II)-loaded (blue) A β_{42} fibrils. Top right (blue): Magnitude FT and FF (inset) extended X-ray absorption fine structure (EXAFS) of **DMPD**-incubated Cu(II)-loaded A β_{42} fibrils showing the experimental data (solid line), simulated spectrum (dashed line), and difference spectrum (dotted line). Shell #1 (N scatterer): $n = 2.3(2)$; $r = 1.889(3)$ Å; $\sigma^2 = 0.0041(4)$ Å 2 ; $\epsilon^2 = 0.93$. Bottom right (red): Magnitude FT and FF (inset) EXAFS of **DMPD**-incubated Cu(I)-loaded A β_{42} fibrils showing the experimental data (solid line), simulated spectrum (dashed line), and difference spectrum (dotted line). Shell #1 (N scatterer): $n = 2.2(2)$; $r = 1.882(4)$ Å; $\sigma^2 = 0.0033(1)$ Å 2 ; $\epsilon^2 = 0.85$.

3.2.3. Proposed Mechanism of **DMPD**'s Control Against A β Aggregation Pathways

(i) Interaction of **DMPD** with Metal-Free A β Monomers

The interaction of **DMPD** with metal-free A β monomers was examined by 2D NMR spectroscopy and MD simulations (Figure 3.5a-c). 2D band-Selective Optimized Flip-Angle Short Transient Heteronuclear Multiple Quantum Correlation (SOFAST-HMQC) NMR experiments were first employed to identify the interaction of **DMPD** with monomeric A β_{40} . When **DMPD** was titrated into ^{15}N -labeled A β_{40} , relatively noticeable chemical shift perturbations (CSPs) were shown for six amino acid residues (particularly for L17, F20, G33, G37, V39, and V40; Figure 3.5a,b). These residues in the self-recognition

(residues 17-21) and C-terminal hydrophobic regions (Figure 3.2a) are reported to be crucial for A β aggregation and cross β sheet formation *via* hydrophobic interactions.^{10,16} The CSP presented for V40 may be due to intrinsic C-terminal disorder rather than interaction with **DMPD**.³¹ The distribution of observed CSPs suggests that **DMPD** could interact with the amino acid residues in A β_{40} near the self-recognition and hydrophobic regions.

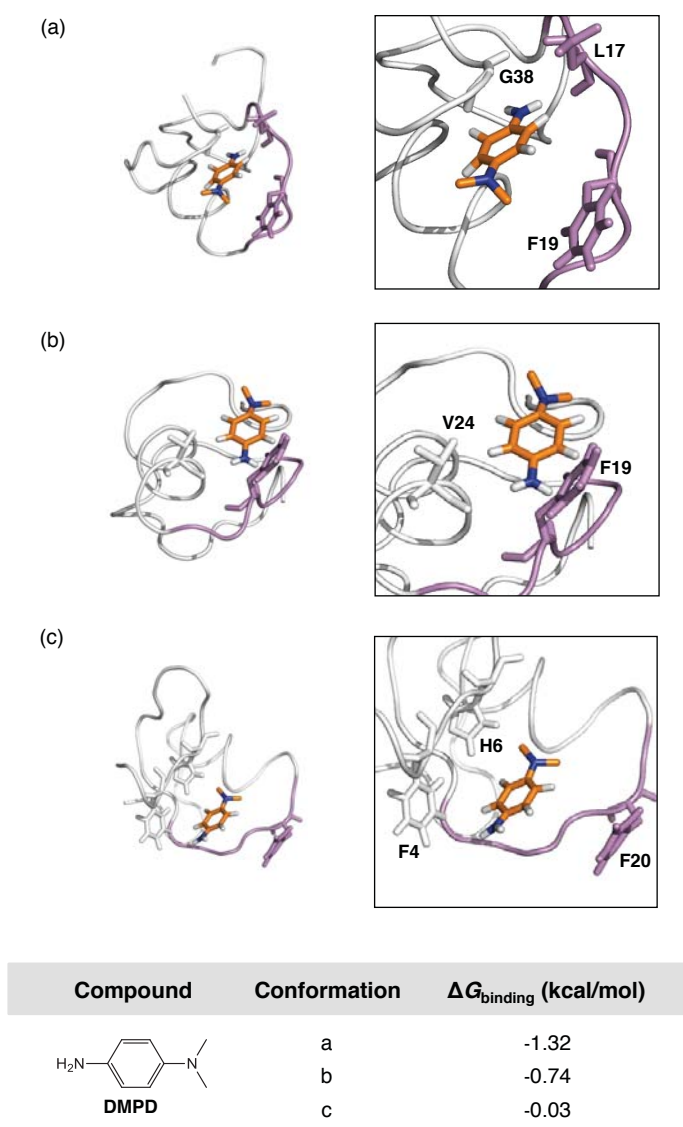


Figure 3.6. Conformations of the A β_{40} -**DMPD** complexes as determined by molecular dynamics (MD) simulations. (a-c) Complexes of **DMPD** with A β_{40} (PDB 1BA4). **DMPD** is shown to interact with A β_{40} . Atoms of **DMPD** are colored as follows: Carbon, orange; hydrogen, white; nitrogen, blue. The self-recognition site of A β_{40} is also highlighted in light violet. Gibb's binding energies ($\Delta G_{\text{binding}}$) for each conformation are summarized in the table (bottom).

To further probe the interaction between metal-free, monomeric A β ₄₀ and **DMPD**, docking and MD simulation studies^{32,33} were also performed. Simulations indicate multiple interactions (Figure 3.5c, and Figure 3.6): (i) a potential binding pocket is formed through hydrogen bonding (2.08 Å) of the amine group (–NH₂) of **DMPD** with the O atom of the backbone carbonyl between L17 and V18; (ii) the aromatic ring of **DMPD** associates with G38 via a N–H– π interaction (3.16 Å); (iii) the methyl group (–CH₃) of the dimethylamino moiety of **DMPD** further stabilizes the A β –**DMPD** interaction by the C–H– π (with the aromatic ring of F19) interaction (4.10 Å). The observation from docking and MD simulation investigations was in agreement with the NMR findings (*vide supra*). Thus, 2D NMR and docking/MD simulation studies demonstrate the direct interaction of **DMPD** with metal-free A β species, as suggested from the results of both inhibition and disaggregation experiments above (Figure 3.2 and Figure 3.3), along with the mass spectrometric (MS) analysis (*vide infra*, Figure 3.12).

(ii) Interaction of **DMPD** with Copper–A β Monomers and Fibrils

Cu K-edge XAS was applied to Cu(I)- and Cu(II)-loaded A β ₄₂ monomers and fibrils to gain insights into the nature of the interaction between copper–A β complexes and **DMPD**. The XAS data for Cu(I)-loaded A β ₄₂ fibrils following **DMPD** incubation are consistent with a linear 2-coordinate Cu(I)(N/O)₂ environment (Figure 3.5d, red). The X-ray absorption near edge structure (XANES) region of the XAS spectrum exhibited a prominent pre-edge feature at 8985.2(2) eV corresponding to the Cu (1s \rightarrow 4p_z) transition. Such a feature is characteristic of linear Cu(I).³⁴ Analysis of the extended X-ray absorption fine structure (EXAFS) region yielded a model consistent with the copper center ligated to two N or O ligands at 1.88 Å. We note that the identity of the ligands to the Cu(I) center could not be definitively determined. Although there are peaks in the magnitude Fourier Transformed EXAFS spectrum in the range of r' = 2.0–4.0 Å that may result from multiple scattering pathways from histidine imidazole rings, but they could not be modeled as such. Surprisingly, the Cu(II)-loaded A β ₄₂ fibrils treated with **DMPD** yielded nearly identical XAS data indicating the complete reduction of Cu(II) to a linear 2-coordinate Cu(I)(N/O)₂ center (blue, Figure 3.5d). This reduction of Cu(II) to Cu(I) is not a result of photoreduction in the X-ray beam. Cu(II) fibrils (or monomers; *vide infra*) show no indication of photoreduction under identical experimental conditions,^{34,35} while studies of **DMPD**-incubated Cu(II) fibrils do not present photochemistry following repeated EXAFS scans under the experimental conditions employed (*i.e.*, the Cu(II) is already reduced to Cu(I) prior to X-ray exposure) (Figure 3.7).

Copper-loaded A β ₄₂ monomers incubated with **DMPD** afforded a dramatically different result compared to the **DMPD**-untreated samples. In the absence of **DMPD**, XAS studies showed a spectrum for the Cu(II)-loaded A β ₄₂ monomers consistent with a square planar Cu(II)(N/O)₄ metal-center with two

imidazole ligands bound to Cu(II), while the Cu(I)-loaded A β ₄₂ monomers contained copper within a linear bis-His coordination environment.³⁴ The XAS data for Cu(II)-loaded A β ₄₂ monomers following **DMPD** incubation was indicative of a complex mixture of reduced Cu(I) and oxidized Cu(II) centers. The reduced samples following treatment with **DMPD** presented that Cu(I) was also contained in a mixture of coordination environments and geometries, making it impossible to yield a physically meaningful solution to the EXAFS data. The different behaviors of copper-loaded A β ₄₂ monomers *versus* fibrils could be the result of either different incubation times necessitated to avoid monomer aggregation, or could be indicative of different fundamental chemistry with **DMPD**. Taken together, the overall observations from the XAS studies suggest the possible redox interaction of the small monodentate ligand (**DMPD**) with copper–A β complexes.

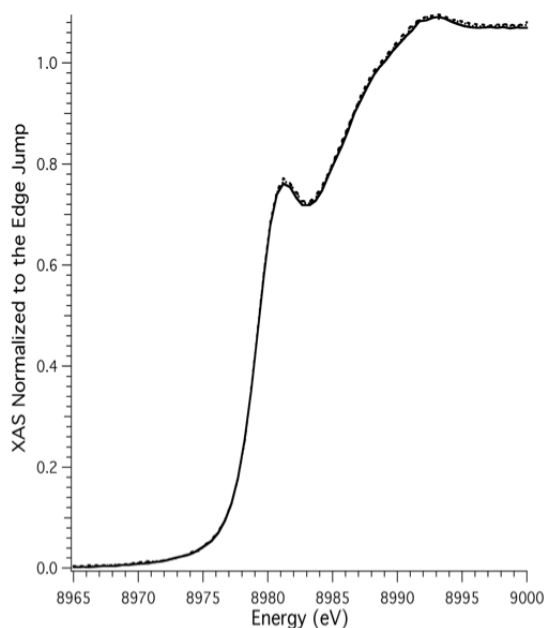


Figure 3.7. XANES region of the XAS spectrum for **DMPD**-incubated Cu(II)-loaded A β ₄₂ fibrils following one (solid), two (dashed), and three (dotted) scans on the same spot. Total exposure time for each scan is *ca.* 45 min.

(iii) Transformation of **DMPD** in the Absence and Presence of A β and Metal Ions

To elucidate how **DMPD** redirects A β peptides into less toxic, off-pathway unstructured A β aggregates, the chemical transformation of **DMPD** with A β was analyzed under various conditions, in addition to its interactions with metal-free and metal-bound A β (*vide supra*). Time-dependent optical changes of **DMPD** were first monitored in the absence and presence of A β ₄₀ with and without CuCl₂ in

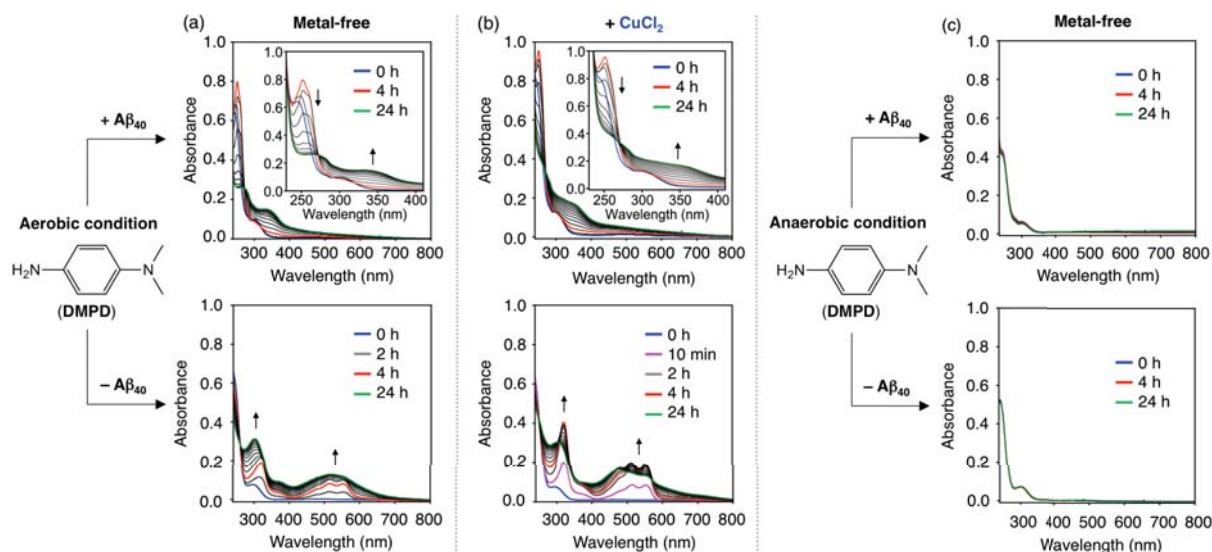


Figure 3.8. Transformation of **DMPD** with or without Cu(II) and/or Aβ₄₀, monitored by UV-vis. (a and b) UV-vis spectra of **DMPD** with or without CuCl₂ in the absence and presence of Aβ under aerobic conditions. (c) UV-vis spectra of **DMPD** with or without Aβ under anaerobic conditions. Blue, red, and green lines correspond to incubation for 0, 4, and 24 h, respectively. Conditions: Aβ (25 μM); CuCl₂ (25 μM); **DMPD** (50 μM); pH 6.6 (for Cu(II) experiments) or pH 7.4 (for metal-free experiments); room temperature; no agitation. (a and c) **DMPD** +/- Aβ₄₀; (b) [**DMPD** + CuCl₂] +/- Aβ₄₀.

buffered solutions (Figure 3.8). **DMPD** treated with Aβ₄₀ in both the absence and presence of Cu(II) exhibited spectral shifts, different from the Aβ₄₀-free condition (Figure 3.8a,b). The optical bands at *ca.* 513 and 550 nm, indicative of the formation of a cationic radical of **DMPD**²⁵⁻²⁷ through an oxidative degradation route (Figure 3.8a,b, bottom), were not observed even after a 24 h incubation of **DMPD** with Aβ (Figure 3.8a,b, top). Upon addition of **DMPD** into a solution containing Aβ₄₀, a red shift in the optical band of **DMPD** (from 295 to 305 nm) immediately occurred (Figure 3.9). Upon incubation over 4 h, a new optical band at *ca.* 340 or 350 nm with an isosbestic point at *ca.* 270 nm began to grow in (Figure 3.8a,b, top). These optical bands at *ca.* 250 and 340 or 350 nm are expected to be indicative of generating a possible adduct of benzoquinoneimine (**BQI**) or benzoquinone (**BQ**) with proteins (or peptides; *via* amine or thiol groups), respectively.^{23,24,27,36-41} The absence of a clean isosbestic point at the early incubation time points is most likely due to the formation of **BQ** from **DMPD** and possibly some contribution from the production of transient complexes between Aβ and **CI** or **BQI** (*vide infra*). The UV-vis spectrum of **BQ** (Figure 3.10a) is identical to the optical spectra of **DMPD** with Aβ₄₀ at 2 and 4 h under aerobic conditions indicating that **DMPD** is transformed into **BQ** before the bands at 250 and 340 or 350 nm begin to grow in, indicative of the covalent adduct formation with Aβ. Furthermore, Aβ₄₀ treated to a solution of **BQ** under identical conditions exhibits one clean isosbestic point over the course

of the 24 h experiment (Figure 3.10b). These results support that the optical changes at the early time points are mainly caused by the generation of **BQ** from **DMPD**. Overall, **DMPD** could be transformed through a different pathway in the presence of $A\beta_{40}$, potentially producing a modified **DMPD** conjugate with $A\beta_{40}$, compared to the $A\beta_{40}$ -absent case.

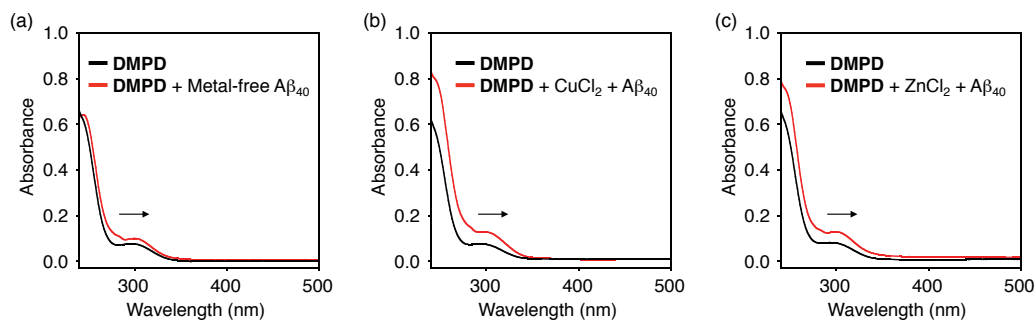


Figure 3.9. UV-vis spectra of **DMPD** with or without $A\beta_{40}$ and/or metal ions. (a) **DMPD** \pm $A\beta_{40}$; (b) **DMPD** \pm [$CuCl_2$ + $A\beta_{40}$]; (c) **DMPD** \pm [$ZnCl_2$ + $A\beta_{40}$]. Black and red lines represent the absence and presence of $A\beta_{40}$, respectively. Conditions: $A\beta_{40}$ (25 μ M); $CuCl_2$ or $ZnCl_2$ (25 μ M); **DMPD** (50 μ M); pH 6.6 (for Cu(II) experiment) or pH 7.4 (for metal-free and Zn(II) experiments); room temperature; no agitation. The spectra were obtained right after addition of metal ions and/or $A\beta_{40}$.

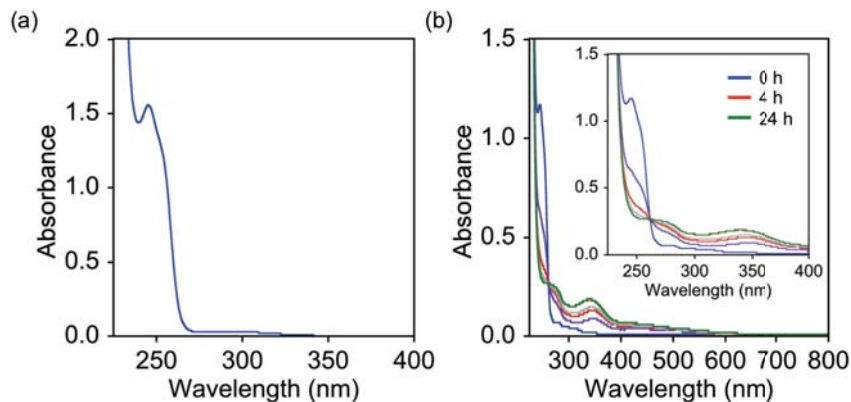


Figure 3.10. Transformation of benzoquinone (**BQ**) in the presence of $A\beta_{40}$. (a) UV-vis spectrum of **BQ** under aerobic conditions. (b) UV-vis spectrum of **BQ** with $A\beta_{40}$ under aerobic conditions. Blue, red, and green lines correspond to incubation periods of 0, 4, 24 h, respectively. Conditions: $A\beta_{40}$ (25 μ M); **BQ** (50 μ M); HEPES buffer (1 mM, pH 7.4); room temperature, no agitation.

In order to gain a better understanding on the spectrophotometric observations indicative of the transformation of **DMPD** when $A\beta$ is present (*vide supra*), additional studies were carried out. First, the UV-vis spectra of **DMPD** were measured in an anaerobic environment with or without $A\beta$ to ascertain the involvement of dioxygen (O_2) in the conversion of **DMPD**. Previous studies report that **DMPD** can be

singly or doubly oxidized to form a cationic radical or a cationic quinoid species, respectively.²⁵⁻²⁷ The spectral alterations of **DMPD**, apparent in an O₂ atmosphere in both the absence and presence of Aβ₄₀, were not observed in an anaerobic condition even after 24 h incubation (Figure 3.8c). In addition, modulation of Aβ aggregation by **DMPD** was not observed under the anaerobic condition, distinguishable from that under the aerobic setting (Figure 3.2c, left). Furthermore, inhibition and disaggregation experiments of **BQ** with Aβ₄₀ and Aβ₄₂ were performed in the absence and presence of metal ions (Figure 3.11). **BQ** exhibited an ability to control and alter the MW distribution of Aβ₄₀ and Aβ₄₂ with and without metal ions in a very similar manner to that which was observed for **DMPD**. Therefore, O₂ is necessary for the transformation of **DMPD** (**DMPD**_{transformed}; *e.g.*, **BQ**) and the capability of **DMPD**_{transformed} to redirect Aβ aggregation into less toxic, off-pathway amorphous Aβ aggregates.

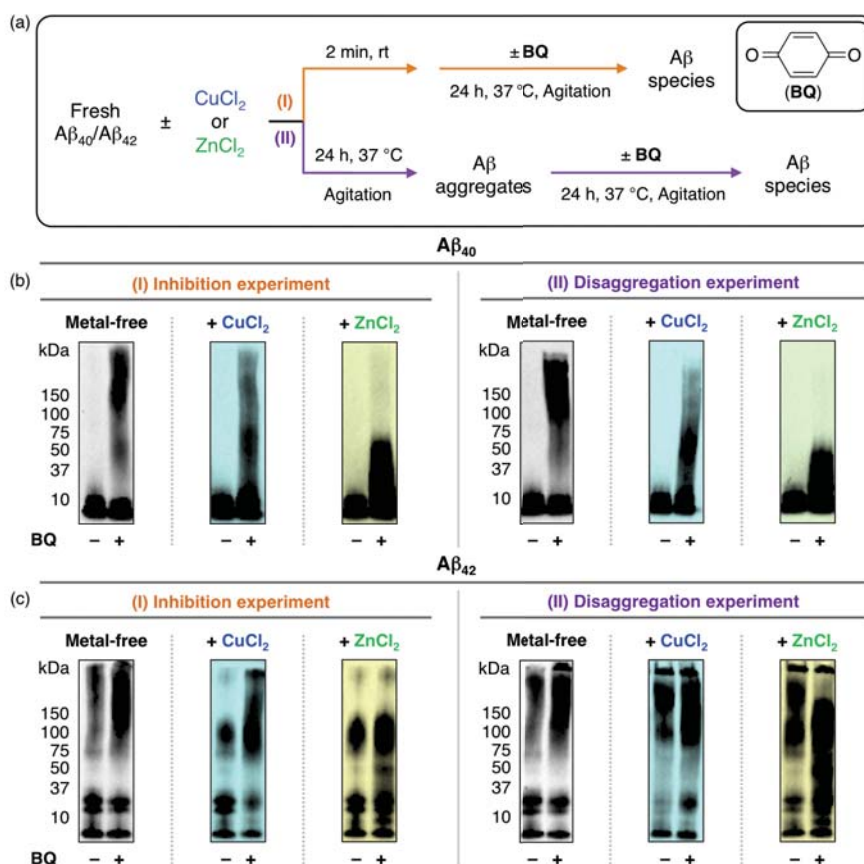


Figure 3.11. Effects of **BQ** on metal-free and metal-induced Aβ₄₀ and Aβ₄₂ aggregation. (a) Scheme of (I) inhibition and (II) disaggregation experiments. (b & c) Analyses of the resultant Aβ species [(b) Aβ₄₀ and (c) Aβ₄₂] from I and II by gel/Western blot using an anti-Aβ antibody (6E10). Conditions: Aβ (25 μM); CuCl₂ or ZnCl₂ (25 μM); **BQ** (50 μM); 24 h; pH 6.6 (for Cu(II) experiments) or pH 7.4 (for metal-free and Zn(II) experiments); 37 °C; constant agitation.

(iv) Analysis of $A\beta$ -DMPD_{transformed} Complexes

MS analysis of DMPD-treated $A\beta_{40}$ samples was further performed in order to identify the formation of $A\beta_{40}$ -ligand complexes. New peaks appeared corresponding to the addition of 103.93 ± 0.04 Da to $A\beta$ (Figure 3.12a, i) proposed to be a covalently bound conversion product of DMPD (e.g., BQ; shown as 5 in Figure 3.12d). To support our proposed mode of $A\beta$ -DMPD interaction, via the transformation of DMPD, the interactions of $A\beta_{40}$ with the structurally homologous BQ were examined under identical experimental conditions. Our data indicates that BQ binds to $A\beta_{40}$ (Figure 3.12b), with a mass shift that is consistent with DMPD incubations (104.1 ± 0.1 Da).

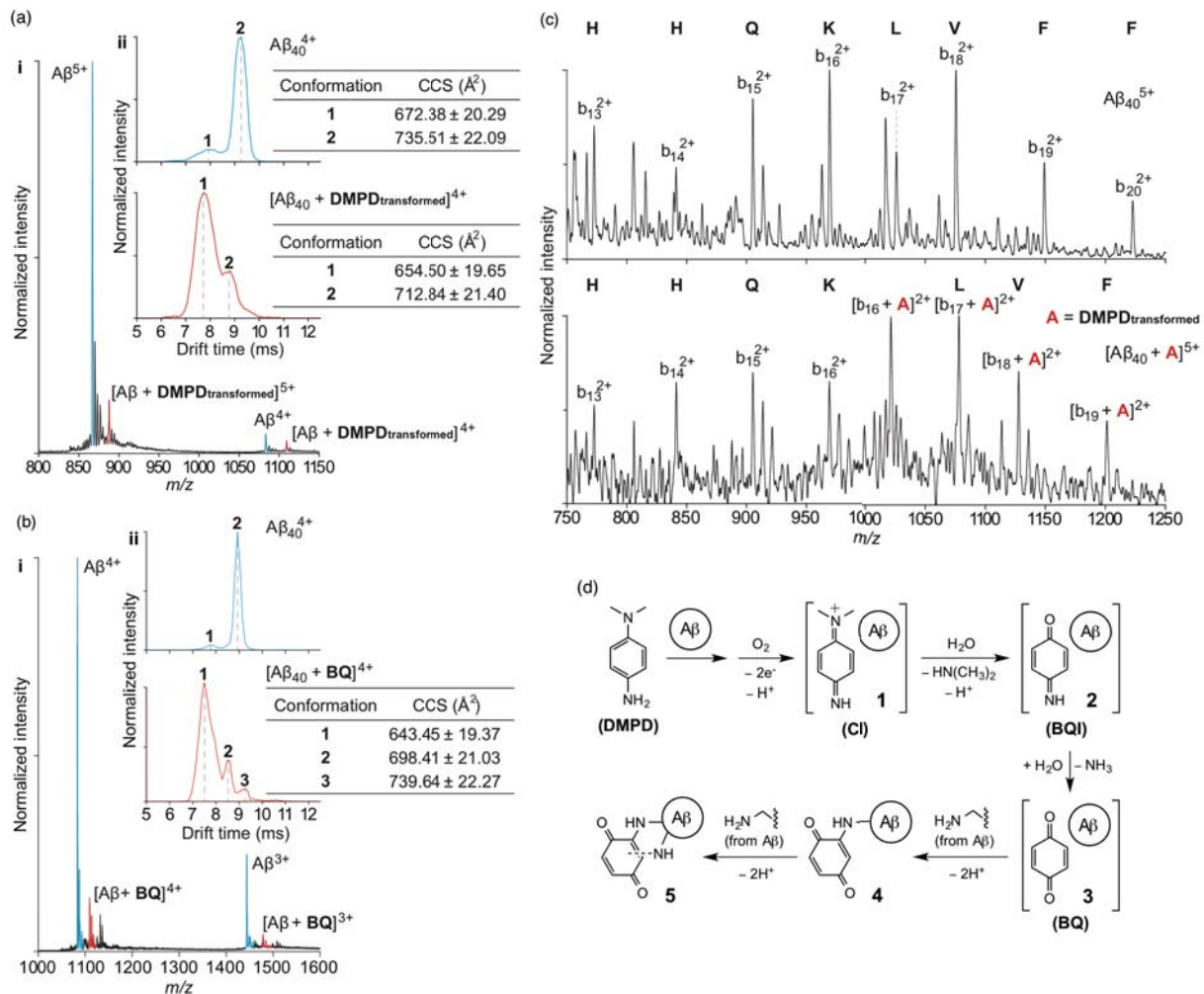


Figure 3.12. Analysis of the resulting species upon interaction of $A\beta_{40}$ with DMPD or BQ by mass spectrometry (MS) and ion mobility-mass spectrometry (IM-MS), as well as a proposed mechanism. (a) MS analysis showing the complex formation of $A\beta_{40}$ (25 μ M) with DMPD_{transformed} (50 μ M) (red lines) in the 4^+ and 5^+ charge states ($[A\beta + DMPD_{transformed}]^{4+}$ and $[A\beta + DMPD_{transformed}]^{5+}$) (i). IM-MS was

applied to the 4^+ charge state to resolve the conformational rearrangement of $A\beta_{40}$ upon addition and conversion of **DMPD** to **DMPD**_{transformed} (ii). Extracted arrival time distributions support the existence of two resolvable structural populations [collision cross section (CCS) data, inset tables]. The interaction with **DMPD**_{transformed} trapped the peptide in a more packed conformation (dominant peak = 1) when compared to the *apo* form (dominant peak = 2). (b) MS analysis showing the complex formation of $A\beta_{40}$ (25 μ M) with **BQ** (50 μ M) supports that **BQ** binds readily to the peptide (red) (i). In line with the **DMPD** data presented above, **BQ**-containing samples support a mass gain of 104 Da attributed to covalent binding with K16 (Figure 3.11). IM-MS was applied to the 4^+ charge state to resolve the conformational rearrangement of $A\beta_{40}$ upon binding **BQ**. Extracted arrival time distributions indicate the existence of three resolvable structural populations (CCS data, inset table) (ii). The first two of these conformations support, within least square error analysis, CCS values consistent with the **DMPD**-bound data (Figure 3.12a). (c) Comparison of tandem MS/MS sequencing using the quadrupole isolated 5^+ charge state (trap collision energy 90 V) of $A\beta_{40}^{5+}$ (top) and $[A\beta + \text{DMPD}_{\text{transformed}}]^{5+}$ (bottom). Analysis of these data in addition to the MS and IM-MS support the attachment of **DMPD**_{transformed} to $A\beta_{40}$ through a covalent modification of the peptide *via* K16 resulting in an observed mass shift of 103.93 ± 0.04 Da calculated from internal monoisotopic calibration data sets. (d) Proposed mechanistic pathways between **DMPD** and $A\beta$. **DMPD** may undergo an oxidative transformation under aerobic conditions to generate a cationic imine (**CI**)- $A\beta$ complex (**1**). **CI** could then generate **BQI** (shown in **2**) through hydrolysis. Once hydrolyzed, **BQI** is proposed to undergo further hydrolytic conversion to generate **BQ** (shown in **3**). Our MS studies support that **BQ** forms covalently bound protein-ligand adducts (**4**) that are capable of forming intramolecular crosslinks (**5**) that trap $A\beta$ in an altered conformational geometry compatible with our IM-MS dataset.

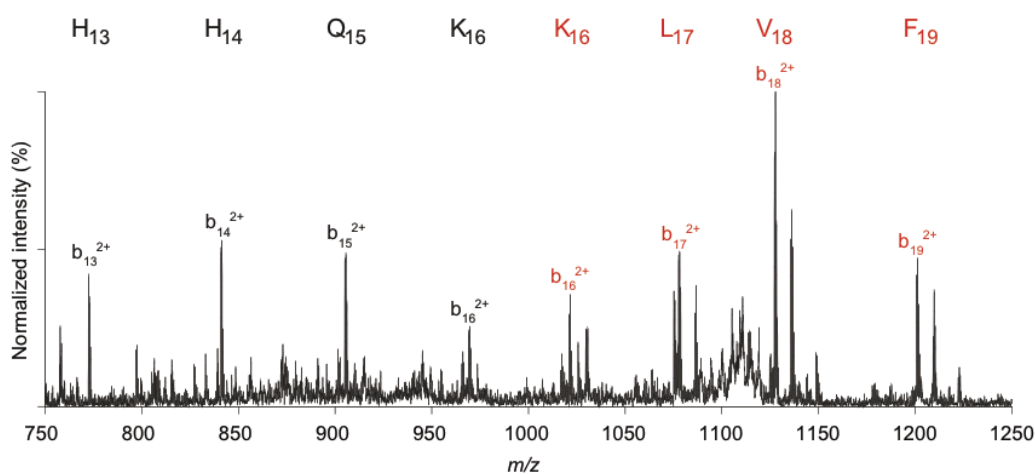


Figure 3.13. MS/MS sequencing of the samples containing **BQ** and $A\beta_{40}$. Complimenting **DMPD** analysis (Figure 3.12), studies were performed on incubated samples of $A\beta_{40}$ with **BQ**. Consistent with $[A\beta_{40} + \text{DMPD}]$ analyses, an adduct of 104.1 ± 0.1 Da was identified to be covalently linked to K16.

Tandem MS (MS/MS) in conjunction with collision induced dissociation (CID) for the 5^+ ligand bound charge state was carried out to determine the nature of the $A\beta_{40}$ -**DMPD**_{transformed} (Figure 3.12c) and $A\beta_{40}$ -**BQ** complexes detected (Figure 3.13). MS/MS data supports that both **DMPD**_{transformed} and **BQ** covalently link to $A\beta_{40}$ *via* K16, with observed masses consistent with the above analysis. Whilst this

ligated mass difference is too small to support a single covalent bond formation between A β and **DMPD**_{transformed}/**BQ** (106.1 Da expected due to the release of two protons upon the formation of an A β –**DMPD**_{transformed} covalent bond), it does agree well with the generation of a second covalent bond between A β and **DMPD**_{transformed}/**BQ** (104.1 Da expected from the concomitant loss of two additional protons upon the formation of the second covalent bond). This data therefore supports that **DMPD**_{transformed}/**BQ** is capable of crosslinking A β , and is consistent with the data previously published for α -synuclein.²⁴ Based on this conclusion, we sought to confirm if **DMPD**_{transformed}/**BQ** is capable of forming inter- and/or intramolecular crosslinks using MS/MS. **BQ**-bound A β ₄₀ dimer dissociation data indicates that **BQ** primarily forms intramolecular crosslinks (Figure 3.14).

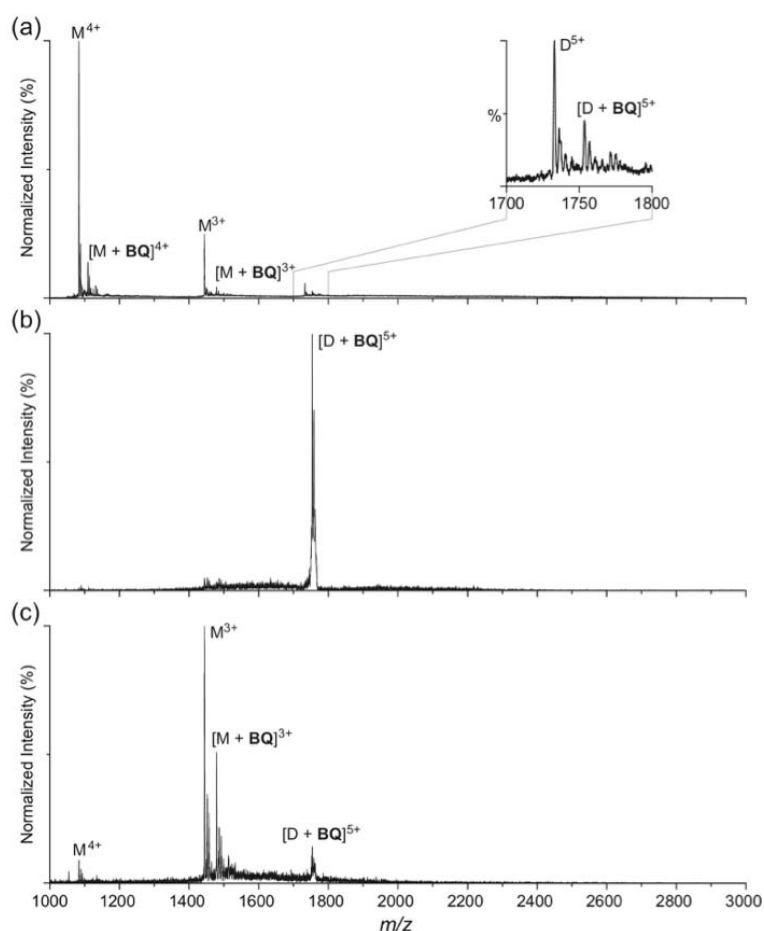


Figure 3.14. MS studies of the **BQ**-bound A β dimer. (a) MS/MS analysis used to identify if **BQ** was capable of forming intermolecular crosslinks in A β dimers (M: A β monomer; D: A β dimer). Upon quadrupole isolation of the **BQ**-bound 5⁺ A β ₄₀ dimer ion (b), it was subjected to collisional activation and subsequent fragmentation (c). These results support that **BQ** forms intramolecular crosslinks, with masses corresponding to intact monomeric *apo* and **BQ**-bound peptides suggesting these conclusions.

In addition, IM–MS studies of the 4⁺ charge state were carried out in order to assess the A β -bound state conformers adopted. When compared to the A β control, A β –**DMPD**_{transformed} complexes possessed a significantly decreased ion mobility (IM) arrival time, indicative of a more compact A β ₄₀ structure (Figure 3.12a, ii). Consistent with this data, A β ₄₀–**BQ** binding also leads to a similar reduction in IM arrival time, again supporting the production of a more compact species than the form adopted by the compound-untreated A β (Figure 3.12b, ii). Combining this data with observations from our MS/MS analysis, we conclude that the **DMPD**_{transformed}/**BQ** crosslinking traps A β in a relatively compact conformational state that is likely off-pathway with respect to amyloid fibril formation.

(v) Proposed Mechanism

Based on these optical and MS results, the covalent bond formation within A β –**DMPD**_{transformed} complexes could occur *via* a possible mechanistic pathway, as described in Figure 3.12d. In the presence of A β , under aerobic conditions, **DMPD** could first undergo a two-electron oxidative transformation to generate a cationic imine (**CI**)–A β complex (**1**). **CI** could be converted *via* hydrolysis to **BQI** (shown in **2**) that could further hydrolyze its imine to generate **BQ** (shown in **3**). **BQ** is then capable of forming a covalently bound A β –**BQ** adduct through interactions with a primary amine containing residue (**4**; A β + 106.1 Da), such as K16, that further crosslinks to an additional residue with a similar functional group (**5**; A β + 104.1 Da), consistent with our MS studies and **BQ**–protein conjugates previously reported.³⁷⁻⁴¹ The covalent complexation of A β with **BQ** could direct the structural compaction, suggested from IM–MS analysis (Figure 3.12a,b), and could account for **DMPD**'s redirection of peptide aggregation pathways into amorphous A β aggregates,^{16,20,21} as found in the gel/Western blot and TEM studies (*vide supra*).

3.2.4. Attenuation of Metal-Free A β -/Metal–A β -Induced Toxicity in Living Cells by **DMPD**

The regulation of A β -/metal–A β -triggered cytotoxicity by **DMPD** was examined using human neuroblastoma SK-N-BE(2)-M17 (M17) cells. **DMPD** was incubated for 24 h with M17 cells pretreated with A β ₄₀ in both the absence and presence of Cu(II) or Zn(II). Viability was increased by *ca.* 10–20% when **DMPD** was introduced to metal-free A β ₄₀- or metal–A β ₄₀-treated M17 cells, relative to the untreated cells (Figure 3.15), as measured by the MTT assay. Note that **DMPD** displayed low toxicity in the range of the tested concentrations (0–100 or 0–50 μ M in the absence and presence of metal ions, respectively; > 80% cell survival; Figure 3.15a-c). Thus, **DMPD** could ameliorate cytotoxicity induced by metal-free A β and metal–A β .

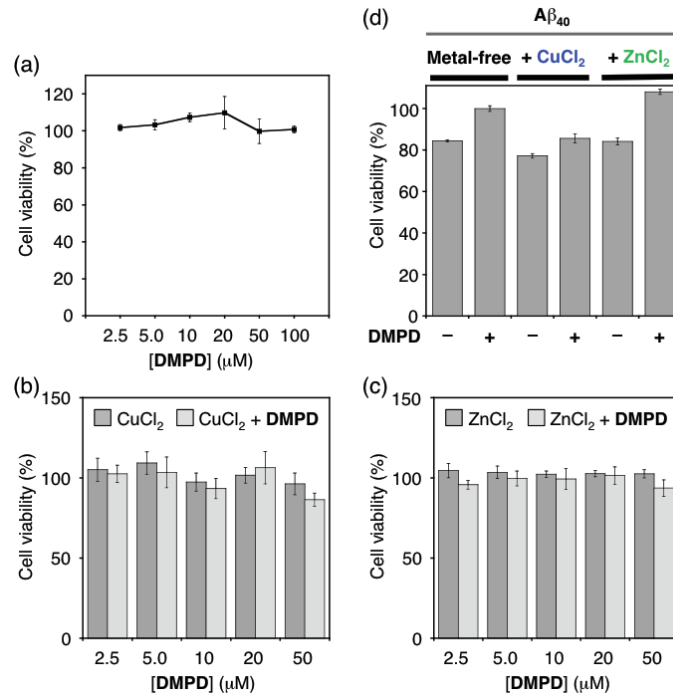


Figure 3.15. Cytotoxicity of **DMPD** in the absence and presence of metal ions, and its effect toward metal-free/metal-treated A β_{40} -triggered cytotoxicity. The cytotoxicity of (a) **DMPD** only (2.5-100 μ M; 1% v/v DMSO); **DMPD** (2.5-50 μ M) with (b) CuCl₂ or (c) ZnCl₂ in a ratio of 1:1 using the human neuroblastoma SK-N-BE(2)-M17 (M17) cells. (d) Viability (%) of M17 cells incubated with A β_{40} (10 μ M), CuCl₂ or ZnCl₂ (10 μ M), and/or **DMPD** (20 μ M) for 24 h. Cell viability, determined in M17 cells by the MTT assay, was calculated in comparison to that treated with DMSO only (1% v/v). Error bars represent standard error from three independent experiments.

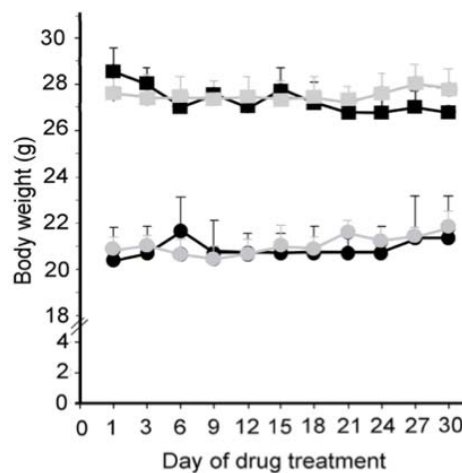


Figure 3.16. Monitoring changes in body weight. No significant difference in body weight was observed between the vehicle- and **DMPD**-treated 5 \times FAD mice. Body weights of male (squares; n = 6 for each treatment) or female (circles; n = 5 for each treatment) 5 \times FAD mice were measured for 30 days

immediately before the daily injection of vehicle (black) or **DMPD** (1 mg/kg/day, i.p.; gray), starting from 3 months of age. All values represent mean + SEM.

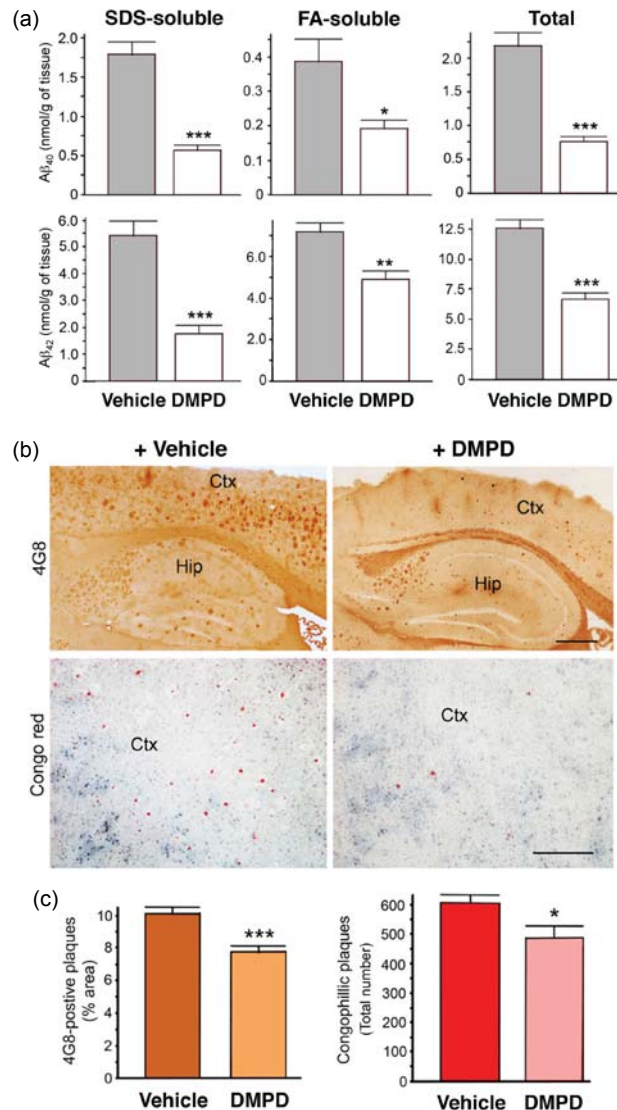


Figure 3.17. Reduction of cerebral amyloid pathology by **DMPD** in the 5×FAD mice. After the total 30 daily i.p. injections of vehicle or **DMPD** (1 mg/kg/day), the brain tissues were collected from the 5×FAD mice at 4 months of age. (a) Bars denote the amounts of SDS-soluble, FA-soluble, or total (PBS plus SDS plus FA) Aβ₄₀/Aβ₄₂ peptides in the whole brains, which were calculated from three independent sandwich Aβ ELISA assays (n = 14–17). (b) Representative microscopic images of 4G8-immuno stained (brown) or Congo red stained (red) brain sections of 5×FAD mice show that **DMPD** significantly reduced the burden of amyloid deposits in the brain. Ctx, cortex; Hip, hippocampus. Scale bar = 100 μm. (c) The load of 4G8-immunoreactive amyloid deposits and the total number of congophilic amyloid plaques in the microscopic photographs of the identical cortical areas (b) were measured in five brain sections taken from each animal. All values represent mean ± SEM (n = 7). **P* < 0.05, ***P* < 0.01, or ****P* < 0.001 by unpaired two-tail t-test.

3.2.5. *In Vivo* Efficacy of DMPD Against Amyloid Pathology and Cognitive Impairment

In order to validate the beneficial effects of **DMPD** on AD pathogenesis *in vivo*, we administered the compound to male 5×FAD mice *via* the intraperitoneal route at 1 mg/kg/day for 30 days from 3 months of age. After 30 total daily treatments of **DMPD**, the mice were subjected to biochemical analysis for cerebral amounts of A β ₄₀/A β ₄₂ and histopathological evaluations of the amyloid deposition load. 5×FAD mice were selected for this study since they develop early and severe phenotypes of AD and behavioral dysfunction.²⁹ At the conclusion of the compound treatment period, there was no significant difference in gross appearance or body weight between the vehicle- and **DMPD**-treated 5×FAD mice (Figure 3.16).

Quantification of cerebral A β peptides by the enzyme-linked immunosorbent assay (ELISA) revealed that the total levels of A β ₄₀/A β ₄₂ containing PBS-, sodium dodecyl sulfate (SDS)-, and formic acid (FA)-soluble A β species which represent soluble, moderately soluble, and completely insoluble A β species, respectively, were decreased by *ca.* 66% and 46%, respectively, compared to the vehicle-treated 5×FAD mice (Figure 3.17a). The levels of SDS-soluble A β ₄₀/A β ₄₂ were more drastically reduced by **DMPD** (*ca.* 69% and 61%, respectively) than those of FA-soluble A β ₄₀/A β ₄₂ levels (*ca.* 52% and 37%, respectively). Furthermore, substantial reductions in amyloid deposits were detected in 5×FAD mice treated with **DMPD**, determined by analyzing the loads of amyloid precursor protein (APP)/A β -immunoreactive 4G8- and Congo red-stained compact amyloid plaques (by *ca.* 23% and 20%, respectively) (Figure 3.17b,c). Overall, these results indicate that **DMPD** is able to delay or reverse the amyloid pathogenesis in the brain of AD model mice.

To evaluate the capacity of **DMPD** to improve cognitive deficits in AD model mice, we tested 4-month-old 5×FAD mice employing the Morris water maze (MWM) test for spatial learning and memory during the final five consecutive days of compound treatment. As demonstrated previously,^{22,29} the 5×FAD mice exhibited impaired spatial learning, showing enhanced difficulty in locating the hidden escape platform in a pool of water compared to their littermate, wild-type mice (Figure 3.18a). In contrast, the repetitive administration of **DMPD** prominently improved the learning and memory capability in the 5×FAD mice, relative to those of the vehicle-treated wild-type mice (Figure 3.18a).

Three hours after the final MWM test, we performed the probe trials, where the escape platform was removed and the mice located its previous position in the water for 60 sec, representing their performance of long-term memory retention. **DMPD**-treated animals took distinguishably less time to reach the platform area and spent significantly more time in the target quadrant (North West, NW), where the platform had been hidden, than vehicle-treated 5×FAD mice (Figure 3.18b,c). Therefore, our behavioral analysis suggests that **DMPD** is capable of rescuing cognitive defects in 5×FAD mice.

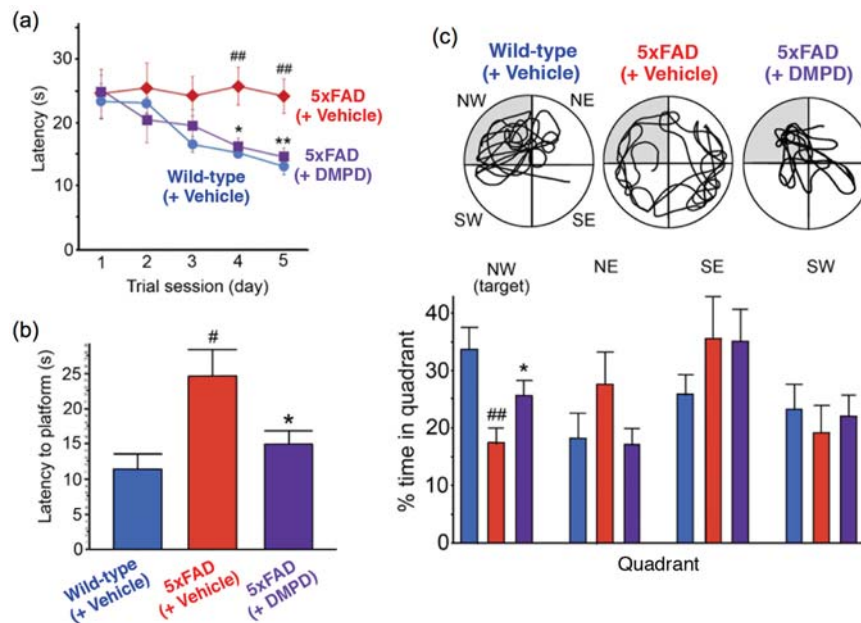


Figure 3.18. Cognitive enhancement by **DMPD** in the 5×FAD AD mouse model. Using the Morris water maze task, spatial learning and memory activities were compared in the 5×FAD and their littermate wild-type mice after thirty consecutive vehicle or **DMPD** (1 mg/kg/day, i.p.) treatments. (a) The escape latency time was daily measured for the final five days of the drug treatment. (b) The probe trials were performed on the day of the final treatment to assess the time when the mice spent to reach the escape platform. (c) Upper circular images display the representative swimming paths for the mice to locate the escape platform in the water maze for 60 sec. Lower graphs show the time how long they spent in the target quadrant (NW, highlighted in gray). The statistical comparisons were performed between 5×FAD and their wild-type littermate mice with vehicle (pound), or between consecutive vehicle and **DMPD** treatments in 5×FAD mice (asterisk), according to the one-way ANOVA followed by a Student-Neuman-Keuls post hoc test. * $P < 0.05$, **, $^{##}P < 0.01$ or ***, $^{###}P < 0.001$ ($n = 17$ for wild-type mice or $n = 14$ for vehicle- or **DMPD**-treated 5x FAD mice).

3.3. Conclusions

AD continues to present a major socioeconomic burden to our society. The absence of treatments and reliable diagnostics for this disease has demanded significant efforts to be made toward the identification of its underlying origins. For this aspect, the development of chemical tools capable of discerning and/or regulating pathognomonic factors of interest has been critical for the establishment of our current understanding of AD and will prove to be a central resource as we continue to unravel the intricacies of the disorder.

For instance, the use of small molecular tools (*i.e.*, oligomer stabilizers) able to specifically interact with and conformationally modulate small, soluble A β has been important for establishing oligomers as pathological factors.⁴ The adverse effects of metal ion dyshomeostasis and miscompartmentalization in AD have been validated by utilizing ionophores [*e.g.*, clioquinol (**CQ**), **PBT2**] that bind and chauffeur

metal ions [*i.e.*, Cu(II), Zn(II)] from extracellular A β plaques across the plasma membrane where it induces a signaling pathway, ultimately activating matrix metalloproteinases, among other enzymes, which assists in the breakdown and clearance of metal-free and metal-bound A β plaques.^{4,42,43} Furthermore, a metal–A β specific tool, **L2-b**, has been designed to provide direct, *in vivo* evidence of the potential role of metal-bound A β species in AD pathogenesis.^{19,22} Upon administration, **L2-b**, targeted and modulated metal–A β species in the brains of 5 \times FAD mice, significantly reduced the overall amyloid deposits, as well as mitigated cognitive dysfunction thus indicating metal–A β as a pathological factor of AD.²² Chemical tools have also been utilized to address the challenges associated with determining the interconnections between multiple facets of AD.^{4,16,21} A multifunctional ligand (**ML**) was designed to elucidate some of these pathological factors (*e.g.*, metal-free and metal–A β aggregation, oxidative stress) associated with neuronal death in AD.²¹ **ML** was shown to exhibit an advantageous control and promotion of protein aggregates toward off-pathway, unstructured species in the absence and presence of metal ions; control the generation of ROS by limiting the redox cycling of the copper center; decrease toxicity in living cells.²¹ Collectively, these results not only identify the vital value of chemical tools to elaborate our comprehension of the disorder, but also assist in the further identification of novel pathways to investigate.

In the current study, a compact chemical tool, **DMPD**, is presented for the redirection of A β aggregation in the absence and presence of metal ions into nontoxic, off-pathway aggregates through a novel approach (*i.e.*, intramolecular crosslinks with aggregation-prone peptides upon transformation of a redox-active small molecule). **DMPD**'s reactivity could be related to its interactions with metal-free A β and metal–A β , along with its redox characteristics, as indicated through multiple biophysical approaches. Mechanistically, **DMPD** is observed through optical and MS analyses to modulate peptide aggregation pathways through its oxidation and successive hydrolytic transformations to generate more structurally compact quinoid-peptide adducts, compared to the compound-untreated A β , through intramolecular covalent crosslinking (*i.e.*, A β –**BQ**). Moreover, the site-specific covalent modification of A β *via* primary amine-containing residues, such as K16, a critical residue for the formation of cross β sheet structures within the self-recognition sequence of the peptide,^{1-4,8-11} could further illuminate **DMPD**'s reactivity *in vitro*. **DMPD** was also evaluated in living cells and *in vivo* to determine the efficacy and beneficial effects associated with its administration in biological settings. Particularly, the ELISA quantification of the cerebral amyloid content of **DMPD**-treated 5 \times FAD mice showed a significant reduction in SDS-soluble forms of A β ₄₀ and A β ₄₂ (*ca.* 60–70% reductions) which are indicative of toxic, soluble pools of A β peptides.⁴⁴⁻⁴⁶ When evaluated by FA-soluble A β ₄₀/A β ₄₂ levels and

amyloid plaque loads,⁴⁶ the nontoxic, amyloid deposits/aggregates were relatively less influenced by **DMPD** (ca. 20–50% reductions). Therefore, these *in vivo* analyses also support that **DMPD** could preferentially influence on the toxic soluble forms of A β peptides with the less reactivity toward the insoluble amyloid aggregates or deposits. In addition, memory and learning capabilities of 5 \times FAD mice were restored upon **DMPD** treatment as evaluated by the Morris water maze task. Still, further investigations to address remaining questions, such as the specificity of **DMPD** to generate protein crosslinks and the location and time of **DMPD**'s transformation *in vivo* are warranted.

Taken together, the findings of **DMPD**'s reactivity with the amyloidogenic peptide, A β , presented in this work, demonstrate novel, pivotal principles that can be applied toward amyloid aggregation control and the establishment of further chemical tools: (i) formation of intramolecular crosslinks between small molecules and peptides may be an effective method to control the self-assembly of amyloidogenic peptides; (ii) effective strategies can still be developed without the need to build up chemical complexity, shown presently within the field.

3.4. Experimental Section

3.4.1. Materials and Methods.

All reagents were purchased from commercial suppliers and used as received unless otherwise stated. *N,N*-Dimethyl-*p*-phenylenediamine (**DMPD**) was purchased from Sigma-Aldrich (St. Louis, MO, USA). A β ₄₀ and A β ₄₂ were purchased from AnaSpec (Fremont, CA, USA) (A β ₄₂ = DAEFRHDSGYEVHHQKL-VFFAEDVGSNKGAIIGLMVGGV-VIA). An Agilent 8453 UV-visible (UV-vis) spectrophotometer (Santa Clara, CA, USA) was used to measure optical spectra. Anaerobic reactions were performed in an N₂-filled glove box (Korea Kiyon, Bucheon-si, Gyeonggi-do, Korea). Transmission electron microscopic (TEM) images were taken using a Philips CM-100 transmission electron microscope (Microscopy and Image Analysis Laboratory, University of Michigan, Ann Arbor, MI, USA) or a JEOL JEM-2100 transmission electron microscope (UNIST Central Research Facilities, Ulsan National Institute of Science and Technology, Ulsan, Republic of Korea). Absorbance values for cell viability assay were measured on a SpectraMax M5 microplate reader (Molecular Devices, Sunnyvale, CA, USA). All ion mobility–mass spectrometry (IM–MS) experiments were carried out on a Synapt G2 (Waters, Milford, MA, USA). NMR studies of A β with **DMPD** were conducted on a 900 MHz Bruker spectrometer equipped with a TCI triple-resonance inverse detection CryoProbe (Michigan State University, Lansing, MI, USA).

3.4.2. A β Aggregation Experiments

Experiments with A β were conducted according to previously published methods.¹⁸⁻²² A β_{40} or A β_{42} was dissolved in ammonium hydroxide (NH₄OH, 1% v/v aq), aliquoted, lyophilized overnight, and stored at -80 °C. For experiments described herein, a stock solution of A β was prepared by dissolving lyophilized peptide in 1% NH₄OH (10 μ L) and diluting with ddH₂O. The concentration of A β peptides in the solution was determined by measuring the absorbance of the solution at 280 nm ($\epsilon = 1450 \text{ M}^{-1}\text{cm}^{-1}$ for A β_{40} ; $\epsilon = 1490 \text{ M}^{-1}\text{cm}^{-1}$ for A β_{42}). The peptide stock solution was diluted to a final concentration of 25 μ M in Chelex-treated buffered solution containing HEPES [4-(2-hydroxyethyl)-1-piperazineethanesulfonic acid (20 μ M); pH 6.6 for Cu(II) samples; pH 7.4 for metal-free and Zn(II) samples] and NaCl (150 μ M). For the inhibition studies, **DMPD** [50 μ M; 1% v/v dimethyl sulfoxide (DMSO)] was added to the samples of A β (25 μ M) in the absence and presence of a metal chloride salt (CuCl₂ or ZnCl₂, 25 μ M) followed by incubation at 37 °C with constant agitation for 24 h. For the disaggregation studies, A β with and without metal ions was incubated for 24 h at 37 °C with constant agitation prior to the treatment with a compound (50 μ M). The resulting A β aggregates were incubated with **DMPD** for 24 h at 37 °C with constant agitation.

3.4.3. Gel Electrophoresis and Western Blot

The samples from the inhibition and disaggregation experiments were analyzed by gel electrophoresis with Western blotting using an anti-A β antibody (6E10).¹⁸⁻²² Each sample (10 μ L) was separated on a 10–20% Tris-tricine gel (Invitrogen, Grand Island, NY, USA) and the protein samples were transferred onto nitrocellulose membrane which was blocked with bovine serum albumin (BSA, 3% w/v, Sigma-Aldrich, St. Louis, MO, USA) in Tris-buffered saline containing 0.1% Tween-20 (TBS-T; 1.0 mM Tris base, pH 8.0, 1.5 mM NaCl) for 2 h at room temperature. The membranes were incubated with a primary antibody (6E10, Covance, Princeton, NJ, USA; 1:2000) in a solution of 2% w/v BSA (in TBS-T) overnight at 4 °C. After washing with TBS-T (3x, 10 min), the horseradish peroxidase-conjugated goat antimouse secondary antibody (1:5000; Cayman Chemical Company, Ann Arbor, MI, USA) in 2% w/v BSA (in TBS-T) was added for 1 h at room temperature. SuperSignal West Pico Chemiluminescent Substrate (Thermo Scientific, Rockford, IL, USA) was used to visualize protein bands.

3.4.4. Transmission Electron Microscopy (TEM)

Samples for TEM were prepared according to previously reported methods.¹⁸⁻²² Glow-discharged grids (Formar/Carbon 300-mesh, Electron Microscopy Sciences, Hatfield, PA, USA) were treated with A β samples from the inhibition and disaggregation experiments (5 μ L) for 2 min at room temperature.

Excess buffer was removed by blotting carefully with filter paper then washed twice with ddH₂O. Each grid was incubated with uranyl acetate staining solution (1% w/v ddH₂O, 5 μ L) for 1 min. Excess stain was blotted off and the grids were air dried at room temperature for at least 20 min. Images from each sample were taken on a Philips CM-100 (80 kV) or a JEOL JEM-2100 TEM (200 kV) at 25,000x magnification.

3.4.5. Computational Procedure

A multistep computational strategy was utilized to explore A β ₄₀-**DMPD** interactions. In the first step, 100 ns MD simulations in an aqueous solution were conducted to obtain the equilibrated structure of the A β ₄₀ monomer. These simulations were performed using the GROMACS program (version 4.0.5)⁴⁷ and GROMOS96 53A6 force field.⁴⁸ The starting structure of the A β ₄₀ monomer was extracted from the NMR structures determined in aqueous SDS micelles at pH 5.1 (model 2, PDB 1BA4).⁴⁹ The root-mean-square deviations (RMSD) indicated that the system reached the equilibration during the time frame of the simulations. In the next step, to include the flexibility of the A β ₄₀ monomer into the docking procedure, 100 snapshots were taken at 1 ns interval throughout the simulation. These snapshots were used for the rigid docking of the **DMPD** molecule using the AutoDock Vina 1.1.2 software.⁵⁰ In this procedure, the receptor was kept fixed, but the ligand was allowed to change its conformation. The **DMPD** molecule was built using the GaussView program (B3LYP/Lan13DZ)^{51,52} and optimized at the level of theory using the Gaussian03 program.⁵³ In the docking procedure, the size of the grid was chosen to occupy the whole receptor–ligand complex. Each docking trial produced 20 poses with an exhaustiveness value of 20. The docking procedure provided 2000 poses. Based on binding energies and the composition of interacting sites, 20 distinct poses were selected for short-term (5 ns) MD simulations in an aqueous solution. From these 20 different simulations, 5 structures were derived and further 20 ns simulations were performed using the same program and force field. These simulations provided a binding site that includes L17, F19, and G38 residues of the A β ₄₀ monomer. The tools available in the GROMACS program package and the YASARA software (v. 13.2.2)⁵⁴ were utilized for analyzing trajectories and simulated structures.

For all simulations, the starting structures were placed in a truncated cubic box with dimensions of 7.0 \times 7.0 \times 7.0 nm. This dismissed unwanted effects that may arise from the applied periodic boundary conditions (PBC). The box was filled with single point charge (SPC) water molecules. Few water molecules were replaced by sodium and chloride ions to neutralize the system. The starting structures were subsequently energy-minimized with a steepest descent method for 3000 steps. The results of these minimizations produced the starting structure for the MD simulations. The MD simulations were then carried out with a constant number of particles (N), pressure (P), and temperature (T) [*i.e.*, NPT

ensemble]. The SETTLE algorithm was used to constrain the bond length and angle of the water molecules,⁵⁵ while the LINCS algorithm was used to constrain the bond length of the peptide.⁵⁶ The Particle-Mesh Ewald (PME) method was implemented to treat the long-range electrostatic interactions.⁵⁷ A constant pressure of 1 bar was applied with a coupling constant of 1.0 ps. The peptide, water molecules, and ions were coupled separately to a bath at 300 K with a coupling constant of 0.1 ps. The equation of motion was integrated at each 2 fs time steps using leap-frog algorithm.⁵⁸

3.4.6. 2D Band-Selective Optimized Flip-Angle Short Transient (SOFAST)–Heteronuclear Multiple Quantum Correlation (HMQC) NMR Spectroscopy

NMR titration experiments were performed following a previously reported method.^{20,21,31} NMR samples were prepared with ¹⁵N-labeled A β ₄₀ (rPeptide, Bogart, GA, USA) which was lyophilized in 1% NH₄OH by resuspending the peptide in 100 μ L of 1 mM NaOH (pH 10). The peptide was then diluted with 200 mM phosphate buffer (pH 7.4), 1 M NaCl, D₂O, and water to yield a final peptide concentration of 80 μ M. Each spectrum was obtained using 256 complex t_1 points and a 1 sec recycle delay at 4 °C. The 2D data were processed using TopSpin 2.1 (Bruker, Billerica, MA, USA). Resonance assignments were carried out by computer-aided resonance assignment (CARA) using published assignments for A β as a guide.^{59,60} Compiled chemical shift perturbation (CSP) was calculated using the following equation:

$$\Delta\delta_{NH} = \sqrt{\left(\Delta\delta H^2 + \left(\frac{\Delta\delta N}{5}\right)^2\right)}$$

3.4.7. Cu K-edge X-ray Absorption Spectroscopy

A β ₄₂ was monomerized as previously described.^{61,62} A β ₄₂ fibrils were grown according to established protocols.⁶³ Following monomerization or fibrillization, all samples were handled under an anaerobic atmosphere (N₂) in a COY anaerobic chamber (COY Laboratory, Grass Lake, MI, USA). A β ₄₂ was dissolved in a 4:1 mixture of 10 mM *N*-ethylmorpholine buffer (pH 7.4) and glycerol (glycerol is used as a deicing agent) followed by addition of one equivalent of CuCl₂. A β ₄₂ monomers were maintained at 5 °C and all procedures performed rapidly to avoid aggregation. Following the addition of CuCl₂, 2 equiv of ascorbate was treated with the resulting samples to reduce the Cu(II)-loaded A β ₄₂ peptides to Cu(I). **DMPD** (2 equiv; in DMSO) was then introduced to each solution. Final A β ₄₂ concentrations were 250 μ M. **DMPD** was incubated with the copper-loaded fibrils for 24 h. To avoid aggregation [confirmed by gel permeation chromatography studies];^{61,62} copper-loaded A β ₄₂ monomers were incubated for 15 min.

Following incubation with **DMPD**, the solutions were injected into Lucite sample holders with Kapton tape windows and quickly frozen in liquid nitrogen. All data were recorded on beamline X-3b at the National Synchrotron Light Source (Brookhaven National Laboratories, Upton, NY, USA). Samples were maintained at ~18 K throughout data collection by means of a He Displex cryostat. Energy monochromatization was accomplished with a Si(111) double crystal monochromator and a low angle Ni mirror was used for harmonic rejection. Data were collected as fluorescence spectra using a Canberra 31 element Ge solid-state detector with a 3 micron Ni filter placed between the sample and detector, and calibrated against a simultaneously collected spectrum of Cu-foil (first inflection point 8980.3 eV). Count rates were between 15–30 kHz, and deadtime corrections yielded no improvement to the quality of the spectra. Data were collected in 5 eV steps from 20–200 eV below the edge (averaged over 1 sec), 0.5 eV steps from 20 eV below the edge to 30 eV above the edge (averaged over 3 sec), 2 eV steps from 30–300 eV above the edge (averaged over 5 sec), and 5 eV steps from 300 eV above the edge to 13 k (averaged over 5 sec). Each data set represents the average of 16 individual spectra. Known glitches were removed from the averaged spectra. The X-ray beam was repositioned every 4 scans, and no appreciable photodamage/photoreduction was noted. Data were analyzed as previously reported using the software packages EXAFS123 and FEFF 7.02. Errors are reported as ϵ^2 values.^{64,65}

3.4.8. Mass Spectrometric Studies

All ion mobility–mass spectrometry (IM–MS) experiments were carried out on a Synapt G2 (Waters, Milford, MA, USA). Samples were ionized using a nano-electrospray source operated in positive ion mode. MS instrumentation was operated at a backing pressure of 2.7 mbar and a sample cone voltage of 40 V. Data were analyzed using MassLynx 4.1 and DriftScope 2.0 (Waters, Milford, MA, USA). The m/z scale was calibrated using 20 mg/ml aqueous cesium iodide. Accurate mass values for covalently bound ligands were calculated using the monoisotopic peak difference between *apo* and ligand bound states. Collision cross-section (CCS) measurements were calibrated externally using a database of known protein, and protein complex CCS values in helium^{66,67} with errors reported as the least square analysis output for all measurements. This least square analysis combines inherent calibrant error from drift tube measurements (3%), the calibration R^2 error and two times the replicate standard deviation error. Lyophilized A β_{40} (AnaSpec, Fremont, CA, USA) was prepared at a concentration of 25 μ M in 1 mM ammonium acetate (pH 7.0). Aliquots of A β_{40} were then incubated with or without 50 μ M **DMPD** or **BQ** (1% v/v DMSO) for 24 h at 25 °C without constant agitation. After incubation, all samples were lyophilized overnight prior to re-suspension of the samples in hexafluoro-2-propanol (HFIP, Sigma-Aldrich, St Louis, MO, USA) ([A β_{40}] = 50 μ M) and sonicated under pulse settings for 5 min. Samples

were diluted 50%, to a final A β ₄₀ concentration of 25 μ M, using 1 mM ammonium acetate (0.5 mM final concentration) immediately prior to mass analysis.

3.4.9. Animals and Drug Administration

Animal studies using the 5 \times FAD mouse model of AD were performed in accordance with the Guidelines for Laboratory Animal Care and Use of the Asan Institute for Life Sciences, Asan Medical Center (Seoul, Korea). 5 \times FAD transgenic mice overexpressing mutant human APP695 [K670N/M671L (Swedish), I716V (Florida), and V717I (London)] and PSEN1 (M146L and L286V) are characterized by early development of pathological marks of AD, such as A β deposits, neurodegeneration, and behavioral disabilities.²⁹ 5 \times FAD mice were produced and maintained on a B6/SJL hybrid background with free access to chow and drinking water under a 12 h light/dark cycle.

In this study, female and male 5 \times FAD mice were daily administered with freshly prepared vehicle (1% v/v DMSO in 20 mM HEPES, pH 7.4, 150 mM NaCl) or **DMPD** (1 mg/kg of body weight) by intraperitoneal injection for 30 days using Ultra-FineTM II insulin syringes (Becton Dickinson, Franklin Lakes, NJ, USA), starting from three months of age. The animals were weighed immediately before the injection. After the final injection and behavioral assessment, the mice were sacrificed under deep anesthesia. A necropsy was performed to evaluate the drug-induced systemic damage.

3.4.10. Tissue Preparation

The right cerebral hemispheres were snap-frozen with liquid nitrogen for biochemical analyses. 12- μ m-thick sagittal sections were collected from the left hemispheres using a cryostat (HM550; Microm, Walldorf, Germany) and mounted onto 1% poly-L-lysine-coated glass slides for histological evaluations.

3.4.11. A β ₄₀/A β ₄₂ Quantification

The right hemispheres were subjected to sandwich ELISA assays for quantitative measurement of A β ₄₀ and A β ₄₂ in the whole brain according to previously described methods.^{22,68} Briefly, the protein homogenates were prepared in PBS (pH 7.4) containing CompleteTM Protease Inhibitor cocktail (Roche Diagnostics, Mannheim, Germany), in 2% SDS (aq), and then in 70% formic acid (FA) by serial centrifugations. The EC buffer-diluted protein fractions were measured using the human A β ₄₀/A β ₄₂ ELISA kit (Invitrogen), where FA-fractions were neutralized with 1 M Tris (pH 11.0). The colorimetric quantifications were determined at 450 nm with the Synergy H1 Hybrid microplate reader (BioTek, Winooski, VT, USA), and the cerebral A β ₄₀/A β ₄₂ levels were calculated as moles per gram of wet brain tissue.

3.4.12. Quantification of A β Plaques

In order to examine the extracellular A β deposits, immunohistochemistry was conducted on the brain sections using an anti-human A β_4 (17-24) antibody (4G8, 1:1000; Covance, Princeton, NJ, USA). After immunological reactions with 4G8 and biotinylated anti-mouse secondary antibody (Vector Laboratories, Burlingame, CA, USA), the tissue sections were developed with 0.015% diaminobenzidine and 0.001% H₂O₂ (in PBS; Vector Laboratories) and examined under a light microscope (Eclipse 80i; Nikon, Tokyo, Japan). In addition, the congophilic amyloid plaques were detected by staining the tissues with Accustain[®] Congo Red amyloid staining solution (Sigma-Aldrich, St. Louis, MO, USA). The loads of amyloid deposits in the cortex were given as the percent area of 4G8-immunoreactive deposits or the total number of congophilic plaques in the randomly selected cortex areas.

3.4.13. Behavioral Evaluation

Spatial learning and memory performance was tested using the Morris water maze (MWM) task.²² The maze consisted of a circular water pool with a cylindrical platform (15 cm in diameter) hidden 0.5 cm under the surface of opaque water at the center of a target quadrant. The mice experienced three trials every day to swim and locate the hidden platform for a maximum of 60 sec, which were performed at 3 h after each drug injection over a period of five consecutive days starting on the day of the 26th drug-injection. The time and swimming track spent to reach the platform were analyzed on SMART Video Tracking System (Harvard Apparatus, Holliston, MA, USA). Three hours after the final MWM task, the mice entered the water again to swim without the platform for 60 sec and the time spent in each quadrant area was recorded.

3.4.14. Statistics

All values are presented as the means \pm standard errors of the mean (SEMs). Statistical analysis was performed using the unpaired t-test, or the one-way analysis of variance (ANOVA) followed by a Student-Neuman-Keuls post hoc test. Differences with P values < 0.05 were considered significant.

3.4.15. Trolox Equivalent Antioxidant Capacity (TEAC) Assay

The assay was performed according to previously reported methods with slight modifications.²¹ To generate turquoise ABTS cation radicals [ABTS^{•+}; ABTS = 2,2'-azino-bis(3-ethylbenzothiazoline-6-sulfonic acid)] diammonium salt; Sigma-Aldrich, St Louis, MO, USA], ABTS (7.0 mM) with potassium persulfate (2.5 mM) was dissolved in 5 mL water and incubated for 16 h in the dark at room temperature.

The resulting solution of ABTS^{•+} was diluted with EtOH to obtain an absorbance of *ca.* 0.7 at 734 nm. ABTS^{•+} solution (200 μ L) was added to the wells of a clear 96 well plate and incubated at 30 °C for 5 min in the plate reader. Various final concentrations of **DMPD** or Trolox (Trolox = 6-hydroxy-2,5,7,8-tetramethylchroman-2-carboxylic acid; dissolved in EtOH) were added and incubated with the ABTS^{•+} solution at 30 °C for 10 min. The percent inhibition was calculated according to the measured absorbance at 734 nm [% inhibition = 100 \times (A₀ - A)/A₀] and was plotted as a function of ligand concentration. The TEAC value of compounds was calculated as a ratio of the slope of the compound to that of Trolox. The measurements were carried out in triplicate.

3.4.16. Parallel Artificial Membrane Permeability Adapted for the Blood-Brain Barrier (PAMPA-BBB) Assay.

PAMPA-BBB experiments were carried out using the PAMPA Explorer kit (*p*ION Inc., Billerica, MA, USA) with modification to previously reported protocols.^{19,21} Each stock solution was diluted with Prisma HT buffer (pH 7.4, *p*ION) to a final concentration of 25 mM (1% v/v final DMSO concentration). The resulting solution was added to wells of the donor plate (200 μ L, number of replicates = 12). BBB-1 lipid formulation (5 μ L, *p*ION) was used to coat the polyvinylidene fluoride (PVDF, 0.45 μ M) filter membrane on the acceptor plate. This acceptor plate was placed on top of the donor plate forming a sandwich. Brain sink buffer (BSB, 200 μ L, *p*ION) was added to each well of the acceptor plate. The sandwich was incubated for 4 h at ambient temperature without stirring. UV-vis spectra of the solutions in the reference, acceptor, and donor plates were measured using a microplate reader. The PAMPA Explorer software v. 3.5 (*p*ION) was used to calculate $-\log P_e$ for each compound. CNS+/- designations were assigned by comparison to compounds that were identified in previous reports.^{19,21}

3.4.17. Metabolic Stability Measurements

From a stock solution of **DMPD** (500 mM), diluted solutions (final concentrations of 5 mM and 10 mM; 150 μ L) were prepared in phosphate buffered saline (PBS). For the assay, a buffer solution [50 mM phosphate buffer (pH 7.4), 1 mM EDTA (pH 8), and 3 mM MgCl₂] and a solution of NADPH (10 mM in ddH₂O) were prepared. To an eppendorf tube, buffer (1308.75 μ L), 10 mM NADPH (37.5 μ L), and **DMPD** (150 μ L) were added. Then, human liver microsomes (3.75 μ L) were treated and the resulting solution was briefly vortexed. Immediately, an aliquot of the resulting solution (150 μ L) was thoroughly mixed with acetonitrile (CH₃CN; 150 μ L) in a plastic HPLC vial and then sealed. Aliquots were taken every 30 min for 4 h for analysis. Samples were analyzed by high performance liquid chromatography [for the sample containing **DMPD** (0.5 mM), stationary: 95% CH₃CN and 5% H₂O, mobile: 95% H₂O,

5% CH₃CN, and 0.1% formic acid; for the sample containing **DMPD** (1 mM), stationary: 95% CH₃CN and 5% H₂O, mobile: 95% H₂O and 5% CH₃CN]. The calculated concentrations from the aliquots were plotted against time (min). The line of best fit was calculated using the first-order kinetic equation $\{[A]_t = [A]_0 \times e^{-kt}$, where $[A]_0$ is the initial concentration of **DMPD**; t is time; k is the rate (dependent variable)}. The values of the rate (k) for **DMPD** (0.5 mM and 1.0 mM) were determined to be 6.5 nM/min and 15 nM/min, respectively. When the concentration was doubled, the rate also doubled, in agreement with first-order kinetics. Using a plot of the inverse of substrate concentration against the inverse of the rate, the values of V_{\max} (maximum rate) and K_M (binding constant) were calculated using the Lineweaver-Burk equation.

3.4.18. Cell Viability Measurements

The human neuroblastoma SK-N-BE(2)-M17 (M17) cell line was purchased from the American Type Culture Collection (ATCC, Manassas, VA, USA). The cell line was maintained in media containing 1:1 Minimum Essential Media (MEM; GIBCO, Life Technologies, Grand Island, NY, USA) and Ham's F12K Kaighn's Modification Media (F12K; GIBCO), 10% (v/v) fetal bovine serum (FBS; Atlanta Biologicals, Flowery Branch, GA, USA), 100 U/mL penicillin (GIBCO), and 100 mg/mL streptomycin (GIBCO). The cells were grown and maintained at 37 °C in a humidified atmosphere with 5% CO₂. M17 cells were seeded in a 96-well plate (15,000 cells in 100 µL per well) according to previously reported methods.¹⁸⁻²¹ These cells were treated with various concentrations of **DMPD** (0–10 µM, 1% v/v DMSO) in the absence and presence of CuCl₂ or ZnCl₂ (1:1 metal/ligand ratio) with and without Aβ₄₀ (Aβ:metal:ligand = 10:10:20 µM). After 24 h incubation at 37 °C, 25 µL MTT [3-(4,5-dimethylthiazol-2-yl)-2,5-diphenyltetrazolium bromide; 5 mg/mL in phosphate buffered saline (PBS), pH 7.4, GIBCO] was added to each well and the plates were incubated for 4 h at 37 °C. Formazan produced by the cells was dissolved in a solution containing *N,N*-dimethylformamide (DMF, 50% v/v aq, pH 4.5) and sodium dodecyl sulfate (SDS, 20% w/v) overnight at room temperature. Absorbance at 600 nm was measured on a microplate reader.

3.5. Acknowledgements

This work was supported by the University of Michigan Protein Folding Disease Initiative (to A.R., B.T.R., and M.H.L.) and the National Research Foundation of Korea (NRF) grant funded by the Korean government [NRF-2014S1A2A2028270 (to M.H.L. and A.R.); NRF-2014R1A2A2A01004877 (to M.H.L.)]; the 2015 Research Fund (Project Number 1.140101.01) of Ulsan National Institute of Science and Technology (UNIST) and the DGIST R&D Program of the Ministry of Science, ICT and Future

Planning of Korea (15-BD-0403) (to M.H.L.); the Asan Institute for Life Sciences, Asan Medical Center, Republic of Korea (2015-7012) and the Basic Science Research Program, National Research Foundation of Korea, Ministry of Education, Republic of Korea (NRF-2012R1A1A2006801) (to J.-Y.L.); the National Science Foundation (NSF) (CHE-1362662) (to J.M.S.); an NIH NCI award (R21CA185370) (to E.J.M.); the NSF (Grant Number 1152846) (to R.P.); the Global Ph.D. Fellowship (GPF) programs of the NRF funded by the Korean government (NRF-2014H1A2A1019838) (to Y.N.). All X-ray absorption studies were performed at the National Synchrotron Light Source (NSLS) in the Brookhaven National Laboratory. Use of the NSLS was supported by the U.S. Department of Energy, Office of Science, Office of Basic Energy Sciences, under Contract No. DE-AC02-98CH10886. Cu K-edge studies were performed on beamline X3-b, which is supported through the Case Center for Synchrotron Biosciences, which is funded through the National Institute of Biomedical Imaging and Bioengineering (NIH P30-EB-009998). We thank the UC Technology Accelerator for funding and an Institutional Clinical and Translational Science Award, NIH/NCR R Grant Number 1UL1RR026314-01. We also thank Dr. Akiko Kochi, and Thomas Paul for assistance for TEM measurement ($A\beta_{40}$ samples) and MD simulations, respectively.

3.6. References

- (1) Chiti, F.; Dobson, C. M. *Annu. Rev. Biochem.* **2006**, *75*, 333–366.
- (2) Beck, M. W.; Pithadia, A. S.; DeToma, A. S.; Korshavn, K. J.; Lim, M. H. Ligand design in medicinal inorganic chemistry Chapter 10 (Wiley, New York, 2014).
- (3) Jakob-Roetne, R.; Jacobsen, H. *Angew. Chem. Int. Ed.* **2009**, *48*, 3030–3059.
- (4) Derrick, J. S.; Lim, M. H. *ChemBioChem* **2015**, *16*, 887–898.
- (5) Alzheimer's Association. *Alzheimers Dement.* **2015**, *11*, 332–384.
- (6) Bales, K. R. *Expert. Opin. Drug. Discov.* **2012**, *7*, 281–297.
- (7) Barnham, K. J.; Masters, C. L.; Bush, A. I. *Nat. Rev. Drug Discov.* **2004**, *3*, 205–214.
- (8) Viles, J. H. *Coord. Chem. Rev.* **2012**, *256*, 2271–2284.
- (9) DeToma, A. S.; Salamekh, S.; Ramamoorthy, A.; Lim, M. H. *Chem. Soc. Rev.* **2012**, *41*, 608–621.
- (10) Kepp, K. P. *Chem. Rev.* **2012**, *112*, 5193–5239.
- (11) Rauk, A. *Chem. Soc. Rev.* **2009**, *38*, 2698–2715.
- (12) Que, E. L.; Domaille, D. W.; Chang, C. J. *Chem. Rev.* **2008**, *108*, 1517–1549.
- (13) Faller, P.; Hureau, C.; La Penna, G. *Acc. Chem. Res.* **2014**, *47*, 2252–2259.
- (14) Telpoukhovskaia, M. A.; Orvig, C. *Chem. Soc. Rev.* **2013**, *42*, 1836–1846.

- (15) Rodríguez-Rodríguez, C.; Telpoukhovskaia, M.; Orvig, C. *Coord. Chem. Rev.* **2012**, *256*, 2308–2332.
- (16) Savelieff, M. G.; DeToma, A. S.; Derrick, J. S.; Lim, M. H. *Acc. Chem. Res.* **2014**, *47*, 2475–2482.
- (17) Perez, L. R.; Franz, K. J. *Dalton Trans.* **2010**, *39*, 2177–2187.
- (18) Hindo, S. S.; Mancino, A. M.; Braymer, J. J.; Liu, Y.; Vivekanandan, S.; Ramamoorthy, A.; Lim, M. H. *J. Am. Chem. Soc.* **2009**, *131*, 16663–16665.
- (19) Choi, J.-S.; Braymer, J. J.; Nanga, R. P. R.; Ramamoorthy, A.; Lim, M. H. *Proc. Natl. Acad. Sci. USA.* **2010**, *107*, 21990–21995.
- (20) Hyung, S.-J.; DeToma, A. S.; Brender, J. R.; Lee, S.; Vivekanandan, S.; Kochi, A.; Choi, J.-S.; Ramamoorthy, A.; Ruotolo, B. T.; Lim, M. H. *Proc. Natl. Acad. Sci. USA* **2013**, *110*, 3743–3748.
- (21) Lee, S.; Zheng, X.; Krishnamoorthy, J.; Savelieff, M. G.; Park, H. M.; Brender, J. R.; Kim, J. H.; Derrick, J. S.; Kochi, A.; Lee, H. J.; Kim, C.; Ramamoorthy, A.; Bowers, M. T.; Lim, M. H. *J. Am. Chem. Soc.* **2014**, *136*, 299–310.
- (22) Beck, M. W.; Oh, S. B.; Kerr, R. A.; Lee, H. J.; Kim, S. H.; Kim, S.; Jang, M.; Ruotolo, B. T.; Lee, J.-Y.; Lim, M. H. *Chem. Sci.* **2015**, *6*, 1879–1886.
- (23) Sato, M.; Murakami, K.; Uno, M.; Nakagawa, Y.; Katayama, S.; Akagi, K.-i.; Masuda, Y.; Takegoshi, K.; Irie, K. *J. Biol. Chem.* **2013**, *288*, 23212–23224.
- (24) Li, H.-T.; Lin, D.-H.; Luo, X.-Y.; Zhang, F.; Ji, L.-N.; Du, H.-N.; Song, G.-Q.; Hu, J.; Zhou, J.-W.; Hu, H.-Y. *FEBS J.* **2005**, *272*, 3661–3672.
- (25) Chung, Y.-C.; Su, Y. O. *J. Chin. Chem. Soc.* **2009**, *56*, 493–503.
- (26) Evmiridis, N. P.; Sadiris, N. C.; Karayannis, M. I. *Analyst* **1990**, *115*, 1103–1107.
- (27) Modestov, A. D.; Gun, J.; Savotina, I.; Lev, O. *J. Electroanal. Chem.* **2004**, *565*, 7–19.
- (28) Meek, A. R.; Simms, G. A.; Weaver, D. F. *Can. J. Chem.* **2012**, *90*, 865–873.
- (29) Oakley, H.; Cole, S. L.; Logan, S.; Maus, E.; Shao, P.; Craft, J.; Guillozet-Bongaarts, A.; Ohno, M.; Disterhoft, J.; Van Eldik, L.; Berry, R.; Vassar, R. *J. Neurosci.* **2006**, *26*, 10129–10140.
- (30) Kirchmair, J.; Howlett, A.; Peironcelly, J. E.; Murrell, D. S.; Williamson, M. J.; Adams, S. E.; Hankemeier, T.; van Buren, L.; Duchateau, G.; Klaffke, W.; Glen, R. C. *J. Chem. Inf. Model.* **2013**, *53*, 2896–2907.
- (31) Savelieff, M. G.; Liu, Y.; Senthamarai, R. R. P.; Korshavn, K. J.; Lee, H. J.; Ramamoorthy, A.; Lim, M. H. *Chem. Commun.* **2014**, *50*, 5301–5303.
- (32) Cook, N. P.; Ozbil, M.; Katsampes, C.; Prabhakar, R.; Marti, A. A. *J. Am. Chem. Soc.* **2013**, *135*, 10810–10816.

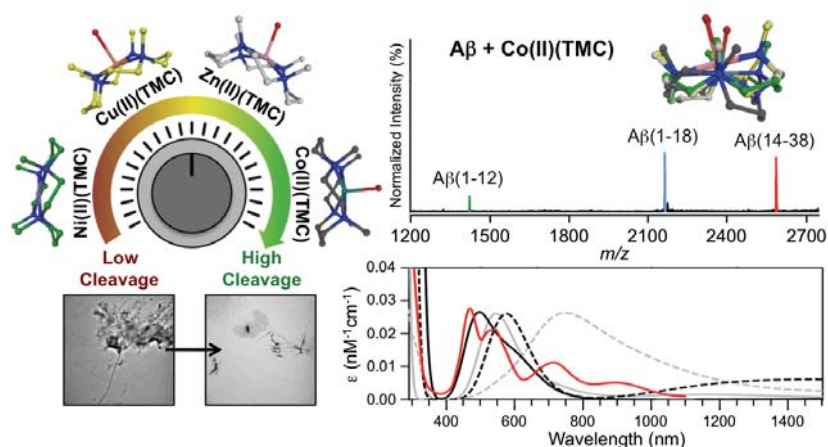
- (33) Echeverria, V.; Zeitlin, R.; Burgess, S.; Patel, S.; Barman, A.; Thakur, G.; Mamcarz, M.; Wang, L.; Sattelle, D. B.; Kirschner, D. A.; Mori, T.; Leblanc, R. M.; Prabhakar, R.; Arendash, G. W. *J. Alzheimers Dis.* **2011**, *24*, 817–835.
- (34) Shearer, J.; Szalai, V. A. *J. Am. Chem. Soc.* **2008**, *130*, 17826–17835.
- (35) See the Experimental Section.
- (36) Corbett, J. F. *J. Chem. Soc. B* **1969**, 213–216.
- (37) Wang, Z.; Li, X.; Wu, Y.; Tang, Y.; Ma, S. *J. Electroanal. Chem.* **1999**, *464*, 181–186.
- (38) Fisher, A. A.; Labenski, M. T.; Malladi, S.; Chapman, J. D.; Bratton, S. B.; Monks, T. J.; Lau, S. *S. Toxicol. Sci.* **2011**, *122*, 64–72.
- (39) Fisher, A. A.; Labenski, M. T.; Malladi, S.; Gokhale, V.; Bowen, M. E.; Milleron, R. S.; Bratton, S. B.; Monks, T. J.; Lau, S. *S. Biochemistry* **2007**, *46*, 11090–11100.
- (40) Bittner, S. *Amino Acids* **2006**, *30*, 205–224.
- (41) Hanzlik, R. P.; Harriman, S. P.; Fraunhoff, M. M. *Chem. Res. Toxicol.* **1994**, *7*, 177–184.
- (42) Bush, A. I.; Tanzi, R. E. *Neurotherapeutics* **2008**, *5*, 421–432.
- (43) Crouch, P. J.; Savva, M. S.; Hung, L. W.; Donnelly, P. S.; Mot, A. I.; Parker, S. J.; Greenough, M. A.; Volitakis, I.; Adlard, P. A.; Cherny, R. A.; Masters, C. L.; Bush, A. I.; Barnham, K. J.; White, A. R. *J. Neurochem.* **2011**, *119*, 220–230.
- (44) Walsh, D. M.; Klyubin, I.; Fadeeva, J. V.; Cullen, W. K.; Anwyl, R.; Wolfe, M. S.; Rowan, M. J.; Selkoe, D. J. *Nature* **2002**, *416*, 535–539.
- (45) Kaye, R.; Head, E.; Thompson, J. L.; McIntire, T. M.; Milton, S. C.; Cotman, C. W.; Glabe, C. G. *Science* **2003**, *300*, 486–489.
- (46) Steinerman, J. R.; Irizarry, M.; Scarmeas, N.; Raju, S.; Brandt, J.; Albert, M.; Blacker, D.; Hyman, B.; Stern, Y. *Arch. Neurol.* **2008**, *65*, 906–912.
- (47) Van Der Spoel, D.; Lindahl, E.; Hess, B.; Groenhof, G.; Mark, A. E.; Berendsen, H. J. *J. Comput. Chem.* **2005**, *26*, 1701–1718.
- (48) Oostenbrink, C.; Villa, A.; Mark, A. E.; van Gunsteren, W. F. *J. Comput. Chem.* **2004**, *25*, 1656–1676.
- (49) Coles, M.; Bicknell, W.; Watson, A. A.; Fairlie, D. P.; Craik, D. J. *Biochemistry* **1998**, *37*, 11064–11077.
- (50) Trott, O.; Olson, A. J. *J. Comput. Chem.* **2010**, *31*, 455–461.
- (51) Becke, A. D. *J. Chem. Phys.* **1993**, *98*, 5648–5652.
- (52) Becke, A. D. *Phys. Rev. A* **1988**, *38*, 3098–3100.

- (53) Gaussian 03, revision C.02. Frisch, M. J.; Trucks, G. W.; Schlegel, H. B.; Scuseria, G. E.; Robb, M. A.; Cheeseman, J. R.; Montgomery, Jr., J. A.; Vreven, T.; Kudin, K. N.; Burant, J. C.; Millam, J. M.; Iyengar, S. S.; Tomasi, J.; Barone, V.; Mennucci, B.; Cossi, M.; Scalmani, G.; Rega, N.; Petersson, G. A.; Nakatsuji, H.; Hada, M.; Ehara, M.; Toyota, K.; Fukuda, R.; Hasegawa, J.; Ishida, M.; Nakajima, T.; Honda, Y.; Kitao, O.; Nakai, H.; Klene, M.; Li, X.; Knox, J. E.; Hratchian, H. P.; Cross, J. B.; Bakken, V.; Adamo, C.; Jaramillo, J.; Gomperts, R.; Stratmann, R. E.; Yazyev, O.; Austin, A. J.; Cammi, R.; Pomelli, C.; Ochterski, J. W.; Ayala, P. Y.; Morokuma, K.; Voth, G. A.; Salvador, P.; Dannenberg, J. J.; Zakrzewski, V. G.; Dapprich, S.; Daniels, A. D.; Strain, M. C.; Farkas, O.; Malick, D. K.; Rabuck, A. D.; Raghavachari, K.; Foresman, J. B.; Ortiz, J. V.; Cui, Q.; Baboul, A. G.; Clifford, S.; Cioslowski, J.; Stefanov, B. B.; Liu, G.; Liashenko, A.; Piskorz, P.; Komaromi, I.; Martin, R. L.; Fox, D. J.; Keith, T.; Al-Laham, M. A.; Peng, C. Y.; Nanayakkara, A.; Challacombe, M.; Gill, P. M. W.; Johnson, B.; Chen, W.; Wong, M. W.; Gonzalez, C.; and Pople, J. A. Gaussian, Inc., Wallingford, CT, USA. (2004).
- (54) Krieger, E.; Vriend, G. *Bioinformatics* **2002**, *18*, 315–318.
- (55) Miyamoto, S.; Kollman, P. A. *J. Comput. Chem.* **1992**, *13*, 952–962.
- (56) Hess, B.; Bekker, H.; Berendsen, H. J. C.; Fraaije, J. G. E. M. *J. Comput. Chem.* **1997**, *18*, 1463–1472.
- (57) Darden, T.; York, D.; Pedersen, L. *J. Chem. Phys.* **1993**, *98*, 10089–10092.
- (58) Hockney, R. W.; Goel, S. P.; Eastwood, J. W. *J. Comput. Phys.* **1974**, *14*, 148–158.
- (59) Vivekanandan, S.; Brender, J. R.; Lee, S. Y.; Ramamoorthy, A. *Biochem. Biophys. Res. Commun.* **2011**, *411*, 312–316.
- (60) Yoo, S. I.; Yang, M.; Brender, J. R.; Subramanian, V.; Sun, K.; Joo, N. E.; Jeong, S.-H.; Ramamoorthy, A.; Kotov, N. A. *Angew. Chem. Int. Ed.* **2011**, *50*, 5110–5115.
- (61) Karr, J. W.; Akintoye, H.; Kaupp, L. J.; Szalai, V. A. *Biochemistry* **2005**, *44*, 5478–5487.
- (62) Karr, J. W.; Kaupp, L. J.; Szalai, V. A. *J. Am. Chem. Soc.* **2004**, *126*, 13534–13538.
- (63) Karr, J. W.; Szalai, V. A. *Biochemistry* **2008**, *47*, 5006–5016.
- (64) Shearer, J.; Soh, P. *Inorg. Chem.* **2007**, *46*, 710–719.
- (65) Bunker, G.; Hasnain, S. S.; Sayers, D. (Hasnain, S. S. Eds.) X-ray absorption fine structure 751–770 (Ellis Horwood, New York, 1991).
- (66) Ruotolo, B. T.; Benesch, J. L. P.; Sandercock, A. M.; Hyung, S.-J.; Robinson, C. V. *Nat. Protoc.* **2008**, *3*, 1139–1152.
- (67) Bush, M. F.; Hall, Z.; Giles, K.; Hoyes, J.; Robinson, C. V.; Ruotolo, B. T. *Anal. Chem.* **2010**, *82*, 9557–9565.

- (68) Oh, S. B.; Byun, C. J.; Yun, J.-H.; Jo, D.-G.; Carmeliet, P.; Koh, J.-Y.; Lee, J.-Y. *Neurobiol. Aging* **2014**, *35*, 511–519.

Chapter 4.

Tunable Divalent Metal Tetramethylcyclam Complexes: Hydrolytic Reactivities Toward Amyloidogenic Proteins and Mechanisms



I thank Professor Jaeheung Cho and Hyeonwoo Tak for their assistance with the synthesis and X-ray crystallography, Professor Kiyoun Park and Jiwan Lee for the DFT calculations, Dr. Sun Hee Kim and Yujeong Kim for EPR analysis, Dr. Shin Jung C. Lee for MS investigations, and Eunju Nam for cell viability studies. I grew the crystals for X-ray analysis, performed the gel/Western blot, TEM, and UV-vis speciation and mechanistic studies. I was also instrumental in the experimental design and proposal of an overall mechanistic understanding as well as the writing of the manuscript with the assistance of Professor Lim.

4.1. Introduction

A comprehensive understanding of the etiology of Alzheimer's disease (AD), the most common form of dementia, is still elusive even after more than a century of research. The consequence of our inability to unravel the intricacies of AD pathology has directly impeded the design and development of effective strategies against the disorder.¹⁻⁵ As a result, the numbers affected by AD have continued to rise.⁶ Such an increase in prevalence translates into billions of dollars annually to provide the necessary care and resources.⁶ Therefore, in order to reverse these trends, more significant efforts to decipher the disease etiology and modes of actions of existing preventative strategies must be made.¹

Since senile plaques predominately composed of amyloid- β ($A\beta$), an aggregation-prone peptide known to assemble into distinctive fibrillar structures, have been identified as a hallmark of AD, a wealth of data has accumulated implicating it as a key contributor to neurodegeneration.^{1-5,7-9} Unfortunately, a detailed molecular-level understanding has yet to be resolved. Current focus has been on the soluble oligomers that have been suggested to be relatively more toxic than the fibrils.^{1-5,7,8} Traditionally, small molecule inhibitors have been used to target the self-recognition sequence (*i.e.*, KLVFF) and the hydrophobic C-terminus of $A\beta$ to prevent its aggregation.^{1,4,7,8} As a new approach, the utilization of transition metal complexes able to modulate the aggregation of $A\beta$ has recently emerged.⁷⁻¹⁶ In addition to their ability to catalyze difficult chemical reactions that are not easily facilitated by organic molecules, the capacity of metal complexes to access various oxidation states, coordination numbers, and stereochemistry can further endow singular approaches as well as provide a degree of tunability that is not easily achieved in small molecules.⁷⁻¹⁶ One such approach to amyloid management is the cleavage of $A\beta$'s amide bonds to produce peptide fragments that generate off-pathway and less toxic species. Co(III)(cyclen) derivatives (the structure of cyclen is shown in Figure 4.1) have been reported to hydrolyze the unactivated amide bonds in $A\beta$ and other non-amyloidogenic and biologically essential proteins.^{7,17-23} Given the high stability of amide bonds under physiological conditions (*i.e.*, half-life of *ca.* 200 years), it is remarkable that such simple metal complexes are able to catalyze the reaction.^{20,22} Unfortunately, apart from a single study, very little has been carried out to understand and utilize this approach for amyloid management.²⁰ For example, in an effort to achieve some degree of selectivity, more than eight-hundred Co(III)(cyclen) derivatives augmented with exotic organic linkers were generated; however, only two complexes exhibited cleavage activity.²⁰ This synthetically cumbersome tactic identifies our limited comprehension of this methodology and thus retards our ability to rationally design effective metal complexes for

peptide cleavage. Instead of using and evaluating such metal complexes, these macrocyclic polyamine ligands (*i.e.*, cyclen and cyclam; Figure 4.1) have been mostly employed as exogenous metal chelators to combat metal-facilitated A β toxicity.^{7,19,24-29} In addition to the inherent problems associated with metal chelation therapy in AD,¹ these ligands, due to the macrocyclic effect, possess high binding affinities and poor metal ion selectivity which may severely limit their biological applications.^{7,19,24-29} Furthermore, unlike macrocyclic polyamine metal complexes, the *apo* ligands (*i.e.*, cyclen and cyclam) are unable to modulate metal-free A β which also aggregates to produce toxic oligomers.^{1,2,4,19,24,27-29} Therefore, it is clear that further studies are warranted into the generation and application of metal macrocyclic polyamine complexes as hydrolytic cleavage agents.

Herein, we report a novel approach to tune the hydrolytic cleavage activity of a series of divalent metal tetra-*N*-methylated cyclam complexes [M(II)(TMC); M = Co, Ni, Cu, and Zn; where M(II)(TMC) is used as an abbreviation for our complexes rather than describing the exact coordination sphere] based on the choice of metal centers. TMC was selected for its distinct properties (*e.g.*, stereochemistry, coordination number) and its ability to accommodate different oxidation and spin states of the metal centers, which we predicted would impart different reactivities of M(II)(TMC) from those of the analogous cyclen complexes, and for the simplicity through which they can be synthesized and structurally modified. Interestingly, among the four M(II)(TMC) complexes, only Co(II)(TMC) is able to significantly inhibit A β aggregation and disassemble preformed A β fibrils. Mass spectrometric investigations reveal that all M(II)(TMC) complexes possess varying capacities to hydrolyze A β . The anti-amyloidogenic activity of Co(II)(TMC) is suggested to be a result of its enhanced aptitude to hydrolyze A β , relative to that of the other complexes.

Through studies by UV-visible (UV-vis) and electron paramagnetic resonance (EPR) spectroscopy [including electron nuclear double resonance (ENDOR) and electron spin echo envelope modulation (ESEEM)], X-ray crystallography, and density function theory (DFT), it has been indicated that the superior cleavage activity of Co(II)(TMC) may be attributed to a combination of its distorted structure which promotes more facile substrate entry and the formation of its more stable pentacoordinate aqua complex which can more easily facilitate the generation of nucleophilic hydroxide anions, relative to the other complexes. In addition, the biological applicability of Co(II)(TMC) is suggested showing its potential blood-brain barrier (BBB) permeability, relatively low cytotoxicity, and preferential cleavage of amyloidogenic proteins over highly structured proteins, such as ubiquitin.³⁰ Taken together, our studies not only

represent, to the best of our knowledge, the first Co(II) complex able to modulate the aggregation pathways of A β *via* hydrolytic cleavage, but also that the degree of hydrolytic excision can be easily tuned through the choice of the metal center. Moreover, the balance between cleavage efficiency and selectivity is established by our studies with Co(II)(TMC) showing that high potency is not required to affect the aggregation characteristics of amyloidogenic peptides. In fact, preference toward amyloidogenic peptides over biologically essential and highly structured peptides was achieved by sterically restraining the binding site. Finally, the mechanistic insights gleaned in our studies will be combined with the metal center dependence to direct the rational design of a series of next-generation tunable cleavage agents.

4.2. Results and Discussion

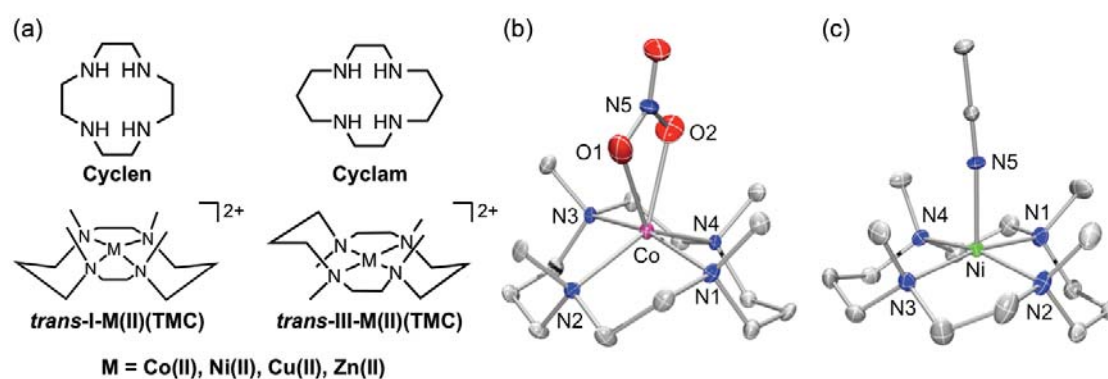


Figure 4.1. Chemical structures of macrocyclic polyamines and their metal complexes. (a) Chemical structures of cyclen, cyclam, and M(II)(TMC) (*trans*-I and *trans*-III isomers). Cyclen = 1,4,7,10-tetraazacyclododecane; cyclam = 1,4,8,11-tetraazacyclotetradecane; TMC = 1,4,8,11-tetramethyl-1,4,8,11-tetraazacyclotetradecane. ORTEP diagrams of (b) [Co(TMC)(NO₃)](NO₃) and (c) [Ni(TMC)(CH₃CN)](NO₃)₂ with ellipsoids drawn at the 30% probability level. Noncoordinated nitrate anions and hydrogen atoms are omitted for clarity. Selected distances (Å) and angles are summarized in Table 4.1.

4.2.1. Design Rationale and Preparation of M(II)(TMC) Complexes

In order to further probe the application of metal macrocyclic polyamine complexes as anti-amyloidogenic agents, a series of divalent metal tetramethylcyclam complexes, M(II)(TMC) [M = Co, Ni, Cu, and Zn; Figure 4.1a], were prepared and evaluated for their ability to modulate A β aggregation pathways. Instead of cyclen, TMC was chosen as the ligand for the metal complexes because of its distinctive stereochemistry (*e.g.*, *trans*-I *versus* *trans*-III; Figure 4.1a) and coordination spheres [*e.g.*, square planar, square pyramidal, trigonal bipyramidal (TBP), and

octahedral geometries], as well as its accommodation of different oxidation and spin states of the metal centers.³¹⁻³⁷ We hypothesize that such properties of TMC may confer a certain degree of tunability in their interactions with A β that is absent in the octahedral Co(III)(cyclen) complexes.^{26,31-37} In addition, M(II)(TMC) complexes can also be easily synthesized in high yields and modified *via* substitution reactions, which will aid in further development of more selective and reactive complexes.³¹ The M(II)(TMC) complexes were prepared following well-established methods of refluxing TMC and Co(NO₃)₂·6H₂O, Ni(NO₃)₂·6H₂O, Cu(ClO₄)₂·6H₂O, or Zn(ClO₄)₂·6H₂O for 12 h in CH₃CN.^{31,37}

4.2.2. Effects of M(II)(TMC) on A β Aggregation

To evaluate the ability of M(II)(TMC) complexes to influence the aggregation pathways of A β ₄₀ and A β ₄₂, gel electrophoresis with Western blotting (gel/Western blot) and transmission electron microscopy (TEM) were employed to analyze the molecular weight (MW) distribution and morphology of the resultant A β species, respectively. Two different experiments were conducted to determine the ability of M(II)(TMC) complexes to either prevent the aggregation of monomeric A β (Figure 4.2a) or to disassemble preformed A β fibrils into smaller species (Figure 4.3a). Under our experimental conditions, compound-untreated samples assemble into large aggregates that can be visualized by TEM, but are too large to penetrate into the gel matrix thus producing limited smearing on the gel/Western blot. The administration of compounds, able to interact with A β and either (i) inhibit the formation of high MW aggregates and/or (ii) disassemble preformed aggregates, typically generates a distribution of smaller A β species that are capable of entering into the gel and inducing a significant amount of smearing compared to the samples containing A β only.

In the inhibition experiment (Figure 4.2), a time-dependent change in the MW distribution of A β ₄₀ species was observed only for the samples treated with Co(II)(TMC). No smearing was discernable at the 4 h incubation time point; however, after 8 h, noticeable bands (*ca.* 10–15 and > 260 kDa) were identified and darker and more significant smearing was detected upon further incubation to 24 h (*ca.* 10–260 kDa; Figure 4.2b, top). The aptitude of Co(II)(TMC) to inhibit A β ₄₂ aggregation appeared to be diminished compared to A β ₄₀. A slight difference in the MW distribution of A β ₄₂ species was noticeable at the 4, 8, and 24 h time points (Figure 4.2b, bottom). Zn(II)(TMC) also seemed to slightly alter the MW distribution of A β ₄₂ at the 24 h time point in the gel/Western blot, but TEM images revealed mostly large clusters of fibrils, similar to those

observed in the samples containing $A\beta_{42}$ only and $A\beta_{42}$ treated with the ligand (TMC), $Cu(II)(TMC)$, and $Ni(II)(TMC)$ (Figure 4.2b,c). In agreement with the gel/Western blot data, a distinct transformation into a distribution of smaller, thinner, and needle-like species or amorphous aggregates (see the inset TEM image) was discerned upon incubation of $A\beta_{42}$ with $Co(II)(TMC)$ (Figure 4.2c).

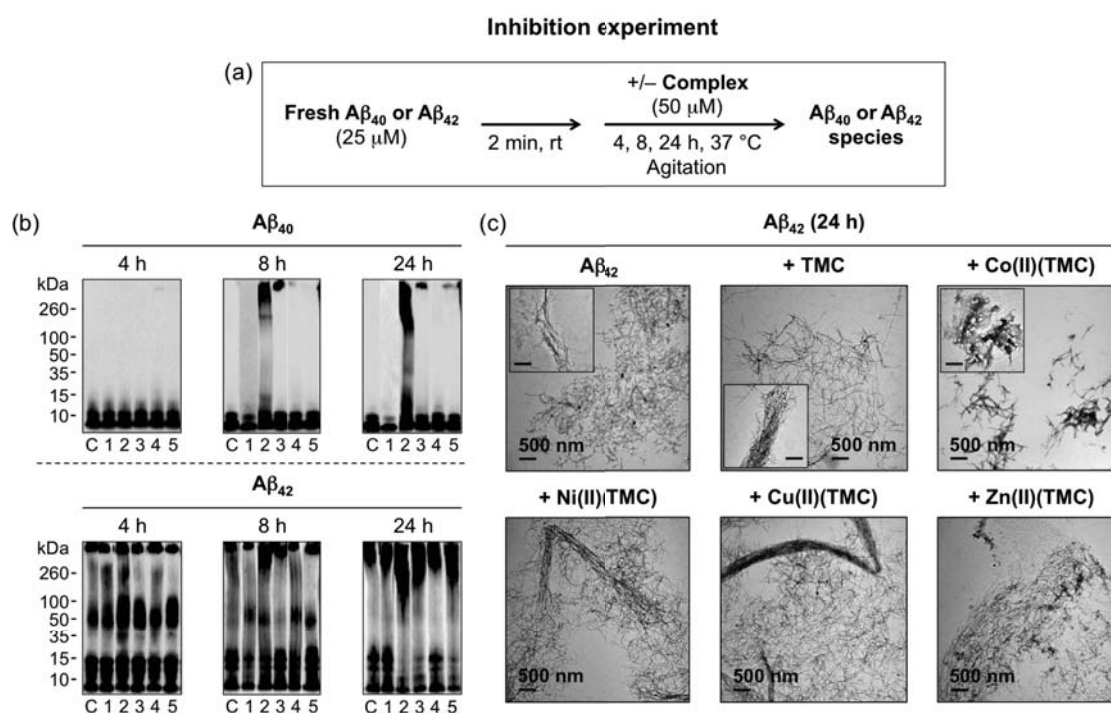


Figure 4.2. Capability of $M(II)(TMC)$ ($M = Co, Ni, Cu,$ and Zn) to control the aggregation pathways of $A\beta_{40}$ and $A\beta_{42}$. (a) Scheme of the inhibition experiment. (b) Analysis of the resultant $A\beta_{40}$ (top) and $A\beta_{42}$ (bottom) species from the inhibition experiment visualized by gel electrophoresis with Western blotting (gel/Western blot) using an anti- $A\beta$ antibody (6E10). Conditions: $A\beta$ ($25 \mu M$); $M(II)(TMC)$ ($50 \mu M$); incubated for 4, 8, or 24 h; pH 7.4; $37 \text{ }^\circ C$; constant agitation. Lanes: “C” denotes the control lane (without compound treatment); (1) $A\beta$ + TMC; (2) $A\beta$ + $Co(II)(TMC)$; (3) $A\beta$ + $Ni(II)(TMC)$; (4) $A\beta$ + $Cu(II)(TMC)$; (5) $A\beta$ + $Zn(II)(TMC)$. (c) TEM images for the $A\beta_{42}$ samples (24 h incubation) from (b). Insets represent the minor species.

Similar trends were also displayed in the disaggregation experiment (Figures 4.3 and 4.4). Only $Co(II)(TMC)$ was able to reverse the assembly of preformed $A\beta_{40}$ and $A\beta_{42}$ aggregates. The reactivity toward $A\beta_{40}$ also appeared to be correlated to the incubation period with no significant bands detected until 8 and 24 h (Figure 4.3b, top). Homologous to the $A\beta_{40}$ conditions, the extent to which $Co(II)(TMC)$ was able to disaggregate preformed $A\beta_{42}$ aggregates also varied with the length of incubation; however,

unlike $A\beta_{40}$, the most significant change in the MW distribution was discernable at the 4 h time point (Figure 4.3b, bottom). The dissimilarity may be attributed to the increased aggregation propensity of $A\beta_{42}$, relative to that of $A\beta_{40}$.^{1-5,7} Administration of Co(II)(TMC) also perturbed the morphologies of $A\beta_{40}$ and $A\beta_{42}$ aggregates from the deposits of large and long fibrils that were detected in the complex-untreated $A\beta$ controls to much smaller clusters of thin and needle-like species similar to those in the inhibition experiment (Figures 4.3c and 4.4).

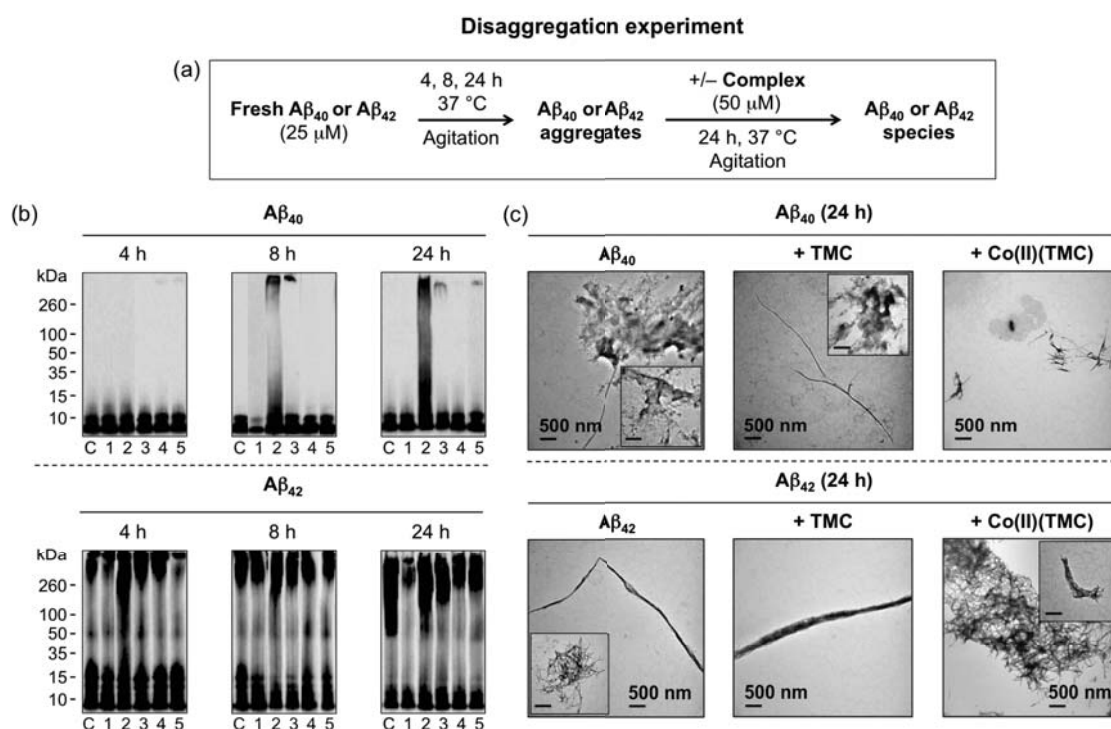


Figure 4.3. Ability of M(II)(TMC) (M = Co, Ni, Cu, and Zn) to disaggregate preformed $A\beta_{40}$ and $A\beta_{42}$ aggregates. (a) Scheme of the disaggregation experiment. (b) Analysis of the resultant $A\beta_{40}$ (top) and $A\beta_{42}$ (bottom) species from the disaggregation experiment visualized by gel electrophoresis with Western blotting (gel/Western blot) using an anti- $A\beta$ antibody (6E10). Conditions: $A\beta$ (25 μ M); M(II)(TMC) (50 μ M); incubated for 4, 8, or 24 h; pH 7.4; 37 °C; constant agitation. Lanes: “C” denotes the control lane (without compound treatment); (1) $A\beta$ + TMC; (2) $A\beta$ + Co(II)(TMC); (3) $A\beta$ + Ni(II)(TMC); (4) $A\beta$ + Cu(II)(TMC); (5) $A\beta$ + Zn(II)(TMC). (c) TEM images for the $A\beta_{40}$ and $A\beta_{42}$ samples (24 h incubation) from (b). Insets represent the minor species.

Our gel/Western blot and TEM investigations indicate that only Co(II)(TMC) is capable of modulating the aggregation pathways of $A\beta_{40}$ and $A\beta_{42}$, while Ni(II)(TMC), Cu(II)(TMC), and Zn(II)(TMC) do not, despite the relatively high affinity binding sites in $A\beta$ for Cu(II) and Zn(II)

(i.e., $K_d = ca. 10^{-9}$ M and 10^{-6} M, respectively).^{1-5,7} In addition, the time-dependent nature of Co(II)(TMC)'s reactivity, particularly in the disaggregation experiments, further suggests that Co(II)(TMC) may be interacting predominately with intermediate to high MW aggregates over monomeric A β because no reactivity is observed until A β has been pre-incubated with the complex for 8 or more hours (Figures 4.2 and 4.3). The potential preference of Co(II)(TMC) to interact with intermediate MW aggregates may also explain why the gel/Western blot studies showed the most significant smearing at the 4 h time point in the disaggregation experiments with the more aggregation-prone A β_{42} isoform.^{1-5,7}

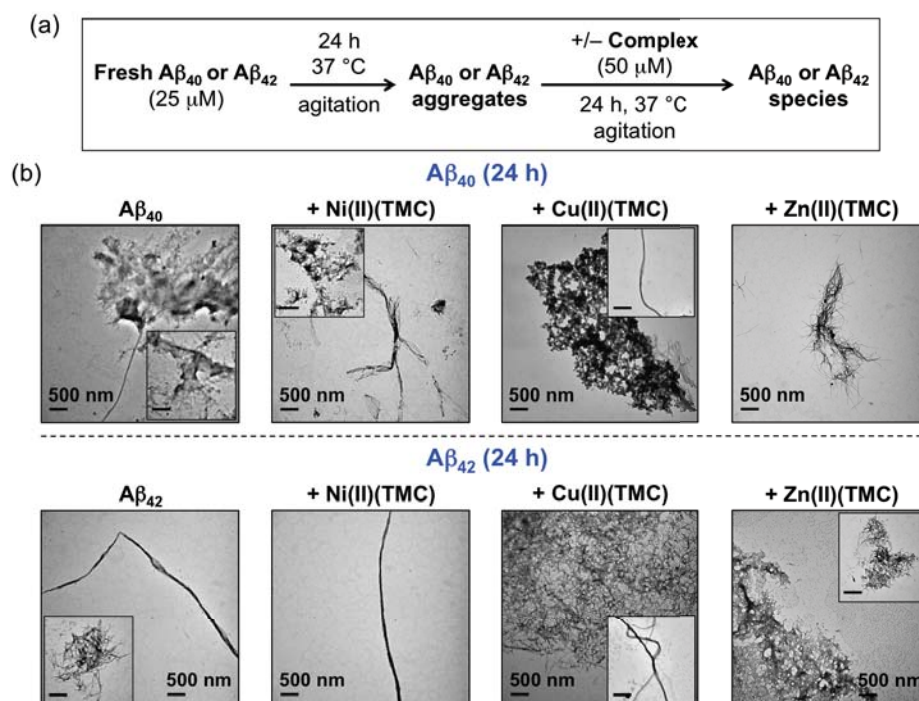


Figure 4.4. Ability of M(II)(TMC) (M = Ni, Cu, and Zn) to alter the morphology of preformed A β_{40} and A β_{42} aggregates. (a) Scheme of the disaggregation experiment. (b) TEM images for the A β_{40} and A β_{42} samples (24 h incubation). Insets represent the minor species.

4.2.3. Mechanistic Studies

(i) Competition Experiments: Evaluating the Strength of the Interaction Between Co(II)(TMC) and A β_{40}

In order to determine why only Co(II)(TMC) can noticeably affect the aggregation pathways of A β , detailed studies to elucidate a mode of action were performed. First, to evaluate the strength

of the interaction between Co(II)(TMC) and A β ₄₀, a competition experiment was conducted and monitored by gel/Western blot. Increasing amounts of sodium azide (NaN₃) and sodium cyanate (NaOCN) (0–200 equiv) were added into a reaction mixture containing fresh A β ₄₀ and Co(II)(TMC) (Figure 4.5a). Due to the sterics associated with all four *N*-methyl moieties positioned on the same side of the macrocyclic plane, M(II)(TMC) complexes bind most strongly to small and linear ligands, such as N₃[−], OCN[−], and OH[−], as opposed to larger ligands (*e.g.*, imidazole) to yield either square pyramidal or TBP structures (Figure 4.5c).^{26,31,32,34–48} Therefore, since the formation of octahedral M(II)(TMC) complexes is unlikely due to the folding down of the macrocyclic ring which prohibits binding of a ligand at the second axial position, Co(II)(TMC) can only interact with A β ₄₀, N₃[−], OCN[−], or H₂O/OH[−].^{26,31,32,34–48} Surprisingly, Co(II)(TMC) maintained its ability to inhibit A β ₄₀ aggregation in aqueous conditions until 100 equiv of NaOCN or 200 equiv of NaN₃ were present (Figure 4.5b).

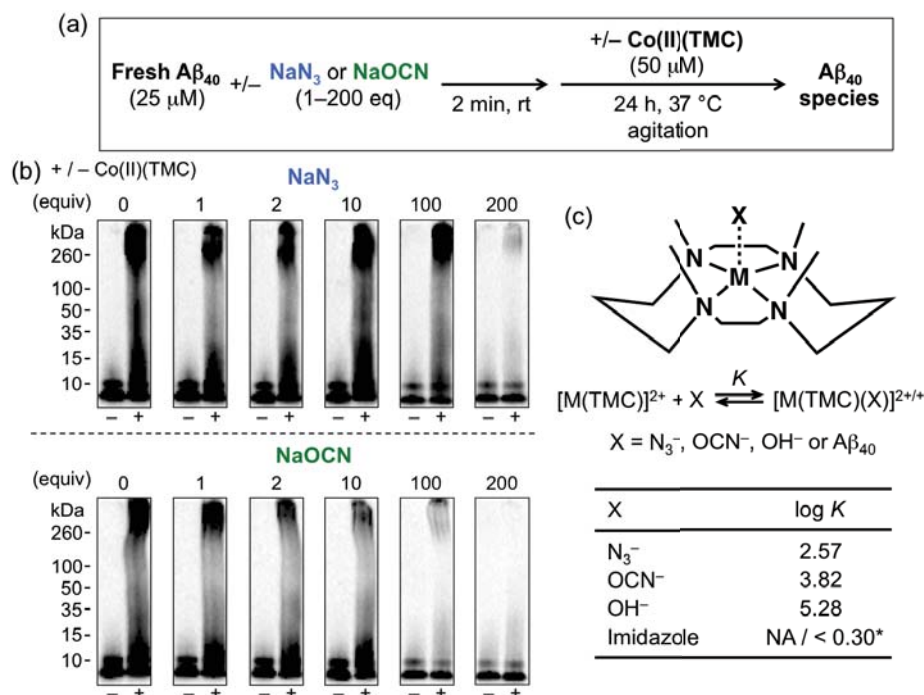


Figure 4.5. Competition experiments. (a) Reaction scheme. (b) Visualization of the A β ₄₀ species upon addition of sodium azide (NaN₃; 0–200 equiv; blue) or sodium cyanate (NaOCN; 0–200 equiv; green) by gel/Western blot utilizing an anti-A β antibody (6E10). Conditions: A β ₄₀ (25 μ M); NaN₃ or NaOCN (0–5 mM); Co(II)(TMC) (50 μ M); incubated for 24 h; pH 7.4; 37 $^\circ$ C; constant agitation. (c) Scheme and chemical equation of the complexation reaction of Co(II)(TMC) with the experimentally reported equilibrium constants obtained from spectrophotometric titrations.³³ *Indicates that the stability constant for the pentacoordinate imidazole complex was not obtained for Co(II)(TMC) and the reported value (< 0.30) is from Ni(II)(TMC).³²

Based on previously measured equilibrium constants for the formation of pentacoordinate Co(II)(TMC) complexes, these results likely suggest that Co(II)(TMC) does not interact with A β *via* ligand association with its histidine residues (*i.e.*, His6, His13, and His14) as has been extensively reported for most metal complexes.^{9-11,13-15,32} Equilibrium constants greater than 1 were reported for the formation of pentacoordinate Co(II)(TMC) with the axial coordination site occupied by OCN⁻ ($K = 3.82$), N₃⁻ ($K = 2.57$), and OH⁻ ($K = 5.28$) (Figure 4.5c).³² The larger equilibrium constant for OCN⁻ explains why only 100 equiv of NaOCN were required to prevent Co(II)(TMC) from inhibiting A β ₄₀ aggregation while 200 equiv were necessary for NaN₃ to produce similar results (Figure 4.5b,c).³² Coordination of an imidazole to Ni(II)(TMC) was indicated to be much less favorable ($K < 0.30$) (Figure 4.5c).³² The equilibrium constant for imidazole binding was determined only for Ni(II)(TMC) because of the sensitivity of its optical spectrum to changes in the coordination sphere; however, the equilibrium constant for imidazole binding to Co(II)(TMC) should be much less than those of N₃⁻, OCN⁻, and OH⁻ based on the trend reported by Micheloni *et al.* (Figure 4.5c).³² Collectively, these experiments suggest that (i) Co(II)(TMC) is able to competitively interact with A β most likely through an interaction that is independent of histidine coordination or that (ii) Co(II)(TMC)'s anti-amyloidogenic activity is dependent on the formation of an aqua or hydroxo complex ([Co(TMC)(H₂O)]²⁺ or [Co(TMC)(OH)]⁺) which may provide the nucleophilic hydroxide source required to catalyze the hydrolytic cleavage of amide bonds. The latter explanation would be the most consistent with the previously measured equilibrium constants and with our spectroscopic and time-dependent DFT (TDDFT) studies which identified the [M(TMC)(H₂O)]²⁺ complexes as the most thermodynamically stable species (*vide infra*).

(ii) Hydrolytic Cleavage of A β by M(II)(TMC) Complexes

In order to determine if the enhanced ability of Co(II)(TMC) to modulate A β aggregation is linked to protein fragmentation, matrix assisted laser desorption ionization–mass spectrometry (MALDI–MS) analyses were carried out on A β ₄₀ samples incubated for 24 h with M(II)(TMC) (Figure 4.6). An immediate difference was noticeable in the MALDI–MS spectrum for the A β ₄₀ samples treated with Co(II)(TMC). The normalized signal intensity of the singly-charged A β ₄₀ monomer peak (*i.e.*, A β ₄₀⁺) at 4328.15 m/z was noticeably reduced upon 24 h incubation with Co(II)(TMC) (Figure 4.6a). Such a significant signal suppression of the singly-charged A β ₄₀ monomer was not observed in the samples treated with Ni(II)(TMC), Cu(II)(TMC), or Zn(II)(TMC) (Figure 4.6a).

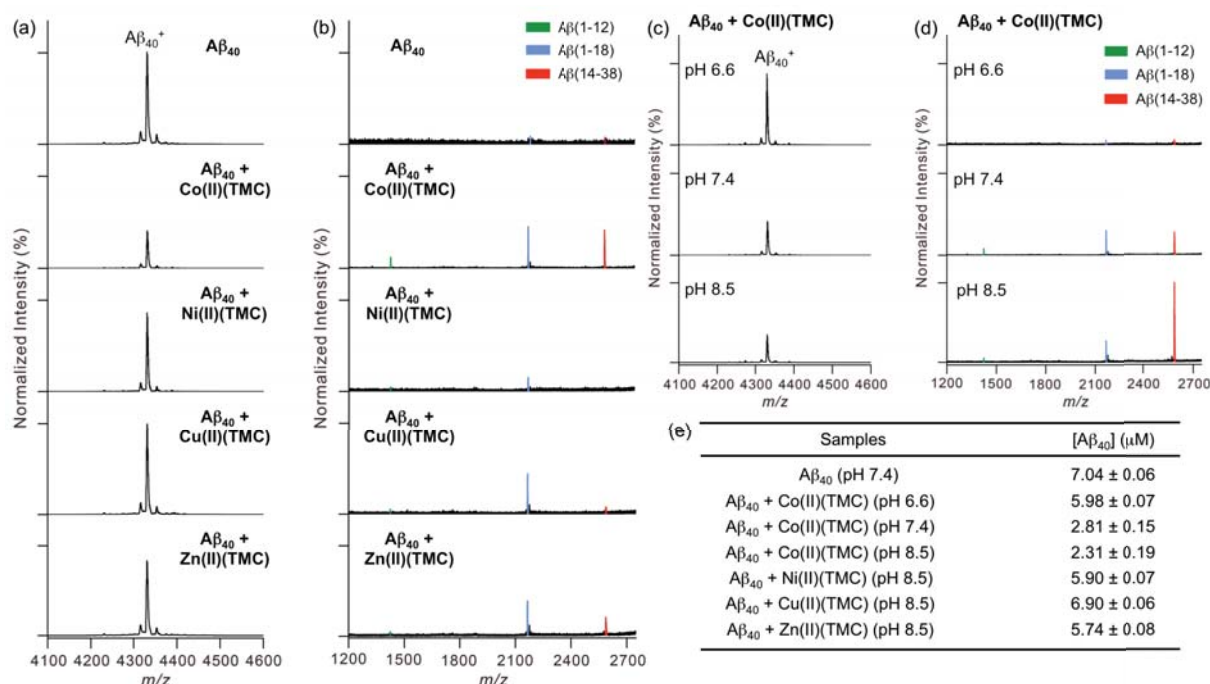


Figure 4.6. MALDI–MS analysis of the A β_{40} samples incubated with M(II)(TMC) (M = Co, Ni, Cu, and Zn). (a) Mass spectra of singly-charged A β_{40} . The peak intensities are normalized to A β_{40} in the absence of M(II)(TMC). (b) The magnified low m/z range of the mass spectra. A β (1-12) [$m/z = 1424$], A β (1-18) [$m/z = 2167$], and A β (14-38) [$m/z = 2587$] are indicated in light green, cyan, and red, respectively. All measurements were conducted with the addition of an internal standard, melittin (5 μ M), and calibrated based on the linear correlation between the concentration and the signal intensity (Figure 4.7). (c) MALDI–MS spectra for A β_{40} incubated with Co(II)(TMC) at different pH values. The peak intensity is normalized to that of A β_{40} without M(II)(TMC) (a, top spectrum). (d) Magnified spectrum (x 40) for each sample. All samples were measured with the addition of an internal standard of melittin (5 μ M). (e) The amount of remaining singly-charged A β_{40} after M(II)(TMC) treatment is estimated and summarized in the table.

To identify whether the A β_{40} signal reduction was a result of a decrease in the monomeric A β_{40} concentration upon incubation with Co(II)(TMC) or due to variation of A β_{40} ionization efficiencies in the presence of Co(II)(TMC), we utilized an internal standard to obtain quantitative information from the mass spectra. An internal standard of melittin, a principle component in honey bee venom,⁴⁹ was selected and added to the MS samples prior to analysis. By comparing the signal intensity of the internal standard in the A β_{40} –Co(II)(TMC) sample to the A β control and ensuring that there was no significant differences in the peak intensity, we were able to verify that the A β_{40} peak suppression was not due to differences in ionization efficiency and was most likely a result of a reduction in the monomeric, singly-charged A β_{40} concentration. To further elucidate

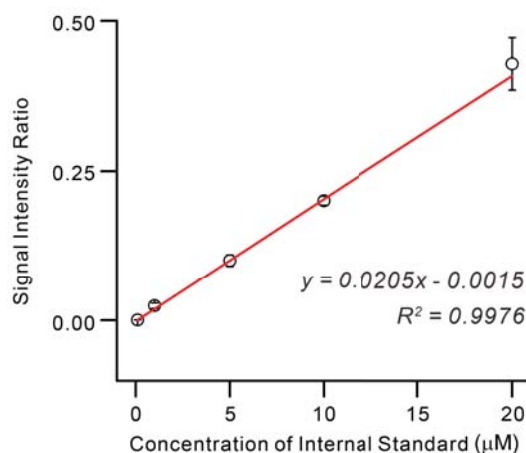


Figure 4.7. Calibration plot of the internal standard, melittin. Internal standards were prepared at different concentrations (100 nM–20 μM). The signal intensity for each sample was measured using MALDI-MS. The y-axis indicates the ratio of the signal intensity for the standards to the sum of intensities for the 30 most dominant peaks. The linear regression of the data is given by the red line ($y = 0.0205x - 0.0015$; $R^2 = 0.9976$).

the relative concentration of singly-charged $A\beta_{40}$ in the absence and presence of M(II)(TMC), a calibration plot was constructed utilizing the melittin internal standard in a concentration range of 100 nM–20 μM ($R^2 = 0.99$; Figure 4.7). As depicted in Figure 4.6e, while all M(II)(TMC) complexes caused a minor decrease in the concentration of $A\beta_{40}$ from *ca.* 7 μM in the $A\beta_{40}$ control to *ca.* 6–7 μM in samples treated with Ni(II)(TMC), Cu(II)(TMC), and Zn(II)(TMC), incubation with Co(II)(TMC) generated a much more significant reduction in the concentration of the singly-charged $A\beta_{40}$ monomer [*ca.* 2.8 μM (60% reduction); Figure 4.6a]. Additionally, upon closer inspection of the low m/z range of the Co(II)(TMC)-treated mass spectrum, three new peaks were detected at 1424, 2167, and 2587 m/z , corresponding to the N- and C-terminal hydrolytic cleavage fragments, $A\beta_{1-12}$, $A\beta_{1-18}$, and $A\beta_{14-38}$, respectively (Figure 4.6b). The $A\beta_{1-18}$ and $A\beta_{14-38}$ fragments were also identified in the $A\beta_{40}$ samples incubated with Cu(II)(TMC) and Zn(II)(TMC) while only the $A\beta_{1-18}$ peak was identified in the Ni(II)(TMC)-treated spectrum. Furthermore, the reduction in the concentration of the singly-charged $A\beta_{40}$ monomer also appeared to be indirectly correlated with the increase in the relative signal intensity of the $A\beta$ fragments (Figure 4.6). It should be noted that the peak intensities of the fragmented $A\beta$ were outside the dynamic range of the melittin calibration plot; thus, an accurate quantification of the concentration from interpolation of the spectral signal intensity could not be obtained. Nevertheless, the extent to which M(II)(TMC) complexes are observed to fragment $A\beta_{40}$ appears to be consistent with the trend observed in the suppression of the $A\beta_{40}$ peak. Co(II)(TMC) was

found produced the largest degree of A β cleavage and monomer degradation while Cu(II)(TMC) and Zn(II)(TMC) exhibited an activity less than Co(II)(TMC), and Ni(II)(TMC) presented the least efficient cleavage (Figure 4.6).

Overall, our initial MALDI–MS investigations suggest that the anti-amyloidogenic activity of Co(II)(TMC) is at least partially due to its ability to cleave A β , likely *via* hydrolysis of the amide bonds. To further support the hydrolytic mode of action for A β cleavage which has been proposed for other Co(III)(cyclen) complexes, MALDI–MS samples of A β ₄₀ incubated with Co(II)(TMC) were prepared at different pHs (*e.g.*, pH = 6.6, 7.4, 8.5; Figure 4.6c-e).^{18,20,50-55} Due to the high pH sensitivity of hydrolysis, we expected to observe significant differences in both the A β ₄₀ peak suppression and fragment signal intensity as the pH of the solution was altered with maximum cleavage occurring around neutral pH as has been previously reported for Co(III)(cyclen) complexes.^{18,22,50,51,56,57} As expected, no significant fragmentation and very little A β ₄₀ peak reduction were observed in the A β ₄₀ samples incubated with Co(II)(TMC) for 24 h at pH 6.6 (Figure 4.6c-e). Upon increasing the pH a noticeable difference in Co(II)(TMC)'s proteolytic activity was observed in the mass spectra (Figure 4.6c-e). Under physiologically relevant (*i.e.*, pH 7.4) and slightly basic (*i.e.*, pH 8.5) conditions, incubation with Co(II)(TMC) significantly decreased the A β ₄₀ peak intensity. Through the use of the internal standard calibration plot we were able to determine that Co(II)(TMC) was slightly more reactive under moderately basic solution conditions ([A β ₄₀]⁺ = 2.8 μ M at pH 7.4; [A β ₄₀]⁺ = 2.3 μ M at pH 8.5; Figure 4.6c-e). In addition, the signal intensity of the A β ₁₄₋₃₈ fragment (2587 Da) was highest in the pH 8.5 sample (Figure 4.6d). The overall pH dependence of Co(II)(TMC)'s cleavage activity supports its hydrolytic mechanism and it appears from our MALDI–MS studies that the anti-amyloidogenic activity of Co(II)(TMC) is a result of its enhanced ability to catalyze the hydrolysis of A β , relative to the other M(II)(TMC) complexes. It is, however, interesting that Co(II)(TMC) is slightly more reactive at pH 8.5 when structurally similar Co(III)(cyclen) complexes are most reactive at neutral pH.^{22,50,51,57} The dissimilarity in pH optimization may suggest a difference in the hydrolytic mechanism between Co(II)(TMC) and Co(III)(cyclen) (*e.g.*, predominant activation of water by Co(II)(TMC) rather than amide bond activation suggested for Co(III)(cyclen)^{22,50,51,57}; *vide infra*).

(iii) Adduct Formation of M(II)(TMC) Complexes with A β

Electrospray ionization–mass spectrometry (ESI–MS) and ion mobility–mass spectrometry (IM–MS) were employed to determine whether the anti-amyloidogenic activity of Co(II)(TMC) was also partially a result of its ability to coordinate to A β and generate structurally altered A β –

Co(II)(TMC) conformers, similar to the mode of action reported for anti-amyloidogenic platinum and Co(III) Schiff base complexes.¹³⁻¹⁵

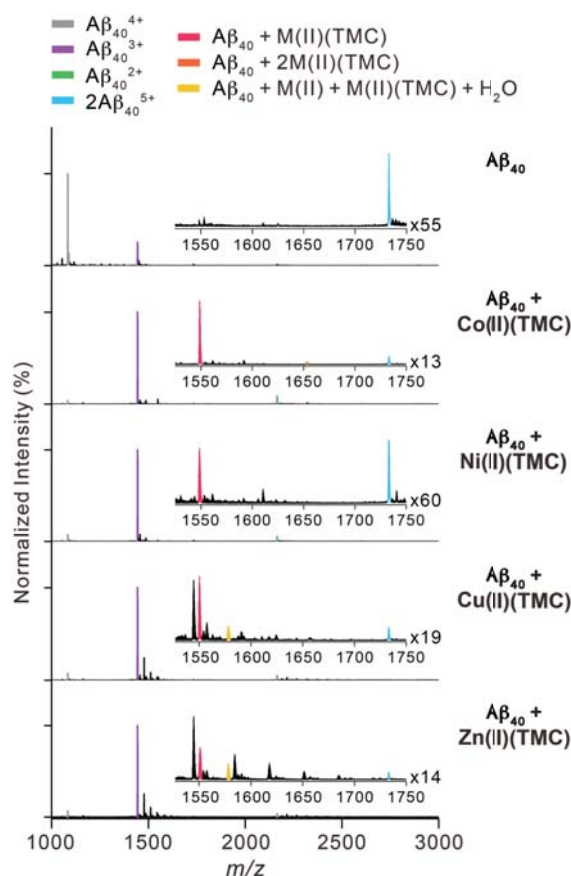


Figure 4.8. ESI-MS spectra of $A\beta_{40}$ incubated with $M(II)(TMC)$ ($M = Co, Ni, Cu,$ and Zn). Inset spectra indicate the magnification between 1500 and 1750 m/z . Colored peaks are assigned above the spectra.

As shown in Figure 4.8, the peaks consistent with $A\beta_{40}$ bound to all four metal complexes [*e.g.*, $A\beta_{40} + M(II)(TMC)$] were detected. The Co(II)(TMC) spectrum, however, did have a unique peak at 1652.40 m/z that was assigned to $A\beta_{40}$ bound to two equivalents of Co(II)(TMC) [*i.e.*, $A\beta_{40} + 2Co(II)(TMC)$], which was not observed in the spectra of the other complexes (Figure 4.8). Additionally, the spectra of Cu(II)(TMC) and Zn(II)(TMC) also had two distinctive signals at 1575.83 and 1576.86 m/z , respectively. These peaks, absent in those of Co(II)(TMC) and Ni(II)(TMC), corresponded to the addition of a water molecule and a labile metal ion (Cu(II) and Zn(II), respectively) to $A\beta_{40}$ [*i.e.*, $A\beta_{40} + M(II) + M(II)(TMC) + H_2O$]. This data suggests that a small amount of Cu(II) and Zn(II) may be removed from TMC possibly by chelating to the N-terminal Cu(II) and Zn(II) binding sites (*e.g.*, His6, His13, His14) in $A\beta$.^{1-5,7-9} The partial metal

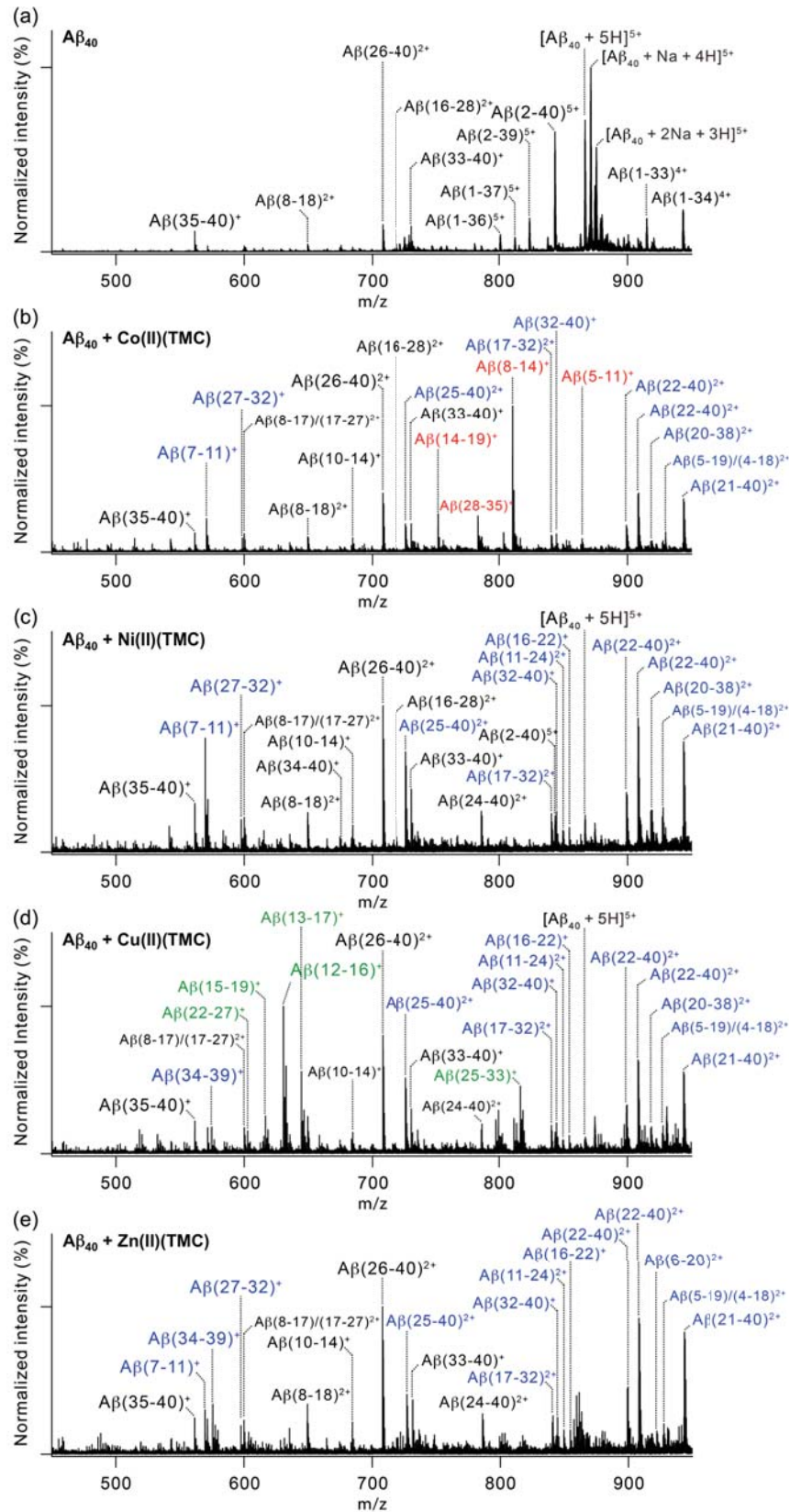


Figure 4.9. The low m/z regions of the ESI–MS spectra for (a) $A\beta_{40}$, (b) $[A\beta_{40} + \text{Co(II)(TMC)}]$, (c) $[A\beta_{40} + \text{Ni(II)(TMC)}]$, (d) $[A\beta_{40} + \text{Cu(II)(TMC)}]$, and (e) $[A\beta_{40} + \text{Zn(II)(TMC)}]$. The newly generated $A\beta_{40}$ fragments formed upon $M(\text{II})(\text{TMC})$ treatment are labeled in blue. Ions only detected in the samples treated with Co(II)(TMC) or Cu(II)(TMC) are labeled in red and green, respectively. All fragments are listed in Table A.3.

ion removal from Cu(II)(TMC) and Zn(II)(TMC) may explain why they did not significantly modulate the aggregation pathways of $A\beta$. Macrocyclic polyamines have been found to be only active against amyloidogenesis in the presence of metal ions [*e.g.*, Cu(II)] because it is the metal complexes generated *in situ* rather than the *apo*-ligands that are active.^{19,24,25,27-29} Therefore, if $A\beta$ is able to remove Cu(II) and Zn(II) from their respective $M(\text{II})(\text{TMC})$ complexes, it should hinder them unreactive, thus explaining the absence of detectable reactivity in the gel/Western blot experiments and the generation of large networks of fibrils similar to those found in metal-bound $A\beta$ [*i.e.*, $\text{Cu(II)}\text{-}A\beta$, $\text{Zn(II)}\text{-}A\beta$] controls, indicated by TEM (*vide supra*; Figures 4.2 and 4.3).⁵⁸⁻⁶¹ In addition to observing $A\beta_{40}\text{-}M(\text{II})(\text{TMC})$ adducts, $A\beta$ fragments similar to those shown in the MALDI–MS studies were also distinguished, further supporting hydrolytic cleavage as the mode of action of Co(II)(TMC) (Figure 4.9). Moreover, +5-charged $A\beta_{40}$ was not detected upon incubation with Co(II)(TMC) and Zn(II)(TMC) , and the trace amounts of +5-charged $A\beta_{40}$ were observed with the addition of Cu(II)(TMC) . It is widely accepted that extended species in the solution phase tend to be transferred into higher charge state ions in the gas phase.⁶² Therefore, the more expanded, +5-charged $A\beta_{40}$ may be more readily accessible to $M(\text{II})(\text{TMC})$ than the lower charge state $A\beta_{40}$ (*e.g.*, +3-charged $A\beta_{40}$; Figure 4.9), which did not show any significant signal depression in the ESI–MS spectra upon administration of $M(\text{II})(\text{TMC})$. Overall, the reduction of +5-charged ion intensities also reflects the cleavage activities of $M(\text{II})(\text{TMC})$ complexes showing the same tendencies found in the MALDI–MS experiments.

IM–MS studies on the +3 charge state were further carried out to assess the conformers adopted upon $A\beta$ binding to $M(\text{II})(\text{TMC})$ (Figure 4.10). When compared to the $A\beta_{40}$ control, the adduct of $A\beta$ with $M(\text{II})(\text{TMC})$ had a slightly longer drift times, indicative of more expanded structures, which may be consistent with the single-site binding of $M(\text{II})(\text{TMC})$ to $A\beta_{40}$, but there was no noticeable difference between Co(II)(TMC) and the other metal complexes (Figure 4.10). Therefore, in agreement with the findings from the isomerization experiments, IM–MS studies suggest that the structural variation of $A\beta$ as a result of coordination to $M(\text{II})(\text{TMC})$ complexes is not the reason why Co(II)(TMC) shows reactivity *in vitro*. Taken together, our MS investigations suggest that the ability of Co(II)(TMC) to modulate $A\beta$

aggregation pathways could be a result of its more active hydrolytic cleavage of A β , relative to that of the other M(II)(TMC) complexes.

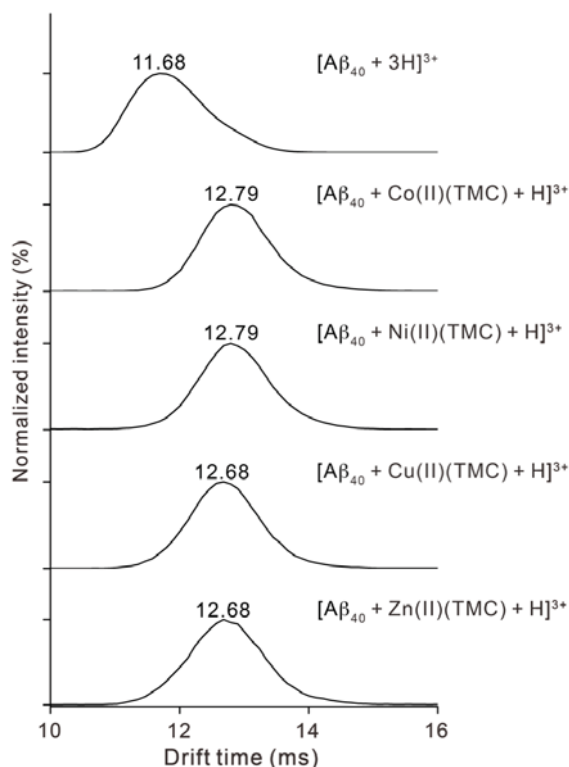


Figure 4.10. ESI-IM-MS spectra of A β_{40}^{3+} or complex ions of A β_{40} with M(II)(TMC) (M = Co, Ni, Cu, and Zn). The drift time values with the maximum intensity are indicated in the spectra.

(iv) Isomerization of M(II)(TMC) Complexes

The ability of M(II)(TMC) complexes to form A β adducts and, in the case of Co(II)(TMC), to competitively interact with A β_{40} in the presence of NaN₃ and NaOCN was unexpected given the steric constraints associated with the *trans*-I conformation (Figure 4.1).^{31,32} The most notable difference between M(II)(TMC) complexes and other platinum and Co(III) complexes for the anti-amyloidogenic activity is that the M(II)(TMC) complexes in the *trans*-I conformation only have one sterically confined coordination site available for A β to bind whereas the other complexes possess two open coordination sites that can facilitate A β binding.^{13-15,20,26,31} Isomerization of the *trans*-I complexes to the less sterically strained *trans*-III isomer which forms octahedral complexes in solution may explain the A β -M(II)(TMC) adduct formations observed in our MS investigations and the competitive interaction between A β and Co(II)(TMC) (Figure 4.1). Additionally, the noticeable anti-amyloidogenic activity of Co(II)(TMC) may also be elucidated if

this complex is able to undergo more facile isomerization, relative to the other M(II)(TMC) complexes. Moore and co-workers have shown that *trans*-I-M(II)(TMC) isomerization to *trans*-III-M(II)(TMC) is highly dependent on solution conditions.³³ Therefore, we monitored the UV-vis spectra of Co(II)(TMC), Ni(II)(TMC), and Cu(II)(TMC) under similar conditions as our *in vitro* aggregation studies to determine (i) if *trans*-III-M(II)(TMC) complexes can be generated and (ii) if Co(II)(TMC) is more easily isomerized, possibly explaining its superior anti-amyloidogenic activity (Figure 4.11).

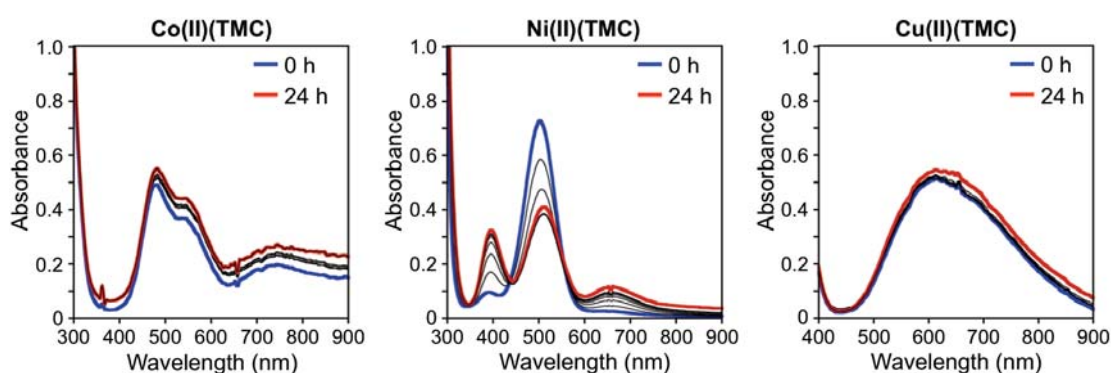


Figure 4.11. Analysis of the potential isomerization of *trans*-I-M(II)(TMC) (M = Co, Ni, and Cu) complexes by UV-vis. Conditions: Co(II)(TMC) (20 mM), Ni(II)(TMC) (10 mM), or Cu(II)(TMC) (2.5 mM); pH 7.4; 37 °C; no agitation.

The peaks at *ca.* 479, 550, and 730 nm [for Co(II)(TMC)]; *ca.* 394, 510, and 658 nm [for Ni(II)(TMC)]; *ca.* 615 nm [for Cu(II)(TMC)] were consistent with previous literature reports of the *trans*-I complexes (Figure 4.11).^{32,34,37} With the exception of Ni(II)(TMC), only slight increases in the absorbance of the *trans*-I-M(II)(TMC) complexes over the course of the experiment were observed and there was no indication of any λ_{max} blue shifts, suggestive of the generation of octahedral *trans*-III complexes (Figure 4.11).³²⁻³⁵ Ni(II)(TMC) did, however, show some significant optical changes in the first *ca.* 4 h of the experiment. This spectral variation at 394, 510, and 658 nm was found to be consistent with previous reports that indicate the slow establishment of an equilibrium between a low-spin four coordinate complex to a distorted, high-spin five coordinate structure.^{63,64} Therefore, our spectral data suggests that isomerization does not occur under our *in vitro* gel/Western blot conditions and that the possibility of A β coordinated to M(II)(TMC) *via* a *bis*-His coordination mode is unlikely.

(v) X-ray Structural Characterization of M(II)(TMC)

Crystals suitable for X-ray analysis for $[\text{Co}(\text{TMC})(\text{NO}_3)](\text{NO}_3)$ and $[\text{Ni}(\text{TMC})(\text{CH}_3\text{CN})](\text{NO}_3)_2$ were obtained by slow diffusion of diethyl ether into CH_3CN solutions of $\text{Co}(\text{II})(\text{TMC})$ and $\text{Ni}(\text{II})(\text{TMC})$ complexes (see Figure 4.1b,c, respectively). The structural data obtained was used to compare the structures of $\text{Co}(\text{II})(\text{TMC})$ and $\text{Ni}(\text{II})(\text{TMC})$ nitrate complexes to each other and to the previously reported $\text{Cu}(\text{II})(\text{TMC})$ and $\text{Zn}(\text{II})(\text{TMC})$ perchlorate complexes.^{35,42,43,46,47} It should be noted that the degree of distortion in the $\text{M}(\text{II})(\text{TMC})$ complexes is highly dependent on the identity of the ligand occupying the open coordination site. For this reason, comparison to calculations that can provide structural information for $\text{M}(\text{II})(\text{TMC})$ complexes with identical ligands at the fifth coordination site was also conducted (*vide infra*).

Table 4.1. Selected crystallographic metrics for $\text{Co}(\text{II})(\text{TMC})$ and $\text{Ni}(\text{II})(\text{TMC})$. The two sets of measurements for $\text{Ni}(\text{II})(\text{TMC})$ correspond to the two unique structures found in the asymmetric unit.

Co(II)(TMC)		Ni(II)(TMC)	
Co–N1	2.181 Å	Ni–N1	2.116 / 2.076 Å
Co–N2	2.184 Å	Ni–N2	2.134 / 2.184 Å
Co–N3	2.172 Å	Ni–N3	2.132 / 2.096 Å
Co–N4	2.189 Å	Ni–N4	2.113 / 2.153 Å
Co–O1	2.360 Å	Ni–N5	2.023 / 2.015 Å
Co–O2	2.217 Å	Distance above macrocyclic plane	0.221 / 0.252 Å
Distance above macrocyclic plane	0.532 Å	N1–Ni–N2	92.57 / 95.02°
N1–Co–N2	91.57°	N2–Ni–N3	85.28 / 84.31°
N2–Co–N3	83.64°	N3–Ni–N4	94.54 / 93.89°
N3–Co–N4	90.99°	N4–Ni–N1	85.13 / 86.07°
N4–Co–N1	83.55°	N1–Ni–N5	95.50 / 100.47°
N1–Co–O1	84.79°	N2–Ni–N5	95.62 / 90.26°
N1–Co–O2	105.28°	N3–Ni–N5	95.49 / 105.81°
O1–Co–N3	107.74°	N4–Ni–N5	97.30 / 91.37°
N1–N2–N3–N4*	28.48°	N1–N2–N3–N4*	1.92 / 24.02°

*The reported dihedral angles (*i.e.*, N1–N2–N3–N4) are the averaged angles of the two measurements obtained by defining the angle by the N1–N3 or N2–N4 axis.

As shown in Figure 4.1, both $\text{Co}(\text{II})(\text{TMC})$ and $\text{Ni}(\text{II})(\text{TMC})$ complexes were in the expected *trans-I* conformation. Interestingly, a nitrate molecule bound to the *syn* face of the macrocycle of $\text{Co}(\text{II})(\text{TMC})$ in an unusual bidentate fashion forming a distorted six coordinate complex. The asymmetric unit of $\text{Ni}(\text{II})(\text{TMC})$ contained two complexes, each with an CH_3CN ligand at the axial site, but with one being slightly more distorted than the typically perfect square pyramidal complexes previously reported (Figure

4.1c shows the square pyramidal structure that is more consistent with previous literature reports).^{38,40,45} To better quantify the degree of distortion, the averaged dihedral angles between the two intersecting planes defined by the four N donor atoms with N1–N3 and N2–N4 axes were calculated and reported in Table 4.1 (*i.e.*, for the N1–N3 axis: plane 1 is defined by N1, N2, and N3 and plane 2 is defined by N1, N3, and N4; for the N2–N4 axis: plane 1 is defined by N1, N2, and N4 and plane 2 is defined N2, N3, and N4; Figure 4.1b,c). The dihedral angle of 28.48° for Co(II)(TMC) was larger than those obtained from previous crystallographic data [*i.e.*, average dihedral angles of 5.9° for Ni(II)(TMC), 24.06° for Cu(II)(TMC), and 16.38° for Zn(II)(TMC)].^{35,38-40,42,43,45-48} The Ni(II)(TMC) structure shown in Figure 4.1c had a dihedral angle of 1.92° (*i.e.*, almost all 4 N atoms coplanar) while the slightly more distorted structure was determined to be 24.02° which was still less than that of Co(II)(TMC). In addition, Co(II) was positioned the farthest above the macrocyclic plan (*i.e.*, 0.532 Å) compared to *ca.* 0.221 Å (or 0.252 Å) for Ni(II)(TMC), 0.303 Å for Cu(II)(TMC), and 0.484 Å for Zn(II)(TMC).^{35,38-40,42,43,45-48} Furthermore, TDDFT predicted structures of the water-bound ground-state M(II)(TMC) complexes (*i.e.*, [M(TMC)(H₂O)]²⁺) also presented a noticeable distortion in the structure of Co(II)(TMC); however, Zn(II)(TMC) also had comparable dihedral angles and distances of its metal center sitting above the macrocyclic plane (Table 4.2). More facile substrate entry (*e.g.*, Aβ entry) to the metal center may be facilitated by the distortion in M(II)(TMC) complexes and by the metal ion sitting farther above the macrocyclic plane because it reduces the adverse steric effects associated with all four methyl groups located on the same side of the macrocyclic plane where the axial ligands coordinate (Figure 4.1b,c).^{26,31,32,34-48} Overall, crystallographic and TDDFT results suggest that structures may help to explain why Co(II)(TMC), showing the more distorted conformation, exhibits enhanced anti-amyloidogenic properties compared to the other M(II)(TMC) complexes (*vide infra*).

Table 4.2. Selected distances and angle measurements of TDDFT-predicted M(II)(TMC) complexes.

Measurement	Co(II)(TMC)	Ni(II)(TMC)	Cu(II)(TMC)	Zn(II)(TMC)
Distance above macrocyclic plane	0.377 Å	0.033 Å	0.207 Å	0.372 Å
N1–N2–N3–N4*	26.75°	0.01°	25.31°	27.56°

*The reported dihedral angles (*i.e.*, N1–N2–N3–N4) are the averaged angles of the two measurements obtained by defining the angle by the N1–N3 or N2–N4 axis.

(vi) EPR Studies of Co(II)(TMC)

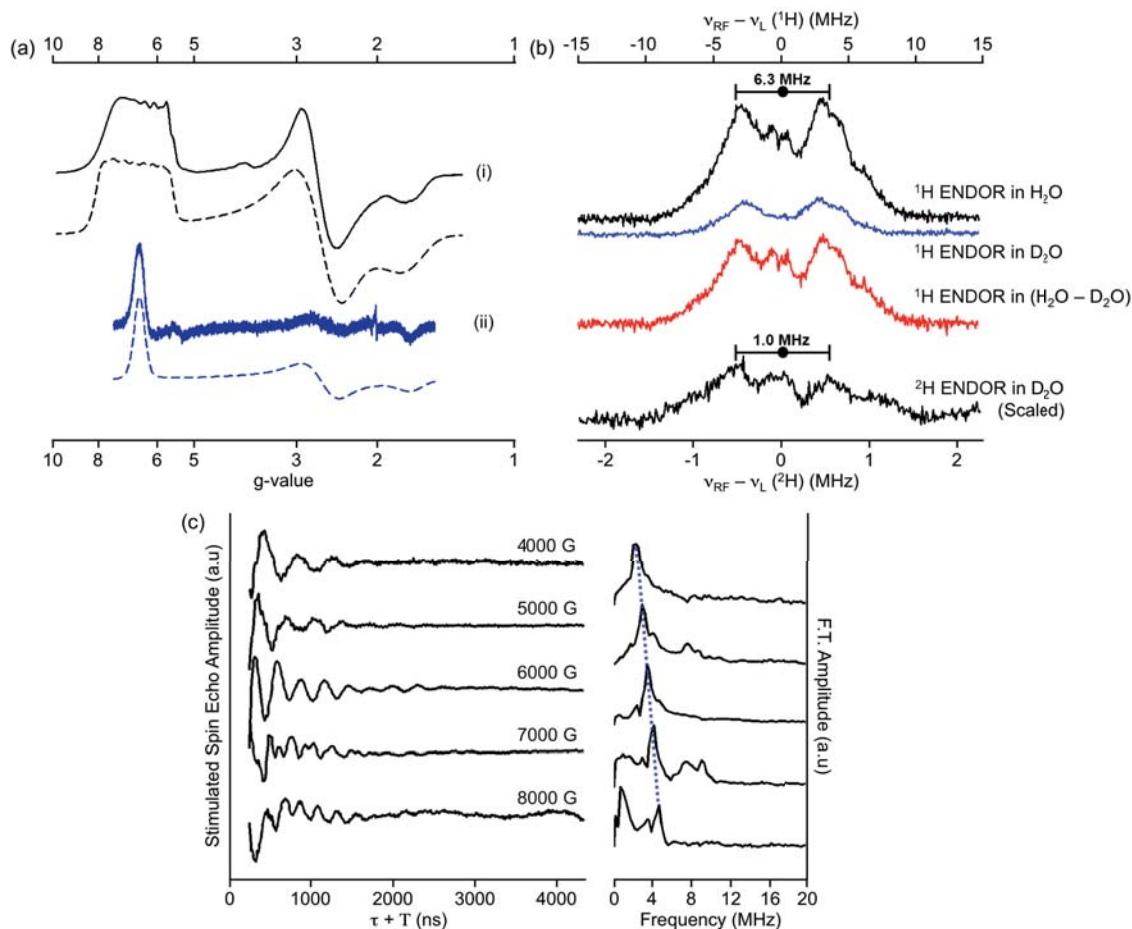


Figure 4.12. EPR measurements of Co(II)(TMC). (a) (i) X-band CW-EPR spectrum of Co(II)(TMC) (solid black) and its simulated spectrum (dashed black); (ii) W-band Electron Spin Echo-detected EPR spectrum (solid blue) of Co(II)(TMC) and its simulated spectrum (dashed blue). The following parameters were used in the simulation: $g = [2.42, 2.42, 2.21]$, $A_{Co} = [0, 60, 0]$ G, $D \geq 13$ cm $^{-1}$, $E/D = 0.3$ (b) 1H Davies ENDOR spectra of Co(II)(TMC) in H_2O (black) and in D_2O (blue). The subtracted 1H ENDOR spectrum is shown in red. 2H Mims ENDOR in D_2O (black). (c) Q-band three pulse time-domain (left) and the frequency domain (right) ESEEM spectra of Co(II)(TMC). The blue dashed line in the frequency domain indicates the ^{17}O Larmor frequency at each field.

In order to characterize the structure of Co(II)(TMC) in solution, continuous wave and pulsed multi-frequency EPR techniques were employed. The X-band CW-EPR of Co(II)(TMC) exhibits a rhombic spectrum with the g tensor, $g_{eff} = [6.3, 2.7, 1.7]$ which arises from high-spin, Co(II) ($S = 3/2$) (Figure 4.12a, i). The hyperfine coupling from ^{59}Co (100%, $I = 7/2$) was observed around $g \approx 6$. To extract more accurate spin Hamiltonian parameters, the multi-frequency EPR experiments were performed. The W-band (94 GHz) EPR displays a rhombic signal similar to the X-band EPR; however, the hyperfine splitting from ^{59}Co cannot be observed (Figure 4.12a, ii). Simulations of

the X-band and W-band CW-EPR were carried out simultaneously to obtain more accurate spin Hamiltonian parameters (Figure 4.12a, dashed lines). The zero-field splitting parameter, D , of high-spin Co(II) is supposed to be large, hence being insensitive in X-band; however, it becomes more sensitive when simulating the W-band EPR spectrum. The spin Hamiltonian parameters obtained from the simulations are similar to those that have a five-coordinated species. In particular, a E/D of *ca.* 0.3 indicates that the complex has a distorted coordination geometry.⁶⁵⁻⁶⁷ Thus, the CW-EPR indicates that Co(II)(TMC) has a distorted five-coordinated geometry, consistent with the UV-vis and TDDFT results.

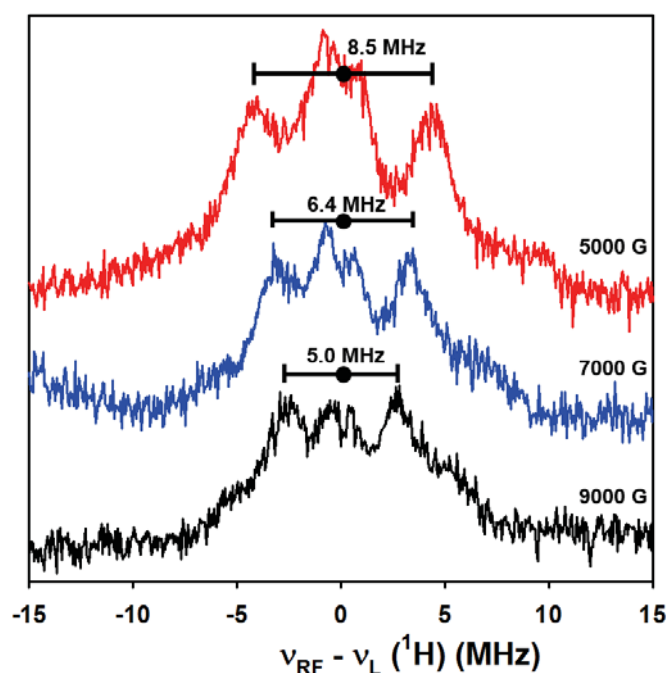


Figure 4.13. ^1H -ENDOR spectra of $\text{CoCl}_2 \cdot 6\text{H}_2\text{O}$ at different magnetic fields.

To examine if water is bound to Co(II)(TMC), we conducted the ^1H as well as ^2H ENDOR experiments (Figure 4.12b). The ^1H ENDOR spectrum exhibits doublets centered at the Larmor frequency of a proton and separated by its hyperfine coupling, A : $\nu_{\pm} = \nu_{\text{H}} \pm A/2$. The hyperfine coupling of *ca.* 6.3 MHz signal in ^1H ENDOR appears also in the sample prepared in D_2O but the ENDOR intensity is decreased significantly. In addition, the ^2H ENDOR was conducted to confirm the existence of the exchangeable proton(s). The ^2H ENDOR exhibits the doublet centered at the ^2H Larmor frequency and is split by *ca.* 1.0 MHz. The magnitude of the hyperfine coupling (1.0 MHz) is comparable to the proton hyperfine coupling of 6.3 MHz if scaled by the magnetogyric ratio of $\gamma(^1\text{H}/^2\text{H})$. Thus, ^1H and ^2H ENDOR indicate that there is an exchangeable

proton(s). To verify if the exchangeable proton is originated from water bound to Co(II), the ^1H ENDOR experiment on CoCl_2 was performed in H_2O . Figure 4.13 presents that the largest hyperfine coupling of a proton is *ca.* 6.4 MHz at $g \approx 3.5$. The magnitude of the hyperfine coupling of ^1H is comparable to the one we observed in Co(II)(TMC). Taken together, these results support that the ^1H ENDOR signal observed in the Co(II)(TMC) spectrum arises from the ^1H -bound water to the cobalt center.

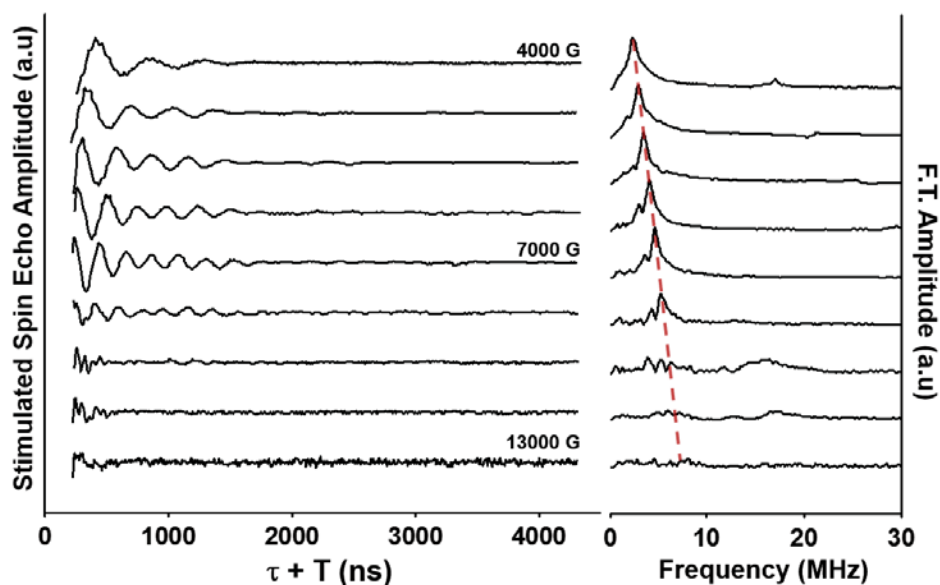


Figure 4.14. Q-band ESEEM time-domain (left) and Fourier transformed frequency domain spectra (right) of $\text{CoCl}_2 \cdot 6\text{H}_2\text{O}$. The red dashed line indicates the ^{17}O Larmor frequency at each field.

Moreover, we have also carried out the ^{17}O ESEEM experiment on the Co(II)(TMC) sample prepared in ^{17}O -labeled water. Figure 4.12c displays the time-domain and the frequency-domain three-pulse ESEEM, respectively. The time-domain spectra (Figure 4.12c, left) displayed the ratio of $^{17}\text{O}/^{16}\text{O}$ to eliminate contributions from other nuclei and also τ , the time between the first and the second pulse, was chosen to maximize the modulation of the ^{17}O nuclei. The time-domain ESEEM exhibits the modulation arising from ^{17}O , and the Fourier-transformed frequency domain further confirms that ^{17}O is coupled to Co(II) by showing the ^{17}O peak around the larmor frequency of the ^{17}O nucleus. To validate the magnitude of the hyperfine coupling of ^{17}O ligated to the Co(II) center, the ^{17}O ESEEM experiments on CoCl_2 prepared in ^{17}O -labeled water (70% enrichment) were performed (Figure 4.14). The ^{17}O three-pulse ESEEM of CoCl_2 shows the similar field-dependent ^{17}O modulation pattern as seen for Co(II)(TMC) prepared in H_2^{17}O , which indicates that the ^{17}O signal arises from the water coordinated to the metal ion (Figure 4.14). Overall, our EPR results demonstrate that water is the ligand bound to the distorted

pentacoordinated (possibly, TBP) Co(II)(TMC) complex in solution, supporting the activation of water by Co(II)(TMC) as the hydrolytic mechanism (*vide infra*).

4.2.4 Computational Mechanistic Insights

Table 4.3. Relative Gibbs free energies (a) of $[M(\text{TMC})(\text{L})]^{2+/+}$ complexes ($M = \text{Co}, \text{Ni}, \text{Cu}, \text{or Zn}$; $\text{L} = \text{H}_2\text{O}$ or OH^-), and experimental and TDDFT-calculated $\text{p}K_a$ values. The Gibbs free energy change (b) for the ligand exchange of the coordinated water molecule with the carbonyl group of the amide bond.

(a) ΔG (kcal/mol)	Co		Ni		Cu	Zn
	S = 1/2	S = 3/2	S = 0	S = 1		
L						
H ₂ O	5.6	0	0 ⁽ⁱⁱⁱ⁾	5.1	0	0
OH ⁻ ⁽ⁱ⁾	29.2	11.9	43.4	10.2	24.8	16.9
$\text{p}K_a$	8.5 / 8.7		10.1 / 7.5 ⁽ⁱⁱⁱ⁾		NA/18.2	NA/12.4
Exp / DFT	(to Co(S = 3/2)-OH)		(to Ni(S = 1)-OH)			
(b)	M-OH ₂ + Amide \rightarrow M-Amide + OH ₂					
ΔG (kcal/mol)	5.74		NA ^(iv)		5.09	3.95

(i) $\Delta G_{\text{solv}}(\text{H}^+) = -265.9$ kcal/mol was used.⁷³ (ii) The four-coordinate $[\text{Ni}(\text{TMC})]^{2+}$ complex. (iii) The dissociation of a hydrogen bond is not considered in the computations. (iv) Data is not available (NA) because the ground state of the Ni(II)(TMC) complex is four-coordinate.

(i) Characterization of M(II)(TMC) Complexes in Aqueous Solutions

Regarding a possible mechanism by which the hydrolysis of A β 's amide bonds is facilitated by the Co(II)(TMC) complex, it needs to be assessed whether a water molecule can be activated to a hydroxide ion by coordinating to the Co(II)(TMC) complex (Figure 4.17b, i and iii). To elucidate the axial ligand of the M(II)(TMC) complexes in aqueous solutions, their water- and hydroxo-ligated forms in possible spin states were calculated, and their ground states were defined on the basis of their computed relative free energies and the reproducibility of ligand-field (LF) transitions observed in the electronic absorption spectra. As summarized in Table 4.3, in aqueous solutions, the axial ligand positions of all M(II)(TMC) complexes are observed to have a water molecule as an axial ligand rather than a hydroxide ligand, except for the case of the Ni(II)(TMC) complex, which stays four-coordinated without having an axial ligand in its ground singlet state. Specifically, the ground state of the cobalt complex is calculated to have a quartet cobalt center with an axial water ligand. The ligand field calculated from this ground-state $[\text{Co}(\text{TMC})(\text{H}_2\text{O})]^{2+}$ complex (S = 3/2) also agrees well with spectroscopic data; amongst the four

species calculated for Co(II)(TMC), the UV-vis absorption feature observed at *ca.* 476 nm ($21,000\text{ cm}^{-1}$) with a relatively low intensity can be best matched with the TDDFT-predicted LF transition of the ground-state complex (Figure 4.15a). The Ni complex is predicted to have a four coordinate singlet ground state due to the Jahn-Teller distortion. To have an axial ligand, either H₂O or OH⁻, the Ni center would need to convert to a triplet spin state. Consistent with these predictions, the TDDFT-calculated LF transition of the four-coordinate [Ni(TMC)]²⁺ complex agrees the best with the UV-vis spectrum (Figure 4.15b). For the Cu(II) and Zn(II) complexes, with no possible variation in the spin state, water-coordinated complexes are predicted to be the ground state. This cannot be spectroscopically validated for the Zn(II) complex due to the absence of its LF transitions, while for the Cu(II) complex, its TDDFT computation matches unambiguously with the UV-vis spectrum (Figure 4.15c and Table 4.3).

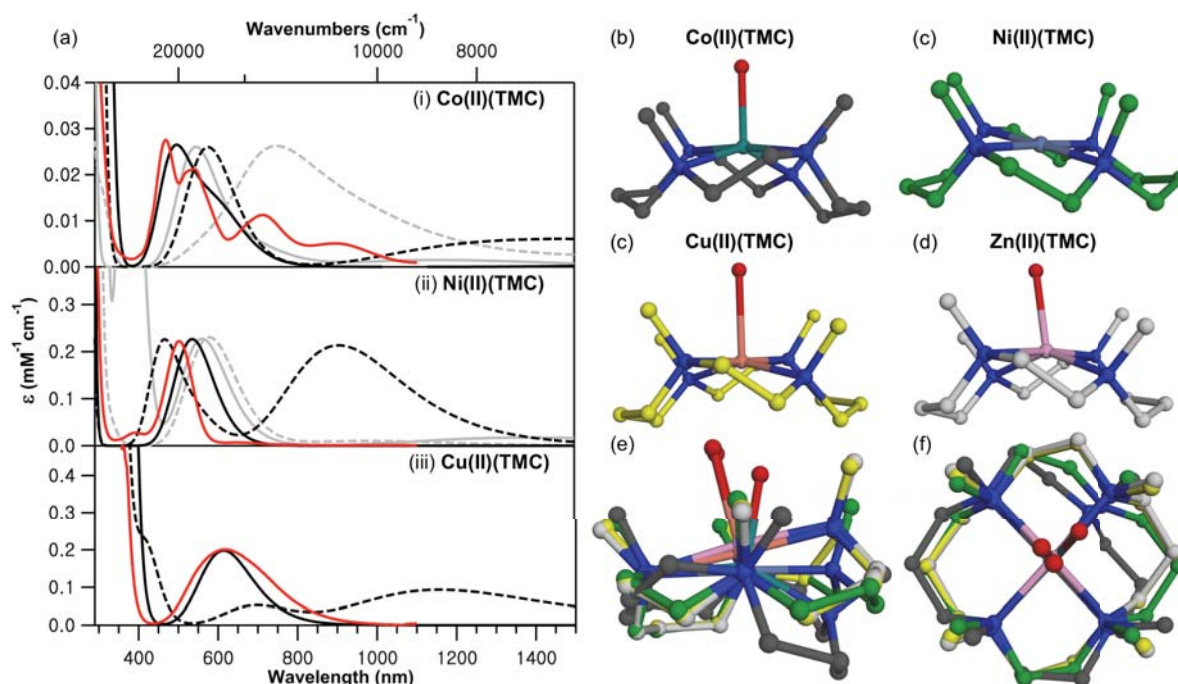


Figure 4.15. Computational examination of M(II)(TMC) complexes. (a) Experimental UV-vis spectrum of (i) Co(II)(TMC) in aqueous solutions (red) and the TDDFT-predicted spectra of [Co(TMC)(H₂O)]²⁺ ($S = 3/2$) (solid black), [Co(TMC)(OH)]⁺ ($S = 3/2$) (dashed black), [Co(TMC)(H₂O)]²⁺ ($S = 1/2$) (solid gray), and [Co(TMC)(OH)]⁺ ($S = 1/2$) (dashed gray); (ii) experimental UV-vis spectrum of Ni(II)(TMC) in aqueous solutions (red) and the TDDFT-predicted spectra of [Ni(TMC)]²⁺ ($S = 0$) (solid black), [Ni(TMC)(OH)]⁺ ($S = 0$) (dashed black), [Ni(TMC)(H₂O)]²⁺ ($S = 1$) (solid gray), and [Ni(TMC)(OH)]⁺ ($S = 1$) (dashed gray); (iii) experimental UV-vis spectrum of Cu(II)(TMC) in aqueous solutions (red) and the TDDFT-predicted spectra of [Cu(TMC)(H₂O)]²⁺ (solid black) and [Cu(14-TMC)(OH)]⁺ (dashed black). (b-d) Calculated structures of (a) [Co(TMC)(H₂O)]²⁺, (b) [Ni(TMC)]²⁺, (c) [Cu(TMC)(H₂O)]²⁺, and (d) [Zn(TMC)(H₂O)]²⁺. (e-f) The overlay of the ground-state M(II)(TMC) structures presented from the side and top.

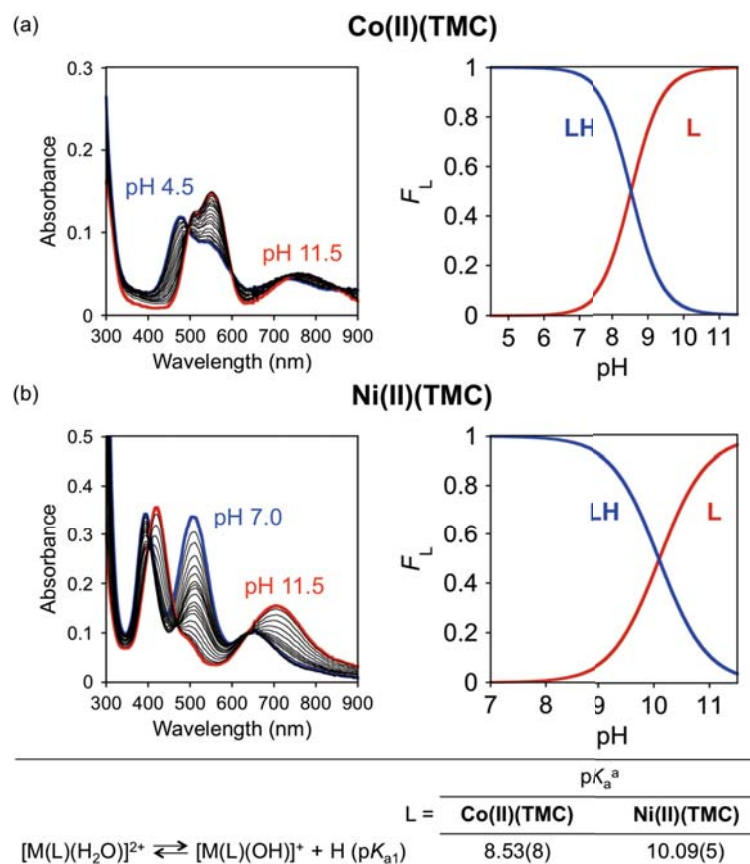


Figure 4.16. Solution speciation studies of Co(II)(TMC) and Ni(II)(TMC). UV-vis variable-pH titration spectra (left) and the solution speciation diagrams (right) of (a) Co(II)(TMC) (pH 4.5–11.5); (b) Ni(II)(TMC) (pH 7–11.5) (F_L = fraction of species at given pH). Acidity constants (pK_a) of $[M(L)(H_2O)]^{2+}$ ($L = \text{TMC}$) are summarized in the table. Experimental conditions: Co(II)(TMC) = 6 mM; Ni(II)(TMC) = 4 mM; $I = 0.10$ M NaCl; room temperature. Charges are omitted for clarity. ^aThe error in the last digit is shown in the parentheses.

(ii) Activation of a Water Molecule by M(II)(TMC) Complexes for Amide Hydrolysis

The spectroscopic and DFT analyses show that, in aqueous solutions, water binds to the metal centers of Co(II)(TMC), Cu(II)(TMC), and Zn(II)(TMC) complexes, not as a hydroxide but as a water molecule. Thus, the energies required to deprotonate these ground-state complexes were calculated (Table 4.3a). The pK_a value of the ground-state $[\text{Co}(\text{TMC})(\text{H}_2\text{O})]^{2+}$ complex is calculated to be 8.7 which is consistent with the experimental value of 8.5 obtained through UV-vis variable-pH titration experiments (Figure 4.16).⁶⁸ Given the range of typical pK_a values of amino acids (4–12.5) and their possible variations depending on microenvironment, the pK_a value of *ca.* 8.5 suggests that the $[\text{Co}(\text{TMC})(\text{H}_2\text{O})]^{2+}$ complex would have a chance to be deprotonated by nearby amino acids thus generating a hydroxide ion (Table 4.4). In contrast, this deprotonation

of a water ligand appears to be less plausible for the other complexes. The complexes of $[\text{Cu}(\text{TMC})(\text{H}_2\text{O})]^{2+}$ and $[\text{Zn}(\text{TMC})(\text{H}_2\text{O})]^{2+}$ are calculated to have $\text{p}K_a$ values of 18.2 and 12.4, respectively. The $\text{p}K_a$ for $[\text{Zn}(\text{TMC})(\text{H}_2\text{O})]^{2+}$ could not be experimentally determined due to the absence of observable optical bands. The UV-vis titration experiment with $\text{Cu}(\text{II})(\text{TMC})$ did not produce any spectral change in a pH titration range of 2–11 (data not shown). These results suggest that $[\text{Cu}(\text{TMC})(\text{OH})]^+$ is already protonated to generate the aqua complex ($[\text{Cu}(\text{TMC})(\text{H}_2\text{O})]^{2+}$) at pH 11 which supports a $\text{p}K_a$ value much greater than 11. Despite the fact that the ground-state Ni(II) complex is calculated to be four-coordinated, the Ni(II) center can be converted to a high-spin state with an axial ligand; the $\text{p}K_a$ for the reaction of $[\text{Ni}(\text{TMC})]^{2+}$ ($S = 0$) + $2\text{H}_2\text{O} \rightarrow [\text{Ni}(\text{TMC})(\text{OH})]^+$ ($S = 1$) + H_3O^+ is known to be 10.1 (Figure 4.16).³⁴ The calculated $\text{p}K_a$ is deviated because this process should involve the dissociation of a hydrogen bond as forming the Ni–O bond, while in computations, this loss of a hydrogen bond could not be considered. The discrepancy between the experimental and DFT-calculated $\text{p}K_a$, however, corresponds to a Gibbs free energy difference of *ca.* 3.6 kcal/mol which lies in the range of reported energies for a hydrogen bond, as expected.^{69,70}

Table 4.4. $\text{p}K_a$ s of amino acids.

Amino Acids	$\text{p}K_a$
Asp	3.71
Glu	4.24
His	6.04
Tyr	10.10
Lys	10.79
Arg	12.5
<i>cf.</i> $[\text{Co}(\text{TMC})(\text{H}_2\text{O})]^{2+}$	8.5

(iii) Activation of an Amide Bond by M(II)(TMC) Complexes

One other way of promoting amide hydrolysis is to activate the amide bond by having the carbonyl oxygen of the amide bond bound to the metal center and thus generate a more electrophilic character (Figure 4.17b, ii). To assess this possibility, the energies required to replace the water ligand of the ground-state M(II)(TMC) complexes with the amide carbonyl oxygen was calculated (Table 4.3b). Except for the case of Ni(II)(TMC) which does not bind to the amide in the singlet ground state, the water ligand could be replaced with a less than 6 kcal/mol free energy. Considering that peptide hydrolysis is down-hill by 2–4 kcal/mol,⁷¹ amide activation *via* its carbonyl ligation to the metal center seems to be thermodynamically feasible

driven by the exergonic peptide hydrolysis (although this does not necessarily suggest fast kinetics). The possibility of having both water and amide ligands on the same metal center was discarded based on its excessive high energy calculated relative to the ground state (Figure 4.17b, iii). Then, combined the two plausible activation pathways discussed above, the binuclear mechanism in Figure 4.17b (iv) can be conclusively suggested for the $[\text{Co}(\text{TMC})(\text{H}_2\text{O})]^{2+}$ complex. Particularly, in the ground state, while other complexes have square pyramidal (or square planar) structures, only the cobalt complex has a TBP structure (Figure 4.15b) which would allow the TMC ligand to be distorted and the open coordination site to be less sterically hindered and thus more easily accommodate substrate entry and possible binuclear interactions, as shown in the structural overlay in Figure 4.15e and f.

4.2.5. Proposed Mechanisms for the Hydrolysis of A β by Co(II)(TMC)

Based on the seminal work with platinum complexes in AD, and the biochemical, spectroscopic, mass spectrometric, and computational studies reported herein, we were able to conceive of two main pathways that may explain the anti-amyloidogenic activity of Co(II)(TMC) which was not observed for the other M(II)(TMC) complexes. The first possible pathway, as shown in Figure 4.17a, is the binding of Co(II)(TMC) to A β that in turn would facilitate conformational changes in A β and thus prohibit the formation of toxic aggregates. This is the mode of action that has been proposed for most metal complexes, including Pt(II/IV) and Co(III) Schiff base complexes.¹³⁻¹⁵ Such a transformation in peptide conformation could be envisioned to occur *via* multiple mechanisms [*e.g.*, through monodentate coordination of A β to the metal center (Figure 4.17a, i), intermolecular binding of A β to two equivalents of M(II)(TMC) (Figure 4.17a, ii), or isomerization to a *trans*-III complex and subsequent formation of an intramolecular octahedral protein–M(II)(TMC) complex (Figure 4.17a, iii)]. The generation of intramolecular protein–M(II)(TMC) complexes (Figure 4.17a, iii) can be reasonably eliminated as a possible mechanism due to the absence of optical changes in the spectra of Co(II)(TMC), Ni(II)(TMC), and Cu(II)(TMC) that would be consistent with the formation of *trans*-III octahedral complexes. Furthermore, while MS studies did detect peaks consistent with the formation of A β –Co(II)(TMC) complexes and IM studies showed a slight increase in the drift time of samples treated with Co(II)(TMC), identical results were also detected for Ni(II)(TMC), Cu(II)(TMC), and Zn(II)(TMC), thus failing to explain the discrepancy in their inhibitory reactivity. In fact, the increase in IM drift time upon administration of M(II)(TMC) suggests that the peptide may be directed toward a slightly expanded conformation relative to the complex-untreated peptide.

Actually, previously reported potent amyloid inhibitors were found to induce structural compaction of A β rather than elongation.^{58,72} Combined, these studies suggest that while the slight change in A β conformation may contribute to the overall reactivity of Co(II)(TMC) toward modulating A β aggregation, it does not alone provide a mechanistic explanation for why only Co(II)(TMC) alters A β aggregation.

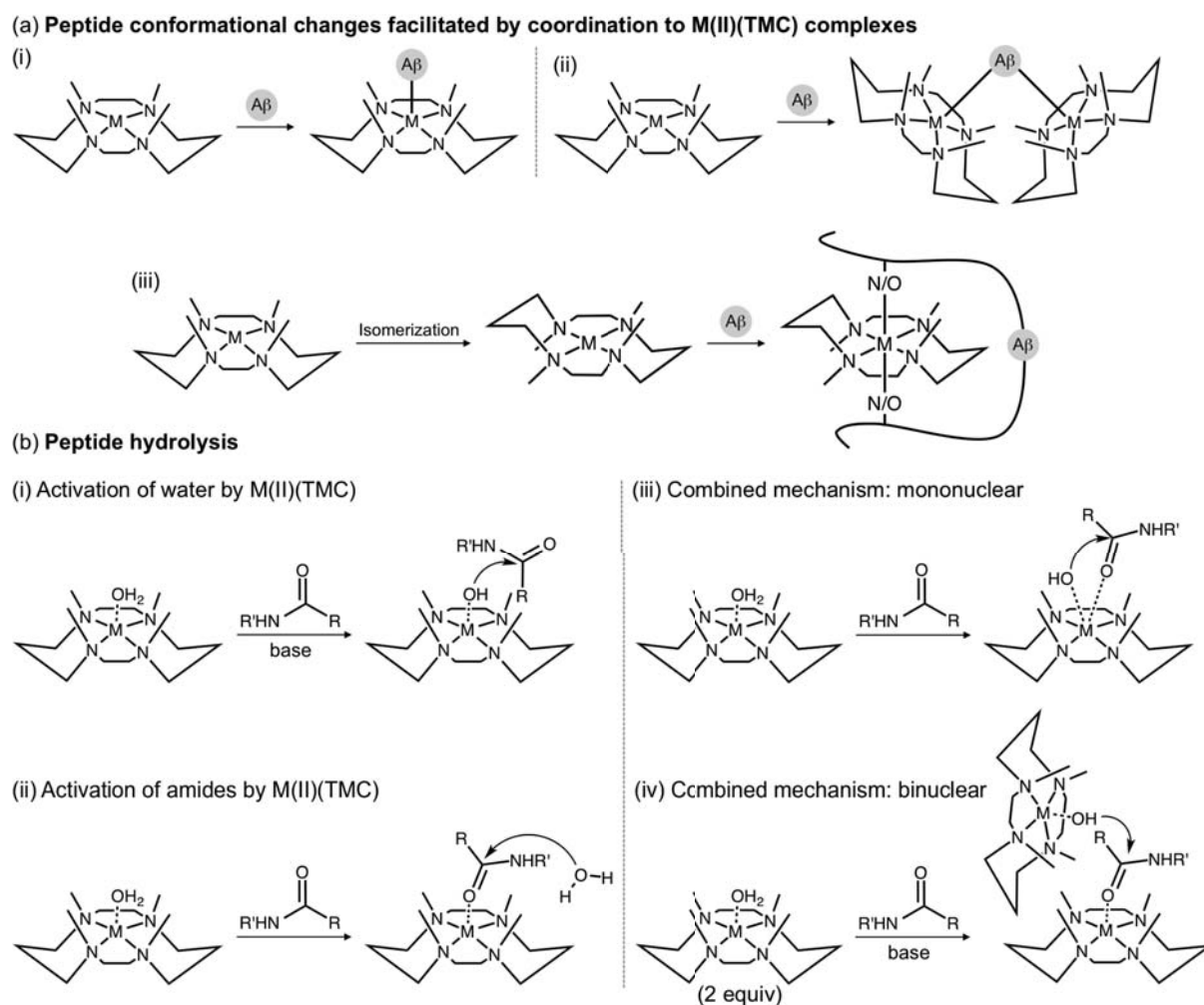


Figure 4.17. Schemes of the potential modes of action of M(II)(TMC) to modulate A β aggregation. (a) The conformation of A β is altered leading to the generation of off-pathway aggregates through (i) coordination to the metal center of M(II)(TMC) [e.g., A β -M(II)(TMC)]; (ii) intermolecular coordination of A β to two equivalents of M(II)(TMC); (iii) isomerization to the *trans*-III stereoisomer and subsequent formation of an octahedral complex. (b) Metal complexes facilitate the hydrolysis of amide bonds to generate A β fragments. Amide bond hydrolysis can be catalyzed by: (i) the activation of water by M(II)(TMC) to generate metal hydroxo nucleophiles; (ii) Lewis acid activation of the amide bonds; (iii) a mononuclear combined mechanisms where both substrates (*i.e.*, water and amide) are coordinated to the

metal complex; (iv) a binuclear combined mechanism where two equivalents of M(II)(TMC) are used to produce the hydroxide source and activate the amide bond.

Hydrolytic cleavage of A β 's amide bonds by Co(II)(TMC) may be an alternate route through which it is able to inhibit the formation of fibrils and disassemble mature aggregates into smaller and amorphous species. As shown in Figure 4.17b, the hydrolysis of amide bonds may proceed through three main pathways. First, hydroxide nucleophiles could be produced by the activation and deprotonation of water molecules by M(II)(TMC) to generate metal–hydroxo species (*i.e.*, [M(TMC)(OH)]⁺) that are capable of attacking the carbonyl and subsequently hydrolyzing the amide bonds (Figure 4.17b, i). Such a mechanism would require the relatively facile deprotonation of the ground-state [M(TMC)(H₂O)]²⁺ complexes. Based on our pH-dependent spectroscopic titration experiments and TDDFT calculations, Co(II)(TMC) would be expected to be the most reactive of the M(II)(TMC) complexes through this mechanistic pathway, thus explaining our observations from the gel/Western blot and TEM studies. The energies required to deprotonate the ground-state M(II)(TMC) complexes were found to be much lower for Co(II)(TMC) (11.9 kcal/mol for Co(II)(TMC) *versus* 16.9–43.3 kcal/mol for the other M(II)(TMC) complexes). It was also determined to have the most acidic p*K*_a value (*ca.* 8.5) which implies that deprotonation of water bound to Co(II)(TMC) by nearby amino acids may be possible. In fact, EPR studies validated the existence of a distorted five-coordinate Co(II)(TMC) with exchangeable protons on the water molecule occupying the open coordination site. Ni(II)(TMC), Cu(II)(TMC), and Zn(II)(TMC), which were determined to have p*K*_a values greater than 10, would be expected to have negligible amounts of metal–hydroxo species generated under physiological conditions thus explaining their lower proteolytic activity. Furthermore, a mechanism for water activation would also explain the enhanced A β ₄₀ monomer signal suppression and fragmentation detected in the Co(II)(TMC)-treated MALDI–MS samples incubated at a slightly basic pH (*e.g.*, pH 8.5).

A second mechanism through which amide bonds could be hydrolyzed involves the ligand exchange of the water molecule of the ground-state complexes with an amide from the backbone of A β . Binding of the carbonyl oxygen atom to the metal center can prime the amide for nucleophilic attack by generating a more electrophilic substrate (Figure 4.17b, ii). Computationally, ligand exchange was found to be energetically feasible for M(II)(TMC) complexes (*ca.* 6 kcal/mol up-hill) especially when one considers the overall exergonic process of peptide hydrolysis (2–4 kcal/mol down-hill); however, this mechanism alone does not seem to explain the enhanced reactivity of Co(II)(TMC). For instance, Co(II)(TMC) was predicted to have the highest energy barrier for ligand exchange (5.74 kcal/mol) while Zn(II)(TMC) would be expected to have the lowest (3.95 kcal/mol; Table 4.3) and thus should be the more reactive cleavage agent if this was the sole mode of action.

Given the respective feasibility of both activation pathways, it also seems plausible that a combined mechanism could occur where the metal complexes could simultaneously generate the metal-hydroxo nucleophiles as well as activate A β 's amide bonds (Figure 4.17b, iii and iv). Theoretically, a combined mechanism may occur through a mononuclear (Figure 4.17b, iii) or binuclear (Figure 4.17b, iv) pathway. The intramolecular mechanism with both water and amide ligands bound to the metal center was excluded due to its relatively high calculated energy. An intermolecular system where one M(II)(TMC) complex generated a hydroxide source while another equivalent complex activates the amide does not seem unreasonable especially considering that our experiments were performed with two equivalents of M(II)(TMC). Overall, our studies suggest the activation of water by M(II)(TMC) to be the likely mechanism of hydrolysis; however, the extent or degree to which they may also activate the amide or participate in an binuclear mode of action is still not completely clear. Moving forward, these mechanistic insights also suggest that hydrolytic cleavage may be further improved by redirecting the mechanism toward the concerted process. Studies are currently underway to test this hypothesis.

Table 4.5. Potential blood-brain barrier (BBB) permeability of Co(II)(TMC).

PAMPA-BBB assay		
$-\log P_e^a$	5.0 ± 0.2 (CNS+)	$-\log P_e < 5.40$ (CNS+) $-\log P_e > 5.70$ (CNS-)

^aPrediction of the ability of the complex to penetrate the central nervous system (CNS) on the basis of literature values. Compounds characterized as CNS+ potentially possess the ability to penetrate the BBB and are available in the CNS. Compounds designated as CNS- are expected to have poor permeability through the BBB; therefore, their bioavailability into the CNS is considered to be minimal.

4.2.6. Biological Applicability of M(II)(TMC) Complexes

In order to gauge the practicality of Co(II)(TMC) as an anti-amyloidogenic agent, we first assessed its ability to penetrate the blood-brain barrier (BBB) with the parallel artificial membrane permeability assay adapted for the blood-brain barrier (PAMPA-BBB; Table 4.5). Co(II)(TMC) was predicted to passively diffuse across the BBB based on its $-\log P_e$ value compared to those of other previously reported BBB-permeable molecules ($-\log P_e = 5.0 \pm 0.2$ where $-\log P_e < 5.40$ is CNS+ and $-\log P_e > 5.70$ is CNS-; CNS = central nervous system). Next, the MTT assay [MTT = 3-(4,5-dimethyl-2-thiazolyl)-2,5-diphenyl-2H-tetrazolium bromide] was employed to evaluate the cytotoxicity of Co(II)(TMC) using the human neuroblastoma SH-SY5Y (5Y) cells (Figure 4.18). The cell viability of *ca.* 98% was measured for 5Y cells treated with up to 20 μ M Co(II)(TMC)

(Figure 4.18). Even with elevated amounts of compound treatment [*i.e.*, 50 and 100 μM Co(II)(TMC)], the cell viability was still *ca.* 80%. These results were particularly interesting given the absence of any A β -targeting moieties augmented onto the ligand framework that could impart substrate specificity to Co(II)(TMC). We hypothesized that this cellular tolerance for Co(II)(TMC) may be due to its preferential cleavage of A β which lacks a well-defined tertiary (or quaternary) structure over essential biological proteins that are highly folded. Therefore, due to the disordered structure, the amide bonds in A β may be more accessible to Co(II)(TMC) for hydrolysis with respect to the amide bonds in highly folded proteins which should be more protected from undesired cleavage.

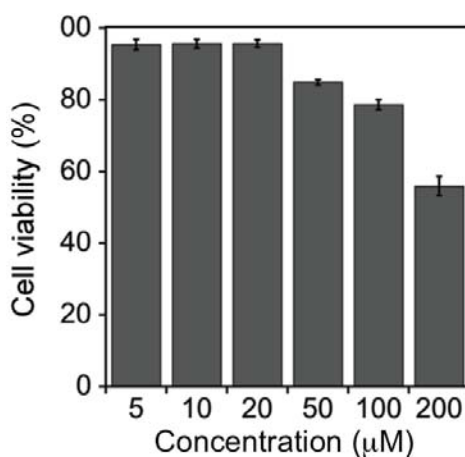


Figure 4.18. Cell viability measurements of Co(II)(TMC) using human neuroblastoma SH-SY5Y cells. Cell viability (%) was determined by the MTT assay compared to cells treated with ddH₂O [MTT = 3-(4,5-dimethyl-2-thiazolyl)-2,5-diphenyl-2*H*-tetrazolium bromide].

In order to test this hypothesis, we analyzed the MALDI-MS spectrum of Co(II)(TMC)-treated ubiquitin samples spiked with internal standards of melittin for monomer suppression and peptide fragmentation (Figure 4.19). Ubiquitin was chosen for its similarity in size to A β (*i.e.*, 8.5 kDa) and its well-defined and tightly folded structure.³⁰ Unlike the A β_{40} samples incubated with Co(II)(TMC), the ubiquitin samples did not produce any detectable fragments and compared to the internal standard, there was no noticeable reduction in the singly-charged monomer peak. Together, these studies show that Co(II)(TMC) is BBB permeable and relatively non-cytotoxic with preferential cleavage activity toward amyloidogenic peptides over highly structured proteins, which suggests its potential to be used for further biological applications.

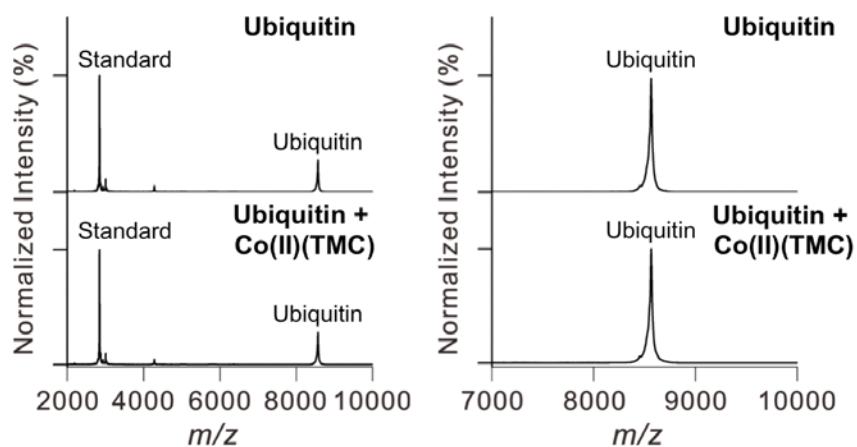


Figure 4.19. MALDI–MS analysis of ubiquitin incubated with Co(II)(TMC). The peak intensities are normalized to ubiquitin in the absence of Co(II)(TMC). All measurements were conducted with the addition of an internal standard, melittin (5 μ M), and calibrated based on the linear correlation between the concentration and the signal intensity.

4.3. Conclusions

Since the initial report of Co(III)(cyclen) complexes, very little has been reported to understand and develop anti-amyloidogenic cleavage agents for AD. In order to further explore the applicability of this approach, we developed a series of divalent metal tetra-*N*-methylated cyclam complexes with the purpose of achieving a degree of tunability and control through their unique stereochemistry and coordination spheres which do not exist in the previously reported octahedral Co(III)(cyclen) complexes.²⁰ To our surprise, we found that Co(II)(TMC) was able to modulate the aggregation pathways of A β ₄₀ and A β ₄₂ as observed by gel/Western blot and TEM, while the other divalent metal complexes [*i.e.*, Ni(II)(TMC), Cu(II)(TMC), and Zn(II)(TMC)] did not. MS and IM–MS studies attributed the anti-amyloidogenic activity of M(II)(TMC) complexes to their ability to promote amide bond hydrolysis rather than induce peptide compaction as has been previously observed for small molecules and Co(III) complexes.^{13,58,72}

Spectroscopic and computational studies into the mechanism of hydrolysis were further performed in order to elucidate the reason for the superior proteolytic activity of Co(II)(TMC) and to find additional strategies to tune the cleavage activity of such compounds. Mechanistically, the activation of water by M(II)(TMC) would explain the enhanced activity of Co(II)(TMC) with respect to the other complexes due to its relatively acidic pK_a of the water-bound ground-state complex, but the activation of amide bonds by M(II)(TMC) could not be completely ruled out due to the overall exergonic process of peptide hydrolysis. Although, by itself M(II)(TMC)-facilitated activation of amides could not explain the metal center dependence observed in the gel/Western

blot and TEM studies. Finally, a concerted mechanism through which a single metal complex binds both a water molecule and an amide was discarded due to the high energy associated with both ligands bound to the sterically confined metal center. Given the feasibility of activating water and amides individually, a combined binuclear mechanism may be plausible.

Overall, our mechanistic studies suggest that in addition to tuning the cleavage reactivity of the metal complexes through the choice of metal ions, we could also further improve the hydrolytic cleavage by promoting a concerted reaction mechanism by providing two or more open *cis* coordination sites on the metal center to facilitate the activation of the amide bond and the production and attack by a hydroxo ligand simultaneously *via* an intramolecular fashion. Furthermore, the biological applicability of Co(II)(TMC) was established by showing its ability to diffuse across the BBB and its relatively low cytotoxicity which appears to be partially a result of its preferential interaction with amyloidogenic proteins over highly structured substrates. Taken together, our findings on the metal center dependence for amyloidogenic peptide cleavage, along with the mechanistic insights, not only bestow a new strategy through which the cleavage activity and selectivity of proteolytic metal complexes can be tuned, but it also shows that high potency, which often leads to poor substrate selectivity, is not required to achieve the desired anti-amyloidogenic reactivity.

4.4. Experimental Section

4.4.1. Materials and Methods

All reagents were purchased from commercial suppliers and used as received unless otherwise noted. A β ₄₀ and A β ₄₂ were purchased from Anaspec (A β ₄₂ = DAEFRHDSGYEVHHQKLVFFA-EDVGSNKGAIIGLMVGGVVIA; Fremont, CA, USA). Trace metal contamination was removed from buffers and solutions used for A β experiments (*vide infra*) by treating with Chelex overnight (Sigma-Aldrich, St. Louis, MO, USA). Optical Spectra were recorded on an Agilent 8453 UV-vis spectrophotometer. TEM images were taken using a JEOL JEM-2100 transmission electron microscope (UNIST Central Research Facilities, Ulsan National Institute of Science and Technology, Ulsan, Republic of Korea). Absorbance values for the PAMPA-BBB assay were measured on a Molecular Devices SpectraMax 190 microplate reader (Sunnyvale, CA, USA). Mass Spectra for investigating the interaction of M(II)(TMC) with A β were taken on a MALDI-TOF/TOF mass spectrometer (UNIST Central Research Facilities, Ulsan National Institute of

Science and Technology, Ulsan, Republic of Korea) and a Synapt G2 ESI–IM mass spectrometer (Waters, Milford, MA, USA).

4.4.2. Preparation of M(II)(TMC) Complexes

4.4.3. [Ni(TMC)](NO₃)₂

TMC (0.13 g, 0.5 mmol) was added to an acetonitrile solution (5 mL) of Ni(NO₃)₂·6H₂O (0.15 g, 0.5 mmol). The resulting solution was refluxed for 12 h. After cooling, the solvent was removed under vacuum to give a bluish green solid. The solid was filtered and the filtrate was then washed with diethyl ether and dried in vacuum. Yield: 0.20 g (90%). UV-vis (H₂O): λ_{max} (ε) = 393 nm (110 M⁻¹cm⁻¹). ESI–MS (in CH₃CN): 157.2 *m/z* for [Ni(TMC)]²⁺ and 376.3 *m/z* for [Ni(TMC)(NO₃)]⁺. Anal. Calcd for C₁₄H₃₂N₆NiO₆: C, 38.29; H, 7.34; N, 19.14. Found: C, 38.28; H, 7.34; N, 19.26.

4.4.4. [Co(TMC)(NO₃)](NO₃)

TMC (0.13 g, 0.5 mmol) was added to an acetonitrile solution (5 mL) of Co(NO₃)₂·6H₂O (0.15 g, 0.5 mmol). The resulting solution was refluxed for 12 h. After cooling, the solvent was removed under vacuum to give a pink solid. The solid was filtered and the filtrate was then washed with diethyl ether and dried in vacuum. Yield: 0.19 g (86%). UV-vis (H₂O): λ_{max} (ε) = 466 nm (50 M⁻¹cm⁻¹). ESI–MS (in CH₃CN): 178.2 *m/z* for [Co(TMC)(CH₃CN)]²⁺ and 377.1 *m/z* for [Co(TMC)(NO₃)]⁺. Anal. Calcd for C₁₄H₃₂CoN₆O₆: C, 38.27; H, 7.34; N, 19.13. Found: C, 37.83; H, 7.30; N, 18.88.

4.4.5. [Cu(TMC)(CH₃CN)](ClO₄)₂

TMC (0.13 g, 0.5 mmol) was added to an acetonitrile solution (5 mL) of Cu(ClO₄)₂·6H₂O (0.19 g, 0.5 mmol). The resulting solution was refluxed for 12 h. After cooling, the solvent was removed under vacuum to give a blue solid. The solid was filtered and the filtrate was then washed with diethyl ether and dried in vacuum. Yield: 0.25 g (96%). UV-vis (H₂O): λ_{max} (ε) = 615 nm (190 M⁻¹cm⁻¹). ESI–MS (in CH₃CN): 159.5 *m/z* for [Cu(TMC)]²⁺, 180.2 *m/z* [Cu(TMC)(CH₃CN)]²⁺, and 418.2 *m/z* for [Cu(TMC)(ClO₄)]⁺. Anal. Calcd for C₁₆H₃₅Cl₂CuN₅O₈: C, 34.32; H, 6.30; N, 12.51. Found: C, 34.05; H, 6.24; N, 12.47.

4.4.6. [Zn(TMC)(CH₃CN)](ClO₄)₂

TMC (0.13 g, 0.5 mmol) was added to an acetonitrile solution (5 mL) of $\text{Zn}(\text{ClO}_4)_2 \cdot 6\text{H}_2\text{O}$ (0.19 g, 0.5 mmol). The resulting solution was refluxed for 12 h. After cooling, the solvent was removed under vacuum to give a white solid. The solid was filtered and the filtrate was then washed with diethyl ether and dried in vacuum. Yield: 0.26 g (99%). ESI-MS (in CH_3CN): 180.6 m/z for $[\text{Zn}(\text{TMC})(\text{CH}_3\text{CN})]^{2+}$ and 419.2 m/z for $[\text{Zn}(\text{TMC})(\text{ClO}_4)]^+$. Anal. Calcd for $\text{C}_{16}\text{H}_{35}\text{Cl}_2\text{N}_5\text{O}_8\text{Zn}$: C, 34.21; H, 6.28; N, 12.47. Found: C, 34.11; H, 6.28; N, 12.32.

4.4.7. A β Aggregation Experiments

All experiments were performed according to previously published methods.⁵⁸⁻⁶¹ Prior to experiments, A β_{40} or A β_{42} was dissolved in ammonium hydroxide (NH_4OH , 1% v/v aq), aliquoted, lyophilized overnight, and stored at -80°C . A stock solution of A β was prepared by dissolving lyophilized peptide in 1% NH_4OH (10 μL) and diluting with ddH_2O . The concentration of the solution was determined by measuring the absorbance of the solution at 280 nm ($\epsilon = 1450 \text{ M}^{-1}\text{cm}^{-1}$ for A β_{40} and $\epsilon = 1490 \text{ M}^{-1}\text{cm}^{-1}$ for A β_{42}). The peptide stock solution was diluted to a final concentration of 25 μM in Chelex-treated buffered solution containing HEPES (20 μM), pH 7.4, NaCl (150 μM). For the inhibition studies,⁵⁸⁻⁶¹ M(II)(TMC) (50 μM) was added to a solution containing A β (25 μM) and incubated at 37°C with constant agitation for 4, 8, or 24 h. For the disaggregation studies,¹⁻⁴ A β was incubated at 4, 8, and 24 h at 37°C with constant agitation prior to treatment with M(II)(TMC) (50 μM). The resulting samples containing A β (preincubated for 4, 8, or 24 h) and M(II)(TMC) were incubated at 37°C with constant agitation for 24 h.

4.4.8. Gel Electrophoresis with Western Blotting

Samples from the inhibition and disaggregation experiments were analyzed by gel electrophoresis with Western blotting utilizing an anti-A β antibody (6E10) following previously reported procedures.⁵⁸⁻⁶¹ Samples (10 μL) were separated on a 10-20% Tris-tricine gel (Invitrogen, Grand Island, NY, USA). Following separation, the proteins were transferred onto nitrocellulose, which was blocked with bovine serum albumin (BSA, 3% w/v, RMBIO, Missoula, MT, USA) in Tris-buffered saline (TBS) containing 0.1% Tween-20 (TBS-T) for 4 h at room temperature. The membranes were incubated with antibody (6E10, 1:2000, Covance, Princeton, NJ, USA) in a solution of 2% BSA (w/v in TBS-T) overnight at 4°C . After washing, the horseradish peroxidase-conjugated goat antimouse secondary antibody (1:5000) in 2% BSA was added for 1 h at room temperature. A homemade ECL kit⁵ was then used to visualize the results on a ChemiDoc MP Imaging System (Bio-Rad, Hercules, CA, USA).

4.4.9. Transmission Electron Microscopy (TEM)

Samples for TEM were prepared according to previously reported methods.⁵⁸⁻⁶¹ Glow-discharged grids (Formar/Carbon 300-mesh, Electron Microscopy Sciences, Hatfield, PA, USA) were treated with A β samples from the inhibition and disaggregation experiments (5 μ L) for 2 min at room temperature. Excess sample was removed by blotting with filter paper followed by washing three times with ddH₂O. Each grid was incubated with uranyl acetate (1% w/v ddH₂O, 5 μ L, 1 min). Upon removal of excess uranyl acetate with filter paper, the grids were dried for at least 30 min at room temperature before measurement. Images from each sample were taken on a JEOL JEM-2100 transmission electron microscope (UNIST Central Research Facilities, Ulsan National Institute of Science and Technology, Ulsan, Republic of Korea) at 120 kV and 25,000x magnification.

4.4.10. Electron Paramagnetic Resonance Spectroscopy (EPR)

All EPR measurements were performed at Western Seoul Center, Korea Basic Science Institute. X-band CW-EPR spectra were collected on a Bruker EMX plus 6/1 spectrometer equipped with an Oxford Instrument ESR900 liquid He cryostat using an Oxford ITC 503 temperature controller. X-band CW-EPR spectra were collected with the following experimental parameters: microwave frequency, 9.6 GHz; microwave power, 1 mW; modulation amplitude, 10 G; time constant, 40.96 ms; 5 scans; temperature, 4 K.

All pulsed EPR measurements were performed at 4 K. Q-band pulsed EPR data were obtained on a Bruker ELEXSYS E580 spectrometer using an EN5107D2 resonator. Cryogenic temperatures were achieved with an Oxford CF-935 cryostat and an Oxford ITC temperature controller. Electron spin echo detected field sweep experiments were carried out using the two pulse sequence, $\pi/2$ - τ - π -echo, with pulse lengths of $t_{\pi/2} = 32$ ns and $t_{\pi} = 64$ ns and inter-pulse time of $\tau = 200$ ns. ESEEM experiments were performed utilizing the three pulse sequence, $\pi/2$ - τ - $\pi/2$ - T - $\pi/2$ -echo, with a pulse length of $t_{\pi/2} = 32$ ns and inter-pulse times of $\tau = 160$ – 168 ns and $T_{initial} = 80$ ns. Davies ENDOR experiments were conducted utilizing the pulse sequence, π - T - $\pi/2$ - τ - π -echo, with microwave pulse lengths of $t_{\pi/2} = 32$ ns and an inter-pulse time τ of 200 ns. A radio frequency (RF) π pulse with a length of 20 μ s was applied during the time T . Mims ENDOR measurements were carried out using the pulse sequence, $\pi/2$ - τ - $\pi/2$ - T - $\pi/2$ -echo, with a microwave pulse length of $t_{\pi/2} = 32$ ns and an inter-pulse time of $\tau = 400$ ns. In this sequence, the RF

power is applied during the time T (20 μ s) to drive nuclear spin transitions. All pulsed ENDOR spectra were obtained using stochastic sampling for a better baseline of the spectra.

W-band EPR data were obtained on a Bruker ELEXSYS E680 spectrometer operating at \sim 94 GHz with a cylindrical high Q-resonator (EN680). Electron spin echo detected field sweep experiments were performed using the two pulse sequence, $\pi/2$ - τ - π -echo, with pulse lengths of $t_{\pi/2} = 20$ ns and $t_{\pi} = 40$ ns and an inter-pulse time of $\tau = 200$ ns.

4.4.11. Matrix-Assisted Laser Desorption Ionization Mass Spectrometry (MALDI-MS).

A β_{40} (100 μ M) samples incubated with M(II)(TMC) (200 μ M) in a Chelex-treated buffered solution containing HEPES (20 mM, pH 7.4) and NaCl (150 μ M) were incubated at 37 $^{\circ}$ C for 24 h with constant agitation. Incubated A β_{40} , matrix [α -cyano-4-hydroxycinnamic acid (5 mg/mL) dissolved in 40% CH₃CN and 2% CF₃COOH], and 50 μ M of the internal standard were mixed in a ratio of 5:4:1 and loaded on the MALDI-MS target plate. After thoroughly drying the samples, MALDI-MS spectra were obtained using an Ultraflex III time-of-flight mass spectrometer (Bruker Daltonics, Bremen, Germany).

4.4.12. Computational Details

All DFT calculations were performed by using the B3LYP functional,⁷⁵⁻⁷⁹ the 6-311G* basis set,⁷⁹⁻⁸¹ and polarizable continuum model (water) with the Gaussian 09 package.⁸²⁻⁸⁶ Initial geometries for geometry optimizations were derived from the X-ray crystal structures of *trans*-I-[Co(TMC)(N₃)]⁺ (KAVSIJ01)⁸⁷, *trans*-I-[Ni(TMC)(N₃)]⁺ (TMCAZN01)⁴⁵, *trans*-I-[Cu(TMC)(H₂O)]²⁺ (DUKPOO)⁴⁶, *trans*-III-[Cu(TMC)(Br)]⁺ (XISVEA)⁸⁸, and *trans*-I-[Zn(TMC)(H₂O)]²⁺ (XACMOD)⁴⁷ by replacing the axial ligand with H₂O or OH⁻. The optimized structures were then used to perform frequency calculations to evaluate the Gibbs free energy corrections and TDDFT calculations to predict electronic absorption spectra. For the calculation of pK_a, $\Delta G_{\text{sol}}(\text{H}^+) = -265.9$ kcal/mol was used to consider a solvated proton.⁷³

Given the known variations in DFT-predicted properties depending on the choice of functionals,^{89,90} we tested the effect of Hartree-Fock exchange in the calculation of UV-vis spectra to select a computational method that can reproduce the electronic structures of the metal complexes correctly. When the *trans*-I-Cu(II)(TMC) and *trans*-III-Cu(II)(TMC) complexes are dissolved in water, they display ligand-field (LF) transitions at *ca.* 617 nm (16200 cm⁻¹) and 549 nm (18200 cm⁻¹), respectively (Figure B.16a,d). The axial ligands of these complexes are supposed to be occupied by water. Thus, the models for the *trans*-I- and *trans*-III-Cu(II)(TMC) complexes having either the water or hydroxo ligand were

calculated using the BP and B3LYP functionals. The TDDFT-predicted UV-vis spectra of these models suggest that, regardless of which functional is used, the complexes in neutral aqueous solution should have a water ligand rather than a hydroxo ligand, because the latter case should cause less split in the ligand field than the water molecule and thus display LF transitions at much lower energies than the experimental observations. The LF transitions of the $[trans-I-Cu(TMC)(H_2O)]^{2+}$ and $[trans-III-Cu(TMC)(H_2O)]^{2+}$ complexes are then better reproduced by using the B3LYP functional than the BP functional, in terms of their energies relative to the intense charge transfer band growing in high energy at $> 400 \text{ nm}$ ($25,000 \text{ cm}^{-1}$). Therefore, the B3LYP functional was employed for all computations.

4.4.13. Competition Experiments

An $A\beta_{40}$ stock solution was prepared by dissolving lyophilized peptide in 1% NH_4OH (10 μL) and diluting with ddH_2O . The concentration of the solution was determined by measuring the absorbance of the solution at 280 nm ($\epsilon = 1450 \text{ M}^{-1}\text{cm}^{-1}$). The peptide stock solution was diluted to a final concentration of 25 μM in Chelex-treated buffered solution containing HEPES (20 μM , pH 7.4) and NaCl (150 μM). Increasing concentrations of sodium azide (NaN_3) or sodium cyanate ($NaOCN$) (0–5 mM) were added to the sample of $A\beta$ (25 μM) and incubated for 2 min at room temperature. $Co(II)(TMC)$ (50 μM) was then added to the reaction mixture and incubated at 37 °C with constant agitation for 24 h. The resultant samples were then analyzed by gel electrophoresis with Western blotting utilizing an anti- $A\beta$ antibody (6E10). Samples (10 μL) were then separated on a 10-20% Tris-tricine gel (Invitrogen, Grand Island, NY, USA). Following separation, the proteins were transferred onto nitrocellulose, which was blocked with bovine serum albumin (BSA, 3% w/v, RMBIO, Missoula, MT, USA) in Tris-buffered saline (TBS) containing 0.1% Tween-20 (TBS-T) for 4 h at room temperature. The membranes were incubated with Antibody (6E10, 1:2000, Covance, Princeton, NJ, USA) in a solution of 2% BSA (w/v in TBS-T) overnight at 4 °C. After washing, the horseradish peroxidase-conjugated goat antimouse secondary antibody (1:5000) in 2% BSA was added for 1 h at room temperature. A homemade ECL kit⁹¹ was then used to visualize the results on a ChemiDoc MP Imaging System (Bio-Rad, Hercules, CA, USA).

4.4.14. Internal Standard Calibration

Melittin, a component in honey bee venom, was purchased from Sigma Aldrich and used without further purification. The concentration of melittin was determined by measuring the absorbance of the solution at 280 nm ($\epsilon = 5570 \text{ M}^{-1}\text{cm}^{-1}$).⁹² Different concentrations (1–200 μM) of melittin were prepared and diluted by 10-fold in order to construct the calibration plot. Melittin,

matrix, and HPLC grade water were mixed at a ratio of 1:4:5 and loaded on the MALDI-MS plate. For MALDI-MS, the matrix solution was prepared with 5 mg/mL of α -cyano-4-hydroxycinnamic acid dissolved in 40% CH₃CN and 2% trifluoroacetic acid (CF₃COOH). The signal intensity ratio was calculated by dividing the signal intensity for melittin by the sum of intensities for the 30 most dominant peaks. The calibration equation was derived from the linear regression of the signal intensity ratio values. The remaining quantity of the singly-charged A β ₄₀ was estimated by utilizing the linear correlation between concentration and signal intensity. The concentration was determined from the experimental intensities of melittin and A β ₄₀.

4.4.15. Electrospray Ionization–Mass Spectrometry (ESI–MS)

A β ₄₀ (100 μ M) was incubated with M(II)(TMC) (500 μ M) in 100 mM ammonium acetate (pH 7.5) at 37 °C for 1 h without agitation. The incubated A β ₄₀ samples were diluted by 10-fold before injection into the mass spectrometer. The capillary voltage, sampling cone voltage, and source temperature were set to 2.8 kV, 70 V, and 60 °C, respectively. The backing pressure was adjusted to 3.2 mbar. To obtain the ion mobility spectra, ion mobility wave height and wave velocity were adjusted to 10 V and 450 m/s, respectively. More than 200 spectra were obtained for each sample at a range of 300–3000 m/z and averaged for analysis.

4.4.16. Isomerization Experiments

The potential isomerization of M(II)(TMC) (M = Co, Ni, and Cu) was followed by UV-vis. M(II)(TMC) was dissolved in Chelex-treated buffered solution containing HEPES (20 mM, pH 7.4) and NaCl (150 μ M) to a final concentration of 20 mM for Co(II)(TMC), 10 mM for Ni(II)(TMC), and 2.5 mM for Cu(II)(TMC). Their optical spectra were monitored over a 24 h period at 37 °C without agitation.

4.4.17. Parallel Artificial Membrane Permeability Adapted for the Blood-Brain Barrier (PAMPA-BBB) Assay.

PAMPA-BBB experiments were carried out using the PAMPA Explorer kit (*p*ION Inc., Billerica, MA, USA) with modifications to a previously reported protocol.^{58,59,61,93-96} Each stock solution was diluted with Prisma HT buffer (pH 7.4, *p*ION) to a final concentration of 25 μ M (1% v/v final DMSO concentration). The resulting solution was added to wells of the donor plate (200 μ L, 12 replicates). BBB-1 lipid formulation (5 μ L, *p*ION) was used to coat the polyvinylidene fluoride (PVDF, 0.45 mM) filter membrane on the acceptor plate. The acceptor plate was placed

on top of the donor plate forming a sandwich. Brain sink buffer (BSB, 200 μ L, *p*ION) was added to each well of the acceptor plate. The sandwich was incubated for 4 h at ambient temperature without stirring. UV-vis spectra of the solutions in the blank, reference, acceptor, and donor plates were measured using a microplate reader. The PAMPA Explorer software v. 3.5 (*p*ION) was used to calculate $-\log P_e$ for each compound. CNS+/- designations were assigned by comparison to compounds that were identified in previous reports.⁹⁴⁻⁹⁶

4.4.18. Cell Viability Measurements

Human neuroblastoma SH-SY5Y (5Y) cells were maintained in media containing 45% minimum essential medium (MEM), 45% F12, and 10% fetal bovine serum (FBS, GIBCO, Grand Island, NY, USA), 100 U/mL penicillin (GIBCO), and 100 mg/mL streptomycin (GIBCO). The cells were grown in a humidified atmosphere with 5% CO₂ at 37 °C. Cell viability upon treatment of Co(II)(TMC) was determined by the MTT assay [MTT = 3-(4,5-dimethyl-2-thiazolyl)-2,5-diphenyl-2*H*-tetrazolium bromide, Sigma-Aldrich]. The cells were seeded in a 96 well plate (15000 cells/100 mL). The cells were then treated with various concentrations of Co(II)(TMC). After 24 h incubation, MTT [25 mM; 5 mg/mL in PBS (pH 7.4, GIBCO)] was added to each well and the plate was incubated for 3 h at 37 °C. Formazan produced by the cells was solubilized by the addition of an acidic solution of *N,N*-dimethylformamide (DMF, 50% v/v, aq, pH 4.5) and sodium dodecyl sulfate (SDS, 20% w/v) overnight at room temperature in the dark. The absorbance was measured at 600 nm using a microplate reader. Cell viability was calculated relative to cells containing an equivalent amount of ddH₂O. Error bars were calculated as standard errors from three independent experiments.

4.5. Acknowledgements

This work was supported by the National Research Foundation of Korea (NRF) grant funded by the Korean government [NRF-2014R1A2A2A01004877 (to M.H.L.); 2014R1A1A2056051 (to J.C.); N01150673 (to K.P.)]; the 2016 Research Fund (Project Number 1.160001.01) of Ulsan National Institute of Science and Technology (UNIST) (to M.H.L.); the Ministry of Science, ICT and Future Planning (16-BD-0403, 2014M1A8A1049320, and 2015M3D3A1064890) (to J.C.); the Ministry of Oceans and Fisheries (20150220) of Korea (to J.C.); the fund (G04140040) of Korea Advanced Institute of Science and Technology (KAIST) (to K.P.); the supercomputing resources (KSC-2015-C2-0002) of Korea Institute of Science and Technology Information (KISTI) (to K.P.); the C1 Gas Refinery Program through the NRF funded by the Ministry of Science,

ICT & Future Planning (2015M3D3A1A01064876) (to S.H.K.); the National Research Council of Science and Technology through the Degree & Research Center Program (DRC-14-3-KBSI) (to S.H.K.). We also thank Eunju Nam for assistance with cytotoxicity measurements.

4.6. References

- (1) Derrick J. S.; Lim M. H. *ChemBioChem* **2015**, *16*, 887–898.
- (2) Savelieff, M. G.; Lee, S.; Liu, Y.; Lim, M. H. *ACS Chem. Biol.* **2013**, *8*, 856–865.
- (3) Savelieff, M. G.; DeToma, A. S.; Derrick, J. S.; Lim, M. H. *Acc. Chem. Res.* **2014**, *47*, 2475–2482.
- (4) Jakob-Roetne, R.; Jacobsen, H. *Angew. Chem. Int. Ed.* **2009**, *48*, 3030–3059.
- (5) Kepp, K. P. *Chem. Rev.* **2012**, *112*, 5193–5239.
- (6) Alzheimer's Association, *Alzheimer's Dementia* **2015**, *11*, 332–384.
- (7) Rodríguez-Rodríguez, C.; Telpoukhovskaia, M.; Orvig, C. *Coord. Chem. Rev.* **2012**, *256*, 2308–2332.
- (8) Scott, L. E.; Orvig, C. *Chem. Rev.* **2009**, *109*, 4885–4910.
- (9) Hayne, D. J.; Lim, S.; Donnelly, P. S. *Chem. Soc. Rev.* **2014**, *43*, 6701–6715.
- (10) Valensin, D.; Gabbiani, C.; Messori, L. *Coord. Chem. Rev.* **2012**, *256*, 2357–2366.
- (11) Hureau, C.; Faller, P. *Dalton Trans.* **2014**, *43*, 1080–1094.
- (12) Collin, F.; Sasaki, I.; Eury, H.; Faller, P.; Hureau, C. *Chem. Commun.* **2013**, *49*, 2130–2132.
- (13) Heffern, M. C.; Velasco, P. T.; Matosziuk, L. M.; Coomes, J. L.; Karras, C.; Ratner, M. A.; Klein, W. L.; Eckermann, A. L.; Meade, T. J. *ChemBioChem* **2014**, *15*, 1584–1589.
- (14) Barnham, K. J.; Kenche, V. B.; Ciccotosto, G. D.; Smith, D. P.; Tew, D. J.; Liu, X.; Perez, K.; Cranston, G. A.; Johanssen, T. J.; Volitakis, I.; Bush, A. I.; Masters, C. L.; White, A. R.; Smith, J. P.; Cherny, R. A.; Cappai, R. *Proc. Natl. Acad. Sci. U.S.A.* **2008**, *105*, 6813–6818.
- (15) Kenche, V. B.; Hung, L. W.; Perez, K.; Volitakes, I.; Ciccotosto, G.; Kwok, J.; Critch, N.; Sherratt, N.; Cortes, M.; Lal, V.; Masters, C. L.; Murakami, K.; Cappai, R.; Adlard, A. P.; Barnham, K. J. *Angew. Chem. Int. Ed.* **2013**, *52*, 3374–3378.
- (16) Donnelly, P. S.; Caragounis, A.; Du, T.; Laughton, K. M.; Volitakis, I.; Cherny, R. A.; Sharples, R. A.; Hill, A. F.; Li, Q. X.; Masters, C. L.; Barnham, K. J.; White, A. R. *J. Biol. Chem.* **2008**, *283*, 4568–4577.
- (17) Kim, H. M.; Jang, B.; Cheon, Y. E.; Suh, M. P.; Suh, J. *J. Biol. Inorg. Chem.* **2009**, *14*, 151–157.
- (18) Chei, W. S.; Ju, H.; Suh, J. *J. Biol. Inorg. Chem.* **2011**, *16*, 511–519.

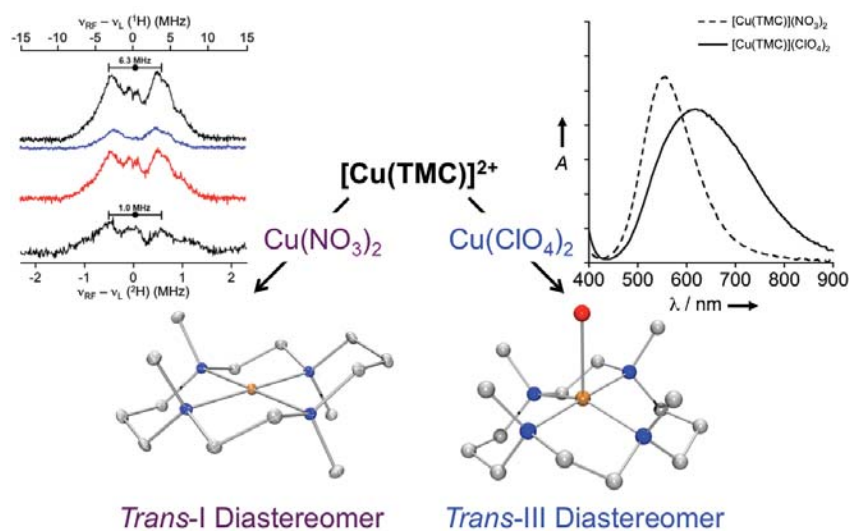
- (19) Lincoln, K. M.; Richardson, T. E.; Rutter, L.; Gonzalez, P.; Simpkins, J. W.; Green, K. N. *ACS Chem. Neurosci.*, **2012**, *3*, 919–927.
- (20) Suh, J.; Yoo, S. H.; Kim, M. G.; Jeong, K.; Ahn, J. Y.; Kim, M.-S.; Chae, P. S.; Lee, T. Y.; Lee, J.; Lee, J.; Jang, Y. A.; Ko, E. H. *Angew. Chem. Int. Ed.* **2007**, *46*, 7064–7067.
- (21) Chei, W.-S.; Lee, J. W.; Kim, J. B.; Suh, J. *Bioorg. Med. Chem.* **2010**, *18*, 5248–5253.
- (22) Jeon, J. W.; Son, S. J.; Yoo, C. E.; Hong, I. S.; Suh, J. *Bioorg. Med. Chem.* **2003**, *11*, 2901–2910.
- (23) Chei, S. W.; Suh, J. In *Progress in Inorganic Chemistry*; Karlin, K. D. Ed.; John Wiley & Sons, Inc.: Hoboken, NJ, USA., **2007**; Vol. 55, p 80–137.
- (24) Gonzalez, P.; da Costa, V. C. P.; Hyde, K.; Wu, Q.; Annunziata, O.; Rizo, J.; Akkaraju, G.; Green, K. N. *Metallomics*, **2014**, *6*, 2072–2082.
- (25) Lanza, V.; D’Agata, R.; Iacono, G.; Bellia, F.; Spoto, G.; Vecchio, G. *J. Inorg. Biochem.* **2015**, *153*, 377–383.
- (26) Liang, X.; Sadler, P. J. *Chem. Soc. Rev.* **2004**, *33*, 246–266.
- (27) Wu, W.-H.; Lei, P.; Liu, Q.; Hu, J.; Gunn, A. P.; Chen, M.-S.; Rui, Y.-F.; Su, X.-Y.; Xie, Z.-P.; Zhao, Y.-F.; Bush, A. I.; Li, Y. M. *J. Biol. Chem.* **2008**, *283*, 31657–31664.
- (28) Yang, Y.; Chen, T.; Zhu, S.; Gu, X.; Jia, X.; Lu, Y.; Zhu, L. *Integr. Biol.* **2015**, *7*, 655–662.
- (29) Chen, T.; Wang, X.; He, Y.; Zhang, C.; Wu, Z.; Liao, K.; Wang, J.; Guo, Z. *Inorg. Chem.* **2009**, *48*, 5801–5809.
- (30) Vijay-Kumar, S.; Bugg, C. E.; Cook, W. J. *J. Mol. Biol.* **1987**, *194*, 531–544.
- (31) Barefield, K. E. *Coord. Chem. Rev.* **2010**, *254*, 1607–1627.
- (32) Micheloni, M.; Paoletti, P.; Bürki, S.; Kaden, T. A. *Helv. Chim. Acta* **1982**, *65*, 587–594.
- (33) Moore, P.; Sachinidis, J.; Willey, G. R. *Chem. Commun.* **1983**, 522–523.
- (34) Herron, N.; Moore, P. *Inorg. Chim. Acta* **1979**, *36*, 89–96.
- (35) Maimon, E.; Zilbermann, I.; Golub, G.; Ellern, A.; Shames, A. I.; Cohen, H.; Meyerstein, D. *Inorg. Chim. Acta* **2001**, *324*, 65–72.
- (36) Crick, I. S.; Tregloan, P. A. *Inorg. Chim. Acta* **1988**, *142*, 291–299.
- (37) Barefield, K. E.; Wagner, F. *Inorg. Chem.* **1973**, *12*, 2435–2439.
- (38) Ram, M. S.; Riordan, C. G.; Ostrander, R.; Rheingold, A. L. *Inorg. Chem.* **1995**, *34*, 5884–5892.
- (39) Reimer, S.; Wicholas, M.; Scott, B.; Willett, R. D. *Acta Cryst.* **1989**, *C45*, 1694–1697.
- (40) Vicente, R.; Escuer, A.; El Fallah, M. S.; Solans, X.; Font-Bardia, M. *Inorg. Chim. Acta* **1997**, *261*, 227–232.
- (41) Crick, I. S.; Hoskins, B. F.; Tregloan, P. A. *Inorg. Chim. Acta* **1986**, *114*, L33–L34.

- (42) Lu, T.-H.; Shui, W.-Z.; Tung, S.-F.; Chi, T.-Y.; Liao, F.-L.; Chung, C.-S. *Acta Cryst.* **1998**, *C54*, 1071–1072.
- (43) Alcock, N. W.; Herron, N.; Moore, P. *Dalton Trans.* **1978**, 1282–1288.
- (44) D’Aniello, M. J.; Mocella, M. T.; Wagner, F.; Barefield, K. E.; Paul, I. C. *J. Am. Chem. Soc.* **1975**, *97*, 192–194.
- (45) Escuer, A.; Vicente, R.; El Fallah, M. S.; Solans, X.; Font-Bardia, M. *Inorg. Chim. Acta* **1996**, *247*, 85–91.
- (46) Lee, T.-J.; Lee, T.-Y.; Hong, C.-Y.; Wu, D.-T.; Chung, C.-S. *Acta Cryst.* **1986**, *C42*, 999–1001.
- (47) Panneerselvam, K.; Lu, T.-H.; Chi, T.-Y.; Tung, S.-F.; Chung, C.-S. *Anal. Sci.* **1999**, *15*, 205–206.
- (48) Burgess, J.; Fawcett, J.; Haines, R. I.; Singh, K.; Russell, D. R. *Transition Met. Chem.* **1999**, *24*, 355–361.
- (49) Terwilliger, T. C.; Eisenberg, D. *J. Biol. Chem.* **1982**, *257*, 6016–6022.
- (50) Suh, J.; Chei, W. S. *Curr. Opin. Chem. Biol.* **2008**, *12*, 207–213.
- (51) Chin, J. *Acc. Chem. Res.* **1991**, *24*, 145–152.
- (52) Buckingham, D. A.; Harrowfield, J. M.; Sargeson, A. M. *J. Am. Chem. Soc.* **1974**, *96*, 1726–1729.
- (53) Buckingham, D. A.; Dekkers, J.; Sargeson, A. M.; Wein, M. *J. Am. Chem. Soc.* **1972**, *94*, 4032–4034.
- (54) Hettich, R.; Schneider, H.-J. *J. Am. Chem. Soc.* **1997**, *119*, 5638–5647.
- (55) Buckingham, D. A.; Keene, F. R.; Sargeson, A. M. *J. Am. Chem. Soc.* **1974**, *96*, 4981–4983.
- (56) Suh, J. *Acc. Chem. Res.* **1992**, *25*, 273–279.
- (57) Takasaki, B. K.; Kim, J. H.; Rubin, E.; Chin, J. *J. Am. Chem. Soc.* **1993**, *115*, 1157–1159.
- (58) Derrick, J. S.; Kerr, R. A.; Nam, Y.; Oh, S. B.; Lee, H. J.; Earnest, K. G.; Suh, N.; Peck, K. L.; Ozbil, M.; Korshavn, K. J.; Ramamoorthy, A.; Prabhakar, R.; Merino, E. J.; Shearer, J.; Lee, J. Y.; Ruotolo, B. T.; Lim, M. H. *J. Am. Chem. Soc.*, **2015**, *137*, 14785–14797.
- (59) Lee, S.; Zheng, X.; Krishnamoorthy, J.; Savelieff, M. G.; Park, H. M.; Brender, J. R.; Kim, J. H.; Derrick, J. S.; Kochi, A.; Lee, H. J.; Kim, C.; Ramamoorthy, A.; Bowers, M. T.; Lim, M. H. *J. Am. Chem. Soc.* **2014**, *136*, 299–310.
- (60) Hyung, S. J.; DeToma, A. S.; Brender, J. R.; Lee, S.; Vivekanandan, S.; Kochi, A.; Choi, J. S.; Ramamoorthy, A.; Ruotolo, B. T.; Lim, M. H. *Proc. Natl. Acad. Sci. U.S.A.* **2013**, *110*, 3743–3748.

- (61) Choi, J.-S.; Braymer, J. J.; Nanga, R. P. R.; Ramamoorthy, A.; Lim, M. H. *Proc. Natl. Acad. Sci. U.S.A.* **2010**, *107*, 21990–21995.
- (62) Wyttenbach, T.; Bowers, M. T. *J. Phys. Chem. B* **2011**, *115*, 12266–12275.
- (63) Lincoln, S. F.; Hambley, T. W.; Pisaniello, D. L.; Coates, J. H. *Aust. J. Chem.* **1984**, *37*, 713–723.
- (64) Newman, K. E. *Inorg. Chim. Acta* **1984**, *89*, L3–L5.
- (65) Kumar, A.; Periyannan, G. R.; Narayana, B.; Kittell, A. W.; Kim, J. J.; Bennett, B. *Biochem. J.* **2007**, *403*, 527–536.
- (66) Bennett, B. *Curr. Top. Biophys.* **2002**, *26*, 49–57.
- (67) Jimenez, H. R.; Salgado, J.; Moratal, J. M.; Morgenstern-Badarai, J. *Inorg. Chem.* **1996**, *35*, 2737–2741.
- (68) Meier, P.; Merbach, A. *Chem. Commun.* **1977**, 36–37.
- (69) Ayoub, A. T.; Tuszyński, J.; Klobukowski, M. *Theor. Chem. Acc.* **2014**, *133*, 1–7.
- (70) Salazar-Salinas, K.; Baldera-Aguayo, P. A.; Encomendero-Risco, J. J.; Orihuela, M.; Sheen, P.; Seminario, J. M.; Zimic, M. J. *J. Phys. Chem. B* **2014**, *118*, 10065–10075.
- (71) Martin, R. B. *Biopolymers* **1998**, *45*, 351–353.
- (72) Beck, M. W.; Oh, S. B.; Kerr, R. A.; Lee, H. J.; Kim, S. H.; Kim, S.; Jang, M.; Ruotolo, B. T.; Lee, J.-Y.; Lim, M. H. *Chem. Sci.* **2015**, *6*, 1879–1886.
- (73) Tissandier, M. D.; Cowen, K. A.; Feng, W. Y.; Gundlach, E.; Cohen, M. H.; Earhart, A. D.; Coe, J. V.; Tuttle, T. R. *J. Phys. Chem. A* **1998**, *102*, 7787–7794.
- (74) Mruk, D. D.; Cheng, C. Y. *Spermatogenesis* **2011**, *1*, 121–122.
- (75) Becke, A. D. *J. Chem. Phys.* **1993**, *98*, 5648–5652.
- (76) Becke, A. D. *Phys. Rev. A* **1988**, *38*, 3098–3100.
- (77) Lee, C.; Yang, W.; Parr, R. G. *Phys. Rev. B* **1988**, *37*, 785–789.
- (78) Vosko, S.; Wilk, L.; Nusair, M. *Can. J. Phys.* **1980**, *58*, 1200–1211.
- (79) McLean, A.; Chandler, G. J. *J. Chem. Phys.* **1980**, *72*, 5639–5648.
- (80) Wachters, A. J. H. *J. Chem. Phys.* **1970**, *52*, 1033–1036.
- (81) Raghavachari, K.; Trucks, G. W. *J. Chem. Phys.* **1989**, *91*, 1062–1065.
- (82) Barone, V.; Cossi, M.; Tomasi, J. *J. Comput. Chem.* **1998**, *19*, 404–417.
- (83) Barone, V.; Cossi, M.; Tomasi, J. *J. Chem. Phys.* **1997**, *107*, 3210–3221.
- (84) Cossi, M.; Barone, V.; Cammi, R.; Tomasi, J. *Chem. Phys. Lett.*, **1996**, *255*, 327–335.
- (85) Cancès, E.; Mennucci, B.; Tomasi, J. *J. Chem. Phys.* **1997**, *107*, 3032–3041.
- (86) Ogliaro, F.; Bearpark, M.; Heyd, J.; Brothers, E.; Kudin, K.; Staroverov, V.; Kobayashi, R.; Normand, J.; Raghavachari, K.; Rendell, A. *Gaussian Inc., Wallingford, CT* 2009.

- (87) Evangelio, E.; Rath, N. P.; Mirica, L. M. *Dalton Trans.* **2012**, *41*, 8010–8021.
- (88) Kickelbick, G.; Pintauer, T.; Matyjaszewski, K. *New J. Chem.* **2002**, *26*, 462–468.
- (89) Holland, J. P.; Green, J. C. *J. Comput. Chem.* **2009**, *31*, 1008–1014.
- (90) Korth, M.; Grimme, S. *Chem. Theory Comput.* **2009**, *5*, 993–1003.
- (91) Mruk, D. D.; Cheng, C. Y. *Spermatogenesis* **2011**, *1*, 121–122.
- (92) Ghosh, A. K.; Rukmini, R.; Chattopadhyay, A. *Biochemistry* **1997**, *36*, 14291–14305.
- (93) Liu, Y.; Kochi, A.; Pithadia, A. S.; Lee, S.; Nam, Y.; Beck, M. W.; He, X.; Lee, D.; Lim, M. H. *Inorg. Chem.* **2013**, *52*, 8121–8130.
- (94) Di, L.; Kerns, E. H.; Fan, K.; McConnell, O. J.; Carter, G. T. *Eur. J. Med. Chem.* **2003**, *38*, 223–232.
- (95) Avdeef, A.; Bendels, S.; Di, L.; Faller, B.; Kansy, M.; Sugano, K.; Yamauchi, Y. *J. Pharm. Sci.* **2007**, *96*, 2893–2909.
- (96) *BBB Protocol and Test Compounds*; pION inc.: Woburn, MA, 2015.

Appendix A.
 Stereochemistry of Tetramethylcyclam Metal Complexes
 Directed by Unexpected Anion Effects



I thank Professor Jaeheung Cho and Hyeonwoo Tak for their assistance with the synthesis and X-ray crystallography measurements. I was involved with identifying the anion effect from preliminary data, growing the crystals for X-ray analysis, and the writing of the manuscript with the assistance of Professor Lim.

A.1. Introduction

N-substituted cyclams have become one of the most widely studied and utilized group of macrocyclic ligands since Barefield and Wagner initially reported the preparation of TMC (1,4,8,11-tetramethyl-1,4,8,11-tetraazacyclotetradecane) and its respective metal complexes in 1973.^{1,2} The rise in popularity of TMC and other similar *N*-substituted cyclams most definitely arose from the unique properties of the ligands (*e.g.*, distinctive stereochemistry, coordination spheres, and accommodation of unusual oxidation and spin states)²⁻⁶, which have directed their use for a broad range of applications spanning many different fields some of which include: medicine,⁷⁻¹⁰ catalysis,¹¹⁻¹³ and biomimetic chemistry.¹⁴⁻¹⁵ In particular, TMC has been critically important in stabilizing high-valent non-heme metal oxo cores to investigate mechanisms and reactive intermediates in biological reactions that are relevant to sustainable energy formation.¹⁴⁻²¹

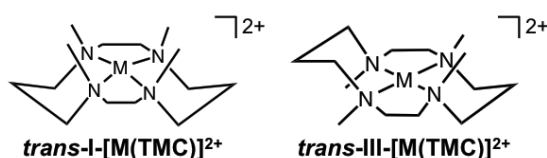


Figure A.1. Chemical structures of $[\text{M(TMC)}]^{2+}$ (TMC = 1,4,8,11-tetramethyl-1,4,8,11-tetraazacyclotetradecane). The two most common diastereomers are presented (*trans*-I and *trans*-III). The *trans*-I conformation forms pentacoordinate complexes by binding one ligand on the *syn* face. The *trans*-III isomer generates octahedral complexes by binding two ligands in the open axial sites.

Perhaps the most interesting property of TMC is the distinctive stereochemistry of its metal complexes that can be theoretically found in five possible diastereoisomeric forms with the two most thermodynamically stable being the *trans*-I and *trans*-III isomers (Figure A.1).² The two isomers have very different fundamental properties (*e.g.*, catalytic activity, kinetic stability, redox chemistry) the most obvious of which are their coordination environments.^{2,13,22-25} The *trans*-I metal complexes that have all four methyl moieties positioned on the same side of the macrocyclic plane almost always generate tetracoordinate square planar complexes or pentacoordinate square pyramidal or trigonal bipyramidal (TBP) structures while the *trans*-III metal complexes tend to exclusively produce hexacoordinate octahedral complexes.² Almost all metal TMC complexes, especially those with 3d metal centers, are found in the *trans*-I structures where isomerization of the *trans*-I complexes to the *trans*-III conformation has been shown to be difficult and highly dependent on solution conditions.^{2,26} As a result, very little is known about the properties and fundamental chemistries of the *trans*-III metal TMC complexes.² Therefore, due to the importance and broad application of TMC and other *N*-methylated cyclam ligands, a facile and fundamental comprehensive approach to selectively and systematically prepare the *trans*-III

metal TMC complexes would be significantly valuable. Herein, we report an unexpected anion effect that directs the stereochemistry of $[\text{Cu}(\text{TMC})]^{2+}$ whereby those prepared with $\text{Cu}(\text{NO}_3)_2 \cdot 6\text{H}_2\text{O}$ yield the unanticipated *trans*-III isomer and those synthesized with $\text{Cu}(\text{ClO}_4)_2 \cdot 6\text{H}_2\text{O}$ gave the expected *trans*-I metal complex. We therefore propose this previously undiscovered anion dependence as a potentially new, simplistic method for the preparation and exploration of additional novel *trans*-III metal TMC complexes.

A.2. Results and Discussion

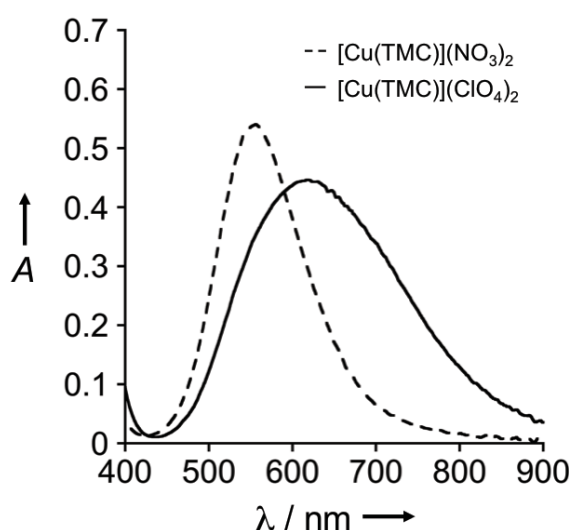


Figure A.2. UV-vis spectra of $[\text{Cu}(\text{TMC})](\text{NO}_3)_2$ and $[\text{Cu}(\text{TMC})](\text{ClO}_4)_2$. The optical spectrum of $[\text{Cu}(\text{TMC})](\text{NO}_3)_2$ (red line) is blue shifted in comparison to $[\text{Cu}(\text{TMC})](\text{ClO}_4)_2$ (blue line) which is consistent with an octahedral *trans*-III- $[\text{Cu}(\text{TMC})](\text{NO}_3)_2$ complex.

A.2.1. Preparation and Optical Properties of $[\text{Cu}(\text{TMC})]^{2+}$

$[\text{Cu}(\text{TMC})](\text{NO}_3)_2$ and $[\text{Cu}(\text{TMC})](\text{ClO}_4)_2$ were prepared in high yields (*ca.* 90%) following identical synthetic procedures adapted from previously reported methods.² TMC was added to an acetonitrile solution containing either an equivalent of $\text{Cu}(\text{NO}_3)_2 \cdot 6\text{H}_2\text{O}$ or $\text{Cu}(\text{ClO}_4)_2 \cdot 6\text{H}_2\text{O}$ and the resulting reaction mixtures were refluxed for 12 h to give purple and blue solids, respectively. Initial evidence to support their difference in stereochemistry was presented in their optical spectra (Figure A.2). The UV-visible (UV-vis) spectrum of $[\text{Cu}(\text{TMC})](\text{ClO}_4)_2$ presented a single broad band at *ca.* 630 nm that was consistent with previous literature reports of pentacoordinate *trans*-I- $[\text{Cu}(\text{TMC})]^{2+}$ complexes which would be expected by following this synthetic procedure (*i.e.*, the direct metalation of TMC; Figure A.2, solid line).³ Surprisingly, the peak in the optical spectrum of $[\text{Cu}(\text{TMC})](\text{NO}_3)_2$ was more intense and

significantly blue-shifted (*ca.* 554 nm) with respect to $[\text{Cu}(\text{TMC})](\text{ClO}_4)_2$ (Figure A.2, dashed line). This spectrum is consistent with previous reports of an octahedral *trans*-III- $[\text{Cu}(\text{TMC})]^{2+}$ complex that was generated by an electrochemically driven comproportionation reaction;²⁷ however, unlike the electrochemically generated complex, this *trans*-III- $[\text{Cu}(\text{TMC})](\text{NO}_3)_2$ complex appeared to be stable irrespective of the solution conditions.^{2,26} Similar blue-shifts in the optical spectra of $[\text{Ni}(\text{TMC})]^{2+}$ complexes have also been reported; thus, further supporting an octahedral *trans*-III structure for the nitrate complex and a pentacoordinate square pyramidal or TBP perchlorate complex.⁴

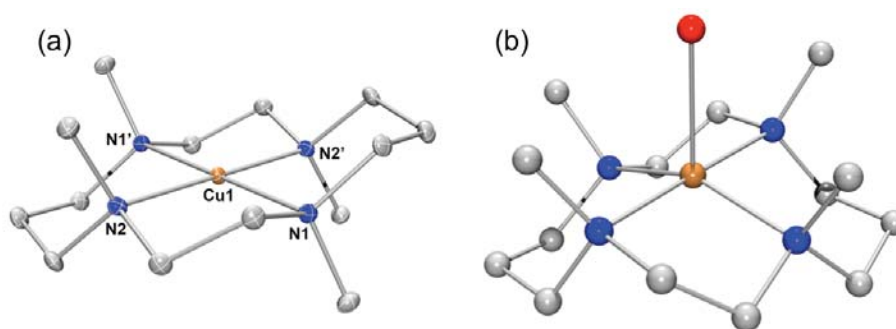


Figure A.3. Chemical structures of $[\text{Cu}(\text{TMC})](\text{NO}_3)_2$ and $[\text{Cu}(\text{TMC})(\text{H}_2\text{O})](\text{ClO}_4)_2$. Hydrogen atoms are omitted for clarity. a) ORTEP diagram of the cationic part of $[\text{Cu}(\text{TMC})](\text{NO}_3)_2$ with thermal ellipsoids drawn at the 30% probability level. b) Ball-and-stick representation of the cationic part of $[\text{Cu}(\text{TMC})(\text{H}_2\text{O})](\text{ClO}_4)_2$ (gray C, blue N, red O, brown Cu). Selected bond distances (Å) and angles (°) are summarized in Table B.1. The crystal structure of $[\text{Cu}(\text{TMC})(\text{H}_2\text{O})](\text{ClO}_4)_2$ is adapted from reference 29 for comparison.

A.2.2. X-ray Crystallographic Analysis of $[\text{Cu}(\text{TMC})]^{2+}$

To further probe the stereochemistry of the $[\text{Cu}(\text{TMC})]^{2+}$ complexes, crystals suitable for X-ray analysis for $[\text{Cu}(\text{TMC})](\text{NO}_3)_2$ were obtained by slow diffusion of diethyl ether into a methanol solution of $[\text{Cu}(\text{TMC})](\text{NO}_3)_2$ and the resulting structural data was compared to previously reported structures for $[\text{Cu}(\text{TMC})](\text{ClO}_4)_2$.^{27,29,30} As shown in Figure A.3, in agreement with our UV-vis data, $[\text{Cu}(\text{TMC})](\text{NO}_3)_2$ was found to be in the hexacoordinate *trans*-III conformation with two nitrate anions occupying the open axial sites while the perchlorate complex, was observed to possess a *trans*-I distorted square pyramidal structure consistent with the steric constraints of having all four methyl moieties located on the same side of the macrocyclic plane.^{2,3} The bond angles (*i.e.*, almost all right angles) and lengths of $[\text{Cu}(\text{TMC})](\text{NO}_3)_2$, particularly the elongated Cu–O bonds (2.612 Å), are consistent with the expected tetragonally elongated octahedral structure characteristic of Cu(II) complexes with strong Jahn-Teller effects (Table A.1) and are comparable to similar structures found in the literature.^{27,31} Additional differences in the two structures that are worth mentioning are the degree of distortion in the macrocyclic

ligand and the distance that the copper center sits above the macrocyclic plane. In [Cu(TMC)](ClO₄)₂ the copper atom is found to be sitting 0.242 Å above macrocyclic plane which is also severely distorted, as can be observed by its averaged dihedral angle of 23.43° (dihedral angles were calculated by measuring the distance between the two intersecting planes defined by the four N donor atoms; Table A.1). This extent of distortion was not observed in the *trans*-III-[Cu(TMC)](NO₃)₂ complex which has its metal center sitting coplanar with the four N donor atoms of the macrocycle.

Table A.1. Selected crystallographic metrics for [Cu(TMC)](NO₃)₂ and [Cu(TMC)](ClO₄)₂.

[Cu(TMC)](NO ₃) ₂		[Cu(TMC)](ClO ₄) ₂ ^a	
Cu–N1	2.074 Å	Cu–N1	2.086 Å
Cu–N2	2.083 Å	Cu–N2	2.040 Å
Cu–O1	2.612 Å	Cu–N3	2.079 Å
Distance above the macrocyclic plane	0.0 Å	Cu–N4	2.094 Å
N1a–Cu–N2a	87.28°	Cu–O1	2.398 Å
N1a–Cu–N2b	92.72°	Distance above the macrocyclic plane	0.242 Å
N1a–Cu–O1a	87.58°	N1–Cu–N2	94.04°
N1b–Cu–O1a	92.42°	N2–Cu–N3	84.93°
N2a–Cu–O1a	89.13°	N3–Cu–N4	94.06°
N2b–Cu–O1a	90.87°	N4–Cu–N1	86.22°
N1a–N2a–N1b–N2b ^b	0.0°	N1–N2–N3–N4 ^b	23.43°

^aThe structure and metrics presented for [Cu(TMC)](ClO₄)₂ were taken from a previous report.²⁹ ^bThe reported dihedral angle (*i.e.*, N1–N2–N3–N4) for [Cu(TMC)](ClO₄)₂ is the average of the two measurements obtained by defining the angle by the N1–N3 or N2–N4 axis.

A.3. Conclusions

In conclusion, an unexpected anion effect that directs the stereochemistry of [Cu(TMC)]²⁺ was reported and fully characterized by X-ray crystallography and UV–vis spectroscopy. We proposed that this anion dependence could be utilized as a new and facile approach to the preparation of *trans*-III metal TMC complexes (or similar N-methylated cyclams), which have been largely unexplored due to the initial challenges associated with their synthesis.² Moreover, not only does this method represent a more rapid and easier approach to generate *trans*-III complexes than previous methods (*i.e.*, electrochemical and cyclam methylation) which, to date, have only yielded *trans*-III-[Ni(TMC)]²⁺ and *trans*-III-[Cu(TMC)]²⁺,^{23,27,28,34} but it also suggests that the first report for direct preparation of *trans*-III-[Cu(TMC)]²⁺ may not be solely due to the synthetic conditions employed (*i.e.*, refluxing with NaOH) and

instead may be partially attributed to the use of copper bis(tetrafluoroborate).³¹ In fact, very few reports of metal TMC complexes with anions other than perchlorate metal salts are available most likely due to the ease with which the perchlorates generate crystals suitable for X-ray analysis. Overall, our initial spectroscopic findings with $[\text{Cu}(\text{TMC})]^{2+}$ support the fact that facile preparation of *trans*-III metal TMC complexes may be prepared by the careful selection of the metal salt. Additional studies are underway to evaluate the extent to which this anion effect may be generalized to other transition metal complexes and even additional tetra-*N*-alkylated cyclams.

A.4. Experimental Section

A.4.1. Materials and Methods

All reagents were purchased from commercial suppliers and used as received unless otherwise noted. Optical Spectra were recorded on an Agilent 8453 UV–vis spectrophotometer. Electrospray ionization mass spectra (ESI-MS) were collected on a Waters (Milford, MA, USA) Acquity SQD quadrupole mass instrument, by infusing samples directly into the source using a manual method. The spray voltage was set at 2.5 kV and the capillary temperature at 80 °C.

A.4.2. X-ray Crystallography.

Single crystal of $[\text{Cu}(\text{TMC})](\text{NO}_3)_2(\text{H}_2\text{O})_{0.5}$ was picked from solutions by using a nylon loop (Hampton Research Co.) on a handmade copper plate mounted inside a liquid N_2 Dewar vessel at ca. -40 °C and mounted on a goniometer head in a N_2 cryostream. Data collections were carried out on a Bruker SMART APEX II CCD diffractometer equipped with a monochromator in the $\text{Mo K}\alpha$ ($\lambda = 0.71073 \text{ \AA}$) incident beam. The CCD data were integrated and scaled using the Bruker-S SAINT software package, and the structure was solved and refined using SHELXTL V 6.12.³⁸ Hydrogen atoms were located in the calculated positions. All non-hydrogen atoms were refined with anisotropic thermal parameters. Crystal data for $[\text{Cu}(\text{TMC})](\text{NO}_3)_2$: $\text{C}_{14}\text{H}_{32}\text{CuN}_6\text{O}_6$, mono- clinic, $P2_1/n$, $Z = 2$, $a = 7.9917(4)$, $b = 15.0923(8)$, $c = 8.3426(5) \text{ \AA}$, $\beta = 106.381(2)^\circ$, $V = 965.38(9) \text{ \AA}^3$, $\mu = 1.175 \text{ mm}^{-1}$, $\rho_{\text{calcd}} = 1.527 \text{ g cm}^{-3}$, $R_1 = 0.0264$, $wR_2 = 0.0883$ for 2395 unique reflections, 126 variables. The crystallographic data are listed in Table S1, and Table 1 lists the selected bond distances and angles.

A.4.3. Preparation of $[\text{Cu}(\text{TMC})](\text{NO}_3)_2(\text{H}_2\text{O})_{0.5}$.

TMC (0.13 g, 0.5 mmol) (TMC = 1,4,8,11-tetramethyl-1,4,8,11-tetraazacyclotetradecane) was added to an acetonitrile solution (5 mL) of $\text{Cu}(\text{NO}_3)_2 \cdot x\text{H}_2\text{O}$ (0.09 g, 0.5 mmol). The resulting solution was

refluxed for 12 h. After cooling, to room temperature, the solvent was removed under reduced pressure to give a blue powder. The solid was filtered and the filtrate was then washed with diethyl ether and dried in a vacuum. Yield: 0.25 g (95%). UV-vis (H₂O): λ_{\max} (ϵ) = 554 nm (216 M⁻¹cm⁻¹) ESI-MS (in CH₃CN): 157.6 *m/z* for [Cu(TMC)]²⁺, 180.1 *m/z* for [Cu(TMC)(CH₃CN)]²⁺, and 381.2 *m/z* for [Cu(TMC)(NO₃)]⁺ Anal. Calcd for C₁₄H₃₃CuN₆O_{6.5}: C, 37.12; H, 7.34; N, 18.55. Found: C, 36.68; H, 7.02; N, 18.86. Crystals suitable for X-ray diffraction were obtained by slow diffusion of diethyl ether into a MeOH solution of [Cu(TMC)](NO₃)₂(H₂O)_{0.5}.

A.4.4. Preparation of [Cu(TMC)](ClO₄)₂

[Cu(TMC)](ClO₄)₂ was prepared following an identical procedure as the one reported for [Cu(TMC)](NO₃)₂ except Cu(ClO₄)₂·6H₂O (0.19 g, 0.5 mmol) was used to give a blue solid. Crystallographic data was obtained from previously reported perchlorate complexes.³⁵⁻³⁷ Yield: 0.25 g (96%). UV-vis (H₂O): λ_{\max} (ϵ) = 615 nm (190 M⁻¹cm⁻¹). ESI-MS (in CH₃CN): 159.5 *m/z* for [Cu(TMC)]²⁺, 180.2 *m/z* for [Cu(TMC)(CH₃CN)]²⁺, and 418.2 *m/z* for [Cu(TMC)(ClO₄)]⁺. Anal. Calcd for C₁₆H₃₅Cl₂CuN₅O₈: C, 34.32; H, 6.30; N, 12.51. Found: C, 34.05; H, 6.24; N, 12.47.

A.5. Acknowledgements

This work was supported by the National Research Foundation of Korea (NRF) grant funded by the Korean government [NRF-2014R1A2A2A01004877 (to M.H.L.); 2014R1A1A2056051 (to J.C.)]; the 2016 Research Fund (Project Number 1.160001.01) of Ulsan National Institute of Science and Technology (UNIST) (to M.H.L.); the Ministry of Science, ICT and Future Planning (16-BD-0403, 2014M1A8A1049320, and 2015M3D3A1064890) (to J.C.); the C1 Gas Refinery Program through the NRF funded by the Ministry of Science, ICT & Future Planning (2015M3D3A1A01064876) (to S.H.K.); the National Research Council of Science and Technology through the Degree & Research Center Program (DRC-14-3-KBSI) (to S.H.K.).

A.6. References

- (1) Barefield, K. E.; Wagner, F. *Inorg. Chem.* **1973**, *12*, 2435–2439.
- (2) Barefield, K. E. *Coord. Chem. Rev.* **2010**, *254*, 1607–1627.
- (3) Micheloni, M.; Paoletti, P.; Burki, S.; Kaden, T. A. *Helv. Chim. Acta* **1982**, *65*, 587–594.
- (4) Herron, N.; Moore, P. *Inorg. Chim. Acta* **1979**, *36*, 89–96.
- (5) Newman, K. E. *Inorg. Chim. Acta* **1984**, *89*, L3–L5.
- (6) Barefield, K. E.; Freeman, G. M.; Vanderveer, D. G. *Inorg. Chem.* **1986**, *25*, 552–558.
- (7) Liang, X.; Sadler, P. J. *Chem. Soc. Rev.* **2004**, *33*, 246–266.

- (8) David, T.; Kubicek, V.; Gutten, O.; Lubal, P.; Kotek, J.; Pietzsch, H.-J.; Rulisek, L.; Hermann, P. *Inorg. Chem.* **2015**, *54*, 11751–11766.
- (9) Kim, S.; Minier, M. A.; Loas, A.; Becker, S.; Wang, F.; Lippard, S. J. *J. Am. Chem. Soc.* **2016**, *138*, 1804–1807.
- (10) Shokeen, M.; Anderson, C. J. *Acc. Chem. Res.* **2009**, *42*, 832–841.
- (11) Froehlich, J. P.; Kubiak, C. P. *J. Am. Chem. Soc.* **2015**, *137*, 3565–3573.
- (12) Cho, J.; Sarangi, R.; Nam, W. *Acc. Chem. Res.* **2012**, *45*, 1321–1330.
- (13) Feng, Y.; England, J.; Que, L. Jr., *ACS Catal.* **2011**, *1*, 1035–1042.
- (14) Nam, W. *Acc. Chem. Res.* **2015**, *48*, 2415–2423.
- (15) Ray, K.; Heims, F.; Schwalbe, M.; Nam, W. *Curr. Opin. Chem. Biol.* **2015**, *25*, 159–171.
- (16) Bang, S.; Lee, Y.-M.; Hong, S.; Cho, K.-B.; Nishida, Y.; Seo, M. S.; Sarangi, R.; Fukuzumi, S.; Nam, W. *Nat. Chem.* **2014**, *6*, 934–940.
- (17) Cho, J.; Jeon, S.; Wilson, S. A.; Liu, L. V.; Kang, E. A.; Braymer, J. J.; Lim, M. H.; Hedman, B.; Hodgson, K. O.; Valentine, J. S.; Solomon, E. I.; Nam, W. *Nature* **2011**, *478*, 502–505.
- (18) Fukuzumi, S.; Morimoto, Y.; Kotani, H.; Naumov, P.; Lee, Y.-M.; Nam, W. *Nat. Chem.* **2010**, *2*, 756–759.
- (19) Cho, J.; Sarangi, R.; Annaraj, J.; Kim, S. Y.; Kubo, M.; Ogura, T.; Solomon, E. I.; Nam, W. *Nat. Chem.* **2009**, *1*, 568–572.
- (20) Bukowski, M. R.; Koehntop, K. D.; Stubna, A.; Bominaar, E. L.; Halfen, J. A.; Munck, E.; Nam, W.; Que, L. Jr., *Science* **2005**, *310*, 1000–1002.
- (21) Rohde, J.-U.; In, J.-H.; Lim, M. H.; Brennessel, W. W.; Bukowski, M. R.; Stubna, A.; Eckard, M.; Nam, W.; Que, L. Jr., *Science* **2003**, *299*, 1037–1039.
- (22) Deming, R. L.; Allred, A. L.; Dahl, A. R.; Herlinger, A. W.; Kestner, M. C. *J. Am. Chem. Soc.* **1976**, *98*, 4132–4137.
- (23) Wagner, F.; Barefield, K. E. *Inorg. Chem.* **1976**, *15*, 408–417.
- (24) Becker, J. Y.; Kerr, J. B.; Pletcher, D.; Rosas, R. *J. Electroanal. Chem. Interfacial Electrochem.* **1981**, *117*, 87–99.
- (25) Gatteschi, D.; Scozzafava, A. *Inorg. Chim. Acta* **1977**, *21*, 223–227.
- (26) Moore, P.; Sachinidis, J.; Willey, G. R. *Chem. Commun.* **1983**, 522–523.
- (27) Maimon, E.; Zilbermann, I.; Golub, G.; Ellern, A.; Shames, A. I.; Cohen, H.; Meyerstein, D. *Inorg. Chim. Acta* **2001**, *324*, 65–72.
- (28) Amatore, C.; Barbe, J.-M.; Bucher, C.; Duval, E.; Guilard, R.; Verpeaux, J. N. *Inorg. Chim. Acta* **2003**, *356*, 267–278.

- (29) Lu, T.-H.; Shui, W.-Z.; Tung, S.-F.; Chi, T.-Y.; Liao, F.-L.; Chung, C.-S. *Acta Cryst.* **1998**, *C54*, 1071–1072.
- (30) Lee, T.-J.; Lee, T.-Y.; Hong, C.-Y.; Wu, D.-T.; Chung, C.-S. *Acta Cryst.* **1986**, *C42*, 999–1001.
- (31) Bucher, C.; Emmanuelle, D.; Espinosa, E.; Barbe, J.-M.; Verpeaux, J.-N.; Amatore, C.; Guillard, R. *Eur. J. Inorg. Chem.* **2001**, 1077–1079.
- (32) Herron, N.; Moore, P. *Dalton Trans.* **1979**, 441–445.
- (33) Alcock, N. W.; Herron, N.; Moore, P. *Dalton Trans.* **1978**, 1282–1288.
- (34) Wagner, F.; Mocella, M. T.; D'Aniello, M. J.; Wang, A. H.-J.; Barefield, K. E. *J. Am. Chem. Soc.* **1974**, *96*, 2625–2627.
- (35) Lee, T.-J.; Lee, T.-Y.; Hong, C.-Y.; Wu, D.-T.; Chung, C.-S. *Acta Cryst.* 1986, *C42*, 999–1001.
- (36) Lu, T.-H.; Shui, W.-Z.; Tung, S.-F.; Chi, T.-Y.; Liao, F.-L.; Chung, C.-S. *Acta Cryst.* 1998, *C54*, 1071–1072.
- (37) Maimon, E.; Zilbermann, I.; Golub, G.; Ellern, A.; Shames, A. I.; Cohen, H.; Meyerstein, D. *Inorg. Chim. Acta* 2001, *324*, 65–72.
- (38) G. M. Sheldrick, SHELXTL, Version 6.12, Bruker AXS, Inc., Madison, WI, 2001.

Appendix B.
Additional Supplementary Data

B.1. $^1\text{H} / ^{13}\text{C}$ NMR Characterization of the Multifunctional Derivatives (AQP2-4 and AQDA1-3)

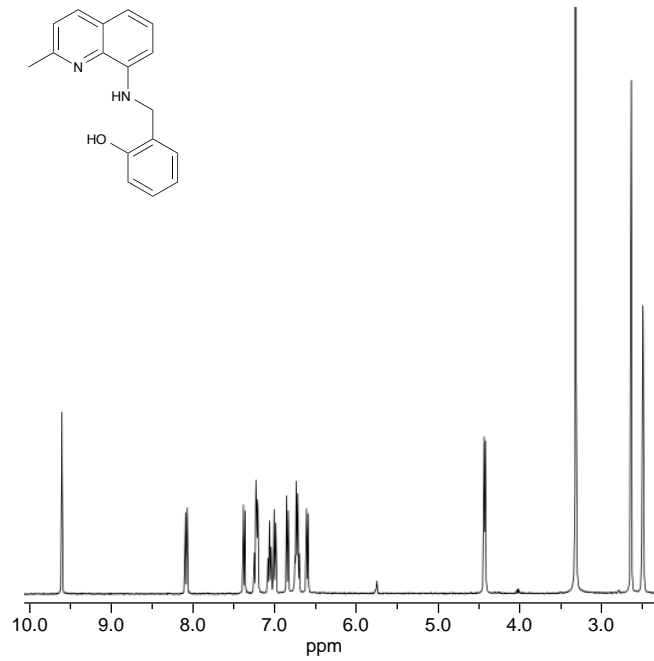


Figure B1.1. ^1H NMR spectrum of **AQP2** [400 MHz, $(\text{CD}_3)_2\text{SO}$].

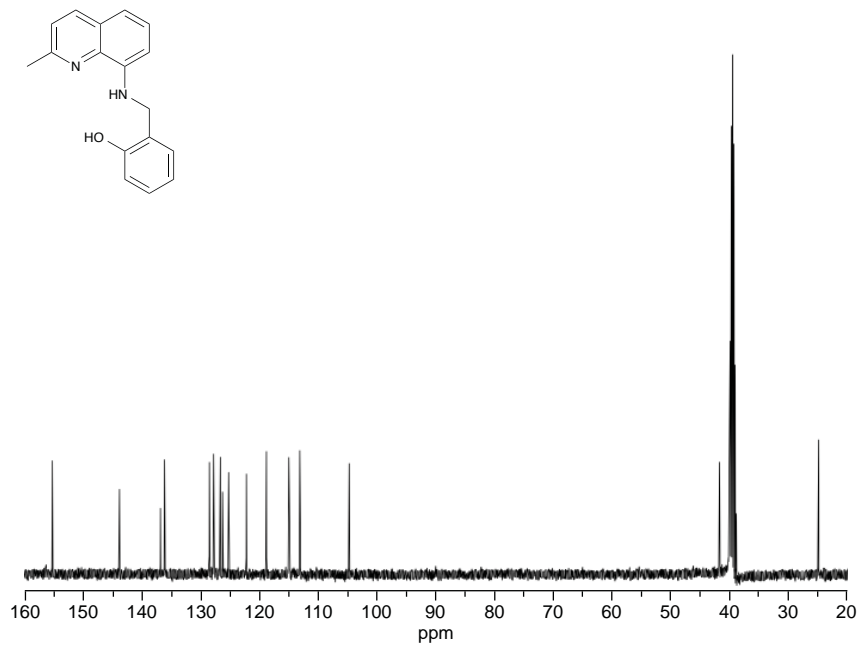


Figure B.2. ^{13}C NMR spectrum of **AQP2** [100 MHz, $(\text{CD}_3)_2\text{SO}$].

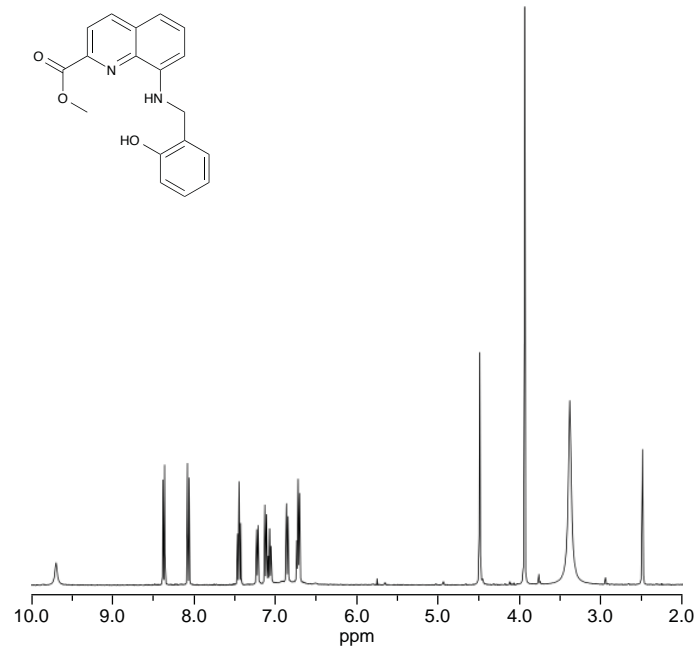


Figure B.3. ¹H NMR spectrum of AQP3 [400 MHz, (CD₃)₂SO].

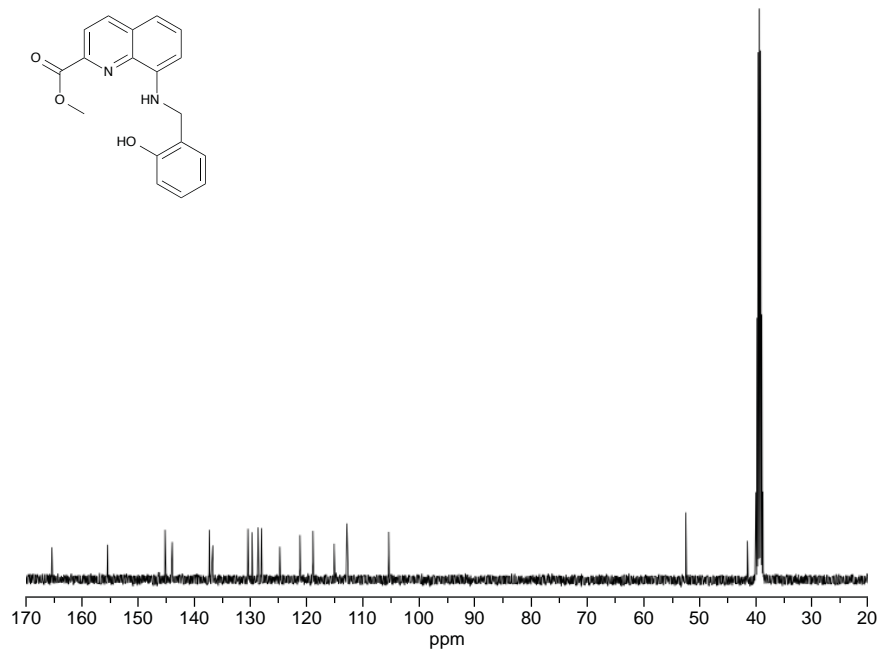


Figure B.4. ¹³C NMR spectrum of AQP3 [100 MHz, (CD₃)₂SO].

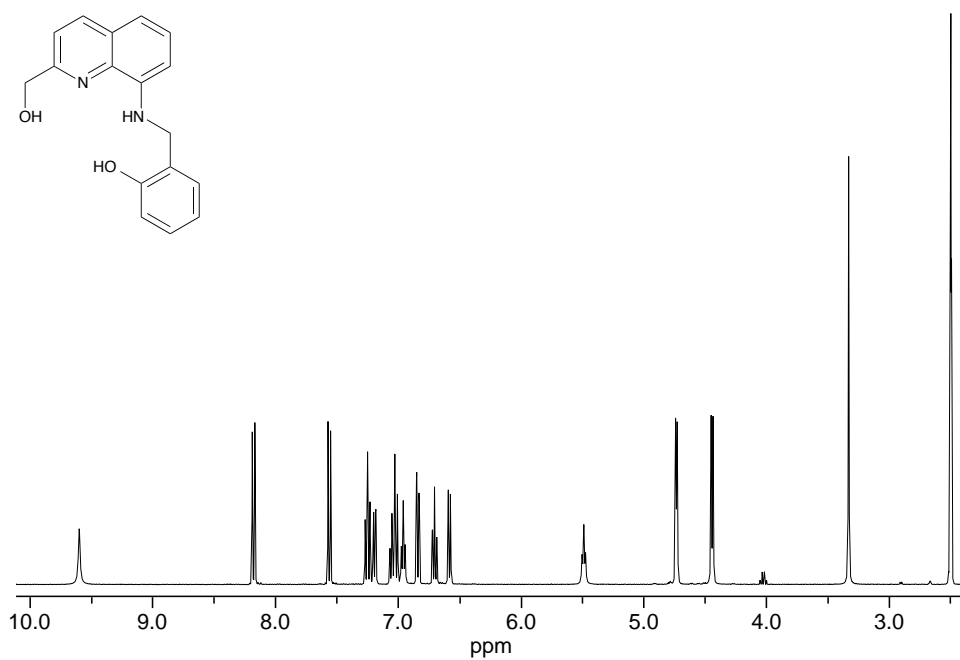


Figure B.5. ¹H NMR spectrum of **AQP4** [400 MHz, (CD₃)₂SO].

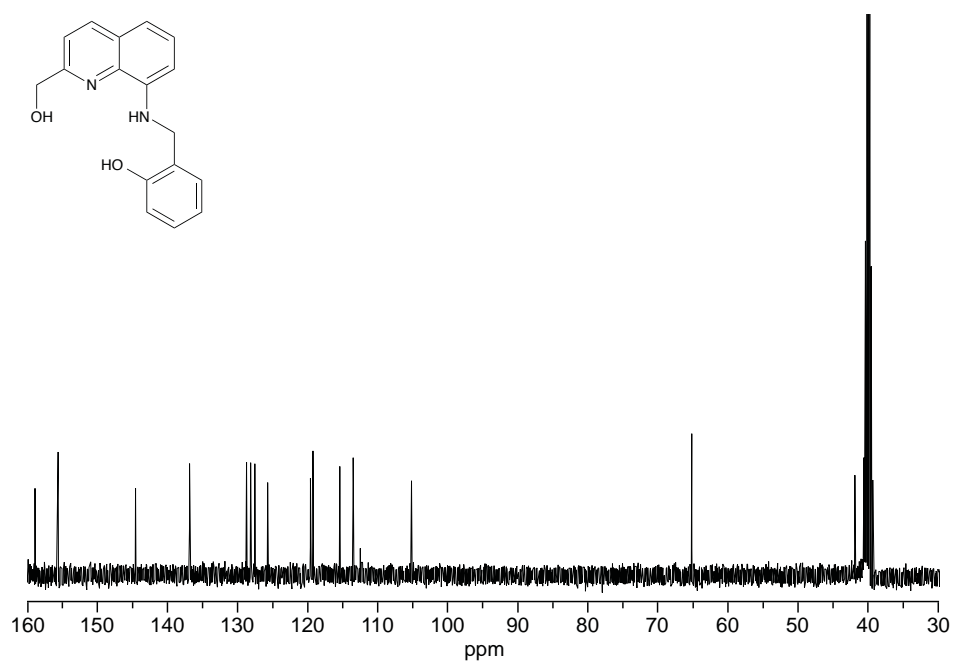


Figure B.6. ¹³C NMR spectrum of **AQP4** [100 MHz, (CD₃)₂SO].

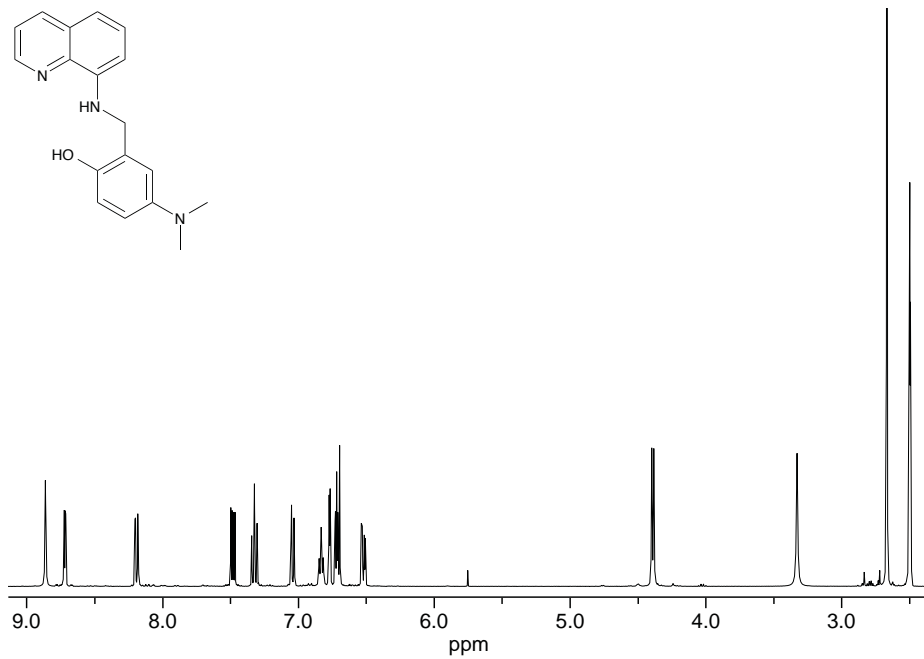


Figure B.7. ¹H NMR spectrum of AQDA1 [400 MHz, (CD₃)₂SO].

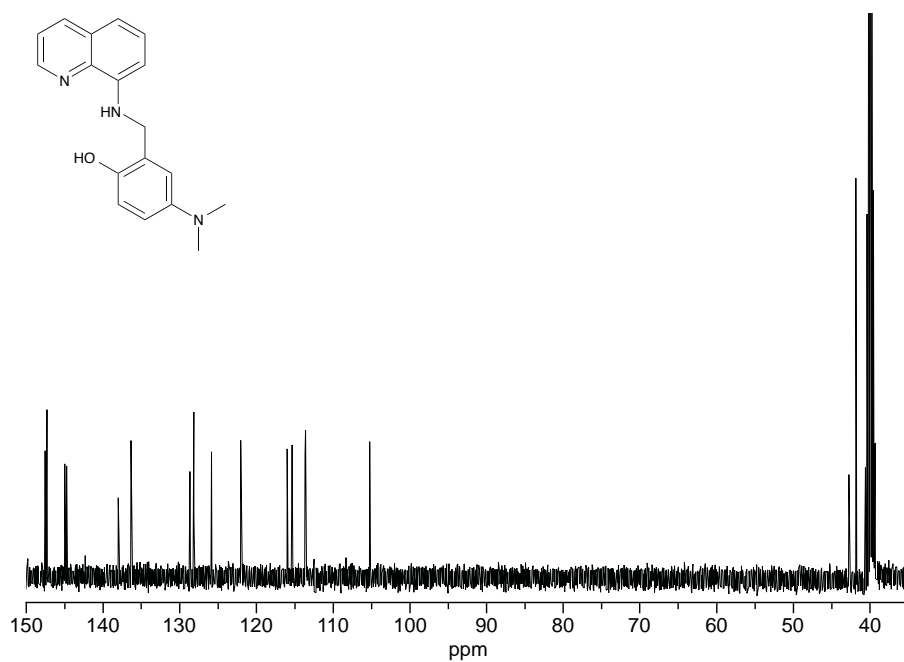


Figure B.8. ¹³C NMR spectrum of AQDA1 [100 MHz, (CD₃)₂SO].

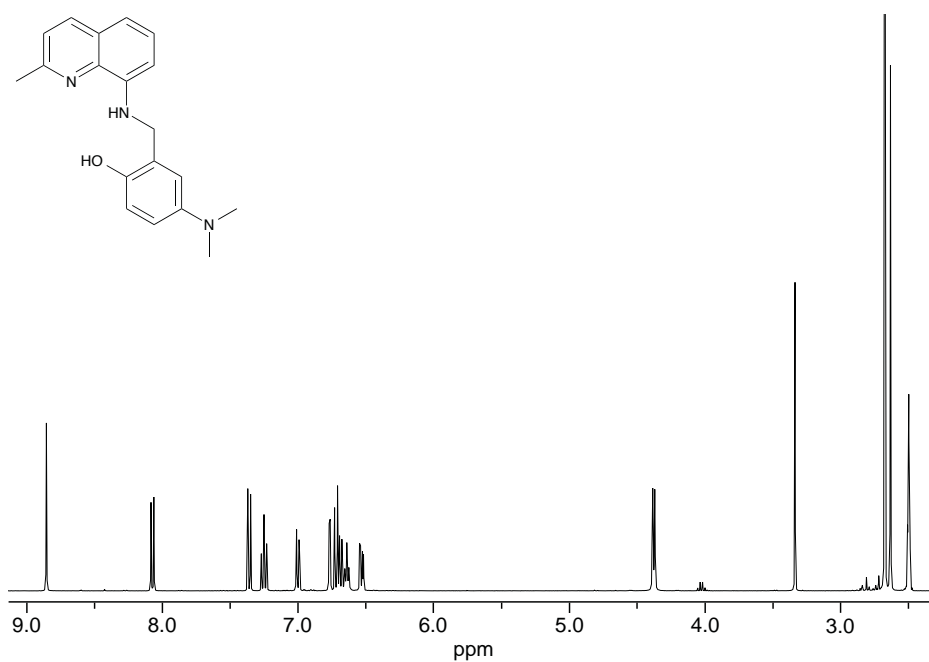


Figure B.9. ^1H NMR spectrum of AQDA2 [400 MHz, $(\text{CD}_3)_2\text{SO}$].

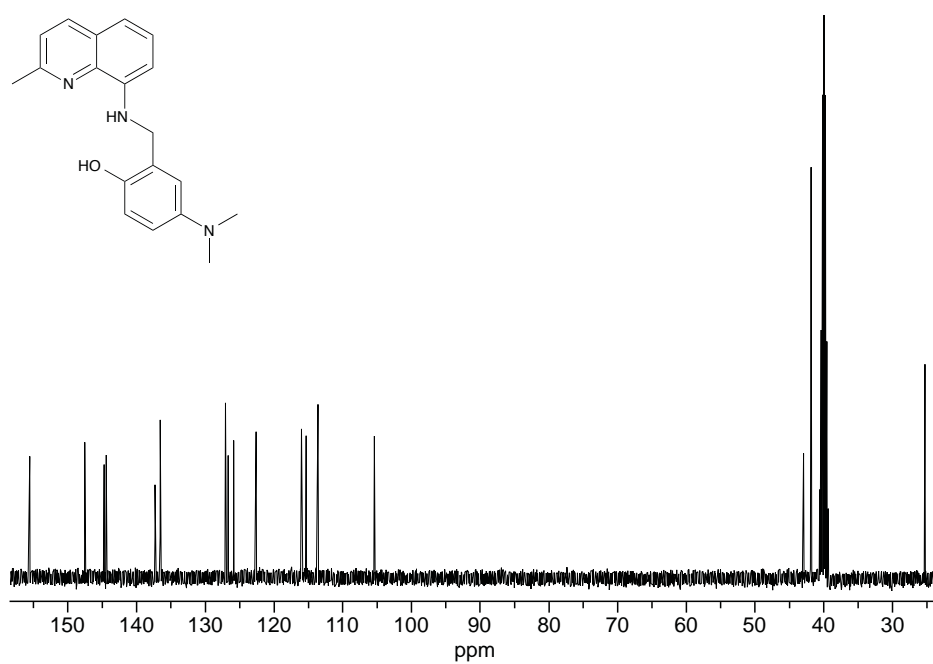


Figure B.10. ^{13}C NMR spectrum of AQDA2 [100 MHz, $(\text{CD}_3)_2\text{SO}$].

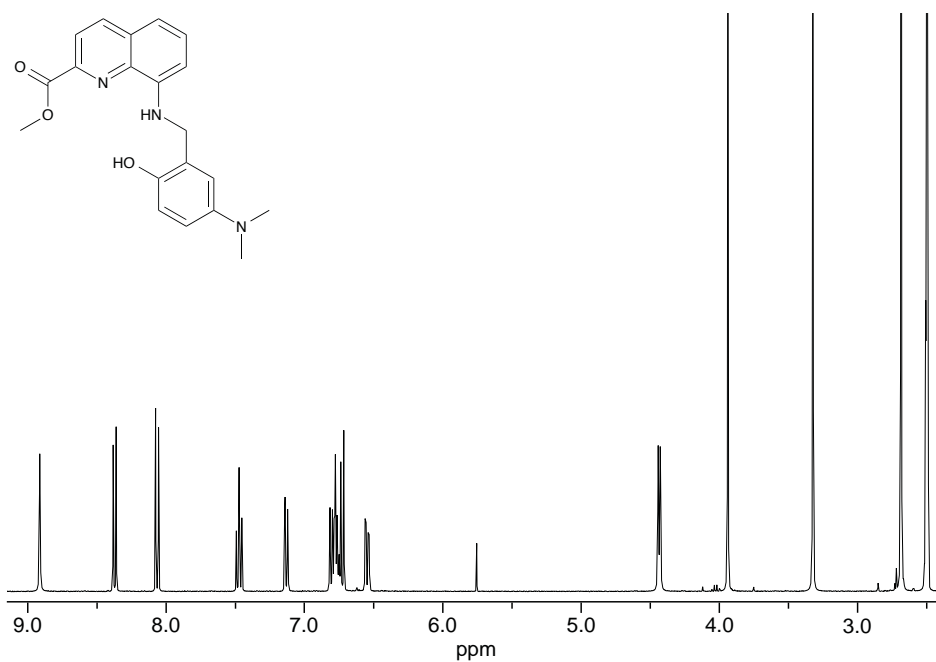


Figure B.11. ¹H NMR spectrum of AQDA3 [400 MHz, (CD₃)₂SO].

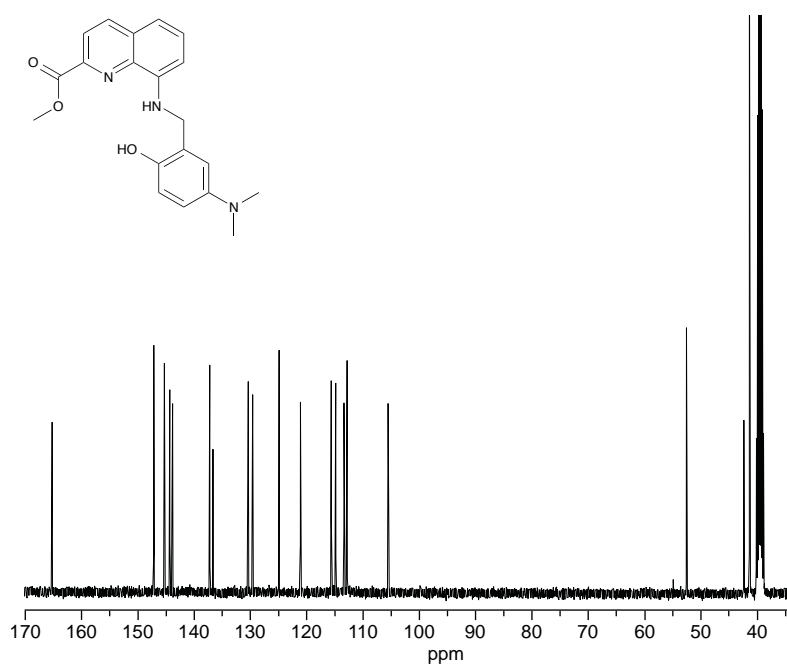


Figure B.12. ¹³C NMR spectrum of AQDA3 [100 MHz, (CD₃)₂SO].

B.2. Supplemental EPR Data for Co(II)(TMC)

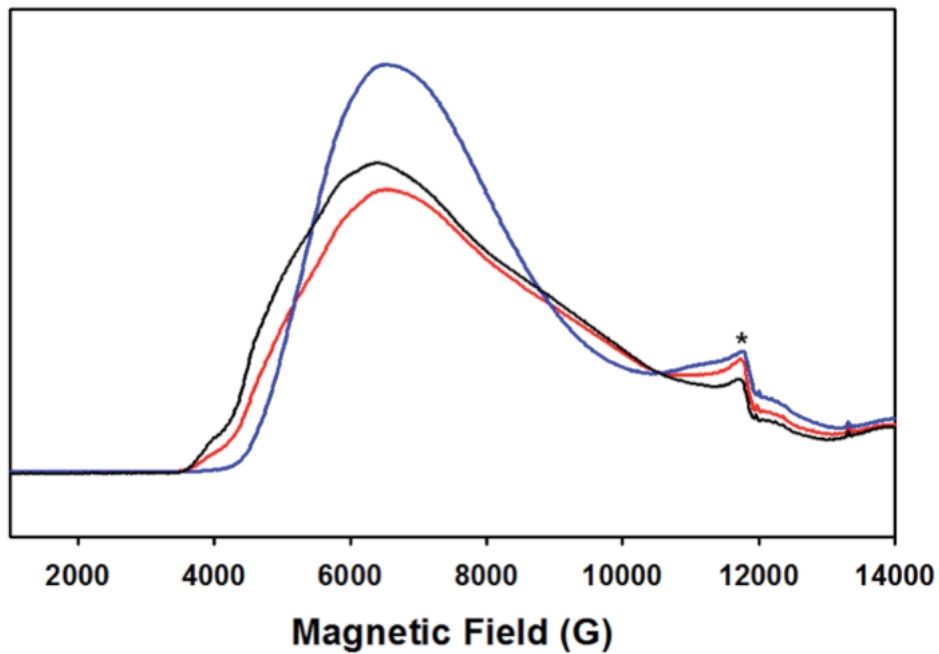


Figure B.13. Q-band ESE-EPR spectra of Co(II)(TMC) complex in H₂O (black), D₂O (blue) and H₂¹⁷O (red). *indicates the background from the resonator.

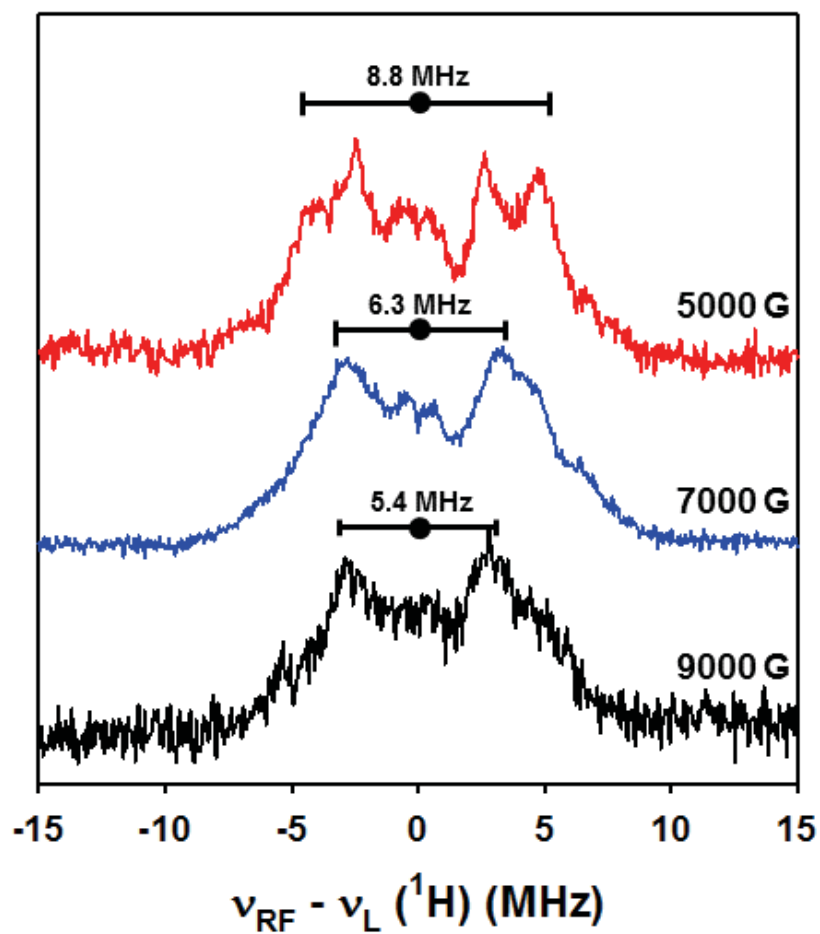


Figure B.14. ^1H -ENDOR spectra of Co(II)(TMC) complex at different magnetic fields.

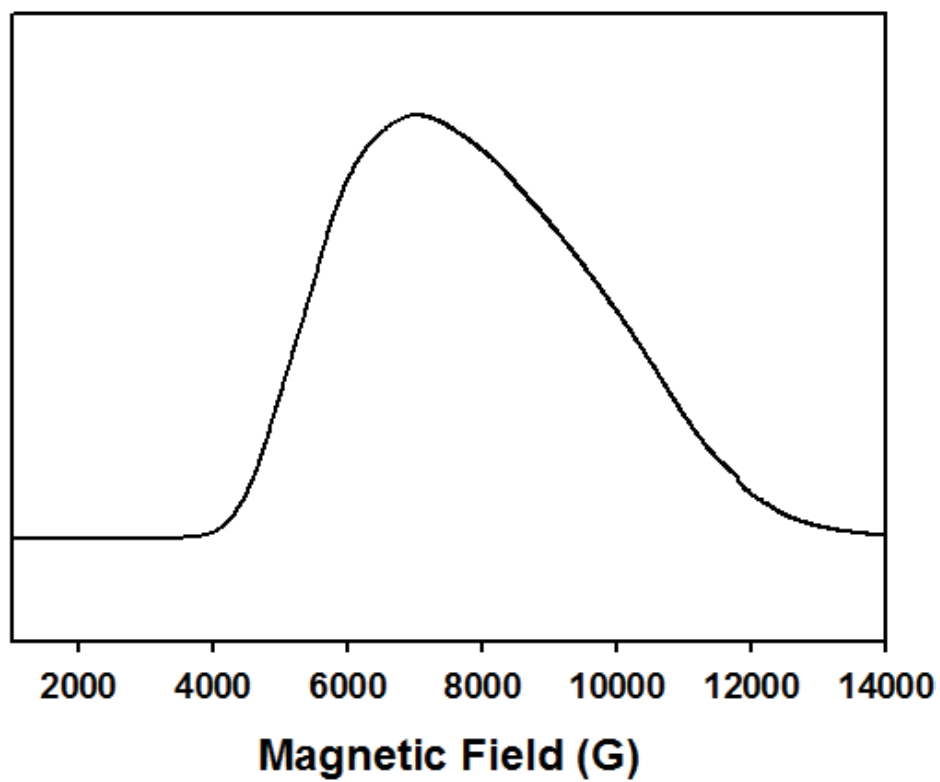


Figure B.15. Q-band ESE-EPR spectrum of $\text{CoCl}_2 \cdot 6\text{H}_2\text{O}$ in aqueous solution.

B.3. Supplemental Computational Data for M(II)(TMC)

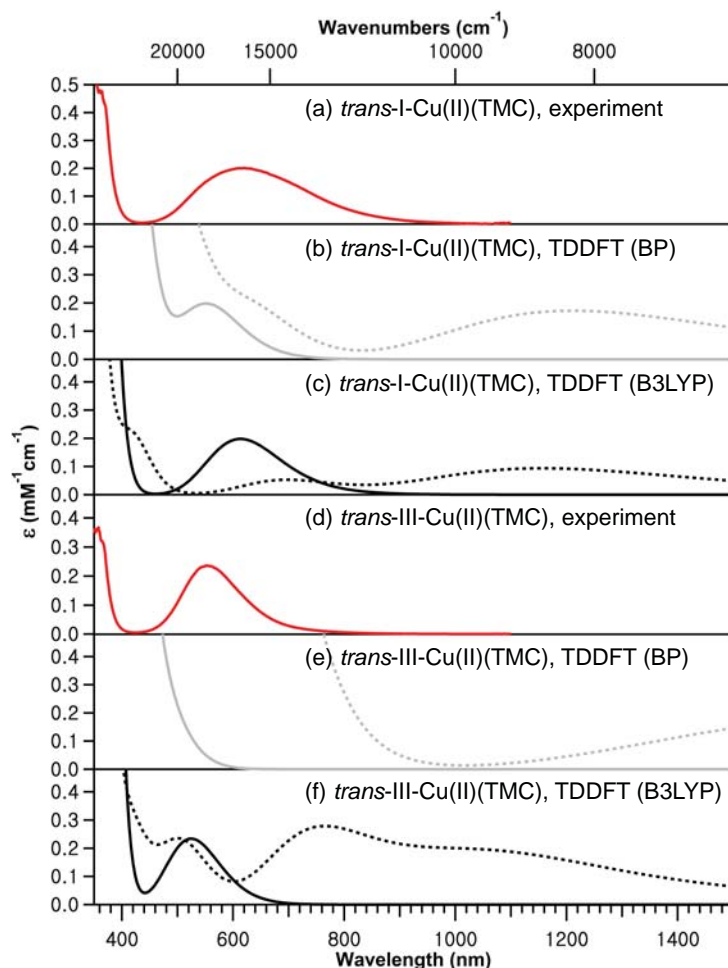


Figure B.16. Electronic absorption spectra of (a) *trans*-I-Cu(II)(TMC) experimentally obtained in aqueous solution; (b) TDDFT-predicted *trans*-I-[Cu(TMC)(OH)]⁺ (dotted gray) and *trans*-I-[Cu(TMC)(H₂O)]²⁺ (solid gray) models obtained using the BP functional; (c) TDDFT-predicted *trans*-I-[Cu(TMC)(OH)]⁺ (dotted black) and *trans*-I-[Cu(TMC)(H₂O)]²⁺ (solid black) models obtained using the B3LYP functional; (d) *trans*-III-Cu(II)(TMC) experimentally obtained in aqueous solution; (e) TDDFT-predicted *trans*-III-[Cu(TMC)(OH)]⁺ (dotted gray) and *trans*-III-[Cu(TMC)(H₂O)]²⁺ (solid gray) models obtained using the BP functional; and (f) TDDFT-predicted *trans*-III-[Cu(TMC)(OH)]⁺ (dotted black) and *trans*-III-[Cu(TMC)(H₂O)]²⁺ (solid black) models obtained using the B3LYP functional.

B.4. Supplemental Mass Spectrometry Fragmentation Data for M(II)(TMC)

Table B.1. The monoisotopic mass (m/z), the charge state (z), and sequence for each fragment ion observed in the ESI-MS spectra (Figure 4.9). Detected peaks are denoted as D. Newly generated $A\beta_{40}$ fragments formed upon M(II)(TMC) treatment are labeled in blue. Ions only detected in the samples treated with Co(II)(TMC) or Cu(II)(TMC) are labeled in red and green, respectively.

m/z	z	Sequence	$A\beta_{40}$	Ni(II) (TMC)	Co(II) (TMC)	Cu(II) (TMC)	Zn(II) (TMC)
561.45	+1	35-40 MVGGVV	D	D	D	D	D
570.60	+1	7-11 DSGYE	-	D	D	-	D
575.58	+1	34-39 LMVGGV	-	-	-	D	D
597.62	+1	27-32 NKGAI - H ₂ O	-	D	D	-	D
599.98	+2	8-17 SGYEVHHQKL	D	D	D	D	D
		17-27 LVFFAEDVGSN					
602.64	+1	22-27 EDVGSN - H ₂ O	-	-	-	D	-
616.52	+1	15-19 QKLVF - H ₂ O	-	-	-	D	-
630.55	+1	12-16 VHHQK - H ₂ O	-	-	-	D	-
644.55	+1	13-17 HHQKL - H ₂ O	-	-	-	D	-
649.54	+2	8-18 SGYEVHHQKLV	D	D	D	D	D
674.57	+1	34-40 LMVGGVV	D	D	D	D	D
684.57	+1	10-14 YEVHH	D	D	D	D	D
708.07	+2	26-40 SNKGAIIGLMVGGVV	D	D	D	D	D
719.05	+2	16-28 KLVFFAEDVGSNK	D	D	D	D	D
727.06	+2	25-40 GSNKGAIIGLMVGGVV - H ₂ O	-	D	D	D	D
731.60	+1	33-40 GLMVGGVV	D	D	D	D	D
753.56	+1	14-19 HQKLVF - H ₂ O	-	-	D	-	-
784.57	+1	28-35 KGAIIGLM - H ₂ O	-	-	D	-	-
786.12	+2	24-40 VGSNKGAIIGLMVGGVV	D	D	D	D	D
800.54	+5	1-36 DAEFRHDSGYEVHHQKLVFFAE DVGSNKGAIIGLMV - H ₂ O	D	-	-	-	-
810.59	+1	8-14 SGYEVHH - H ₂ O	-	-	D	-	-
811.96	+5	1-37 DAEFRHDSGYEVHHQKLVFFAE DVGSNKGAIIGLMV - H ₂ O	D	-	-	-	-
816.56	+1	25-33 GSNKGAIIG	-	-	-	D	-
823.35	+5	2-39 AEFRHDSGYEVHHQKLVFFAE VGSNKGAIIGLMVGGV	D	-	-	-	-
840.61	+2	17-32 LVFFAEDVGSNKGAI	-	D	D	D	D
843.17	+5	2-40 AEFRHDSGYEVHHQKLVFFAE VGSNKGAIIGLMVGGVV	D	D	-	D	D
844.69	+1	32-40 IGLMVGGVV	-	D	D	D	D
849.63	+2	11-24 EVHHQKLVFFAEDV	-	D	D	D	D
852.51	+1	15-21 QKLVFFA	-	-	D	-	-
854.69	+1	16-22 KLVFFAE	-	D	D	D	D
863.64	+1	5-11 RHDSGYE	-	-	D	-	-
886.58	+5	1-40 DAEFRHDSGYEVHHQKLVFFAE DVGSNKGAIIGLMVGGVV	D	D	-	D	-
899.18	+2	22-40 EDVGSNKGAIIGLMVGGVV - H ₂ O	-	D	D	D	D
908.17	+2	22-40 EDVGSNKGAIIGLMVGGVV	D	D	D	D	D
914.60	+4	1-33 DAEFRHDSGYEVHHQKLVFFAE DVGSNKGAIIG - H ₂ O	D	-	-	-	-
918.17	+2	20-38 FAEDVGSNKGAIIGLMVGG	-	D	D	D	D
922.17	+2	6-20 HDSGYEVHHQKLVFF	-	D	D	D	D
927.14	+2	5-19 RHDSGYEVHHQKLVF	-	D	D	D	D
		4-18 FRHDSGYEVHHQKLV					
942.86	+4	1-34 DAEFRHDSGYEVHHQKLVFFAE DVGSNKGAIIGL - H ₂ O	D	-	-	-	-
943.68	+2	21-40 AEDVGSNKGAIIGLMVGGVV	-	D	D	D	D

B.5. Supplemental X-ray Crystallographic Data

Table B.2. Crystal data and structure refinement for [Co(TMC)(NO₃)](NO₃).

Identification code	[Co(TMC)(NO ₃)](NO ₃)
Empirical Formula	C ₁₄ H ₃₂ CoN ₆ O ₆
Formula weight	439.38
Temperature	113(2) K
Wavelength	0.71073 Å
Crystal System	Orthorhombic
Space group	<i>Pna</i> 2 ₁
Unit cell dimensions	a = 17.0670(8) Å α = 90° b = 12.9148(6) Å β = 90° c = 8.7358(5) Å γ = 90°
Volume	1925.52(17) Å ³
Z	4
Density (calculated)	1.516 g/cm ⁻³
Absorption coefficient	0.936 mm ⁻¹
F(000)	932
Reflections collected	54666
Independent reflections	3780
Absorption correction	Multi-scan
Refinement method	Full-matrix least-squares on F ²
Data/restraints/parameters	3780/1/248
Goodness-of-fit on F ²	0.796
Final R indices [I > 2σ(I)]	R1 = 0.0573, wR2 = 0.1424
R indices (all data)	R1 = 0.0918, wR2 = 0.1729

Table B.3. Crystal data and structure refinement for $[\text{Ni}(\text{TMC})(\text{CH}_3\text{CN})](\text{NO}_3)_2$.

Identification code	$[\text{Ni}(\text{TMC})(\text{CH}_3\text{CN})](\text{NO}_3)_2$
Empirical Formula	$\text{C}_{16}\text{H}_{35}\text{N}_7\text{NiO}_6$
Formula weight	480.22
Temperature	133(2) K
Wavelength	0.71073 Å
Crystal System	Tetragonal
Space group	$P4_3$
Unit cell dimensions	$a = 13.407(2)$ Å $\alpha = 90^\circ$ $b = 13.407(2)$ Å $\beta = 90^\circ$ $c = 24.102(4)$ Å $\gamma = 90^\circ$
Volume	4332.3(16) Å ³
Z	8
Density (calculated)	1.472 g/cm ⁻³
Absorption coefficient	0.943 mm ⁻¹
F(000)	2048
Reflections collected	60414
Independent reflections	10902
Absorption correction	Multi-scan
Refinement method	Full-matrix least-squares on F ²
Data/restraints/parameters	10902/1/551
Goodness-of-fit on F ²	0.974
Final R indices [I > 2σ(I)]	R1 = 0.0587, wR2 = 0.1377
R indices (all data)	R1 = 0.1107, wR2 = 0.1650

Table B.4. Crystal data and structure refinement for [Cu(TMC)](NO₃)₂.

Identification code	[Cu(TMC)(NO ₃) ₂]
Empirical Formula	C ₁₄ H ₃₂ CuN ₆ O ₆
Formula weight	443.99
Temperature	173(2) K
Wavelength	0.71073 Å
Crystal System	Monoclinic
Space group	<i>P12₁/n1</i>
Unit cell dimensions	a = 7.9917(4) Å α = 90° b = 15.0923(8) Å β = 90° c = 8.3426(5) Å γ = 90°
Volume	965.38(9) Å ³
Z	2
Density (calculated)	1.527 g/cm ⁻³
Absorption coefficient	1.175 mm ⁻¹
F(000)	470
Reflections collected	39083
Independent reflections	2395
Absorption correction	Multi-scan
Refinement method	Full-matrix least-squares on F ²
Data/restraints/parameters	2395/0/126
Goodness-of-fit on F ²	0.801
Final R indices [I > 2σ(I)]	R1 = 0.0264, wR2 = 0.0883
R indices (all data)	R1 = 0.0343, wR2 = 0.0977

Acknowledgements

First and foremost I would like to express my eternal gratitude to my advisor, Professor Mi Hee Lim. Without her assistance, guidance, and support none of the work presented in this dissertation would have been possible. Furthermore, if it wasn't for her exceptional amount of patience that it took to train and educate me I would not have been able to accomplish all that I have to date. Professor Lim was the first one to give me an opportunity to do research in her laboratory at the University of Michigan, and I had the distinct honor of being able to learn directly from her. She took the time out of her incredibly busy schedule each day to work with me. In addition to chemical training, I was also extremely fortunate enough to gain first hand experiences in writing numerous reviews, manuscripts, and grants with Professor Lim as well as having the amazing opportunity to follow her to Ulsan, South Korea, to pursue a Masters of Science at Ulsan National Institute of Science and Technology (UNIST). Not only did Professor Lim provide the means for me to come to UNIST, but she also gave me the opportunity to present our research at numerous international conferences, which were instrumental for me to further develop the communication skills necessary to effectively and efficiently present my scientific findings. I will never be able to fully express my gratitude to Professor Lim for all of the things she has done for me throughout these past three years. She honestly cares deeply about the success of her students and while that often means having to meet her very high expectations, I or my other lab members, would not have accomplished anything without her exceptional mentorship. Therefore, the only thing I can do to truly show my appreciation to Professor Lim is to continue to work hard and participate in great science in order to make her and the Lim Lab proud.

I would also like to thank and express my deep appreciation for the people whom I have collaborated with and who are recognized for their contributions at the beginning of each chapter. In particular, I would like to acknowledge and show my appreciation for Professor Jaeheung Cho, Hyeonwoo Tak, Professor Kiyoung Park, Jiwan Lee, Dr. Sun Hee Kim, Yujeong Kim, Professor Brandon T. Ruotolo, and Dr. Richard Kerr who were especially helpful and without their specific expertise this work would not have been possible. I also want to thank all of my Lim Lab group members, both past and present, for their assistance, mentorship, friendship, and scientific discussion. In particular, the following colleagues were particularly helpful: Dr. Akiko Kochi, Dr. Michael Beck, Dr. Shinjung Lee, Dr. Hyuck Jin Lee, Dr. Masha Savelieff, Dr. Amit Pithadia, Kyle Korshavn, Juhye Kang, Eunju Nam, Yonghwan Ji, Mike

McLane, Jiyeon Han, Jong Min Suh, Misun Lee, and Suwon Lee.

I would also like to thank and express my eternal gratitude to Mi Sook Lim. Without Mi Sook's friendship, assistance, guidance, and support I could not have survived in Korea these past two years. I hope to have the opportunity to repay you in the future.

I would also like to thank my dissertation committee members Professor Jung-Min Kee and Professor Tae-Hyuk Kwon for taking the time to read and evaluate my thesis and for providing helpful and insightful comments and critiques.

Lastly, I would like to thank my brother, Jacob Derrick, my sister, Marisa Derrick, my grandma, Jackie Derrick, and my parents, Paula and Mark Derrick for their support and encouragement throughout these past few years and for all of the sacrifices they have made to give me the opportunity to pursue a higher education and achieve my dreams.

Jeffrey S. Derrick

Work Address:
Ulsan National Institute of Science and Technology
(UNIST)
50 UNIST-gil, Eonyan-eup, Ulju-gun
Ulsan 44919, Korea
Phone: +82-2-217-5422
Email: jderrick@umich.edu

Home Address:
2641 Edgemont St.
Trenton, Michigan 48183
Phone: 734-775-1389

Education:

- | | |
|--------------------------|---|
| Sept. 2010 – August 2014 | University of Michigan , Ann Arbor, MI, USA
B.S., Chemistry |
| March 2015 – June 2016 | Ulsan National Institute of Science and Technology (UNIST) ,
Ulsan, South Korea
M.S., Chemistry
Advisor: Professor Mi Hee Lim |

Honors, Awards & Fellowships:

- | | |
|---------------|--|
| March, 2016 | Honorable Mention, National Science Foundation Graduate Research Fellowship Program |
| August 2014 | Poster Award, The Second International Symposium on Molecular Neurodegenerative Disease Research, Daejeon, South Korea |
| July 2014 | Poster Award, BioMetals, Duke University, Durham, NC |
| March 2014 | University of Michigan University Honors |
| December 2013 | University of Michigan University Honors |
| March 2013 | University of Michigan University Honors |

Publications:

11. Nam, E. J.[‡]; **Derrick, J. S.[‡]**; Lee, S. J. C.; Lim, M. H. "Influence of Catecholamine Derivatives on Pathological Factors of Alzheimer's Disease" ([‡]Co-first authorship) *Manuscript in Preparation (2016)*.
10. **Derrick, J. S.**; Kim, Y.; Tak, H.; Cho, J.; Kim, S. H.; Lim, M. H. "Stereochemistry of Tetramethylcyclam Metal Complexes Directed by Unexpected Anion Effects" *Manuscript in Preparation (2016)*.

9. Beck, M. W.; Kerr, R. A.; **Derrick, J. S.**; Kang, J.; Jang, M.; Korshavn, K. J.; Larsen, S. D.; Ramamoorthy, A.; Kim, K. S.; Ruotolo, B. T.; Lim, M. H. “Minor Structural Variations of Small Molecules to Regulate Distinct Pathological Factors in Alzheimer’s Disease” *Manuscript in Preparation* (2016).
8. **Derrick, J. S.**; Lee, J.; Lee, S. J. C.; Kim, Y.; Tak, H.; Kim, S. H.; Park, K.; Cho, J.; Lim, M. H. “Tunable Divalent Metal Tetramethylcyclam Complexes: Hydrolytic Reactivities Toward Amyloidogenic Proteins and Mechanisms” *Submitted for Publication*, 2016
7. Beck, M. W.[‡]; **Derrick, J. S.**[‡]; Kerr, R. A.; Oh, S. B.; Cho, W. J.; Lee, S. J. C.; Tehrani, Z. A.; Suh, N.; Kim, S.; Ji, Y.; Larsen, S. D.; Kim, K. S.; Lee, J.-Y.; Ruotolo, B. T.; Lim, M. H. “Engineering Structure-mechanism-based Chemical Regulators for Distinct Pathological Factors in Alzheimer’s Disease” ([‡]Co-first authorship) *Submitted for Publication*, 2016.
6. **Derrick, J. S.**; Kerr, R. A.; Korshavn, K. J.; McLane, M. J.; Kang, J.; Nam, E.; Ramamoorthy, A.; Ruotolo, B. T.; Lim, M. H. “Importance of the Dimethylamino Functionality on a Multifunctional Framework for Regulating Metals, Amyloid- β , and Oxidative Stress in Alzheimer’s Disease” *Inorg. Chem.*, 2016, 55, 5000–5013.
5. **Derrick, J. S.**; Kerr, R. A.; Nam, Y.; Oh, S. B.; Lee, H. J.; Earnest, K. G.; Suh, N.; Peck, K. L.; Ozbil, M.; Korshavn, K. J.; Ramamoorthy, A.; Prabhakar, R.; Merino, E. J.; Shearer, J.; Lee, J.-Y.; Ruotolo, B. T.; Lim, M. H. “A Redox-Active, Compact Tool for Crosslinking Amyloidogenic Peptides into Off-Pathway Aggregates: *In Vitro* and *In Vivo* Efficacy and Molecular Mechanisms” *J. Am. Chem. Soc.*, 2015, 137, 14785–14797.
4. **Derrick, J. S.**; Lim, M. H. “Tools of the Trade: Investigations into Design Strategies of Small Molecules to Target Components in Alzheimer’s Disease” *ChemBioChem*, 2015, 16, 887–898.
3. Savelieff, M. G.; DeToma, A. S.; **Derrick, J. S.**; Lim, M. H. “The Ongoing Search for Small Molecules to Study Metal-Associated Amyloid- β Species in Alzheimer’s Disease” *Acc. Chem. Res.*, 2014, 47, 2475–2482.
2. Lee, H. J.; Korshavn, K. J.; Kochi, A.; **Derrick, J. S.**; Lim, M. H. “Cholesterol and Metal Ions in Alzheimer’s Disease” *Chem. Soc. Rev.*, 2014, 43, 6672–6682.
1. Lee, S.; Zheng, X.; Krishnamoorthy, J.; Savelieff, M. G.; Park, H. M.; Brender, J. R.; Kim, J. H.; **Derrick, J. S.**; Kochi, A.; Lee, H. J.; Kim, C.; Ramamoorthy, A.; Bowers, M. T.; Lim, M. H. “Rational Design of a Structural Framework with Potential Use to Develop Chemical Reagents that Target and Modulate Multiple Facets of Alzheimer’s Disease” *J. Am. Chem. Soc.*, 2014, 138, 229–310.

Presentations:

13. **Derrick, J. S.** “A Redox-Active, Compact Molecule for Cross-Linking Amyloidogenic Peptides into Nontoxic, Off-Pathway Aggregates: *In Vitro* and *In Vivo* Efficacy and Molecular Mechanisms” Oral presentation, 117th Korean Chemical Society Meeting, Ilsan, South Korea, April, 2016.
12. **Derrick, J. S.**; Kerr, R. A.; Nam, Y.; Oh, S. B.; Lee, H. J.; Earnest, K. G.; Suh, N.; Peck, K. L.; Ozbil, M.; Korshavn, K. J.; Ramamoorthy, A.; Prabhakar, R.; Merino, E. J.; Shearer, J.; Lee, J.-Y.;

- Ruotolo, B. T.; Lim, M. H.; “A Redox-Active, Compact Molecule for Cross-Linking Amyloidogenic Peptides into Nontoxic, Off-Pathway Aggregates: *In Vitro* and *In Vivo* Efficacy and Molecular Mechanisms” Poster, 117th Korean Chemical Society Meeting, Ilsan, South Korea, April, **2016**.
11. **Derrick, J. S.;** Kerr, R. A.; Nam, Y.; Oh, S. B.; Lee, H. J.; Earnest, K. G.; Suh, N.; Peck, K. L.; Ozbil, M.; Korshavn, K. J.; Ramamoorthy, A.; Prabhakar, R.; Merino, E. J.; Shearer, J.; Lee, J-Y.; Ruotolo, B. T.; Lim, M. H.; “A Redox-active, Compact Tool for the Crosslinking of Amyloidogenic Peptides in Nontoxic Off-pathway Aggregates: *In Vitro* and *In Vivo* Efficacy and Molecular Mechanisms” Poster, 5th International Symposium on Metallomics, Beijing, China, September, **2015**.
 10. **Derrick, J. S.;** Lim, M. H. “Rational Development of Small Molecules that Target and Modulate Multiple Facets of Alzheimer’s Disease” Poster, 7th Asian Biological Inorganic Chemistry Conference, Gold Coast, Australia, December, **2014**.
 9. **Derrick, J. S.** “Rational Design of a Structural Framework with Potential Use to Develop Chemical Reagents that Target and Modulate Multiple Facets of Alzheimer’s Disease” Oral presentation, The Second International Symposium on Molecular Neurodegenerative Disease Research, Daejeon, South Korea, August, **2014**.
 8. **Derrick, J. S.** “Rational Development of Small Molecules that Target and Modulate Multiple Facets of Alzheimer’s Disease” Poster, The Second International Symposium on Molecular Neurodegenerative Disease Research, Daejeon, South Korea, August, **2014**.
 7. **Derrick, J. S.;** Lim, M. H. “Rational Development of Small Molecules that Target and Modulate Multiple Facets of Alzheimer’s Disease” Poster, BioMetals, Duke University, Durham, NC, July, **2014**.
 6. **Kerr, R. A.;** **Derrick, J. S.;** Beck, M. W.; Nam, Y.; Lim, M. H.; Ruotolo, B. T. “Ion Mobility-Mass Spectrometry for Screening Amyloid Formation Inhibitors within Rationally-designed Bifunctional Small Molecules Libraries” Poster, Protein Quality Control Pathways and Disease, Ann Arbor, MI, September, **2014**.
 5. **Kerr, R. A.;** **Derrick, J. S.;** Beck, M. W.; Nam, Y.; Lim, M. H.; Ruotolo, B. T. “Ion Mobility-Mass Spectrometry for Screening Amyloid Formation Inhibitors within Rationally-designed Bifunctional Small Molecule Libraries” Poster, The Annual American Society for Mass Spectrometry Conference, Baltimore, MD, June, **2014**.
 4. **Derrick, J. S.;** Lim, M. H. “Rational Development of Small Molecules that Target and Modulate Multiple Facets of Alzheimer’s Disease” Poster, Amyloid and Human Diseases: From Chemistry to Biology, Ann Arbor, MI, May, **2014**.
 3. **Derrick, J. S.;** Lim, M. H. “Rational Development of Small Molecules that Target and Modulate Multiple Facets of Alzheimer’s Disease” Poster, Chemistry Biology Interface Training Program Symposium, Ann Arbor, MI, March, **2014**.
 2. **Derrick, J. S.;** **McLane, M. J.;** Lee, S.; Zheng, X.; Krishnamoorthy, J.; Savelieff, M. G.; Park, H. M.; Brender, J. R.; Kim, J. H.; Kochi, A.; Lee, H. J.; Kim, C.; Ramamoorthy, A.; Bowers, M. T.; Lim, M. H. “Small Multifunctional Ligands as Chemical Tools to Uncover Molecular-Level

Insights into Metal-Free and Metal-Associated Amyloid- β Species in Alzheimer's Disease" Poster, UM Chemistry Undergraduate Poster Session, Ann Arbor, MI, October, **2013**.

1. **Derrick, J. S.; McLane, M. J.**; Lee, S.; Zheng, X.; Krishnamoorthy, J.; Savelieff, M. G.; Park, H. M.; Brender, J. R.; Kim, J. H.; Kochi, A.; Lee, H. J.; Kim, C.; Ramamoorthy, A.; Bowers, M. T.; Lim, M. H. "Small Multifunctional Ligands as Chemical Tools to Uncover Molecular-Level Insights into Metal-Free and Metal-Associated Amyloid- β Species in Alzheimer's Disease" Poster, Atomic View of Biomolecular Function Symposium, Ann Arbor, MI, July, **2013**.